UNIVERSITY OF SOUTHAMPTON

FACULTY OF ENGINEERING & THE ENVIRONMENT

Water and Environmental Engineering Group

Field Trials and Development of a Hydrostatic Pressure Machine

by

Nicholas Paul Linton

Thesis for the degree of Doctor of Philosophy

December 2013

Dedication

To my parents, Dr. Keith and Pamela Linton for the years of patient love and support they have lavished on their children

UNIVERSITY OF SOUTHAMPTON

ABSTRACT

FACULTY OF ENGINEERING AND THE ENVIRONMENT

Water and Environmental Engineering Group

Thesis for the degree of Doctor of Philosophy

FIELD TRIALS AND DEVELOPMENT OF A HYDROSTATIC PRESSURE MACHINE

Nicholas Paul Linton

Hydrostatic Pressure Machines (HPM), are a class of hydropower energy converter designed to operate at sites with heads below 3 meters; sites receiving increasing interest as the demand for power from renewable energy sources grows.

The HPM is a 'Pressure machine', applying the pressure produced by differing water levels at a site, directly to the blades of the device to extract power. Prior to the current research, these machines had only existing as laboratory models.

This thesis describes the design, construction and testing of a 5 kW prototype HPM installed at a re-activated mill site in Bavaria. Observations and performance test results from this full scale unit are then compared with the results of scale model tests carried out in the laboratory.

New theory is developed to account for the geometry of the prototype machine and the variations in water levels encountered during operation. This is found to give very good agreement with performance measurements from both prototype and model tests, with no scale effects identified between the scales over the normal operating range of the machine.

Several alternative rotor designs are tested at model scale, which demonstrate useful performance gains compared with the prototype machine.

Direct blade force and cell pressure measurements are also obtained during model operation which has increased our understanding of the energy exchanges taking place between rotor and fluid within the machine. This in turn helps to identify the key machine geometries which impact performance.

Table of Contents

ABSTRACT i

Table of Contents iii

List of Figures xiii

List of Tables xix

DECLARATION OF AUTHORSHIP xxi

Acknowledgments xxiii

Notation xxv

Chapter 1: Introduction 1

1.1 Context of this research 1

1.2 Scope of this Thesis 2

1.3 Structure of this Thesis 4

1.4 Claims for the current work 6

1.5 Publications Resulting from the Present Work 6

Chapter 2: Literature Review Part 1: - Low Head Hydropower. 7

2.1 Hydropower Basics 7

2.1.1 Power, Head and Flow 7

2.1.2 Energy Extraction Processes and Hydropower devices 8

2.1.3 Operating Ranges for Hydropower devices 15

2.2 Ultra Low Head Resources and Potential 17

2.2.1 Europe 17

2.2.2 World Wide: Irrigation Systems 18

2.3 Challenges of Ultra Low Head Development 19

2.3.1 Typical Installation and Flow Conditions 19

2.3.2 Costs and Economics 20

2.3.3 Environmental Impact 21

2.4 Ultra-low Head Hydropower Devices 22

2.4.1 Scope and Limitations. 22

2.4.2 The devices: 23

2.5 Summary 31

Chapter 3: Literature Review Part 2: Hydrostatic Pressure Machine Development & Theory 33

3.1 The basic characteristics of Hydrostatic Pressure Machines. 33

3.2 Historical Development 35

3.2.1 Zuppingerrad 1847 36

3.2.2 Saltford University Machines 1989 38

3.2.3 “Damming-up Effect Wheel” 2000 40

3.2.4 Brinnich’s Stem Pressure Machine 2001 41

3.2.5 Seniors’ HPM 2009 42

3.2.6 Linton MSc. Rotor Developments 2009 44

3.2.7 The HYLOW Project 2008 – 2012 46

3.3 HPM Theory 48

3.3.1 Published theory 48

3.3.2 Classical 2D Theory 48

3.3.2.3 Losses in the real machine 53

3.3.3 Limitations of Classical Theory 58

3.4 Summary & Gaps in Knowledge 60

3.5 Aims of this research 61

3.6 Research Objectives 62

Chapter 4: Field Trial Unit Design & Construction 63

4.1 Rationale behind the Prototype Unit 63

4.2 The Partenstein Site 64

4.2.1 Location and Lay out 64

4.2.2 River Flow Conditions 66

4.2.3 Selection of Design Flow 67

4.2.4Flood Conditions 68

4.3 Installation Design 69

4.3.1 Design Constraints 69

4.3.2 Description of Overall Scheme 69

4.3.3 Hydraulic Design 71

4.3.4 Mechanical Design of the HPM 73

4.3.5 Power Take Off and Control 76

4.3.6 Ancillary Equipment 81

4.3.6.3 Fish Pass 83

4.4 Installation Costs 84

Chapter 5: Performance Testing Methods 87

5.1 Flow Measurement Techniques 87

5.1.1 Sharp Crested Weir 87

5.1.2 Velocity Meters 89

5.1.3 HPM Rotor Speed 90

5.2 Water Level Measurements 90

5.3 Power Measurement 93

5.3.1 Electrical Output 93

5.3.2 Rotor Speed 94

5.4 Performance Test Methods 94
5.4.1 Inverter Control 94
5.4.2 Load Bank Control 95
5.5 Observation of Rotor Behaviour 96
5.6 Estimation and measurement of loss factors. 96
5.6.1 Hydraulic Losses – Leakage. 97
5.6.2 Friction and Transmission Energy Losses 98
5.6.2 Electrical Losses 102
Chapter 6: Field Test Results and Observations 103
6.1 Field Test Conditions 103
6.1.1 Overview 103
6.1.2 The 9/11 Test Series. 104
6.1.2 The 1/12 Test Series. 104
6.1.3 The 2/12 Test 104
6.2 Observations of Machine Behaviour 105
6.2.1 Inlet Channel Flows 105
6.2.2 Rotor Cell Filling and Blade Entry 106
6.2.3 Rotor Noise Production 110
6.2.4 Exit Flow 111
6.2.5 Rotor Speed Variations 113
6.2.6 PTO and Control System Behaviour 113
6.3 Performance Test Results 117
6.3.1 Flow Measurements 117
6.3.2 Power Output 118
6.3.3 Efficiency 121
6.3.4 Power and Efficiency 124
6.4 Estimation of Measurement Errors 126

6.4.1 Power Output Errors 127
6.4.2 Measured Head Errors 127
6.4.3 Flow Rate 127
6.4.4 Impact of Errors on Performance Curves 128
6.5 Summary 129
Chapter 7: Analysis and Review of Field Trials 133
7.1 Comparison with Classical Theory: 133
7.1.1 Modifications required for prototype 133
7.1.2 Comparison with 1/12A Data Set 135
7.2 HPM 3-D Theory 138
7.2.1 Geometry 138
7.2.2 Continuity Equations 139
7.2.3 Head Drop due to Flow 140
7.2.4 Pressure Forces on the Blade 140
7.2.5 Total 'ideal' torque and power 142
7.2.6 Turbulence Losses 142
7.2.7 Inflow Acceleration 143
7.2.8 Exit flow acceleration 144
7.2.9 Unvented Cell Losses 146
7.2.10 Losses due to partial ventilation 149
7.3 New Theory Compared with Prototype Data 152
7.3.1 The 1/12A Data Set 152
7.3.2 The 9/11 Data Set 155
7.3.3 Initial Conclusions 156
7.4 Overall engineering assessment of Prototype Unit 157
7.4.1 Performance 157
7.4.2 Costs 159

7.4.3 Environmental Impact 159
7.4.4 Engineering driven areas for development 160
7.5 Implications for the model test programme 161
Chapter 8: Model Scaling, Test Apparatus & Experimental Methods 163
8.1 Model Scaling 163
8.1.1 Hydraulic Similarity 163
8.1.2 Geometric Similarity 163
8.1.3 Dynamic Similarity – matching Froude number 164
8.1.4 Velocity & Time scaling arising from Froude Similarity 165
8.2 The Test Flume 166
8.2.1 Lay-out and flow control 166
8.2.2 Water Level and Discharge Measurement 167
8.3 Flume Installation 170
8.3.1 Installation Model 170
8.3.2 Machine Output Torque Measurement 170
8.4 Rotor Installation 172
8.4.1 Rotor Construction 172
8.4.2 Rotor Sensors 172
8.5 Calibration Methods 174
8.5.1 Water Level Readings 174
8.5.2 Hub Pressure Sensor 174
8.5.3 Strain Gauged Blade 176
8.5.4 Load Cells 176
8.6 Experimental Methods 177
8.6.1 Performance Testing 177
8.6.2 Modifications for alternate model Test Series 178

8.6.3 Estimation of Leakage 179
8.6.4 Estimation of Rotor Friction 179
Chapter 9: Performance Test Results & Analysis 181
Introduction & Navigation 181
9.1 Section 1: Test Conditions & Measures 181
9.1.1 Summary of Test Conditions 181
9.1.2 Model & Flume Behaviour 183
9.1.3 Parametric Performance Comparisons 189
9.2 Section 2: Scale Performance Tests 191
9.2.1 Performance Comparison of all Test Conditions 191
9.2.2 Hydraulic Parameter Comparisons 193
9.2.3 Further Comparison of 1/12A Test Condition: Theory and Data 196
9.2.4 Conclusions from Section 2 200
9.3 Section 3: Performance Improvement Testing 201
9.3.1 Deep Water Testing 201
9.3.2 Alternative Rotor Configurations 208
9.3.2.1 'Flap Wheel' Rotor 209
9.3.3 Conclusions from Alternate Rotor Test Series 217
Chapter 10: Cell Process & Rotor Energy Exchange Results 219
10.1 Introduction to Rotor Processes 219
10.1.1 The 'Four Stroke' Analogy 219
10.1.2 Cell Processes 220
10.2 'Time Series' Measurements 221
10.2.1 Limitations of the Data 221
10.2.2 Terminology 222
10.2.3 Low Speed Blade Moment and Hub Pressure Variations 223

10.2.4 The Power Generation Mechanism 225
10.2.5 Rotor Torque due to a Single Blade derived from Blade Bending Plots 226
10.2.6 Cell Processes compared with Rotor Torque Variations 228
10.2.7 Variation of Torque and Hub Pressures with Speed: 12 blade rotor 230
10.2.8 Comparison of 12 and 6 Blade Rotors 234
10.2.9 Variation of Torque and Hub Pressures with Speed: 6 blade rotor 236
10.2.10: Speed Variations in 6-Blade and 12 blade Rotors 238
10.2.11 Hub Pressure Variations with Downstream Water levels 241
10.2.12 Summary of Time Series Data 243
10.3 Video Observation Studies 244
10.3.1 Blade Entry 244
10.3.2 Cell Filling 247
10.3.3 Transit, Power and Cell Draining 249
10.3.4 Blade Exit 253
10.3.5 Summary of Key Findings from Video Observations 255
Chapter 11: Overall Discussion 257
11.1 Introduction 257
11.2 Prototype Machine – Highlighted Issues 257
11.3 Cell Processes 258
11.4 Blade Entry 259
11.4.1 Model Observations 259
11.4.2 Simplified Blade Impact Analysis 259
11.4.3 Summary of Blade Entry Findings 263
11.5 Cell Filling 264
11.5.1 An Important Process 264
11.5.2 Observed Behaviour 264
11.5.3 Simplified Cell Filling Analysis 265

11.5.4 Summary of Cell Filling Findings....270
11.6 Transit Phase....271
11.6.1 Observations....271
11.6.2 Implications for Design....271
11.7 Power Phase....272
11.7.1 Observations....272
11.7.2 Pressure Changes through the Working Section....272
11.7.3 Pressure – Blade Interactions in the 12 blade rotor....273
11.7.4 Summary of Power Stroke Findings....277
11.8 The Exhaust Phase....277
11.8.1 Drain Process....277
11.8.2 Blade Exit....278
11.8.3 Implications for Design....278
11.9 Output Torque Variations....279
11.9.1 Torque variations in the Complete Rotor....279
11.9.2 Implications for Design....281
12 Future HPM Developments....283
12.1 Introduction....283
12.2 Divergent Futures....283
12.2.1 Power Take-Off Design – the Strategic Factor....283
12.2.2 Accepting Low & Variable Speed – Developing the existing HPM Concept283
12.2.3 High Speed HPM Concepts....284
12.3 A Future for HPMs?....285
Chapter 13: Conclusions....287
Chapter 14: Recommendations....291
14.1 Scope....291

14.2 Modifications to Existing Full Scale Prototype 291

14.3 Fundamental Research Areas 294

14. 4 Future HPM Architectures 297

References & Bibliography: 299

Appendix: Basic Cell Process Theory 307

A.1 Introduction 307

A.2 Blade Entry 307

A.2.1 Characteristics 307

A.2.2Von Karman Analysis applied to HPM Blade Entry 307

A.2.3 Simplified Geometry 309

A.2.4 Simplified Impact Analysis 311

A.3 Cell Filling 313

A.3.1 Observed behavior 313

A.3.2 Simplified Cell Filling Model 315

A.3.4 Estimation of Blade Drag Forces 321

A.4.1 Pressure Changes through the working Section 323

Remarks: 326

List of Figures

2.1	Flow and Head in a River	7
2.2	Pure Potential Machines	10
2.3	Pelton turbine installation	11
2.4	Cur-Away of a Kaplan Turbine	12
2.5	Kaplan & Francis Runners & Draft Tube Fabrication	14
2.6	Hydraulic Motors from the 1800's	15
2.7	Hydrostatic Pressure Machine Compared with other Devices	16
2.8	Typical Low Head Hydropower Installations	20
2.9	Typical Installation Costs for Small Scale, Low Head Schemes	21
2.10	Baseline generation tariff degression	21
2.11	Archimedes Screw Turbines	23
2.12	Zuppinger Water Wheel	24
2.13	Steffturbine Trial Unit	25
2.14	Siphon Turbines	26
2.15	VLH Turbine	27
2.16	Schneider Lift Translator	28
2.17	Free Vortex Propeller Turbines	29
2.18	Gravitational Vortex Power Plant	30
3.1	Hydrostatic Pressure Machine – Test Model	33
3.2	The Generation of Blade Force in HPMs	34
3.3	HPM Performance from Model Tests	35
3.4	Zuppinger's Wheel from 1848	37
3.5	Bassett Under Water Turbine	38
3.6	Lay-out of the full size Underwater Machine	39
3.7	Performance results for "Damming-up Effect" Wheel	40
3.8	The Stem Pressure Machine	41
3.9	The Hydrostatic Pressure Wheel	42
3.10	Senior's HPM Model	43
3.11	Foreign Object entry into HPM models with rigid and flexible blades	44
3.12	Flexible Rotor	45
3.13	The HPM installation, River Iskar, Bulgaria	46

3.14	The 5kW HPM installation at Partenstein, Bavaria	47
3.15	HPM at the static condition	49
3.16	HPM in Operation	50
3.17	Performance of an “ideal’ HPM	52
3.18	Control Volume used for Momentum Analysis	53
3.19	HPM performance with losses	56
3.20	The effect of leakage on HPM performance	58
4.1	The Location of Partenstein	64
4.2	Mill House and Zuppinger Wheel, circa 1920’s	64
4.3	Overview of the Partenstein Site	65
4.4	Total flow at the mill in Partenstein (Lohr)	66
4.5	Flood Conditions at Partenstein Mill	68
4.6	General Layout of Partenstein Mill Scheme	70
4.7	:EstimatedHPM Performance Curve	71
4.8	Model Geometry, compared with Prototype Geometry	72
4.9	Leading Dimensions of the HPM Installation at Partenstein.	73
4.10	HPM Design	74
4.11	Blade Seal details:	75
4.12	Alternative Transmission Designs	77
4.13	The two belt drives used	78
4.14	HPM Control System	79
4.15	The Generator Sub Assembly	80
4.16	Inverter & Control System	81
4.17	Sluice Gate, with marine ply blade, and access platform	82
4.18	The Fish Screen	82
4.19	The Fish Pass	83
4.20	Larinier Super Active Baffle Fish Pass	84
4.21	Summary of Project Costs	85
5.1	General view of HPM installation	87
5.2	Velocity Measurement Equipment	89
5.3	Velocity Measurement Test section	89
5.4	The Water Level Measurement Station	91
5.5	Survey Levels of water measurement scales	92
5.6	Set up for electrical power measurements	93
5.7	Using the Fish Screen to throttle inlet flow during Inverter control tests	95

5.8	Test set up for Load Bank Control	96
5.9	Leakage Flows during Static Rotor Test	97
5.10	Measurement of rotor friction force	98
5.11	Variation of Electrical Efficiency with Generator Speed	102
6.1	Inlet Turbulence at 11.6 rpm	105
6.2	Cell Side Filling at 3.7 rpm	106
6.3	Cell Side Filling at 5.7 rpm	106
6.4	Local surface depression following blade entry at 6.3rpm	107
6.5	Blade splash at differing water depths at rotor speeds of 9 rpm	108
6.6	The violence of blade splash at 10.6 rpm	108
6.7	Re-circulating flow caused by blade entry at 6.7 rpm	109
6.8	Ventilation Reduction Test	111
6.9	Exit Flow Close to the wheel	112
6.10	Turbulent and asymmetric flow conditions in the exit channel	112
6.11	Comparison of Flow Measurement Techniques	117
6.12	Raw data plots for all prototype test conditions	119
6.13	Shaft Power variation with Rotor Speed – all prototype tests	120
6.14	Non Dimensionalised Performance parameters – all Prototype tests	121
6.15	HPM Efficiency:	122
6.16	Shaft Efficiency grouped according to downstream water level	123
6.17	Power & Efficiency Variation with Rotor Speed	125
6.18	The direct comparison of Parametric Power with Efficiency	126
6.19	The impact of Measurement Errors on Performance Plots	128
7.1	Geometry differences between theory and Prototype	132
7.2	Parametric Comparison of 1/12A Test Data and Theory	135
7.3	Absolute Comparisons of 1/12A Test Data and Theory	136
7.4	Complexity of Prototype Installation Geometry	137
7.5	Simplified 3D Installation Geometry	138
7.6	Blade Force Pressure Components	139
7.7	Inflow Acceleration Control Volume	142
7.8	Exit Flow Acceleration Control Volume	143
7.9	Unvented Cell Elevation	146
7.10	Unvented Acceleration Control Volume	147
7.11	Comparison of Measured Power with theory – 1/12A Data Set	151
7.12	Comparison of Measured Efficiency with theory – 1/12A Data Set	152

7.13	Impact of Leakage Flow to Parametric Performance – 1/12A Data Set	153
7.14	Comparison of Parametric Performance Measures with 3D Theory	155
7.15	Theoretical Loss Components – 1/12A Geometry and Levels	157
8.1	General dimensions of Test Flume	164
8.2	Schematic of model test flume flow controls and level measurements	165
8.3	Discharge Weir definitions	166
8.4	Coefficient of discharge	167
8.5	Non scale modification to inlet Channel floor	168
8.6	Model Test Flume Details	169
8.7	Scale model rotor during assembly	170
8.8	Detail of Rotor Mounted Sensors	171
8.9	Side view of wheel installation	172
8.10	Typical Hub Pressure Sensor Calibration Curve	173
8.11	Strain Gauged Blade Calibration method & typical curve	174
8.12	The Flume during a typical Performance Test	175
8.13	Estimation of Model Rotor Friction	177
9.1	Variations in Leakage Flow due to Downstream water-levels	182
9.2	Speed-Flow Curves for Later Tests	183
9.3	Speed-Flow Curves Errors in Early Tests	183
9.4	Speed-Flow Curves with Corrections	184
9.5	Variation in Output Torque During Rotation - 'Rubbing Torque'	185
9.6	Parametric Power Comparison between Prototype and Scale Model	189
9.7	Gross Flow Efficiency Comparison of Prototype and Model Test	190
9.8	Net Flow Efficiency Comparisons of Prototype and Model Tests	191
9.9	Comparison of Power and Head coefficients	192
9.10	Variation of Flow Coefficient with Head Coefficient	193
9.11	Parametric Comparison of 1/12A Test at Model & Prototype Scales	194
9.12	Theory and Data compared at Model & Prototype Scales	195
9.13	Absolute Measured Values Compared with Theory 1/12AModel	197
9.14	Deep Water Test Conditions	199
9.15	Parametric Comparison of Deep Water Test Series	200
9.16	Power and Efficiency Comparisons with Theory – Deep Water	201
9.17	'Flap Wheel' rotor during blade 'Deep Water' testing	202

9.18	'Flap Wheel' Rotor Performance in Deep Water Tests	203
9.19	6-Blade Rotor, DS-125 Test, with modified Exit Channel	204
9.20	6- Blade Rotor with Modified Exit Channel	205
9.21	'Flap Wheel' Concept	207
9.22	6-Blade Rotor compared with standard 12-Blade *Unit*	208
9.23	Direct Comparison of Alternate Rotor Power Outputs	210
9.24	Direct Comparison of Alternate Rotor Net Efficiencies	211
9.25	Parametric Comparison of Alternate Rotors	212
9.26	Alternate Rotor Tests Compared with Theory	214
10.1	The 'Four Stroke' Phases of HPM operation	217
10.2	Detail 'Cell Processes' during HPM operation	219
10.3	Time Series Terminology	220
10.4	Bending moment and hub pressure variations - low rotor speed	221
10.5	Form of Blade Bending Moment Measurements	223
10.6	Bending moments compared with derived shaft torque	226
10.7	Cell Process & Torque Variation Compared	227
10.8	Variation of Torque and Hub Pressure with speed: 12-blade rotor	230
10.9	Direct Comparison of 6 and 12 Blade Rotor Characteristics	233
10.10	Variation of Torque and Hub Pressure with speed: 6-blade rotor	235
10.11	Rotor Speed Variations in 6 and 12 Blade Units	237
10.12	Angular Velocity Variations for 6 Blade Rotor	238
10.13	The impact on Downstream Water Level on Hub Pressure Variation	240
10.14	Blade Entry of the Scale Model at Differing Speeds	242
10.15	Blade impact in Alternate Rotor Designs at High rpm	243
10.16	6-Blade Flap Wheel after Making contact with the upstream surface	244
10.17	The Cell filling Sequence	245
10.18	Change in Cell Filling Angle with Rotor Speed 6 & 12 Blade Rotors	247
10.19	Dwell, Power and Cell Drain Processes:	248
10.20	The interaction of Cell draining and the power stroke compared	249
10.21	Drag Forces During Blade Exit	252
10.22	'Water Lifting' due to the vertical velocity component of blades	253
11.1	Blade Motion simplified to vertical component only	257
11.2	'Added Mass' during blade impact	258
11.3	Comparison of Impact Theory with Model Test Results	259
11.4	Schematic of flow around advancing Blade	261

11.5	Schematic of Cell Filling Process	262
11.6	Initial stage of cell filling	263
11.7	Cell filling after water contact by the following blade	264
11.8	Comparison of Cell Filling Theory with Experimental Data	265
11.9	Blade Entry and Cell Filling Theory Compared with Measurements	266
11.10	Pressure Variation Assumed in the Analysis	270
11.11	The Working Section	271
11.12	Simple Pressure-Blade Theory compared to measurements	272
11.13	Higher Blade pressure differences in a 6 blade rotor	273
11.14	Schematic of the Cell Draining Process	274
11.15	Combined Output Torque at 1/12A test condition	277

A.1	Von Karman 'Added Mass'	298
A.2	Actual HPM Blade Geometry	299
A.3	Blade Motion simplified to vertical component	299
A.4	Limits of rotation used in Impact analysis	300
A.5	'Added Mass' at an instant	300
A.6	Schematic of flow around advancing Blade	303
A.7	Schematic of Cell Filling Process	304
A.8	Simplified Blade Geometry for Cell Filling	305
A.9	Conditions at start of Cell Filling	306
A.10	Initial stage of cell filling	307
A.11	Cell filling after water contact by the following blade	310
A.12	The point of leading cell closure	313
A.13	During the power stroke, with the leading cell on the point of opening	313
A.14	At the end of the 2nd stage of the power stroke	314
A.15	Leading cell vented to atmosphere, negative blade torque occurs	315
A.16	Higher Blade pressure differences in a 6 blade rotor	316

List of Tables

2.1	Hydropower Classifications by Head	8
2.2	Hydropower Classifications by Power Output	8
4.1	Flow Summary – Partenstein Mill	67
4.2	Summary of Project Costs	84
5.1	Summary of Rotor and Transmission Friction -Torque	100
6.1	Summary of Prototype Field Test Conditions	103
6.2	Full Summary of Prototype Test Results	130
9.1	Summary of Model Test Conditions	180
9.2	Summary of 'Deep Water' Test Conditions	181
9.3	Comparison of Leakage Flow Rates for 1/12A Test Condition	196

DECLARATION OF AUTHORSHIP

I, Nicholas Paul Linton declare that this thesis entitled *Field Trials and Development of a Hydrostatic Pressure Machine* and the work presented in it are both my own, and have been generated by me as the result of my own original research.

I confirm that:

1. This work was done wholly or mainly while in candidature for a research degree at this University;
2. Where any part of this thesis has previously been submitted for a degree or any other qualification at this University or any other institution, this has been clearly stated;
3. Where I have consulted the published work of others, this is always clearly attributed;
4. Where I have quoted from the work of others, the source is always given. With the exception of such quotations, this thesis is entirely my own work;
5. I have acknowledged all main sources of help;
6. Where the thesis is based on work done by myself jointly with others, I have made clear exactly what was done by others and what I have contributed myself;
7. Part of this work have been published as Muller, Linton & Schneider, 2012

Signed:.....

Date:.....

Acknowledgments

A great many people have very kindly aided me over the four years of work represented by this thesis.

First my thanks go to my supervisors: Dr. G Muller for enabling me to join the project in the first place and, Dr. W Batten for his practical help and advice during the complex laboratory test programme.

Mention must also be made of the extraordinarily generous hospitality give to the me by the Kunkel family: Jurgen, Simone, Jonass and Michael, who tolerated the disruption caused by having a research project based in the back garden of their home, supplied the workforce with endless cups of coffee and pieces of cake and, introduced the 'friendly Englishman' to the welcoming community of Partenstein.

Thanks also go to my good friend Phil Woodward and my brother Tim Linton who kindly gave up big chunks of their annual leave to give me the benefit of their considerable engineering skills and shear hard work as we got the prototype installation up and running.

I was also privileged to work with other students from TU Darmstadt over the course of this project. Silke Schneider helped me run prototype performance tests, often working for hours in freezing rain to obtain flow measurements as well as acting as my personal travel agent making arrangements for countless trips to Partenstein and Fammersbach. I also worked with both Sagun Paudel and Olivier Schwyzer during their own research projects, which I very much enjoyed and always found our discussions stimulating.

Thanks must also go to my father, Dr. Keith Linton for his many hours proof reading this manuscript – any errors remaining are entirely my own.

Finally I must also acknowledge the skilled craftsmanship of Earl Peters in the Civil Engineering workshop for his help with the tricky bits of the model making and Karl Scammell who gave me the run of the Hydraulics lab and his office throughout the period of these studies. Karls' cheerful advice and constant banter helped keep me sane, during the many long and sometime frustrating, hours in the laboratory – particularly when things were going horribly wrong!

Notation

Symbol	Definition	Units
ΔF_{rvent}	net increase in acceleration force due to lack of ventilation	N
Δh_1	Head drop due to increase in dynamic head immediately upstream of Station 'T'	m
$\Delta P_{exitvent}$	Change in acceleration power loss due to lack of cell ventilation	Watts
Δt	time increment	s
ΔVol_{in}	Volume of fluid entering cell over a small time period	m^3
$A_{in\theta}$	Area along the perimeter of blade through which fluid may enter during cell filling	m^2
be	Effective width of weir	m
$BF_{A,B,C}$	Blade force arising from pressure areas A, B or C	N/m^2
bl	blade length from hub to outside diameter	m
C_D	Empirical loss coefficient	-
C_d	Discharge coefficient	-
C_{dis}	Discharge Coefficient applied during cell filling	-
CDQ	an empirical coefficient, representing the portion of cell volume that may drain in one second	1/s
$cr_{A,B,C}$	centrod radius from rotor axis of area A, B or C	m
C_{T3D}	Empirical loss coefficient for a 3 dimensional machine	-
D	Outside diameter of rotor	m
d_1	Elevation of upstream surface above datum	m
d_2	Elevation of downstream surface above datum	m
$D_{blade\theta}$	Depth of blade below upstream surface at angle θ	m
$D_{cell\theta}$	Depth of fluid in the cell at angle θ	m

F	Froude Number	-
F_{3Dacc}	Force required to accelerate fluid in a 3 dimensional machine	N
F_{acc}	Force required to accelerate in flow	N
F_{blade}	Force exerted on blade	N
F_{dse}	External force due to downstream water pressure acting on exit control volume	N
F_{Hub}	Force exerted on Hub	N
F_{Hubacc}	Force acting on the control volume due to the hub during in flow acceleration	N
$FillRatio_{\theta}$	The fraction of total cell volume filled with fluid at angle θ	-
F_{net}	Net force on blade after losses are accounted for	N
F_{p}	Force due to action of fluid pressure	N
F_{pdown}	Blade force due to downstream pressure	N
F_{pe}	External force in direction of rotation at rotor exit acting on control volume	N
F_{pevent}	External force in direction of rotation at rotor exit acting on control volume of unvented cell	N
F_{pnet}	Net Force on blade due to water pressures	N
F_{rotor}	Combine acceleration and pressure force considered to be acting on the rotor	N
F_{rvent}	Combine acceleration and pressure force considered to be acting on the rotor of an unvented cell	N
F_{side}	Force acting on fluid due reaction at Stub Weirs / Side plates	N
F_{turb}	Opposing Force applied to the rotor representing turbulence losses	N
F_{turb3D}	Opposing Force applied to the rotor representing turbulence losses for the 3 dimensional machine	N
F_{us}	Force acting of the fluid due to upstream water pressure	N
F_{x}	Component of force in 'x' direction	N
F_{θ}	Force on blade at angle θ	N

g	acceleration due to gravity	m/s^2
GFT	Gearbox Friction Torque - derived from measurement	Watts
H	Head	m
h	Height of flow surface above weir crest	m
h_e	Effective head of water surface above weir crest	m
k_h	Surface tension and viscosity correction factor	m
L	Angular Momentum	Kgm^2/s
L_m	Unit of length used in model	m
L_p	Unit of length used in prototype	m
m	mass	Kg
$\dot{m}$	mass flow rate	Kg/s
Mom_θ	Momentum at angle θ	Kg m/s
N	Number of blades in rotor	-
n	Revolutions of rotor completed per second	1/s
P	Power	Watts
p	Pressure	N/m^2
$p_{a,b\& c}$	pressure at points a, b & c	N/m^2
p_{bav}	average' pressure acting over area of blade	N/m^2
p_{closed}	pressure in a 'closed' cell in the working section	N/m^2
P_{exit}	Power loss due to exit flow acceleration	Watts
P_{flow}	Power contained in fluid passing through machine	Watts
P_{ideal}	Power of ideal machine, with no energy losses	Watts
$P_{ideal3D}$	Ideal Power output from 3 dimensional machine	Watts
$p_{inner\theta}$	pressure on the blade due to contents of cell at angle θ	N/m^2
$Pitch_{cell}$	Pitch length between adjacent blades measured at the mean radius	m
$PL_{gearbox}$	Mechanical power loss in gearbox	Watts
PL_{rotor}	Mechanical Power Loss in Rotor	Watts
P_{max}	The maximum Power output obtained	Watts

P_{net}	Net Power output after hydraulic losses are accounted for	Watts
P_{norm}	Normalized Power	-
$p_{outter\theta}$	pressure acting ahead of the blade at angle θ	N/m²
$P_{partial}$	Power loss due to partial ventilation of a cell	Watts
P_{unvent}	Total additional power loss in a fully unvented cell	Watts
p_{up}	pressure acting on upstream side of blade	N/m²
P_{zvent}	Power loss due to elevation increase	Watts
Q	Volume Flow Rate	m³/s
Q_{drain}	Constant exit flow rate assumed in partially vented cell	m³/s
Q_{gross}	Total Flow passing through the installation including leakage	m³/s
Q_L	Leakage flow rate ata given operating point	m³/s
Q_{L0}	Leakage flow rate with the rotor stationary	m³/s
$Qmax$	The maximum theoretical discharge	m³/s
Q_{net}	Flow rate passing through the rotor	m³/s
Q_θ	Volume Flow Rate entering cell at angle θ	m³/s
r	radius from axis of rotation	m
r_0	Radius of surface of Hub tube from rotation axis	m
RFT	Rotor Friction Torque - derived from measurements	Nm
r_{mean}	radius of blade centroid from axis	m
rpm_m	Rotor speed in model - revolutions per minute	1/minute
rpm_p	Rotor speed in prototype - revolutions per minute	1/minute
r_{tip}	Radius of outer edge of blade from rotor axis	m
T	Torque	Nm
t	time	s
T_{acc}	Torque about rotor axis due to force required to accelerate fluid in 3 dimensional machine	Nm

$T_{cell\theta}$	Torque about rotor axis due to pressure forces on blade during cell filling at angle θ	Nm
$T_{FA,B,C}$	Torque about rotor axis due to area A, B or C	Nm
T_{ideal}	Torque due to blade pressure forces without losses	Nm
T_m	Time experienced in model	s
T_p	Time experienced in prototype	s
T_θ	Torque about rotor axis at angle θ	Nm
V	velocity	m/s
v_1	Horizontal Velocity at station 1	m/s
v_2	Horizontal Velocity at station 2	m/s
V_{drain}	Volume of fluid able to leave cell before ventilation occurs	m^3
$V_{in\theta}$	Velocity of fluid entering cell at angle θ	m/s
V_m	Mean velocity in model	m/s
v_{max}	The maximum theoretical velocity of fluid achieved at a given set of water levels	m/s
Vol_{blade}	Volume displaced by the structure of a single blade	m^3
$Vol_{cell\theta}$	Volume of fluid in the cell at angle θ	m^3
$Vol_{Total\theta}$	Total Volume of cell at angle θ	m^3
V_p	Mean velocity in prototype	m/s
VR_{belt}	Velocity Ratio - Belt drive	-
VR_{Gbox}	Velocity Ratio - Gearbox	-
V_T	Velocity at blade centroid at bottom dead centre of rotation	m/s
V_θ	Tangential Velocity Component ('whirl')	m/s
W_1	Width of channel at station 1	m
W_2	Width of channel at station 2	m
$work$	work done	joules
WS_{z0}	Upstream Water surface elevation above rotor axis	m

W_T	Width of Rotor	m
X	The Scale used for model geometry	
Z	elevation above a reference level	m
Z_{vent}	Increase in elevation occurring in cell prior to ventilation	m
α	Angle	radians
α'	Corrected angle of blade inclination from the horizontal	radians
η	Efficiency	-
η_{hyd}	Hydraulic Efficiency power excluding mechanical losses compared with flow passing through the machine	-
η_{ideal}	Efficiency of ideal machine with no energy losses	-
η_{out}	Overall efficiency	-
η_{vol}	Volumetric efficiency	-
θ	Angle of rotation from Top Dead Centre	radians
θ_{fc}	Rotor angle at which the blade first contacts the surface of upstream water	radians
θ_{follow}	Rotor angle at which following blade contacts the water surface	radians
Π_1	Discharge Coefficient	-
Π_2	Head Coefficient	-
Π_3	Power Coefficient	-
ρ	density	Kg/m^3
φ_{vent}	Angle after bottom dead centre at which ventilation of cell takes place	radians
ω	angular velocity	rads/s

Chapter 1: Introduction

1.1 Context of this research

Hydropower remains the world's most significant renewable source of electricity accounting for some 19% of world-wide production (Paish, 2002).

Highly developed turbine designs are widely available for sites with heads ranging from 5 to 1800 meters and, the rate of resource development over the last 100 years has been very high (Gulliver & Arndt, 2005).

However, the potential to further increase hydropower capacity with these technologies is becoming limited by the dwindling availability of suitable sites. This, combined with the continued drive to develop low carbon sources of energy, has led to increased interest in very low head sites, the development of which has hitherto been largely neglected, due to their modest power outputs (DoECC Hydropower Resource Assessment Report, 2010).

While the number of potential very low head sites is large, the choice of available energy converters suitable for this application is strictly limited. Although a number of innovative devices are available, a dominant technology has yet to emerge and considerable scope for innovation remains in this area (Eichenberger et. al. 2011).

The Hydrostatic Pressure Machine (HPM) is one such very low head energy converter technology, first studied by Senior& Muller at laboratory scale (Senior et. al. 2008). An unusual energy extraction principle was identified in the machines and preliminary theory developed.

Following on from this early work, the HYLOW project was launched as a wide ranging collaborative programme of research between 7 European Universities undertaking a series of laboratory studies, field trails and environmental impact assessments of the new technology.

1.2 Scope of this Thesis

This thesis is the result of a four year programme of research carried out at the University of Southampton, both during and subsequent to the completion of the HYLOW project.
The specific aims and objectives for this project are formally presented following the literature review in Chapter 3.

However, the authors' overall goal in undertaking this research was primarily to add sufficiently to the current level of knowledge to enable the design of future, full scale HPM devices, to be carried out reliably and be able to achieve higher levels of performance than is possible at present.This is regarded as an essential pre-cursor to development of these machines as viable hydropower devices.

This goal required a wide range of issues to be addressed and the following principle activities have been carried out:

- Design and installation of a full scale 5KW prototype unit for field trials, complete with mechanical power take off, generation, control and ancillary equipment to permit supply of electricity to the local grid network.
- Completion of performance testing and detail observations of HPM behaviour over a wide range of flow conditions.
- Accumulation of considerable operational experience with the field trial unit leading to the identification of several important limitations in the existing HPM concept.
- Refurbishment of the existing model test facility at The University of Southampton.
- Constructing of an exact 1/6 scale model of the field trial HPM, fully instrumented for detail laboratory testing.
- Completion of model performance testing for direct comparison with field test results and the assessment of the impact of Scale Effects.
- Direct measurements of blade force and pressure variations occurring during rotation of model machine under a range of operating conditions to permit changes in energy extraction processes to be assessed.

- Accumulation of video test evidence to study detailed aspects of rotor-fluid interactions during HPM operation.
- Design, construction and model testing of alternate HPM rotors with a view to increasing performance over the original base unit.

This research has a very strong practical, experimental and observational bias to the approach adopted. This has been deliberate: the development of HPMs are in their infancy, with very limited supporting theory currently available and careful observation of detailed physical behaviours occurring in and around the device is an essential precursor to future theoretical development.

Since a large portion of the work carried out in this research has involved the design and construction of a prototype HPM device, and since this machine will continue to be used for research purposes by other teams, the author has also endeavoured to describe the design of this installation in considerable detail.

Partly this is to ensure that the technical development of this installation is properly recorded, but primarily the intent has been that armed only with this thesis, future designers should be able to improve the performance of the next generation of devices. For this reason also, short comings in the current HPM design are highlighted along with the limitations in the accuracy and repeatability of experimental performance data. In engineering design, more is usually learned from tests that fail than from tests that succeed (Reinertsen 2001) and "In the history of everything that works was a time when it didn't" (McGarry 1999): and as shall be seen as this thesis progresses, teething troubles encountered with the prototype machine have led directly to increased understanding of the hydraulic events occurring within it, and suggest improvements to basic machine design.

1.3 Structure of this Thesis

To aid the reader in navigating this document, the contents of this thesis are outlined below.

1. **Introduction** – this section.

2. **Literature Review Part 1 : Low Head Hydropower -** this puts the work into the wider context of existing technology, particularly ultra low head energy extraction developments and the potential world wide applications for such devices. Readers pressed for time and thoroughly familiar with this field may skip past this chapter.

3. **Literature Review Part 2: Hydrostatic Pressure Machine Development& Theory** – the long development of hydrostatic pressure machines is traced before the 'classical' theory for these devices is presented in a modified form. Specific gaps in knowledge are identified and the specific research aims and objectives for the present research developed. This marks the limit of previous work and all chapters from this point on represent original contributions to knowledge made by this research.

4. **The field Trial Unit Design and Construction** – this chapter describes the full scale prototype unit. It also highlights ways in which the hydraulic design of the prototype were compromised compared with earlier test model geometries – an important reference point for interpreting subsequent results.

5. **Performance Field Testing Methods** – explaining what was measured and how, and the basis for the estimations made in interpreting data readings.

6. **Field Test Results and Observations** – are presented and partially interpreted in this chapter since they inform subsequent model testing.

7. **Analysis & Review of Field Trials:** –field trial unit results are compared with existing theory, and new theory developed which better accounts for the observations made. The prototype unit is then critically reviewed to identify key areas for future developments in both theory and design. This is a key chapter in this work.

8. Model Scaling, Test Apparatus & Experimental Methods – describing the design and construction of the model test equipment and instrumentation, along with the experimental methods and calibration techniques employed.

9. Performance Test Results and Analysis – data from scale model performance tests are presented and compared with those for the prototype machine. The presence of scale effects is investigated, and the new theory used to predict performance at both model and prototype scales under a range of operating conditions. Modified rotor designs are also tested and compared with the base unit and modified theory. This is another key chapter in this research.

10. Cell Process & Rotor Energy Exchange Results – consisting primarily of the presentation and analysis of direct rotor blade force and pressure measurements along with detailed observations made from the video record. Detailed and often subtle deductions regarding the energy exchange processes taking place within the machine are made here.

11. Overall Discussion – the understanding gained through the experiments is highlighted and the implications of this knowledge to HPM rotor and installation geometry highlighted.

12. Practical Application to Future HPM Developments– how the knowledge gained by this research may influence future stages of HPM development is briefly considered and two divergent approaches suggested.

13. Conclusions and Recommendations

Appendix - simple cell process theory representing blade impact, cell filling and power extraction stages of rotation are developed. Since this theory is only preliminary it is presented here to aid future workers.

1.4 Claims for the current work

The author believes the work described in this thesis, makes the following original contributions to scientific knowledge:

1. The worlds' first full scale, grid connect installation of a Hydrostatic Pressure Machine has been constructed and performance test data obtained.
2. Important operational weaknesses in this design have been identified.
3. New performance theory has been developed, accounting for the 3-dimmensional geometry of a real machine, the effect of variations in downstream water level and the presence of inadequate cell ventilation. This theory has been found to successfully predict measured power and efficiency levels at both model and prototype scales.
4. Performance results for an exact scale model have been compared with those of the full size prototype which have enabled the impact of scale effects to be properly assessed.
5. Blade torque and hub pressure variations occurring during rotation within the model scale machine have been measured under a range of operating conditions.
6. Detailed observations have revealed a number of energy exchange processes occurring between the rotor and fluid during machine operation –these have been identified and presented in a form that aids the selection of suitable installation geometry.

1.5 Publications Resulting from the Present Work

1. Müller, G., Linton, N. und Schneider, S. (2012): Das Projekt Hylow: Die Wasserdruckmaschine Feldversuche mit einem Prototypen (The project Hylow: The hydrostatic pressure machine, field tests with a prototype), KorrespondenzWasserwirtschaft – KW, No. 1, p. 22 – 39.

2. Paudel, S., Linton, N., Zanke, U., Saenger, N., (2013): Experimental investigation on the effect of channel width on flexible rubber blade water wheel performance, Renewable Energy, Vol. 52 p. 1-7

Chapter 2: Literature Review Part 1: - Low Head Hydropower.

2.1 Hydropower Basics

2.1.1 Power, Head and Flow

The two characteristics of a body of water from which energy is to be extracted that define the potential available power are the "*Flow Rate*" referring to the volume of water available per second for power extraction and the vertical drop or *"Head"*, available between upstream and downstream sections of the river or water channel (Figure 2.1).

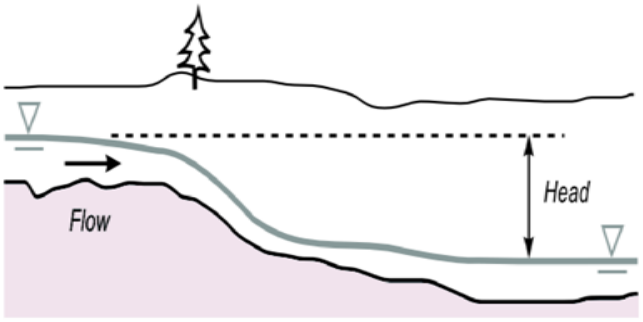

Figure 2.1: Flow and Head in a River *(Senior, 2009)*

The power *(P),* which can be extracted from the flow by any hydropower machine, is given by:

$$P = \eta \rho g Q H \qquad (2.1)$$

where:

η is the decimal *Efficiency* of the device

ρ is the *density* (for water =1000kg/m^3)

g is the *acceleration due to gravity* (m/s^2)

Q is the *Flow Rate* in cubic meters per second

H is the *Head* in meters

The engineering challenge in hydropower is to devise cost effective installations where the efficiency is as high as possible for a given set of site conditions. High head water sources (for example in mountainous regions) are by far the easiest resources to exploit; the energy is in a very 'concentrated' form and large amounts of power can be

extracted from compact powerful turbines. The low head resources of a typical river require much larger volumes to be processed in order to extract useful amounts of power. With the large energy conversion devices and supporting structures required, the economics of such schemes are often marginal.

Hydropower schemes are subdivided in two ways. The first classification is according to head available at a site which helps to identify the most suitable types of turbine to be used. Exact classifications vary across the industry, but the definitions used in this report are shown in Table 2.1.

Table 2.1: Hydropower Classifications by Head

Classification	High	Medium	Low	Ultra Low
Head (m)	>50	10-50	4-10	<3

The second classification is according to the power output of the installation which gives a good indication of the installation costs and complexity that can economically be supported by a particular site. Once again, there are no industry wide definitions: the classifications used in this report are shown in Table 2.2. In the UK, the majority of low head projects would fall into the 'Micro-hydro' and "Pico-hydro" categories (Bacon, 2004), while the experimental Hydrostatic Pressure Machine described in this report, can be placed in the micro and Pico-hydro category.

Table 2.2: Hydropower Classifications by Power Output

Classification	Small	Mini-hydro	Micro-hydro	Pico-hydro
Power	>10MW	>2MW	<100kW	<5kW

2.1.2 Energy Extraction Processes and Hydropower devices

From equation 2-1 it can be seen that all hydropower is derived from the potential energy of the flow, i.e. the energy released as the mass of the fluid falls under the acceleration due to gravity. However, a fundamental property of a fluid is that the energy contained in it, exists in three components; *potential* energy, as already described, *kinetic* energy derived from the velocity of the fluid's motion and the energy

contained in the *pressure* of the fluid. For an *"ideal"* fluid, while the total energy content of the fluid must remain constant (the principle of conservation of energy), the proportion of each energy form changes in response to hydraulic conditions, and can, to a large extent be manipulated by the hydropower designer. In practice, of course, the behaviour of real fluids results in losses as exchanges take place between the energy forms, and the key judgment in hydropower machine selection is to best match the performance of a device, to the prevailing conditions of the site, whilst keeping these losses to a minimum. Mathematically we can represent the *energy per unit mass* of fluid using the *Bernoulli Energy equation*, here presented in the hydraulic engineering form:

$$Z \quad + \frac{V^2}{2g} + \frac{p}{\rho g} = Constant = Total\ Energy \tag{2.2}$$

where:

Z = elevation (m) g = acceleration due to gravity ρ = fluid density (Kg/m^3)

V = velocity of the flow (m/s) P = pressure in the fluid (N/m^3)

The three terms on the left hand side of this equation express the proportion of energy in the fluid in each form, here expressed as "heads" with units in meters.

The Z term is the *static head* and expresses the *potential* energy of the flow, the $V^2/2g$ term is the *dynamic head* and reflects the *kinetic* energy content, while the $p/\rho g$ term is the *pressure* head due to the pressure energy content of the fluid.

All hydropower devices extract energy making use of one or more of these energy forms (Bodmir, 1895).

Potential devices use the potential energy of the Z term, to directly drive the power output shaft of the machine. Work is done against an applied load as water, usually contained in buckets, falls under gravity. Good examples of this kind of device are shown in the overshot water wheel and highly unusual "Chain Turbine" in Figure 2.2. In both of these devices, dynamic and pressure head content of the flow is not recovered.

Figure 2.2: Pure *Potential* Machines: a & b. Yiu Hwa Chain Turbine *(Nguyen Minh Duy, 2012)*, **c. Overshot water wheel** *(HydroWatt)*.

Impulse turbines use the transfer of *kinetic* energy that takes place when fast moving water strikes the blades or buckets of a rotor, to extract power. At high-head hydropower sites, the potential energy of fluid is first converted to pressure energy in the penstock pipe, and, then to kinetic energy as water is passed through a series of nozzles. These produce high speed water jets impacting the buckets of *Pelton*, or *Turgo* type runners driving against an external load. Figure 2.3 shows a Pelton installation for the Jostedal Power plant in Norway (28.5 m^3/s flow rate, 1130 m head and 288MW power output) alongside the *Pelton* runner for a 1 MW machine at the Bieudron Power Plant in Switzerland, examined by the author during maintenance.

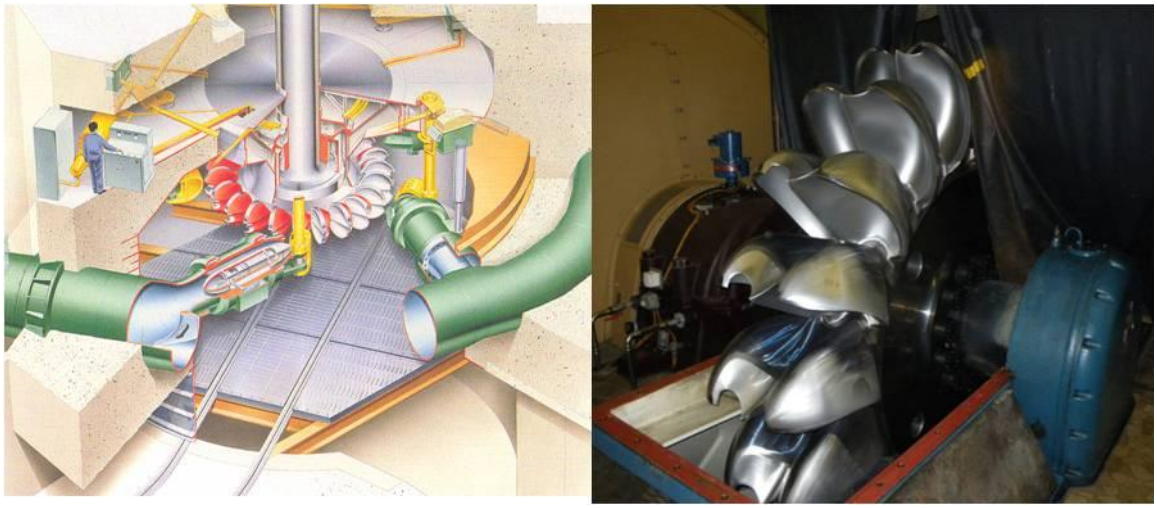

Figure 2.3: *left* - **Pelton turbine installation at the 1130 m head Jostedal Power Plant in Norway** *(Krogstadt, 2009), right* **- 1MW turbine runner at the Bieudron Power Plant, Switzerland, undergoing maintenance** *(the author).*

Reaction, or ***Over Pressure***, turbines retrieve power from both the *kinetic* and *pressure* components of total fluid energy. The two most common forms of reaction turbine are the *Francis* (first developed in 1849) and the *Kaplan*, first patented in 1913 (Hansson, 1977). Both of these devices share a similar inlet design, and a cut-away view of a *Kaplan* unit is shown in Figure 2.4.Water enters the *spiral casing* which surrounds the turbine, steadily accelerating the fluid as it is distributed evenly around the inlet to the rotor area. A series of movable *wicket gates* controlled via a *Finc ring*, direct the flow towards the rotor at the most efficient angle for the given operating conditions.

A portion of the *pressure energy* of the fluid is converted into *kinetic energy* of the flow during this process, and together with the adjustable guide vanes, the spiral casing imparts a considerable tangential velocity component (V_θ) to the inflowing water, (termed "whirl"), before the water enters the turbine casing. At this point, referring to Figure 2.4, water is flowing radially, from the spiral casing towards the shaft of the turbine runner.

Francis and Kaplan turbines differ in their operating principal at this stage. In a Kaplan turbine, the shaping of the shaft cover in the whirl chamber turns this flow so that it

enters the propeller-like runner axially, in the direction of the shaft, while in a Francis machine, the flow is turned within the runner itself, entering radially and leaving in an axial direction.

To aid the discussion of potential improvements to HPM designs described in later chapters, basic turbo-machine theory covering the energy exchange that takes place as the whirling water passes through the runners of the turbine will be considered here.

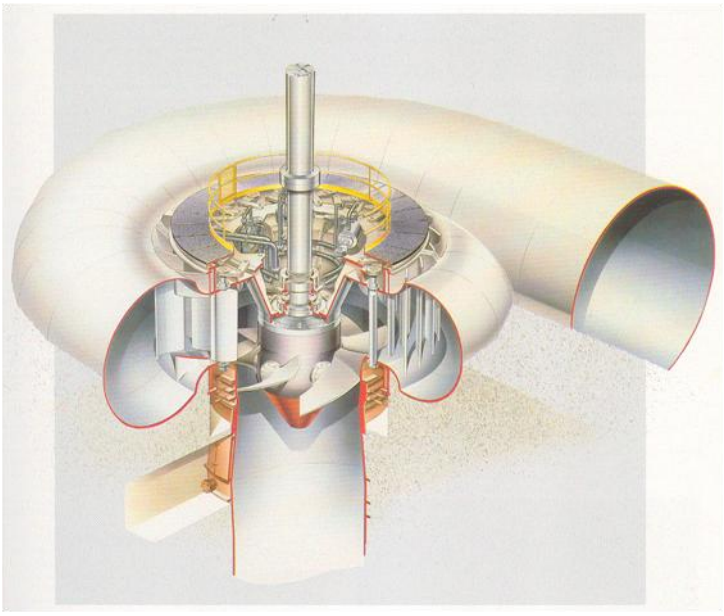

Figure 2.4: Cut-Away of a Kaplan Turbine *(Krogstadt, 2009)*

From Newtons' second law, Torque (T) can be defined as the rate of change of angular momentum:

$$T = {}^{dL}/_{dt} \tag{2.3}$$

Angular momentum (L) is defined as the moment of momentum:

$$L = mV_\theta r \tag{2.4}$$

Where m represents the mass of fluid at radius r from the axis.

If no mass is lost or gained by the system, the Torque produced between the inlet and outlet of the turbine is given by:

$$T = \frac{(m_2 V_{2\theta} r_2 - m_1 V_{1\theta} r_1)}{t} = \dot{m}(V_{2\theta} r_2 - V_{1\theta} r_1) \tag{2.5}$$

where $\dot{m}$ is the *mass flow rate* per second passing through the machine. From basic mechanics, Power is torque times rotational speed (ω):

$$P = T\omega = \dot{m}\omega(V_{2\theta}r_2 - V_{1\theta}r_1) \qquad (2.6)$$

To make this equation more generalised, it is useful to consider the energy exchange occurring per unit mass of fluid, so dividing the equation through by the mass flow-rate, results in the *Euler Work Turbo-machine Equation*:

$$Work = \omega(V_{2\theta}r_2 - V_{1\theta}r_1) \qquad (2.7)$$

This equation is fundamental to all turbo machines and we note the following (Ingram, 2009):

1. The equation yields negative values for a turbine extracting energy ***from*** the flow, with positive ones for compressors doing work ***on*** the flow.
2. The power input and output is entirely due to the change in the tangential velocity component. This is important, since maximum power will result when the whirl component at the exit of the machine falls to zero. While fixed geometry can achieve this condition at one flow rate, the ability to alter the wicket gate angles extends this range of conditions much further for the Francis, while the ability to change the angle of the turbine runner blades themselves in the Kaplan turbine (the Francis runner being fixed), extends the efficient range of operation further still.
3. Since power is a product of mass, radius and tangential velocity, the radius of the machine has an impact on power output and radial flow machines like the Francis, tend to deliver more power for a given size than axial flow devices such as the Kaplan.

The principle energy exchange mechanism for both machines is through the reaction of the rotor to the momentum exchange that occurs as the flow is turned by the hydrodynamic lifting forces around the runner blades. *Kinetic* energy is exchanged as the whirl velocity component is removed from the flow, *and* a considerable *pressure* drop occurs across the rotor to compensate for the energy extracted.

Water leaves these machines at considerable velocity, the kinetic energy of which would be lost to the system were it not for the draft tube, (first used on Jonval turbines in 1843). The draft tube smoothly expands the water passage, slowing the exit water producing a reduction in pressure at the exit to the turbine runner. This reduction in

pressure (the so called *suction head*), increases the available head difference across the hydropower machine and permits a proportion of the kinetic energy in the exit flow to be recovered, boosting overall system efficiency.

Examples of Kaplan and Francis runners, together with a draft tube under construction are shown in Figure 2.5.

Figure 2.5: a. Large Kaplan runner *(Voith Hydro)*, **b. Francis runner from the 710 MW Three Gorges Project, China** *(Krogstadt, 2009)*, **c. Draft Tube Fabrication,** *(NHE Nepal).*

What should be clear from the above description is the complexity and number of energy exchanges taking place in reaction turbines. High efficiencies depend on exploiting the available energy contained in both the kinetic *and* pressure constituents of the flow - a point that we will return to in later chapters when we consider the future development of HPMs.

In ***pressure*** machines, energy is extracted by using the hydrostatic pressure of the fluid directly to act against an external load acting though a blade or piston, moving in an enclosed cylinder or passageway. Such machines are *positive displacement* devices – the volume of fluid passing through the pistons is directly proportional to the speed of the piston, and so machine speed must change if flow rate is altered. The energy contained in the motion of the fluid is lost to the system, as is the energy required to overcome turbulence and friction as fluid enters the working chamber. Such machines, therefore, must operate at comparatively low speeds.

Figure 2.6 shows two such devices dating from the 1800's: the Schmidt Hydraulic Motor resembling a stationary steam engine using pressurised water fed to a double

acting cylinder to extract power, and the Armstrong Rotary Motor, thought to be the first rotary hydraulic machine to be constructed, built in 1838.

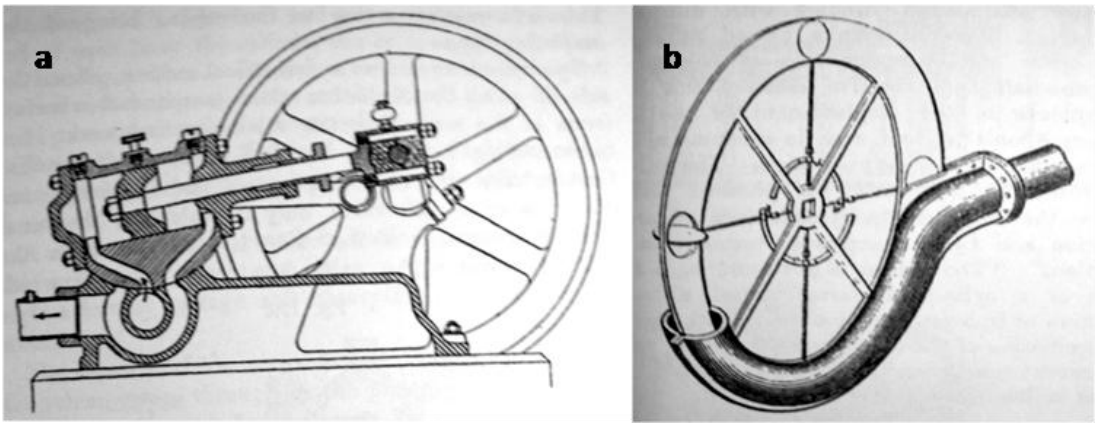

Figure 2.6: Hydraulic Motors from the 1800's. a. Schmidt's Hydraulic Motor, b. Armstrong's Rotary Motor, (Bodmer, 1895)

In Armstrong's machine, moveable blades attached to a rotor, move within an enclosed water channel through which the pressure of the fluid acts. While the blade control mechanism is a relatively complex detail, there is a natural progression from this device to the series of Hydrostatic Pressure Machines described in later sections.

2.1.3 Operating Ranges for Hydropower devices

The differing energy extraction and loss processes, together with practical mechanical engineering limitations on the construction of devices combine to limit the range of flow and head conditions for which each type of hydropower device can be applied. This is summarised in Figure 2.7, which in addition to the Pelton, Turgo, Francis and Kaplan turbines already described, includes Cross flow turbines, Archimedes screws and conventional water wheels. As can be seen, existing machines cover a considerable range of operating conditions and conventional turbine designs have reached a very high level of development. However, there is a gap in the performance graphs for very low heads (below 3 meters) and at moderate to high flow rates. This is the area of performance in which the HPM developed in the present work is intended to operate.

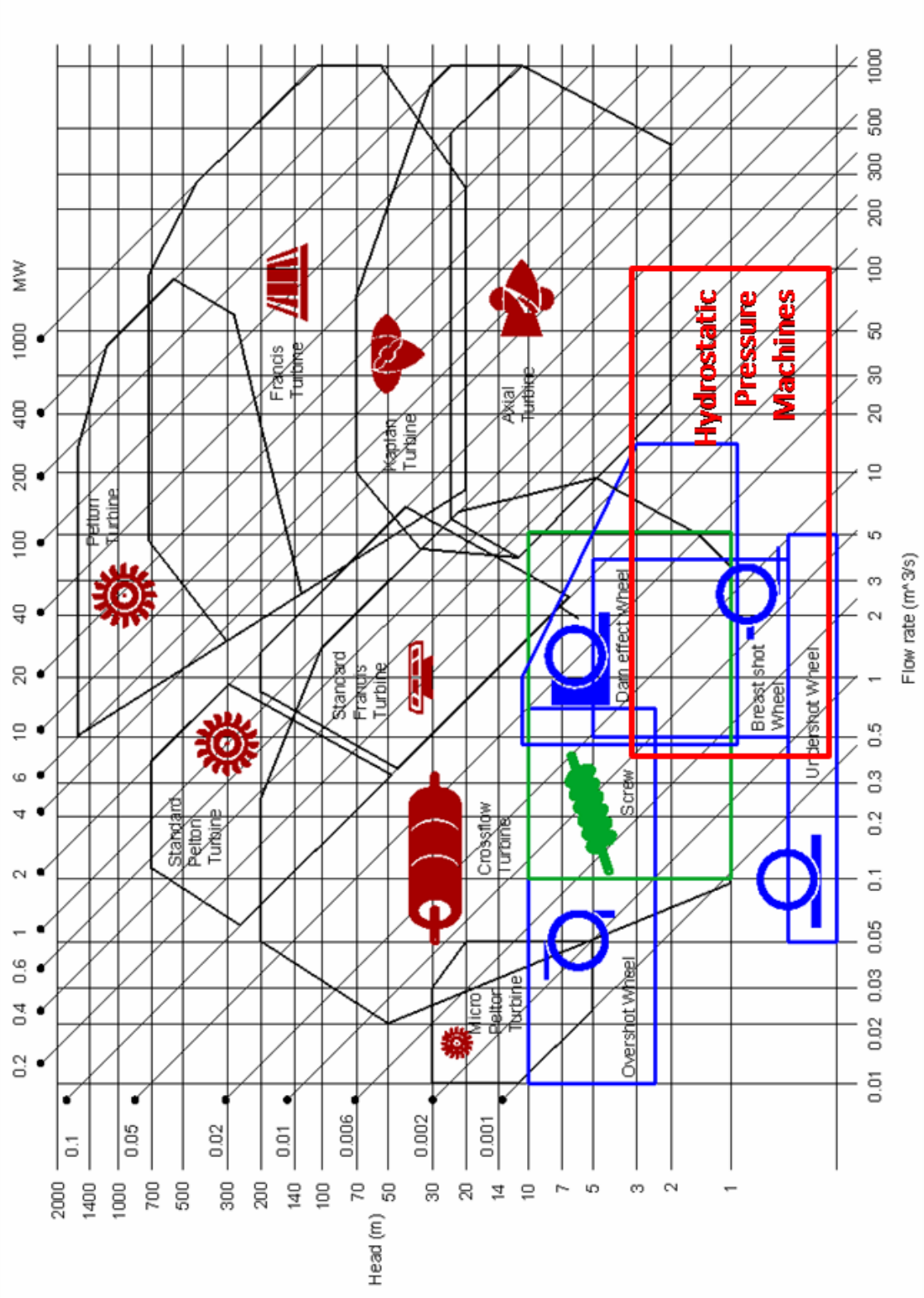

Figure 2.7: How the Hydrostatic Pressure Machine compares with other Hydropower machines *(after Senior, 2009)*

2.2 Ultra Low Head Resources and Potential

2.2.1 Europe

Paish (2002), estimated that river and waterway systems in Europe contained a potential 13GW of untapped energy potential, mostly at low head sites. A comprehensive study of hydropower resource in England & Wales was carried out by the Department of Energy & Climate Change in 2010 (Hydropower Resource Assessment Report 2010), reviewing previous resource estimates in the light of technological and financial developments. For the first time this included sites with heads down to 1 metre, and potential power outputs, below 25kW, thus increasing the estimated potential hydropower resource from the 34MW previously reported (ETSU,1989) to146-248MW. This indicates a likely under reporting of resource historically, in previous studies for both the UK and Europe. This potential resource is contained in the following locations:

a. ***Existing Mill sites*** are widely distributed across Europe and, due to the presence of existing diversion structures and leats, may reduce installation costs by up to 60%, (Muller & Kauppert 2002). There are some 20,000 deactivated mill sites in the UK, while over 30,000 mill sites were licensed in Germany as late as 1925. If fully reactivated these sites could produce around 600MW in the UK and 500MW in Germany.

   In France the position is even more favourable, with 100,000 mill sites in operation at the end of the 19th Century,30,000 of which were "*fonde en titre*", enjoying perpetual water extraction rights (Durin 2010). The installation potential of these sites is estimated at 2GW. However, most mill sites have low power outputs in the range of 5 – 20 kW and while the introduction of feed-in tariffs has boosted interest in their redevelopment, economic exploitation remains cost sensitive.

b. ***Weirs and Flow Control Barriers*** are features of rivers across Europe. Germany contains an estimated 1 weir per square kilometer of land area (Wiemann & Senior 2008), while in the UK, a recent survey identified almost

26,000 “barriers” with hydropower potential (Entec UK 2010). Of these, 16,725 were weirs with an average generation potential of 23kW. It was noted that at 4,190 of these sites, hydropower developments incorporating fish passes, would improve river ecology by removing blockages to fish migration and were therefore to be encouraged.

Weir sites *can* be attractive propositions for development due to the relative simplicity of construction, and avoidance of depleted river flows downstream of the installation (Pickard et al. 2003). The costs of such developments are greatly offset, if included in the refurbishment of weir structures at the end of their operating life (Goring 2000).However, as for mill sites, economic development of weirs will require “fish friendly” devices of significantly lower cost to those currently available.

c. Waste Water Treatment Works have two potential areas for hydropower developments. In mountainous areas, the direct turbining of waste water from high elevation communities as it enters lower level treatment plants is well established (Boelli, 2008). However, since all waste water treatment plants discharge clean water into the local river system, this represents an additional potential resource with steady and predictable flow rate and a useful head drop since outfalls must be located safely above river flood levels. In the UK, several water authorities are trialling hydropower installation using a range of devices.

2.2.2 World Wide: Irrigation Systems.

Irrigation systems consist of extensive networks of highly engineered waterways, of which, the Indus Valley system is the worlds’ largest. While the hydropower potential of the biggest canal and flow control structures are under development, (Majeed 2006), the resource contained within secondary distribution canal networks, is unexploited.

Irrigation canals are constructed with frequent weir structures at changes of elevation to control flow velocities and therefore erosion and silting. These “drop weirs” are standardised for given systems at between 1 to 3 meters in height and offer considerable scope for distributed micro hydro generation.

Rangnekar & Krishnamachar (2005) considered the power potential of 27km of the Hebbakavdi canal in Southern India, concluding that 9.5 MW of electricity could be generated from 20 drop structures. Extrapolating this result suggests that 20GW of similar potential may exist in the 60,000km distribution canal network on the Pakistan side of the Indus Valley with installations ranging from 100 kW to 1MW.

Schneider (2009), estimated that the USA contained 7,000 viable low head barrage and weir sites with an electrical energy potential of 8GW, while a detailed study of the Californian irrigation and water supply system (Kane & Sison-lebrilla 2006), identified 255MW of possible low head generation capacity.

Exploiting these resources, would require large numbers of standardised units offering significant cost reductions through economies of scale. With typical unit power outputs of 100kW and above, this application is an attractive prospect for technology development.

2.3 Challenges of Ultra Low Head Development

2.3.1 Typical Installation and Flow Conditions

Low head installations are invariably 'run of river' schemes without upstream water storage structures. Instead, a proportion of the river flow is diverted through the power extraction system to be returned to the river at some distance downstream. Figure 2.8 shows two typical arrangements.

An important operational characteristic of 'run of river' projects is that, since they are unable to regulate their water supply, they must be able to deal with high variations in flow rates, both on a daily and seasonal basis. In addition, high water and flood events change the effective head across the site as downstream water levels back up, requiring a higher degree of flexibility in terms of operating range from the hydropower device employed.

Also, since the total available head at such sites is by definition low, the head losses resulting from inlets, trash racks and energy losses in the leat, become very significant, and greater care is required to maximise the *Net Head* available at the power-plant.

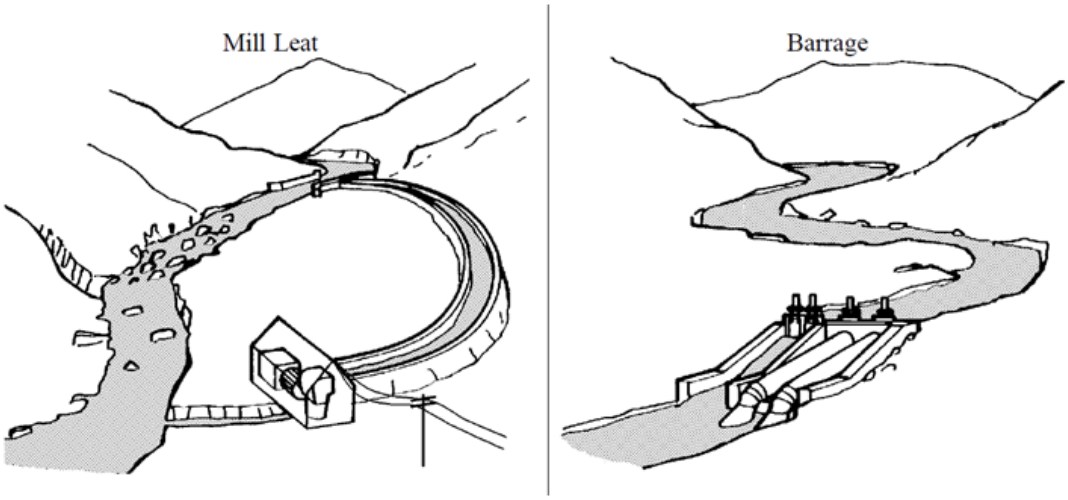

Figure 2.8: Typical Low Head Hydropower Installations
(British Hydropower Association, 2005)

2.3.2 Costs and Economics

Bacon (2004), presented data for the complete installation costs of a number of low head hydro power schemes ranging from 100kW to 10MW installed capacity. This information is presented in Figure 2.9 at several different values for available head. This graph presents cost data from 2004 and inflation needs to be taken into account along with developments within the industry, which have reduced the relative cost in small hydro as more suppliers and equipment become available for this market sector. However, two features are clear from the graph: firstly economies of scale are involved, with larger schemes giving significant cost advantages on a cost per kW basis and secondly, available head significantly impacts costs at all installation sizes.

This graph implies that the profitable exploitation of the low head resource already described requires very careful cost control. The Feed-in Tariff incentive system was introduced into the UK in 2010. These payments are in addition to the savings in power / sales of electricity to the grid and are designed to give a financial return for well designed sites of around 5 – 8%. This tariff reduces over time as the industry efficiencies develop and the schedule of rates is shown in Table 2.3. This has significantly impacted hydro development across all installation sizes, although initial installation cost remains a key issue, particularly at the typical power outputs (3 – 20kW) associated with most mill reactivation sites (British Hydropower Association Feed-in Tariff Review 2012).

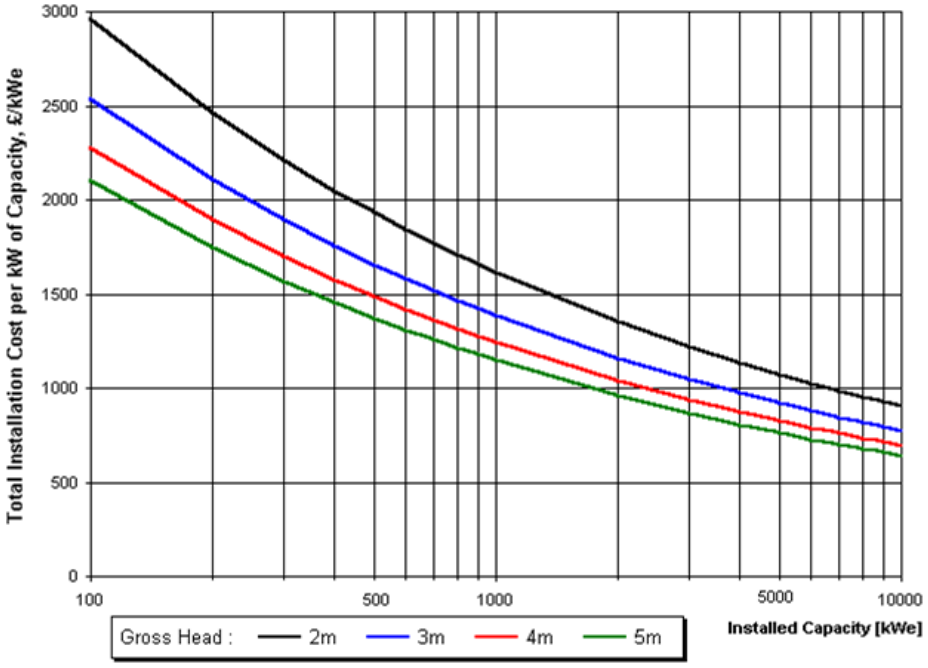

Figure 2.9: Typical Installation Costs for Small Scale, Low Head Schemes

(Bacon 2004)

Technology	Tariff band (kW capacity)	Generation tariff for new installations (p/kWh, 2012 prices)								
		2012/13 (from 1 Dec)	2013/14	2014/15	2015/16	2016/17	2017/18	2018/19	2019/20	2020/21
Hydro	≤15	21.00	21.00	19.95	18.95	18.00	17.10	16.25	15.44	14.67
	>15-≤100	19.70	19.70	18.72	17.78	16.89	16.05	15.24	14.48	13.76
	>100-≤500	15.50	15.50	14.73	13.99	13.29	12.62	11.99	11.39	10.82
	>500-≤2000	12.10	12.10	11.50	10.92	10.37	9.86	9.36	8.89	8.45
	>2000-5000	4.48	Tariff set at RO equivalent							

Table 2.10: Baseline generation tariff based on default degression.

(British Hydropower Association Feed In Tariff Review 2012)

2.3.3 Environmental Impact

No hydropower project will be allowed to proceed in the UK and Europe, unless it can demonstrate a minimal environmental impact on its surroundings. In the UK this impact is assessed by the Environment Agency and such is the importance of their role that Bacon (2004) identified them as 'the crucial factor in all projects'.

A fish pass is a requirement of all run of river hydropower schemes in the UK (Entec UK 2010). It is the potential for injuring creatures as they pass through the hydropower

device that is of interest here, since it will dictate the extent and spacing of fish screens required. Fish screens are of importance from the initial cost point of view (closer spacing has higher costs) and for operational efficiency since finer screens produce higher reductions in head and require substantially more effort to maintain.

Turnpenny et. al. (2000 & 2005) has compared the fish injury rates for several low head devices, showing mortality rates of up to 40% for Kaplan turbines, due to fish contact with the blade, and damage due to high pressure variations within the machine. The slow motion and pressure changes in water wheel type devices were found to present a low fish hazard. This was confirmed by Kibel & Coe (2008) conducting fish passage studies on the first Archimedes screw turbine installed in the UK on the river Dart in 2005. Specific fish passage studies carried out under the HYLOW programme suggest that HPM installations, compare favourably with screw turbines (Karlsson & Uzunova, 2012).

2.4 Ultra-low Head Hydropower Devices

2.4.1 Scope and Limitations.

Since work began on HPM's in 2006, considerable progress has been made by other teams working in similar fields, and in order to properly evaluate the potential of the HPM as a practical hydropower device, it is important to see how it compares with these technologies now approaching maturity. While many machine designs exist in concept or laboratory form, for brevity we will limit our study to devices currently in production or very close to commercial availability, reflecting the real world choices faced by would-be hydropower developers. Data for the brief descriptions contained in the following pages are drawn from Eichenberger et. al, 2011, Mead & Hunt, 2009, Applegate, 2010, and Weimann e.t al.,2008.

2.4.2 The devices:

Archimedes Screw Turbines: First introduced in the UK in 2005, 22 installations were completed by 2011 (Lashofer et.al.,2011). These rugged machines are perceived by the Environment Agency to be "fish friendly", simplifying permissions process (Environment Agency, 2009), while the number of successful installations has boosted developer confidence in the technology. Civil works are a significant component of cost, but are far simpler than for an equivalent Kaplan turbine.

Practical water-to-wire efficiencies of 72% are achieved (Rose, 2011), while test data (Brada, 1999), and theory (Muller & Senior, 2009), suggests hydraulic efficiencies of 80% are obtained over a wide flow range.

Status:	Serial Production
Performance Data:	
Head Range:	1.2 – 6 m
Flow Rate:	0.3 – 6.0 m^3/s
Power Output:	3 – 300kW
Speed Range:	20-80 rpm
Practical Efficiency:	70 – 80%
Fish Screen Spacing:	100mm

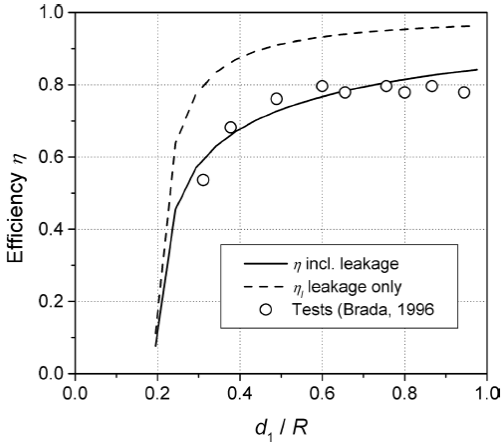

Figure 2.11: ***(top to bottom),*** **First UK Installation on River Dart** *(the author),* **200kW rotor Fabrication** *(Rose, 2011),* **Efficiency Curve** *(Muller et.al. 2009).*

Water Wheels: For ultra low head applications, Zuppringer and Breast Shot machines are used, with typical diameters of 4.5 to 7.7m and slow, rotational speeds of 4 – 6 rpm. Hydrowatt, are an established manufacturer, although the simplicity of these machines, permit construction by local fabrication companies, to traditional designs and reduced unit cost (Figure 2.12).

The flat efficiency curve enables operation of these water wheels over a wide range of flow conditions (Muller & Wolter, 2004). However, high ratio gearboxes must be used to connect the slow moving wheels to the generators, resulting in mechanical losses of 5 - 8%.

Status:	Serial Production
Performance Data:	
Head Range:	1.2 – 2.5 m
Flow Rate:	0.3 – 5.0 m^3/s
Power Output:	3 – 100kW
Speed Range:	4-6 rpm
Practical Efficiency:	70 – 80%
Fish Screen Spacing:	100mm

Figure 2.12: ***(top to bottom),*** **Zuppringer** *(HydroWatt),* **Locally manufactured Breast Shot Wheel** *(the author),* **and typical Breast Shot Wheel Efficiency Curve** *(Muller & Wolter, 2004)*

Steffturbine: Described by the originating team as an "evolution of the water wheel", this device, using a series of buckets connected in a continuous chain to drive a generator, is currently in the pre-production phase of development (Malcherek et.al. 2010). The developers state that the steffturbine is a potential energy machine, however, it shares some of the characteristics of a Hydrostatic Pressure machine: the unit is designed to run with full cells (Figure 2.13 middle), and its maximum efficiency is achieved at low rotor angular velocity, steadily falling as speeds increase – both characteristics of the HPM described in the next chapter.

The efficiency curve in Figure 2.13 (bottom), is for a unit at a flow rate of 23.5 litres/second, inclined at 50° to the horizontal.

An engineering prototype has been on field test for a year, and while the bolt-in installation and integrated generator are attractive features, the large number of wear points within the mechanism leads to concerns over long term reliability of the device.

Status:	Pre-Production
Performance Data:	
Head Range:	1.2 – 4 m
Flow Rate:	0.1 – 0.4 m^3/s
Power Output:	3 – 12kW
Speed Range:	unknown
Practical Efficiency:	80% (Hydraulic)
Fish Screen Spacing:	12.5mm (Estimate

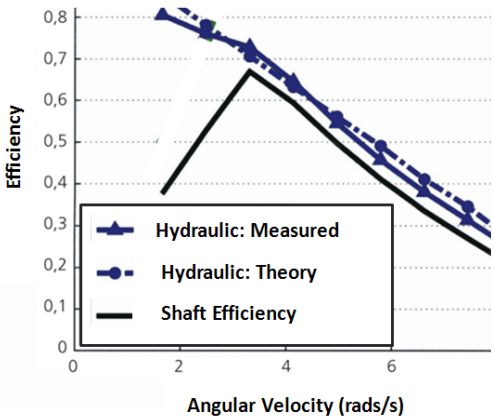

Figure 2.13: ***(top to bottom),*** **Steffturbine Field Trial Unit, Close up of cell filling, Efficiency Curve showing variation with rotor speed & leakage flow.**
(Malcherek et.al. 2010)

Siphon Turbines: These installations reduce the costly civil engineering works required by conventional Kaplan or Propeller turbines, by using the siphon effect to transfer water over the flow control barrier. This has the added advantage of keeping turbines above water level for maintenance, and eliminating the need for inlet gates since the unit can be shut down merely by breaking the air seal. However under marginal flow conditions, this start / stop process can be lengthy leading to significant lost generating time.

Such devices are offered by a many manufacturers, ranging from simple, modular, fixed blade propeller runners that require multiple units to cater for a range of flows, to highly developed variants using fully adjustable runner blades, and variable speed generators, offering hydraulic efficiencies of around 90%, for higher volume sites (Figure 2.14). Multiple, identical units can be used, at high flow sites. The high speed of such devices present a hazard to fish and, screening of installations is essential (Turnpenny & O'Keeffe, 2005).

Status:	Serial Production
Performance Data:	
Head Range:	1.5 – 3.5 m
Flow Rate:	1.0 – 14 m^3/s/ unit
Power Output:	1 – 180kW/unit
Speed Range:	100 – 600 rpm
Practical Efficiency:	75%-90%
Fish Screen Spacing:	6-12.5mm

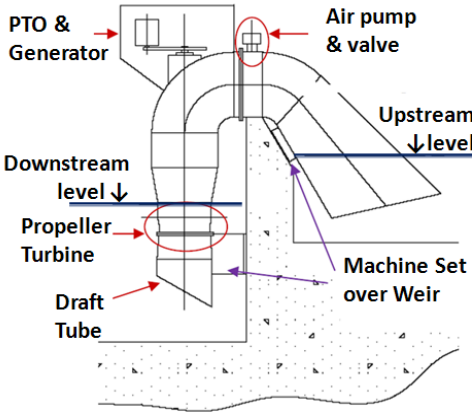

Figure 2.14: ***(top to bottom),*** **Propellor devices** *(Applegate, 2010)*, **Schematic of Siphonic Installation & 85 kW Siphon Turbines Installed at Vallorbe,** *(Choulot et. al. 2010).*

VLH Turbine: The Very Low Head Turbine was developed to avoid the civil engineering costs required by conventional Kaplan machines**.** It is designed to be installed in rectangular channels and consists of an eight bladed Kaplan with a fixed angle wicket gate array. Double regulation is achieved by allowing the speed of the rotor to vary during operation, using a variable speed, permanent magnet generator integrated into the hub of the rotor. Rotor speed is very low at below 41 rpm so losses in the electrical system will be high with estimated efficiency of only 80%. Bozhinova et.al (2012), extracted hydraulic efficiencies from reported laboratory tests to create the efficiency curve in Figure 2.15. The peak hydraulic efficiency of 86% translates into a water-to-wire efficiency of around 68%. Nevertheless, the VLH is a well design machine, addressing the maintenance and ecological issues faced by operators and 16 units were commissioned by 2010 at heads of up to 4 m.

Status:	Serial Production
Performance Data:	
Head Range:	1.3 – 4.0 m
Flow Rate:	10 – 30 m^3/s/ unit
Power Output:	100 – 450kW/unit
Speed Range:	30 - 41rpm
Practical Efficiency:	40 – 70%
Fish Screen Spacing:	12.5mm

Figure 2.15: ***(top to bottom),*** **VLH Installation & Cut away of the machine** *(Eichenberger, 2011),* **Hydraulic Efficiency Curve from model tests** *(Bozhinova et.al., 2012).*

Schneider Lift Translator (SLT): First developed in 1978 (Warnick et.al. 1984), this device is offered by Natel Energy, California. It is a very unusual form of reaction turbine, where energy is extracted in two stages by vanes mounted on a belt drive. This drive is contained within a removable cassette, indicating that wear is expected in this item, which is a potential weakness in the concept.

Installations ranging from 10kW to 180kW have been carried out during the development process, with a commercial pilot plant commissioned in 2009. Two standard units are offered, the SLH10 at 50kW and the SHL 100 at 500kW.

The efficiency curve from the current test unit reported by the company is compared with a Kaplan in Figure 2.16, and appears to show a useful operating range, despite having fixed guide vane angles.

Status:	Preproduction
Performance Data:	
Head Range:	1.5 – 6 m
Flow Rate:	0.92 – 12.0 m^3/s
Power Output:	10 – 500kW
Speed Range:	Unknown
Practical Efficiency: (Hydraulic)	70 – 80%
Fish Screen Spacing:	12.5mm

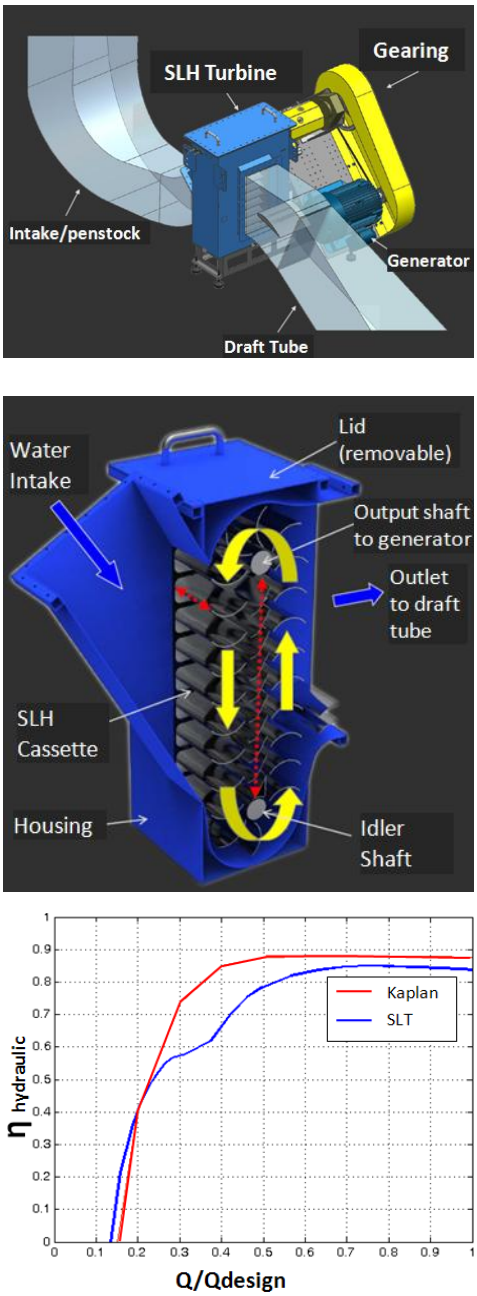

Figure 2.16: *(top to bottom),* **Installation, Cut away of rotor, Efficiency Curve,** *(Schneider, 2010).*

Free Vortex Propeller Turbines: A range of basic, fixed geometry propeller devices, using a combination of fixed vanes and shaped inlets to initiate a swirl component to the incoming flow have been investigated by several workers (Alexander et.al., 2009, Singh & Nestmann 2009). Such devices are offered by a number of manufacturers, with costs ranging from $500 US to $2000 US for a 1kW model. A Power Pall installation at a reactivated mill site in the UK is shown in Figure 2.17 along with locally manufactured devices used in a multi drop irrigation project in the Shan State of Myanmar.

While peak efficiencies of 74% were reported by Singh & Nestman, as for all propeller turbines, the operating flow range for good efficiency is narrow. However, the simplicity of these installations is clear from the figure, and multiple units can be readily employed to cater for variable flow conditions. These devices appear to offer a cost effective solution at small mill sites.

Status:	Serial Production
Performance Data:	
Head Range:	1.0 – 2.5 m
Flow Rate:	0.03 – 0.13 m^3/s
Power Output:	200 - 1000W
Speed Range:	unknown
Practical Efficiency:	50-70%
Fish Screen Spacing:	6mm

Figure 2.17: ***(top to bottom),*** **Inlet trough for Power Pal turbine, 1kW grid connected unit installed at mill site, Rural electrification Project, Ma Mya Dam, Myanmar** *(powerpal)*.

Gravitational Vortex Power Plant:

This novel, experimental device created by Franz Zotloterer relies on the rotational velocity of a stable, gravitational vortex, impinging on a slow moving central drag rotor, to extract power (Figure 2.18). Rotor speed is variable, up to 21 rpm, necessitating the use of a large gear box / inverter system for grid connection and electro-mechanical losses are high. While the machine itself produces a hydraulic efficiency of 41%, water-to-wire efficiency reduces to 23.5% (Eichenburger et. al. 2011).

While efficiencies are low, the device is able to pass fish, debris and sediment through the rotor without harm, although the bulk of the installation cannot be considered to have a low environmental impact.

Status:	Experimental
Performance Data:	
Head Range:	0.7 – 1.4 m
Flow Rate:	0.8 – 2.2 m^3/s
Power Output:	11 kW
Speed Range:	21 rpm
Practical Efficiency:	23.5%
Fish Screen Spacing:	100mm

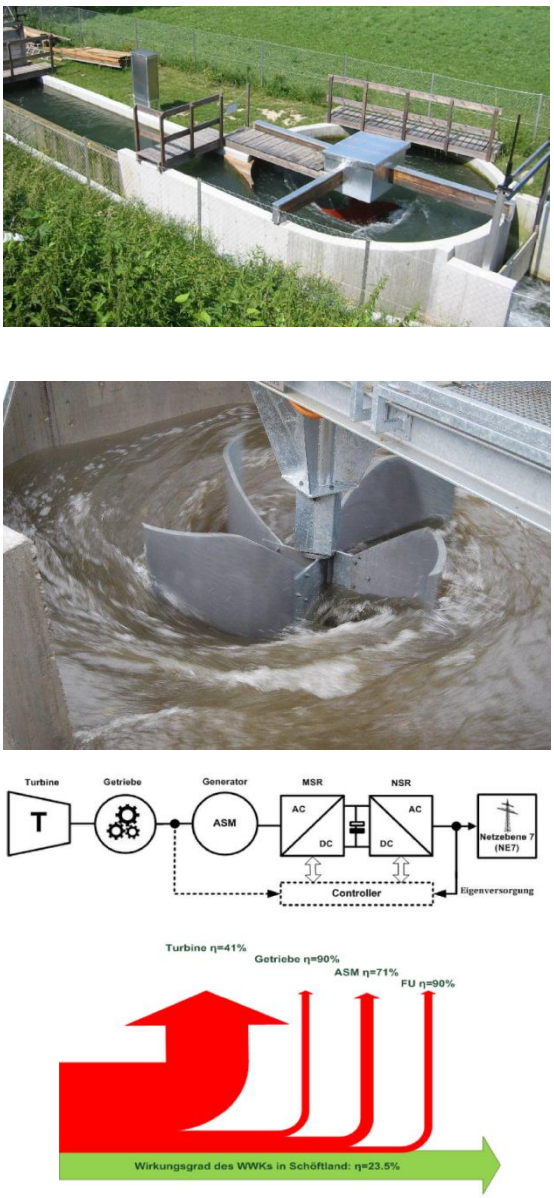

Figure 2.18:*(top to bottom),* **General view of Vortex machine, Mk2 propeller design, transmission losses**
(Eichenburger et. al, 2011).

2.5 Summary

So far in this chapter, we have reviewed the means by which conventional hydropower machines extract energy from available water flows and noted how several machines exploit more than one energy transfer mechanism in their design. In particular we have briefly reviewed basic Turbo-machine theory as applied to Kaplan and Francis reaction turbines, relevant to later discussions on future HPM developments.

We have also seen that the market for ultra low head hydropower machines is becoming increasingly widely recognized, with the potential for significant numbers of machines to be usefully deployed to make a valuable contribution to renewable electricity generation. While the economics of low head hydro development remains challenging, particularly at low power sites, a number of robust and effective machines are beginning to establish themselves in the market place. Any future HPM developments must offer significant advantages over these competing devices, in terms of cost, reliability and environmental impact, at least in a significant number of applications, if these machines are to be commercially viable.

Chapter 3: Literature Review Part 2: Hydrostatic Pressure Machine Development & Theory

3.1 The basic characteristics of Hydrostatic Pressure Machines.

The Hydrostatic Pressure Machine (HPM), as described by Senior (2009) was conceived as a pure *pressure* engine extracting energy from the flow exclusively through the pressure difference produced by up and downstream water levels acting either side of the blades of a slow moving rotor. The basic features of the device are shown in Figure 3.1.

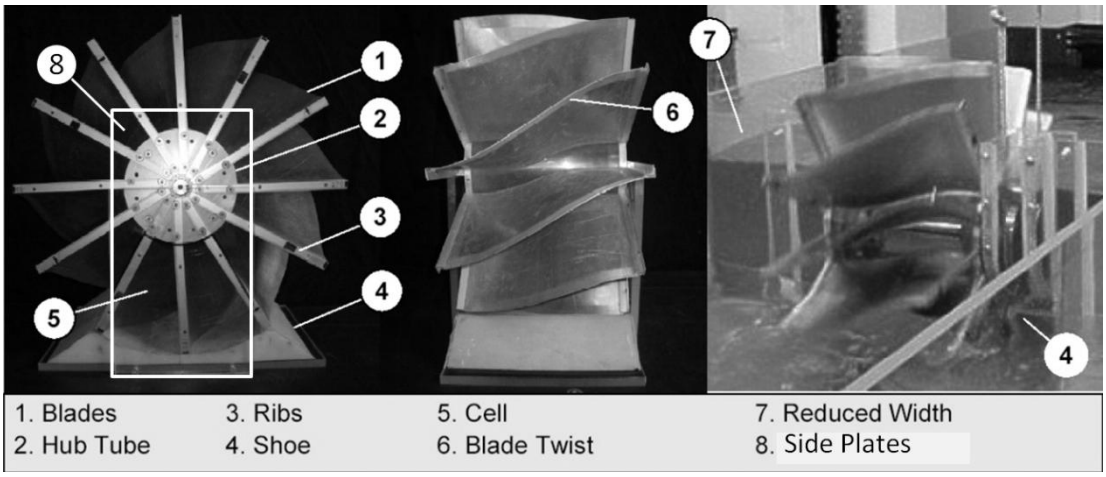

Figure 3.1: Hydrostatic Pressure Machine – Test Model *(Linton et. al. 2009)*

The *rotor* consists of a *hub tube (2),* to which 12 *blades (1)*, supported by *ribs (3),* are attached, forming an assembly free to spin about its axis. The hub tube acts as a weir, separating up and downstream water levels, to maintain a head difference acting across the device. The segment of the rotor formed between adjacent blades is termed a *'cell' (5)*, and is the working chamber of the device into which fluid enters and leaves and from which power is extracted, during rotation. The *blade twist* or in the case of flat blades *inclination (6),* aids efficient filling and emptying of the cells, encouraging water to enter from the sides of the machine as it resides in a channel significantly wider than the machine itself (7). A *shoe (4)* is shaped to seal off the bottom of the rotor, preventing leakage of flow along the channel bed and together with the *side plates* (8),

forms the *working section* of the machine.

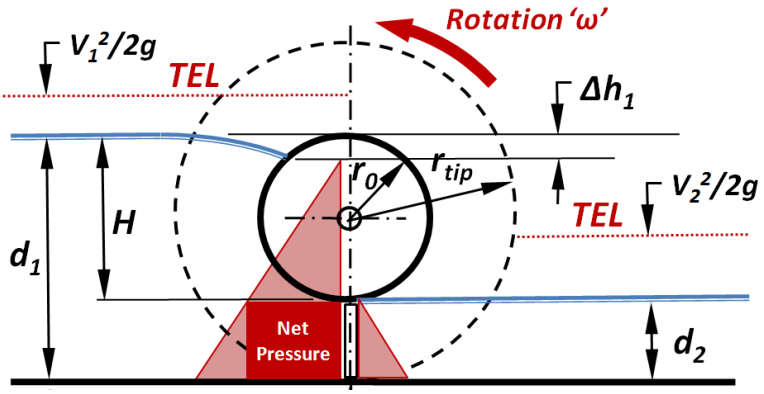

Figure 3.2: The Generation of Blade Force in HPMs

The difference in static pressure either side of the rotor acts on the blades as they pass through the working section of the machine to generate torque causing the rotor to spin against an external load, thus extracting power. The basic operating condition of a simple machine is shown in Figure 3.2.

Since even small head differences can produce very high blade forces and rotors can be scaled to accommodate large flow volumes, the concept appears well suited to ultra low head applications. However, a number of loss mechanisms need to be considered.

- Since the upstream water depth is greater than the downstream, fluid must accelerate as it passes through the rotor. Force must be applied by the machine and the surrounding structure to accelerate the flow and so any work done by the machine to bring about this momentum change is lost from the energy extraction process.

- As the fluid accelerates, the free surface drops to keep the total energy of the flow constant, resulting in a reduction of local pressure head and thus torque at the rotor. This head drop increases with flow hence the torque produced by the machine due to pressure forces alone, must fall as rotor speed increases.

- Changes in momentum and the creation of turbulence as fluid enters and leaves the cells, as the large blades contact the fluid, and as they are moved through the standing water on the upstream side, produce significant drag and kinetic energy losses becoming increasingly dominant at higher rotor speeds.

- Practical rotor assemblies have clearance gaps between the moving and fixed parts of the installation, which allows some leakage flow to occur, by-passing the machine. The energy of this leakage is lost to the energy available for extraction and at low rotor speeds these leakage losses dominate the performance characteristics of the machine.

An additional characteristic of HPMs that is important to note is that, since cells are designed to be completely filled during rotation, these are *positive displacement devices*, where rotor speed must alter in proportion to changes in flow rate. This is in marked contrast to most other conventional hydropower machines where rotation speed is more usually fixed to that required by the generator.

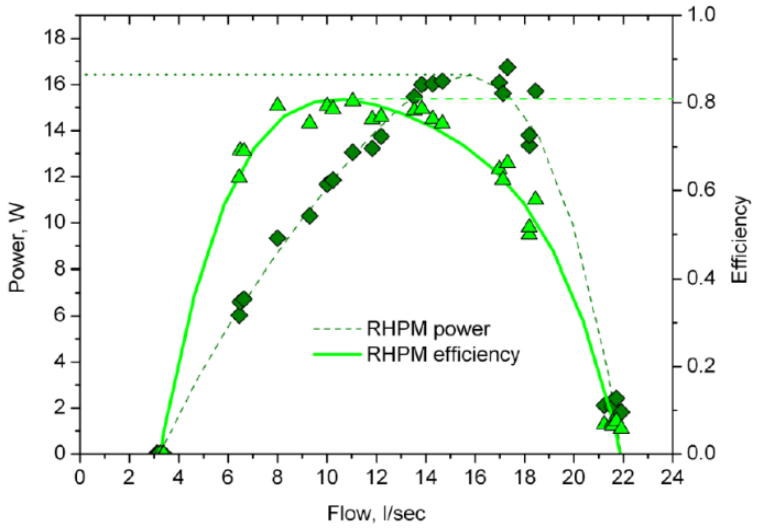

Figure 3.3: HPM Performance from Model Tests *(Senior 2009)*

Typical performance characteristics for a lab scale device are shown in Figure 3.3. The maximum efficiency of 80% occurs at low rotor speed while the flow rate corresponding to maximum power is achieved at a significantly higher flow rate (16 rpm compared with 10 rpm for peak efficiency with this model). While the output curve is quite peaked, efficiency remains reasonably high (better than 70%) over a reasonable range of flows.

3.2 Historical Development

In this section a number of devices and research efforts that have contributed to the overall development of hydrostatic pressure machine concepts will briefly reviewed. The emphasis here is on reviewing the design of devices, and the context in which the work was undertaken. A review of theory development follows in section 3.3.

3.2.1 Zuppingerrad 1847

This machine was developed sometime around 1847, although the elevation and plan views of the device shown in Figure 3.4 are taken from Weisbach (1883). No performance data is preserved and it is unclear whether this machine was ever constructed at full scale or only in model form. Bozhinova et.al (2012), quotes Weisbach as ascribing power extraction by the machine as being due to the weight of water.

Careful study of these engravings yields intriguing additional information. First the very large, curved blades form cells which are exposed to full hydrostatic pressure from upstream for much of their rotation, indicating that this is more a pressure machine than a potential device. Second, the use of the hub tube as a means of creating a "damming effect" to separate up and downstream water levels was noted by Senior (2009) and represents part of the genesis for his machine. Thirdly, the cells are fed from either side of the wheel with inlet water being divided into two troughs.

However, what appears not to have been noted before is that these troughs, together with a lower shroud, (high-lighted in red on Figure 3.4), isolate the periphery of the wheel from the standing water on the upstream side of the machine, minimising the potential for drag and turbulence losses. With this detail, Zuppringer appears to have very elegantly removed an important source of energy loss from his machine, (one from which later chapters will show first generation HPMs suffer greatly), crucially enabling this machine to operate at significantly higher rotor speeds than more conventional water wheel designs.

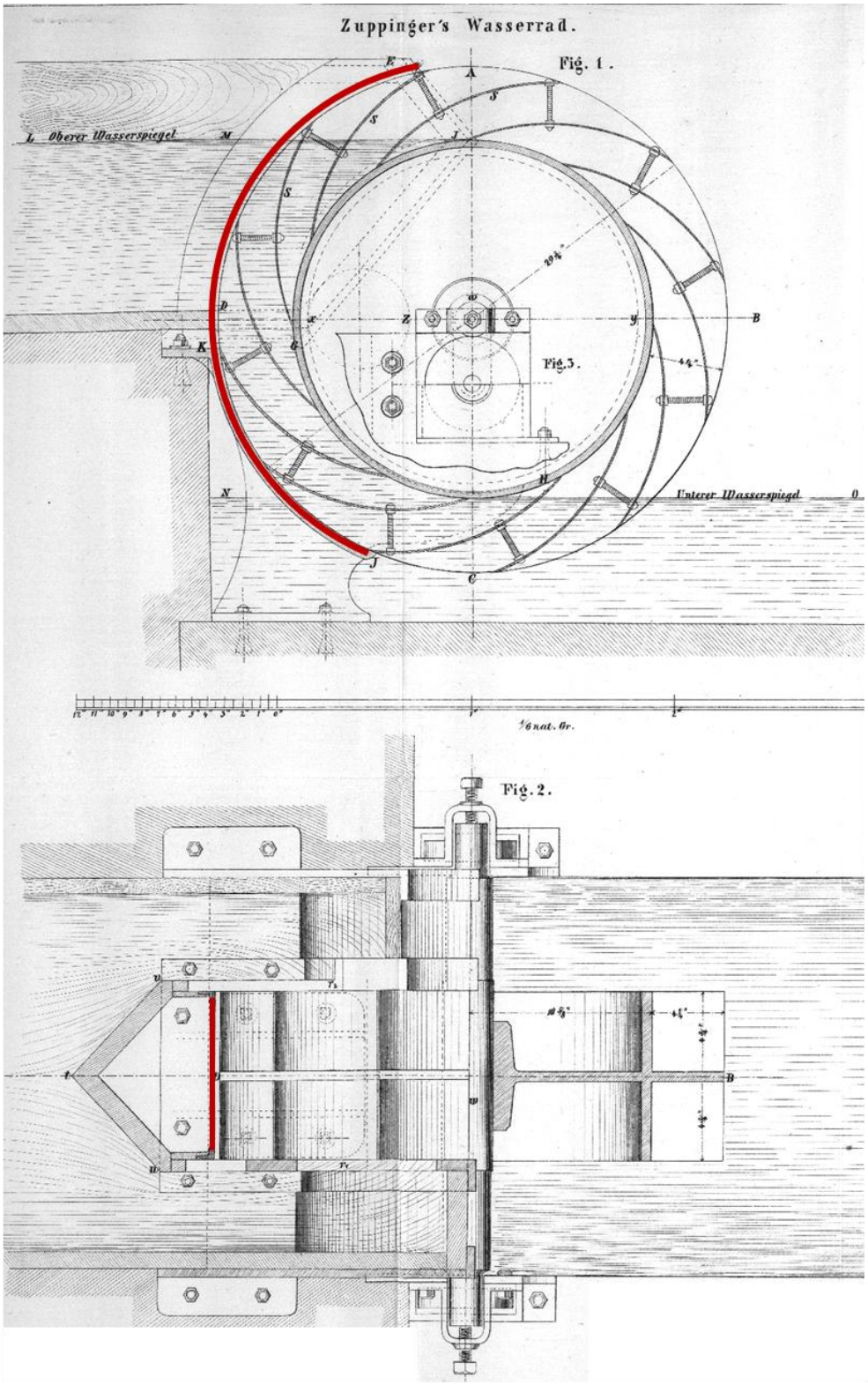

Figure 3.4: Zuppinger's Wheel from 1848 *(Weisbach, 1883)* – red lines indicate extent of the shroud separating the rotor and standing water to minimise drag and turbulence losses

The engineering 'cost' of this feature would have been in the high leakage rate that would have been present around the long periphery of the wheel sides – this would have significantly impacted the efficiency of the machine, particularly at low rotor speeds.

It should also be noted that, since the cells of this machine are designed to run full, rotational speed will be directly linked to flow rate. While this presents a significant challenge when seeking to drive electricity generators in the modern era, it would have posed real problems for the direct mechanical drive of machinery in Zuppinger's day, and may explain why few if any machines were constructed.

Nevertheless, this machine represents a very promising approach, with ideas that will be 'borrowed' in the HPM developments described in later chapters.

3.2.2 Saltford University Machines 1989

After initially unsuccessful attempts to develop a reciprocating machine, Bassett (1989), developed the 'Underwater Motor' device at Saltford University, shown in Figure 3.5.

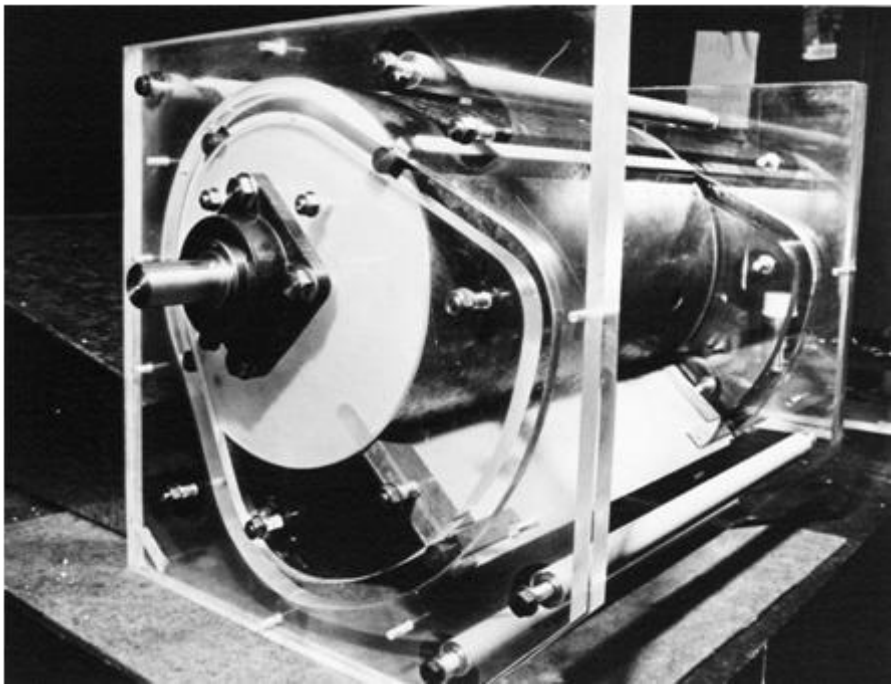

Figure 3.5: Bassett Under Water Turbine*(Bassett 1989)*

This is a clever adaptation of a sliding vane air compressor design, where the flat blades of the rotor are free to slide in and out of a central shaft. When extended, the blades run very close to the curved wall of the casing, thus creating a working section. In air compressors, centrifugal forces alone are sufficient to ensure blade deployment, but at the lower speeds of the Underwater Motor, Bassett found it necessary to control the position of the blades with pins attached to each blade running in a guide slot. A schematic of his complete device is shown in Figure 3.6. Note that the rotor is placed within a turbine-like casing and runs fully submerged.

The head difference either side of the blade in the rotor exerts a hydrostatic pressure difference resulting in torque. The speed of the rotor is dependent on the load applied, as is the flow rate through the machine. Although Bassett did not explicitly identify the principle involved, his device is a Hydrostatic Pressure Machine with characteristic performance.

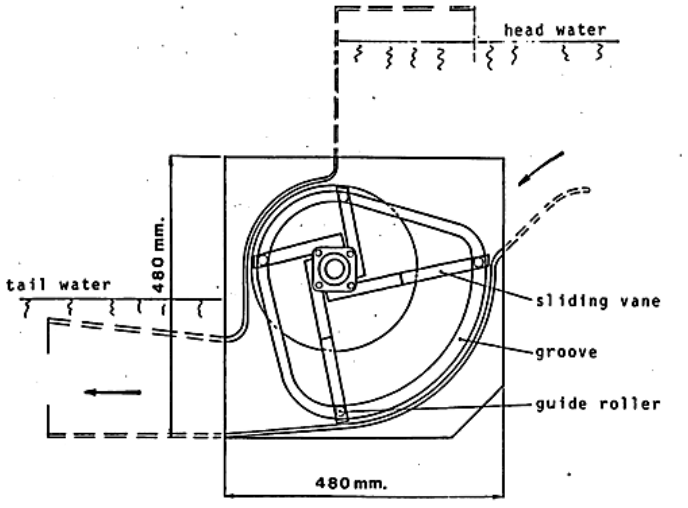

Figure 3.6: Lay-out of the full size Underwater Machine *(Bassett 1989).*

Maximum efficiency was found to be 80%, occurring at a rotor speed of 18 rpm, which decreased with increased rotor speed. Maximum power was produced at rotor speeds of around 40rpm at 60% hydraulic efficiency. The sliding blade effectively reduces blade drag losses from the device, while the complete containment of the rotor within the casing permits both the use of a penstock for water input, and a draft tube for partial recovery of the kinetic energy content of the exit flow. The high rotor speeds make coupling of the unit to generator equipment relatively straight forward. Although Bassett patented his design, the device does not appear to have been developed commercially.

3.2.3 "Damming-up Effect Wheel" 2000

A team of Japanese irrigation engineers, Gotoh, Kowata, Okuyama& Katayama, (2000 & 2001), conducted a series of experiments on a basic undershot water wheel, primarily intended to recover kinetic energy from flowing water. They were interested in the performance of this device, when subjected to flow conditions in a confined channel, and their wheel consisted of 12 blades, set to run with a small clearance (3mm), between the perimeter of the wheel and the bottom of the channel; no shoe profile was used. They noted that power output from the machine increased, as load was applied to the shaft, and the flow in the test flume was backed up. This created an increase in water depth upstream of the wheel and the team noted that energy was being recovered by the device through both kinetic energy transfer and hydrostatic pressure. Maximum efficiencies of 45% were measured at lower rotor speeds than maximum power output and they summarised their results by plotting power output against wheel efficiency for various values of wheel shaft torque (Figure 3.7). The authors saw potential for extracting power from existing irrigation networks, although, no further work from this team appears to have been published.

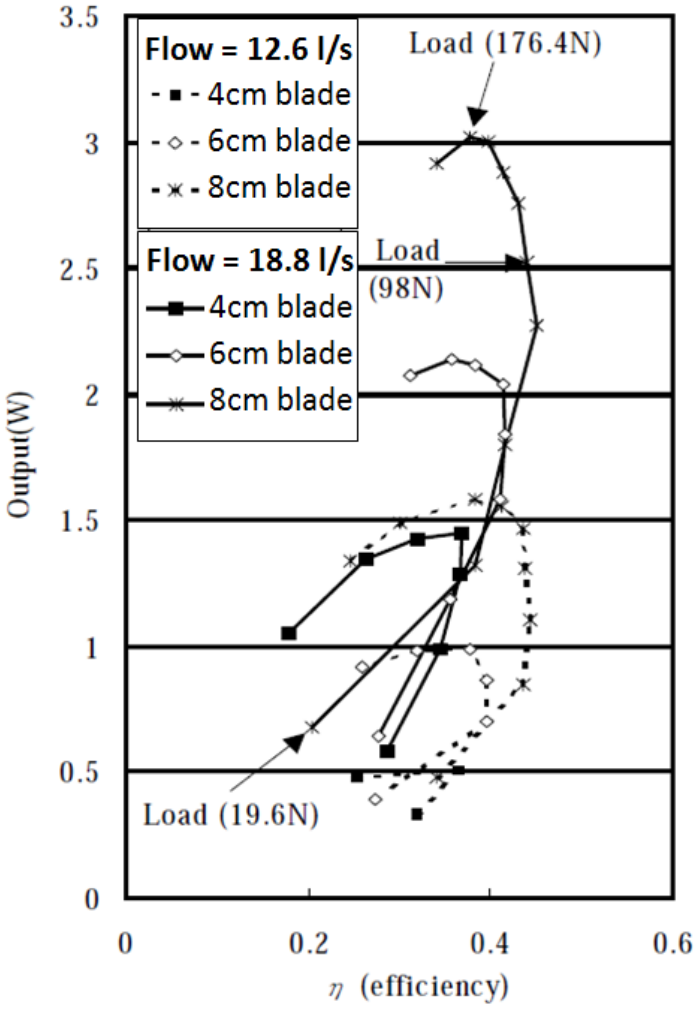

Figure 3.7: Performance results for "Damming-up Effect" Wheel. *(Gotah et.al 2000)*

3.2.4 Brinnich's Stem Pressure Machine 2001

Brinnich was awarded two patents in 2001 and 2006 for his 'damming-effect machine' and two variants have been constructed, shown in Figure 3.8.

Figure 3.8: The Stem Pressure Machine:*(top to bottom),* The Mk1 unit, MK2 installation, speed increaser system *(Brinnich 2011)*

The device is intended to extract energy from heads of between 0.5 and 3 meters and, like the Zuppingerrad, uses the machine itself, to create a head difference between up and downstream flows during operation. From Brinnich's self published articles (Brinnich, 2001 & 2011), it is clear that, while he recognised the importance of hydrostatic pressure as a component of energy extraction for the device, he also appears to have assumed significant kinetic energy transfer took place ('*the energy of the flow*') and to have grossly underestimated energy losses in the device. While he allowed for reductions in power due to leakage and mechanical friction, hydrodynamic losses due to acceleration, turbulence etc. are ignored, leading to his unrealistic assessment for the efficiency of the device as being over 90%.

Nevertheless, his device was a significant development: using hydrostatic pressure as the primary energy extraction process, using the rotor to generate head difference across the unit, and the use of angled blades to ease entry into the flow during rotation are all useful features carried over into designs by future workers. By comparing, the Mk1 and Mk2 machines in Figure 3.8, it is clear that he attempted to address energy loss issues intuitively, even if the theoretical basis was not clear to him (a very common occurrence in engineering), with much smaller, angled blades on the Mk2 unit, to reduce dynamic drag losses, replaceable blade edges to

increase damage tolerance and the reduction of machine width relative to the channel width on the upstream side of the device to promote side filling of the cells. The lower picture also shows that some attention was paid to the problems of increasing the output speed of this slow moving device for electricity generation, although the use of a three stage tooth belt system integrated into the wheel itself, with a speed ratio of approximately 200:1, may be a little optimistic.

3.2.5 Seniors' HPM 2009

Senior carried out model tests on the Mk1 Stem Machine, obtaining performance data and deriving a basic theory of operation (Senior, 2009). He found peak Stem machine efficiencies to be around 40% and through observation identified the lack of ventilation to the cells during filling and emptying as a major source of energy loss. He also noted that the addition of a shoe to seal the working cells during power extraction would further increase performance.

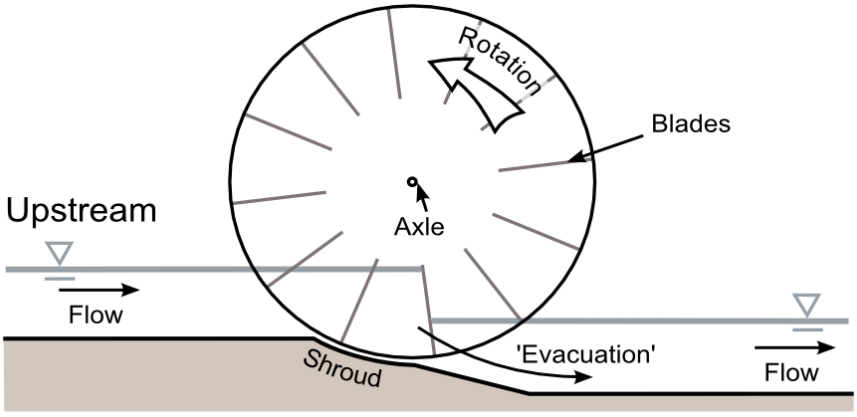

Figure 3.9: The Hydrostatic Pressure Wheel *(Senior, 2009)*

From these tests, two hydrostatic pressure devices were developed (Senior, 2009). The first, termed the *Hydrostatic Pressure Wheel*, (Figure 3.9), resembled a stream wheel with the addition of a shaped *shoe* between the periphery of the device and the floor of the channel and was intended for head differences that could be accommodated across the depth of a single working blade. The second device, the *Hydrostatic Pressure Machine,* is the subject of this present work and, while already described above along with summary performance data, is shown schematically in Figure 3.10.

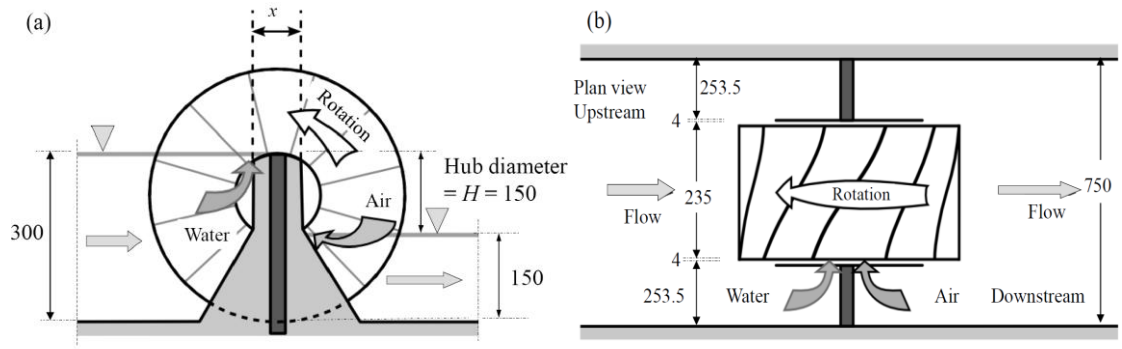

Figure 3.10: Senior's HPM Model, a. Elevation, b. Plan (Senior, 2009)

Senior's key developments were: the addition of a shoe between the rotor and channel floor to reduce leakage, twisting of the blades in a reduced width channel to encourage water to enter the machine from the sides, and improved ventilation of cells to increase the efficiency of the cell filling process. Senior's device showed significant improvements in performance compared with the original *Stem* machine, and the theory he developed (presented in a later section), has remained largely unaltered to date.

However, he observed several negative characteristics in the machine during operation which he highlighted as areas for improvement for subsequent designs:

1. There was significant speed variation produced by the machine as each blade passed through the working section, with variations measured of +/- 19% of mean rotor speed. Only one water level condition was tested by Senior, hence no indication of how this phenomenon may change with operating conditions was obtained.
2. As rotor speeds increased, significant energy is lost as splash and turbulence are produced by blades impacting the upstream surface, during entry into the flow and in turbulence during cell filling.
3. At high rotor speeds, water was lifted by the upper surface of the blade as it emerged from the downstream flow. Rotation speed was too fast to allow water to drain sufficiently and considerable energy was lost by this effect.

3.2.6 Linton MSc. Rotor Developments 2009

Empirical model testing was carried out on a range of different rotor and installation configurations and geometries (Linton, 2009) with the aim of addressing the performance issues of the original machine identified by Senior.

A wide range of factors were studied including, alternative helical shaping of rigid blades at various aspect ratios, a novel flexible blade design able to deflect under adverse loads to reduce drag, and variations in installation geometry covering clearance gaps, shoe profile and side plate asymmetry.

In addition work was carried out on the effect of up and downstream channel widths on performance along with preliminary assessments of the resistance of the machine to ingestion of foreign objects (Figure 3.11).

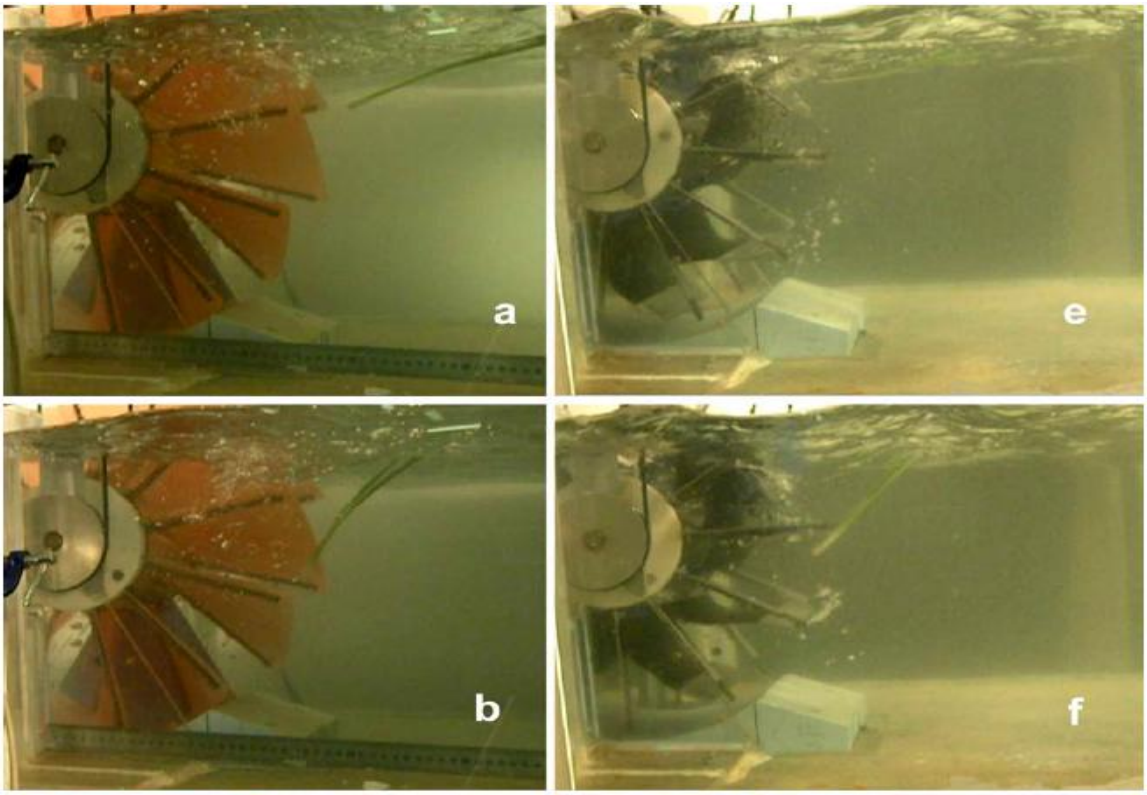

Figure 3.11: Foreign Object entry into HPM models with rigid and flexible blades: while strong entrainment of flow from the inlet surface was observed during filling no object was observed to cross from upstream into the machine once filling was completed. In the figure a rigid rotor is shown on the left while a machine with flexible blades is shown in the right hand pictures.
(Linton, 2009)

The analysis of this work was limited and some of the results were misinterpreted, however the key observations and developments that can be gleaned from these experiments are:

1. The details of HPM installations have a very large effect on measured performance. The implication of this is two-fold: first, careful installation design is important for successful field deployments of HPMs, and second, the direct comparison of results from model tests is difficult unless detail installation geometry is carefully controlled. Rotor clearances, shoe profile, side wall geometry and the width of the rotor compared to the width of the inlet and exit channels were all found to have significant effects on measured performance.

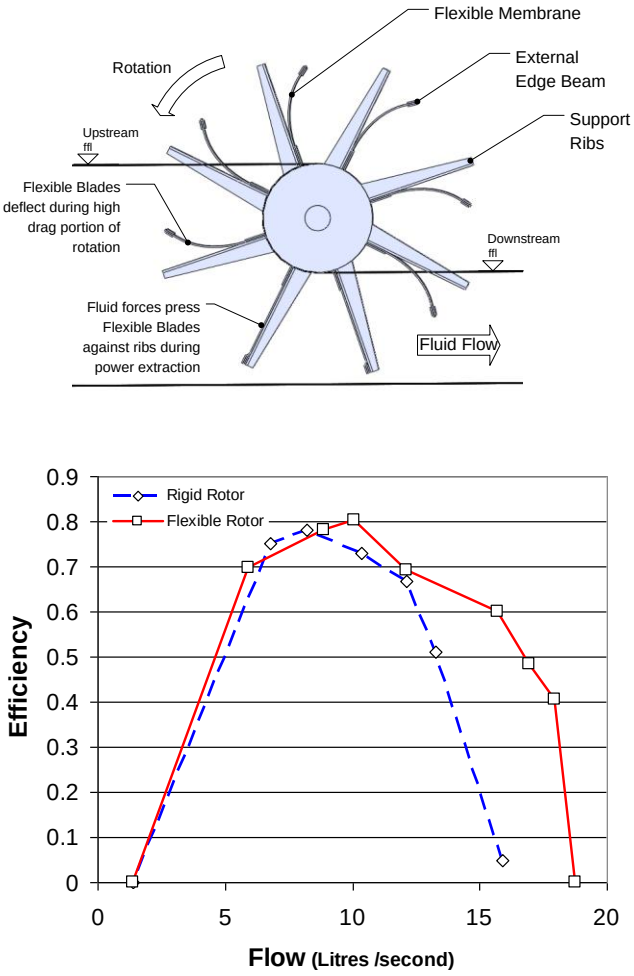

Figure 3.12: Flexible Rotor. Schematic *(above),* Efficiency Improvement *(below), (Linton et. al. 2010)*

2. Foreign Object tests indicated that there was a strong entrainment of flow from the upstream surface while the cell was filling. However, once cell filling was complete, objects introduced at mid depth in the inlet channel would not pass the boundary of the machine to enter the cell, indicating that little or no fluid crosses into the rotor after cell filling is complete. We will return to this detail in later chapters of this work since it offers important insights into the interaction between cell filling, blade drag and acceleration processes.

3. A new series of rotor designs using flexible blade elements was developed in an attempt to reduce the very high drag and turbulence losses produced by the Senior device. The key concept was that flexible blades would deflect under drag loads, to present a lower drag profile to the flow, yet extend against supportive struts during power extraction. A schematic of the device, together with performance comparisons with rigid blade rotors are shown in Figure 3.12 and a UK patent was awarded for the concept in 2010.

3.2.7 The HYLOW Project 2008 – 2012

The Hylow project was a large scale co-operative research programme between a number of European Universities, to develop energy conversion devices suitable for ultra low head applications. HPM development was part of this project and two field trial units were installed to study machine performance and to carry out assessment of the environmental impact of such units both on river sediment transport and on the safe passage of aquatic life forms.

The 10 kW unit, built into a barrage across the river Iskar in Bulgaria, is shown in Figure 3.13 (Bozhinova et.al, 2012).

Figure 3.13: The HPM installation, River Iskar, Bulgaria. Operating in high water *(left),* Close up of welded steel rotor *(right).* *(Bozhinova et.al. 2012)*

A smaller 5kW unit, deployed in a grid-connected, mill reactivation site, on the river Lohr in Bavaria, is shown in Figure 3.14. This latter unit was the responsibility of the author, the detailed study of which forms a large part of later sections of this document.

Figure 3.14: The 5kW HPM installation at Partenstein, Bavaria

Alongside these field trials, model tests were also undertaken at TU Darmstadt, to both validate numerical studies (Narrain& Wright, 2012) and to examine the interaction of the machine with fish and sediment, in a controlled environment (Schneider et. al. 2012).

However, there were several practical limitations to this work:

1. Numerical studies were carried out at a single operating speed using geometry approximated to TU Darmstadt laboratory models. This limits their usefulness to understanding observed machine behaviour across the operating speed range.

2. Several model geometries were studied in physical testing at TU Darmstadt, where a number of interesting performance characteristics such as efficiency changes with variations of downstream water level, were identified. However, no tests was carried out using models with exact geometric scaling of rotor and installation compared with field trial or other model tests. Given the sensitivity of performance results to the details of model installations described previously, direct comparison of results obtained from different machines is difficult and may in some circumstances be suspect.

3. Without exact geometrical similitude, a definitive assessment of scale effects in comparing results is not possible based on TU Darmstadt data.

3.3 HPM Theory

3.3.1 Published theory

The earliest published theory (Senior, Wiemann & Muller, 2008), described the hydrostatic energy extraction principle for ideal machines, with a limited treatment of losses.

A more detailed theory was presented by Senior (2009), which included losses due to leakage, acceleration and turbulence for an idealised machine of unit width. However, several variations in the treatment of momentum changes occurring to the flow as it passes through the rotor are presented in subsequent papers: acceleration losses are incorporated into a general empirical loss coefficient by Senior et.al (2010), and an alternative treatment based around an 'acceleration loss Coefficient' is used by Muller et.al (2012).

The following 2-dimensional theory is derived from Senior's original analysis slightly re-cast to clarify key issues. Due to the importance of acceleration losses on alternative HPM design approaches described in later chapters, acceleration losses are treated separately from turbulence although, as subsequent results will demonstrate, for the classical HPM design presented here, this may be an arbitrary distinction.

3.3.2 Classical 2D Theory

The following theory refers to a 2-dimensional machine of unit width, with the rotor, upstream and downstream channel widths all being equal.

3.3.2.1 Static Condition

Let us first consider the machine in the static condition when hydrostatic forces and moments are balanced by the reaction of the machine bearings and transmission system (Figure 3.15).

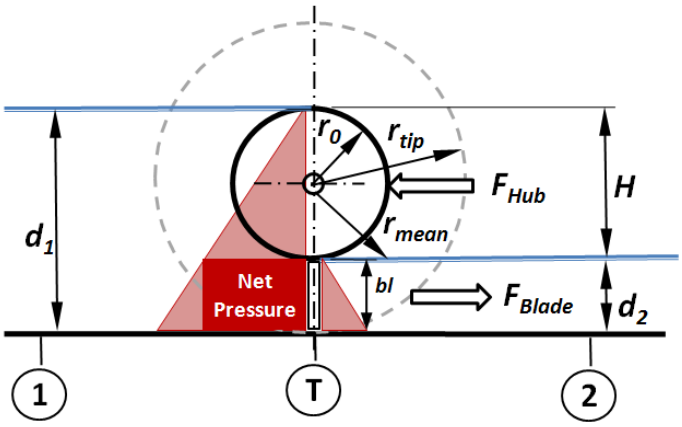

Figure 3.15: HPM at the static condition

In the static condition the up and downstream water depths (d_1 & d_2), are level with the top and bottom of the hub respectively, so that the hub diameter ($2r_0$), is equal to the static head (H), across the machine. The overall diameter of the machine is '$2r_{tip}$'. The bed of the two channels and the base of the machine are all on the same level. The machine is stationary and there is no flow.

Hydrostatic pressure acting across the blade is uniform, producing a blade force of:

$$F_{blade} = \frac{\rho g}{2} d_2(d_1 - d_2) \qquad \text{- 3.1}$$

And a force acting through the stationary hub of:

$$F_{Hub} = \frac{\rho g}{2} (d_1 - d_2)^2 \qquad \text{-3.2}$$

Since the hub is cylindrical and hydrostatic forces act normal to a surface at any given point, the hub reaction produces no torque. Torque due to the force acting on the blade must be reacted by the power take off (PTO), system fitted to the rotor.

3.3.2.2 Operating Condition of an 'ideal' machine

We next consider an HPM during operation (Figure 3.16). The machine has an angular velocity of 'ω' producing a flow rate of 'Q' while the mean velocity at the centre of the blades 'v_2' is assumed to be equal to the downstream water velocity leaving the machine.

The length of machine blade is *'bl'* with the blade centroid radius taken to be *'r_{mean}'*. The machine works in an ideal fluid, with no leakage or energy losses.

From the energy equation:

$$\frac{v_1^2}{2g} + d_1 = \frac{v_2^2}{2g} + d_2 \qquad (3.3)$$

From continuity:

$$Q = v_1 d_1 = v_2 d_2 \qquad (3.4)$$

Therefore,

$$v_1 = v_2 \frac{d_2}{d_1}$$

or

$$v_2 = v_1 \frac{d_1}{d_2} \qquad (3.5)$$

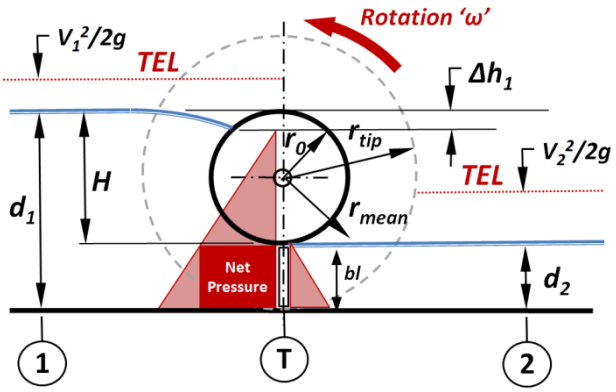

Figure 3.16: HPM in Operation

Flow through the rotor induces a head drop across the HPM at station 'T' as fluid is accelerated and dynamic head increases:

$$\Delta h_1 = \frac{v_2^2 - v_1^2}{2g} \qquad (3.6)$$

Since the machine speed is related to downstream velocity, it is convenient to rearrange equation 3.6 to eliminate the upstream velocity term:

$$\Delta h_1 = \frac{v_2^2}{2g}\left(1 - \left(\frac{d_2}{d_1}\right)^2\right) \qquad (3.7)$$

Assuming hydrostatic pressure forces only are acting on the blade, the force due to this pressure *'F_p'* is given by:

$$F_p = \rho g b l (d_1 - d_2 - \Delta h_1) \qquad (3.8)$$

For an ideal machine with no leakage losses, flow rate and velocities in up and downstream channels are directly proportional to wheel speed:

$$Q = \omega r_{mean} bl = d_2 v_2 \tag{3.9}$$

and:

$$v_2 = \omega r_{mean} \tag{3.10}$$

Power output of the ideal machine is given by:

$$P_{ideal} = F_p v_2 \tag{3.11}$$

Which may be written as:

$$P_{ideal} = \rho g d_2 v_2 \left[d_1 - d_2 - \frac{v_2^2}{2g}\left(1 - \left(\frac{d_2}{d_1}\right)^2\right)\right] \tag{3.12}$$

The hydraulic power available from the flow passing through the machine is:

$$P_{flow} = Q \rho g H \tag{3.13}$$

Which for this installation may also be written:

$$P_{flow} = \rho g d_2 v_2 (d_1 - d_2) \tag{3.14}$$

Enabling the ideal Efficiency of the machine to be calculated as:

$$\eta_{ideal} = \frac{d_1 - d_2 - \frac{v_2^2}{2g}\left(1 - \left(\frac{d_2}{d_1}\right)^2\right)}{(d_1 - d_2)} \tag{3.15}$$

For comparison of performance data, it is highly desirable to normalise both power and flow rate.

Power is normalized by dividing the power obtained at a given operating point by the maximum power obtained from the given conditions.

$$P_{norm} = {}^{P}/_{P_{max}} \tag{3.16}$$

Flow rate is normalized by comparison with 'Qmax', the maximum theoretical discharge that can be obtained from the given operating condition when all of the available static head is converted to downstream dynamic head (Toreicellis' Theorem). Including allowance for the velocity of the incoming flow, the maximum theoretical velocity is given by:

$$v_{max} = \sqrt{2g(d_1 - d_2) + v_1^2} \tag{3.17}$$

Applying this velocity across the area of the blade gives the maximum theoretical flow that can be achieved through the device:

$$Q_{max} = d_2 v_{max} \tag{3.18}$$

Parametric Power and Hydraulic efficiency for an ideal machine are plotted in Figure 3.17.

Note the important implication of equations 3.7 and 3.8 which is that even for a 'perfect' machine with no energy losses, blade forces must inevitably reduce as flow rate increases in a device that relies exclusively on static head to extract power from the flow.

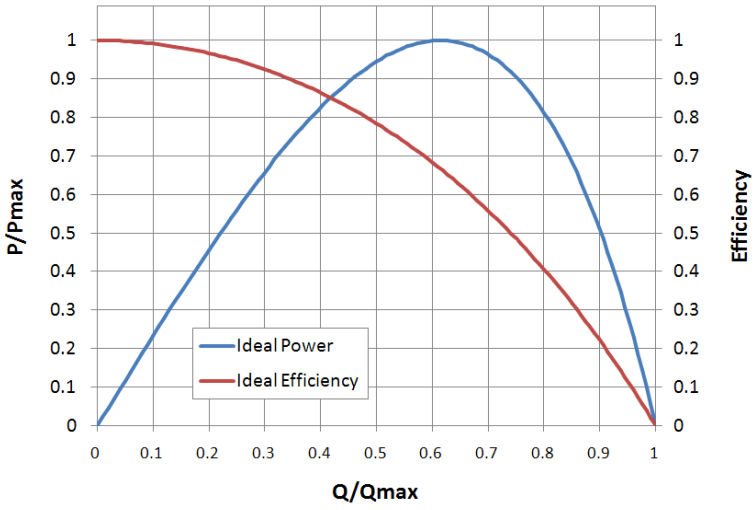

Figure 3.17: Performance of an "ideal' HPM

This is inevitable for any machine that is unable to make use of the dynamic head of the incoming and exit flows and limits the practical operating speed of a 'pure' HPM. We will re-visit this issue when we consider improvement to HPM design in later chapters.

3.3.2.3 Losses in the real machine

In Flow Acceleration

Flow accelerates as it passes into the machine from v_1 to v_2 resulting in a loss of head and therefore force available for power extraction. We estimate the magnitude of this force by considering a control volume drawn from Station 1 to station T, bounded by the wetted surfaces of the machine and the free surface of the upstream channel (Figure3.18). We assume that acceleration takes place within this control volume, is uniform and steady, and without turbulence or friction losses.

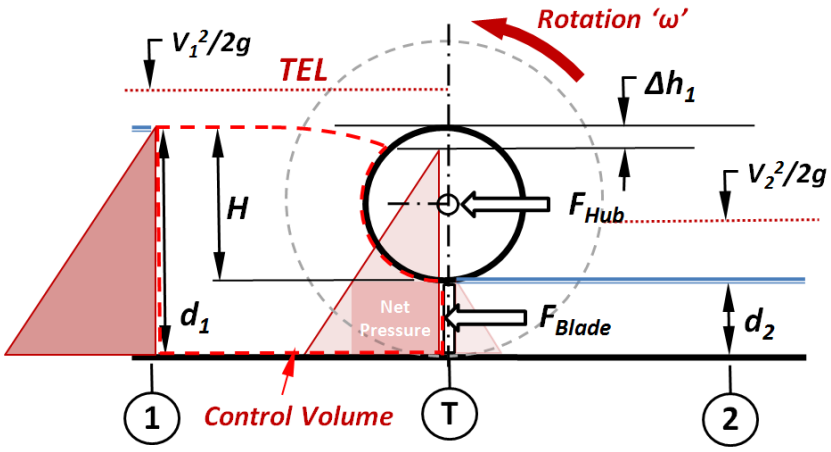

Figure 3.18: Control Volume used for Momentum Analysis

The momentum theorem applied to this case can be written as:

$$\sum F_x = \rho Q(v_2 - v_1) \tag{3.19}$$

We consider only horizontal forces and select the direction of flow as positive.

The force due to upstream water pressure is:

$$F_{us} = \frac{\rho g}{2} d_1^2 \tag{3.20}$$

The Force acting on the Hub is:

$$F_{Hubacc} = \frac{\rho g}{2}(d_1 - \Delta h_1 - d_2)^2 \tag{3.21}$$

The blade force has already been given from equation 3.8 as:

$$F_p = \rho g b l (d_1 - d_2 - \Delta h_1)$$

Therefore equation 3.11 becomes:

$$F_{acc} + F_{us} - F_{Hubacc} - F_p = \rho Q (v_2 - v_1) \qquad (3.22)$$

$$F_{acc} = \rho Q (v_2 - v_1) + F_{Hubacc} + F_p - F_{us} \qquad (3.23)$$

There is some room for debate as to exactly where the reaction to the acceleration force is applied by the HPM installation. Senior's early assumption carried over by Muller et. al. (2012) is that the HPM installation acts as a nozzle initiating flow acceleration some distance upstream of the working section of the device. Interpreting observations by Linton (2009) suggests that the acceleration of flow is much more localized and is in reality induced by the action of the blade on the fluid as the machine rotates.

Since acceleration of the flow by the fixed structure will do no work on the output shaft of the machine, it does not necessarily result in an energy loss to the system. Acceleration due to the action of the rotor blades on the other hand, does result in a direct loss in extracted power. The reality is almost certainly some combination of the two, and is likely to be very strongly influenced by the detail of the rotor and installation design.

This is another issue that will be re-examined in later chapters when we consider improvements to the basic design of HPMs. However for now, we will follow Senior's original method in representing the head loss due to acceleration as an opposing blade force acting at the centroid of the blade area at the bottom dead centre of rotation.

Turbulence

Turbulent losses are caused by both the disturbance of flow as it passes through the machine and the difference in behavior of a real liquid compared with the ideal fluid considered in the analysis.

For simplicity, it is assumed that these turbulence losses result in a force applied to the area of the blade in the opposite direction to rotation defined as:

$$F_{turb} = C_D b l \rho \frac{(v_2 - v_1)^2}{2} \quad (3.24)$$

Since the *details* of hydraulic processes occurring within the machine are *unknown*, the value of the loss coefficient must be estimated empirically, with values selected to give the best fit between theory and measured data. In practice, this makes it impossible to separate turbulence from acceleration losses and the two are effectively combined when comparing theory with data. This lack of knowledge regarding energy exchanges within the rotor is a serious gap in understanding as will be discussed at the end of this chapter, and which will be addressed in later chapters of this work.

The net force on the blade if turbulence and acceleration losses are included becomes:

$$F_{net} = F_p - F_{acc} - F_{turb} \quad (3.25)$$

And equation 3.11 is adapted to yield the net power output:

$$P_{net} = F_{net} v_2 \quad (3.26)$$

For comparison of theory to practical results, a few clarifications regarding the terms used to describe the various power outputs and efficiencies we are calculating will be useful here.

In hydropower engineering, it is conventional to refer to the 'hydraulic efficiency' of the machine as the efficiency based on the power produced at the shaft of the machine, including hydraulic losses, but excluding any leakage flows (Mosonyi, 1987).

'P_{net}' represents in effect the 'Shaft Power' of the machine, including hydraulic losses, but excluding any mechanical power losses due to friction in the rotor bearings, seals and transmission.

Hydraulic Efficiency following this convention becomes:

$$\eta_{hyd} = \frac{P_{net}}{P_{flow}} \quad (3.27)$$

The graph shown in Figure 3.19 compares power and efficiencies for the ideal machine, a machine including acceleration losses and finally shaft power and hydraulic efficiency

for a machine including both acceleration and turbulence.

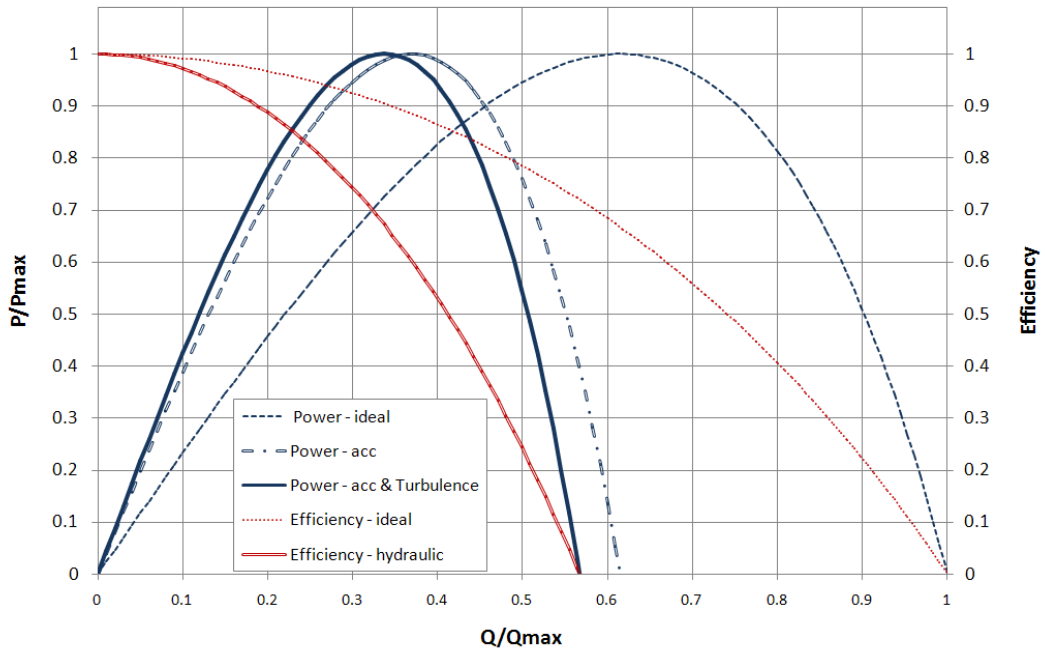

Figure 3.19: HPM performance with losses

In this case, an arbitrary C_D factor of 1.5 has been selected, with a ratio of d1/d2 = 2.4, but the graph demonstrates the dominant impact of acceleration on power output if the assumptions made by this analysis, are correct.

Leakage

Leakage is caused by the need for clearance gaps to exist between the fixed and moving parts of the machine. Although these can be estimated quite effectively in a stationary rotor by analysing gaps as submerged orifices, values of leakage are usually established by experiment. Since leakage flow rates are dependent on the head across the machine, leakage will reduce as flow rates increase and the Δh term grows.

Let the leakage flow rate calculated or measured for a stationary rotor be 'Q_{L0}'.

The leakage occurring at any given operating point will be:

$$Q_L = Q_{L0}(1 - \frac{\Delta h}{H}) \qquad (3.28)$$

Once we introduce leakage, we need to clarify which flow rate we are referring to in our calculations, so a little more terminology is required.

From here on we will identify the total flow passing through the installation as the 'gross flow', and the portion of flow that actually passes through the machine after leakage losses are drawn off as the 'net flow'.

So far, flow calculation above may be considered as referring to 'net flow', i.e.

$$Q_{net} = Q \tag{3.29}$$

So gross flow is given by:

$$Q_{gross} = Q_{net} + Q_L \tag{3.30}$$

Strictly speaking, leakage should result in a re-evaluation of the Δh_1term, but for machines where leakage is low (<3%Qmax), may be neglected.

The assumption is made that leakage flow is lost to the power extraction process therefore power can only be obtained from the net flow remaining.

The 'volumetric efficiency' of the machine is given by:

$$\eta_{vol} = \frac{Q_{net}}{Q_{gross}} = \left(1 - \frac{Q_L}{Q_{gross}}\right) \tag{3.31}$$

And overall efficiency '$\boldsymbol{\eta}_{out}$' at any given operating point as:

$$\eta_{out} = \eta_{vol} . \eta_{hyd} \tag{3.32}$$

Leakage constitutes a high proportion of the flow at very low rotor speeds hence volumetric efficiencies are low and have the greatest impact on efficiency and power output in the low flow region of HPM operation (Figure 3.20).

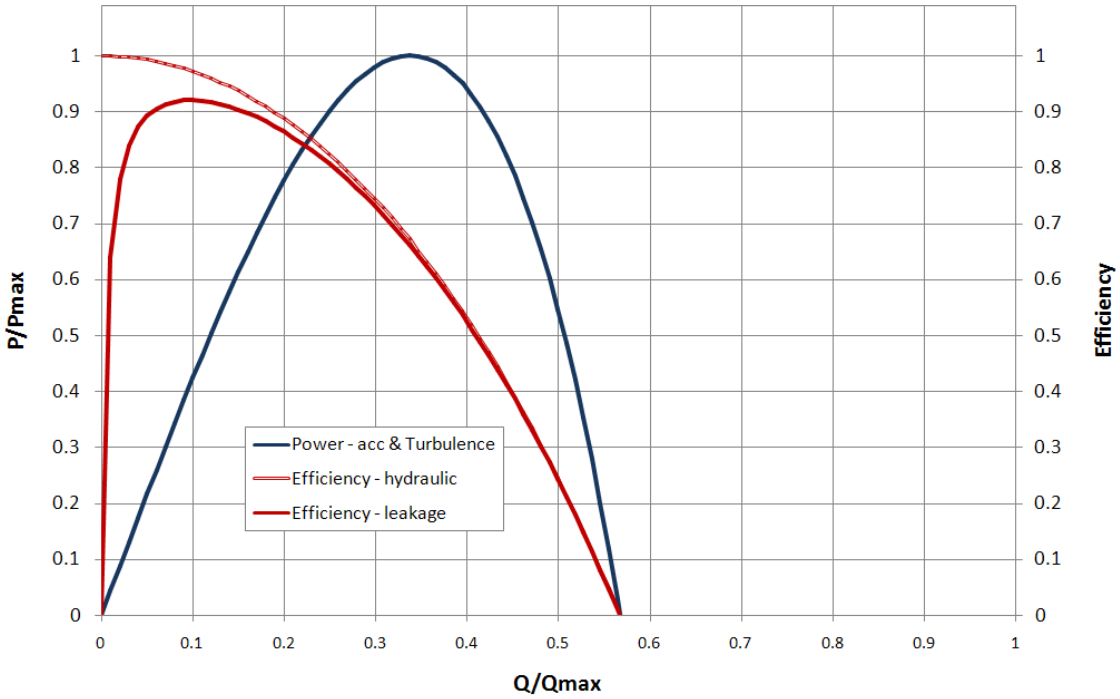

Figure 3.20: The effect of leakage on HPM performance

3.3.3 Limitations of Classical Theory

The basic HPM theory presented here has been shown to successfully model the general behaviour of machines at laboratory scale. However it has several practical limitations.

1. The theory addresses idealized machines of simple geometry and model test dimensions are generally set up to represent this. However, in practical machines, particularly those designed for mill reactivation sites, significant deviations from these geometries is often unavoidable due both to the constraints of pre-existing water channels and the variability of up and downstream water levels typical in low head sites. It is unclear how applicable classical HPM theory will be in such circumstances.
2. The reliance on empirical factors to model losses draws a 'veil of ignorance' over the detail of the hydraulic energy exchange occurring within the machine and installation. While this is largely inevitable given the likely complexity of

interactions between the rotor and the fluid, it presents three significant problems to developers of the machine:

a. With no theoretical alternative, installation design becomes dependant on model testing to predict the performance of full scale units. However without some knowledge of the hydraulic processes involved, scale effects cannot be fully allowed for, reducing the confidence in performance predictions based on model testing.
b. The marginal costs of many ultra low head projects will not support the expense of model test studies. Some means of estimating machine losses based on machine and installation geometry is therefore required, which in turn implies a more detail understanding of loss and energy transfer mechanisms occurring *within the machine itself*.
c. The current theory offers little guidance to would-be designers in selecting the detailed geometry for the rotor and installation likely to give the best performance from the conditions at a given site. The shape of side plates, shoe profile, blade design and width of the rotor compared with the inlet and exit water channels have all been shown to have important impacts on performance in model tests but the mechanism by which they reduce energy losses is entirely unknown.

3.4 Summary & Gaps in Knowledge

In this chapter we have traced the long development of machines using hydrostatic pressure difference as a primary source of energy extraction. These machines were often developed through engineering intuition and without the benefit of supporting theory.

In addition we have described the work being carried out by other Universities on HPM performance as part of the HYLOW project which ran partly concurrently with the work described in this thesis. We have noted significant variations in model geometries contained in their work which makes comparison of results between data sets difficult and limits the potential to assess scale effects with any certainty.

We have reviewed the basic HPM theory developed by Senior and Muller which effectively models the general overall behaviour of laboratory scale HPM machines.

However it is unclear as to how effective this theory, based on simplified geometry will be when applied to the more complex geometries encountered in full scale installations.

In addition we have noted that since this theory relies on empirical loss coefficients, the model offers little insight into the actual energy exchange processes occurring within the HPM installation, and the impact that machine geometry may have upon them.

The use of empirical loss coefficients derived from model testing is of limited value to the designer of practical HPM installations, unless losses can be more clearly linked to the geometry of the machine to enable sensible design selections and trade-off to be made.

We have also noted at several points, that classical theory suggests some scope for performance improvement over the basic HPM design which are worth investigating.

Addressing these gaps in knowledge is important if HPM development is to progress to the design of commercially viable designs and largely defines the scope of the research described in the remainder of this thesis.

3.5 Aims of this research

The aim of the current work is to add sufficiently to our understanding of HPM devices to enable the hydraulic design of future full scale machines to be carried out, with a more predictable performance and higher efficiency at peak power than is possible with current knowledge. This is regarded as a necessary precursor to the commercial exploitation of viable HPM devices.

For this to be possible a wide range of problems need to be addressed – at least in sufficient detail to enable design judgments to be made. This may lack purely scientific rigour, but such a synthesis is necessary if sufficient progress is to be made to fulfil this aim within the limited time and budget constraints of the current research.

It is anticipated that this work will provide initial insights in HPM function to enable more rigorous analysis to be carried out by future workers.

Specific areas of study will be:

1. The behavior of full scale devices compared with classical theory and the results of model tests for geometrically similar machines in order to assess the impact of scale effects on performance prediction.

2. Energy transfer processes occurring between the rotor and the fluid will be studied and the extent to which these may be affected by geometry selections assessed.

3. Alternative HPM designs will be studied in the light of energy transfer knowledge with a view to improving performance.

3.6 Research Objectives

To fulfill the stated aims for the research the work has been broken down into the following key objectives:

1. Investigate experimentally the performance of a full scale HPM installation in the context of a 'live' mill reactivation site. This objective involves the design, construction and performance testing of an appropriate prototype unit to enable performance to be compared to classical theory.

2. Investigate experimentally the presence of scale effects between geometrically similar machines at laboratory scale and full size. This objective involves the construction of an exact scale model of the test installation of objective 1 and comparison of performance measurements between scale and prototype units.

3. Investigate experimentally the energy transfer processes occurring during rotation of an HPM. This objective involves direct measurement of force and pressure variations taking place during testing of the laboratory scale device of objective 2, through suitable instrumentation.

4. Interpret the results from objective 3, seeking to relate energy transfer mechanisms to the geometry of specific machine features. It is accepted that, due to the complex nature of real flows, any analysis developed will be approximate but suitable to yield indicative information to aid future machine design.

5. Investigate experimentally alternative rotor and machine designs with a view to reducing energy losses or undesirable operating characteristics of machines identified from objectives 1 – 4 above.

Chapter 4: Field Trial Unit Design & Construction

4.1 Rationale behind the Prototype Unit

In order to fulfil the first aim of the research, namely to compare the performance of a full scale HPM to both theory and model test results, a prototype unit was designed and installed at Partenstein Mill, in Germany. This represented a substantial body of work which in addition to the purely scientific first aim of the project also supported the overall research objective by enabling practical design and operational experience of the HPM to be obtained under realistic field conditions.

This experience was gained in the following areas:

1. The performance measurement of a full size HPM prototype under in 'real world' conditions for later comparison with model tests and theory.
2. Direct experience of the compromises in machine geometry required in a mill reactivation scheme, and assessment of the overall system requirements that such installations demand.
3. The use of the HPM as a grid-connected, electricity generator. This was the first installation of its kind in the world and produced insights, into the complex control and performance issues that arise in this application.
4. Construction allowed realistic cost data to be accrued with which a better assessment of the cost effectiveness of the technology can be made.
5. Valuable operational experience was gained with the device that uncovered several practical limitations to its operating range, and areas in which future development of the technology should be focused.

A significant additional factor in the design of this prototype installation was the agreement made by the HYLOW project, to leave the mill owner with a fully functional hydropower plant on completion of the research. The test unit therefore became a full product prototype rather than a simple large scale test installation with considerable implications for overall system design and reliability. To aid future workers, a detailed description of the design of the machine and installation is presented in the following sections.

4.2 The Partenstein Site

4.2.1 Location and Lay out

The site for the HPM installation was the "ObereMuhle" (Upper Mill), in the village of Partenstein, in the Northern Bavaria region of Germany (Figure 4.1). The prototype installation was situated on the river Lohr, approximately 4 Km downstream from the gauging station at rammersbach.

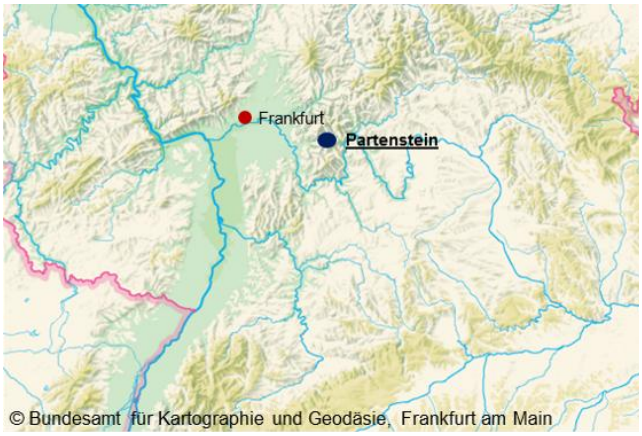

Figure 4.1: The Location of Partenstein *(BKG, 2001)*

The mill was active until the late 1940's, powered by a 5.5 meter diameter Zuppinger wheel of 1.5 meter width, producing around 6 kW of mechanical power (Figure 4.2).

Figure 4.2: Mill House and Zuppinger Wheel, circa 1920's *(Kunkel Family Album)*

It was first used for processing grain, before being adapted for milling the mineral barite.

The mill was deactivated in the 1950s becoming derelict before being restored as a private home by the current owner around 1996. Since the water wheel was dismounted, hydropower has not been used at this site, although the mill race remains active and in good condition.

The lay-out at Partenstein is fairly typical for a run of river site, (Figure 4.3). There is no mill pool but, instead, headrace works consisting of three stone abutments, divert a portion of the river flow into the mill race. The abutments are fitted with stop logs permitting a crude degree of level control in response to changing river conditions. From the inlet, the mill race transports water the 100 meters to the original wheel site, and from thence a further 50 meters downstream to rejoin the main river channel. The

mean width of the mill race is 2.2 meters, reducing to 1.9 at the site of the orriginal Zuppinger Wheel. The head drop across the inlet works is generally set to around 0.5 meters, resulting in a head of 1.2 meters at the location of the wheel site.

Figure 4.3: Overview of the Partenstein Site

This leaves a depleted region in the river (i.e. that portion experiencing reduced flow when the mill is in operation), of around 150 meters total length. In addition, the head-works and stop logs represent a potential barrier to migration of aquatic life forms and both of these factors played an important role in negotiations, conducted with the local River Officer, regarding the environmental impact of the test installation.

4.2.2 River Flow Conditions

The estimated flow duration curve for the Partenstein Mill and a summary of key flow parameters are shown in Figure 4.4, and Table 4.1.

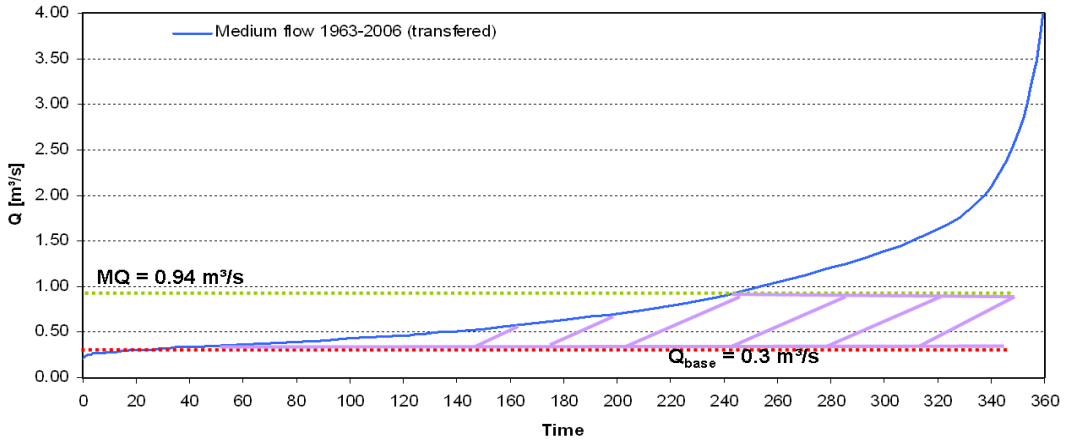

Figure 4.4: Total flow at the mill in Partenstein (Lohr) with residual flow (0.3 m³/s) and medium discharge (1.37 m³/s)

These were derived from a combination of historical data obtained from the Fammersbach gauging station (3.5 km upstream) between 1963 and 2006, and site flow measurements recorded between June 2009 and November 2010 (Schneider (2010)).

As can also be seen from the table, the variation of flow between minimum flow and high water conditions is high, indicating a river with a high flow index (Environment Agency (2009)), with quite high and rapid variations in flow levels occurring in response to prevailing conditions. In addition, this natural high variation in flow is compounded by the intermittent operation of the "Black Mill" hydropower plant located 2 km upstream of the test site – which resulted in high daily flow variations coinciding with peak generation demands.

4.2.3 Selection of Design Flow

Standardised design flow estimation methods are usually mandated by which every agency has the environmental authority for flood control, water abstraction and ecological preservation of a given location.

Flow Condition	Flow Rate (m^3/s)
Minimum Flow (NQ)	**0.21**
Mean Minimum Flow (MNQ)	**0.29**
Mean Flow (MQ)	**0.94**
Mean High Flow (MHQ)	**6.15**
Maximum High Flow (HQ)	**16.83**

Table 4.1: Flow Summary – Partenstein Mill

Once any potential flood risk due to the presence of the new plant has been assessed, (often easier for the reactivation of a former mill site), discussions usually hinge around the measures required to minimize the environmental impact of the project and, from a hydropower designer's point of view, the flow that must be maintained through the depleted region of the river during operation. In the UK, this "residual flow" would be calculated based on the naturally occurring low river flow (defined as the flow rate exceeded 95% of the time in an average year) added to a "Hands Off Flow" defined to ensure that "hunting" of the hydropower device due to repeated start ups and shut downs under marginal operating flow conditions does not occur. An additional residual flow margin may also be imposed depending on the environmental sensitivity of the site.

The mandatory requirements governing micro hydro developments in Bavaria are slightly less demanding and are governed by the requirements of "ArbeitsanleitungzurAbschätzung von Mindestabflüssen in wasserkraftbedingtenAusleitunsstrecken" (work instruction for the estimation of minimum flows in the natural river due to water power use). Under these requirements, mandatory minimum flow is defined as either "Q_{eco}" defined as 5/12MNQ (taken from Table 4.1 above), or the minimum operational turbine flow defined as 4% of the design flow of the turbine, whichever is the greater value.

However, local River Officers have considerable discretion in negotiating actual flow requirements and by local agreement a higher than mandated "residual Flow" of 0.3 m^3/s was to be maintained through this reach, whenever the mill is operating. This

gave a design flow of 0.64m³/s (see Figure 4.4), allowing 120 days of operation at full power, with a further 155 days at reduced power. In addition, the regulations regarding grid connection of renewable energy sources in Bavaria are very straight forward for power outputs of 5kWe or less, but become considerably more complex for power outputs above this level. Although a 6kW power output was theoretically possible from the available flow and could be accommodated during performance testing, for simplicity, the grid connection power output was limited to 5kWe.

4.2.4Flood Conditions

The micro hydro designer must take care to design for the effect of high water flood if any system design is to be reliable (Harvey et.al. (2008)). Based on recorded data, a high flow condition of 4.4m³/s could be anticipated at this site each year. The maximum flood condition of 29.64m³/s was recorded in 1970 (Figure 4.5), and an early decision taken to mount all electrical equipment safely above this flood level became a significant constraint in the design of the power take off.

Figure 4.5: Flood Conditions at Partenstein Mill : Electrical Equipment needed to be mounted above the stone block seen here to the left of the water drop.
(Kunkel Family Album)

4.3 Installation Design

4.3.1 Design Constraints

In order to develop an installation design suitable for general mill reactivation applications, the following constraints were imposed:

1. The machine should fit within the existing mill channel without disturbing the existing stonework or requiring additional excavation.
2. The machine structure should be self-supporting and minimize loads transferred to the existing mill structure.
3. Access for heavy machinery was restricted and the maximum mass of any one assembly was limited to 500 kg.
4. The target budget for the electro-mechanical elements of the installation was limited to £25,000 (later increased to £32,000).

The degree to which these constraints impacted the evolution of the HPM installation design will become apparent in the following sections of this chapter.

4.3.2 Description of Overall Scheme

The overall layout of the site, together with views of key installation details, is shown in Figure 4.6.

The river inlet (1) was split into two sections: Section "a" contained a temporary "slot and pool" fish ladder to aid migration of fauna, while Section "b" was built up with stop logs as required by prevailing conditions to maintain the required operating head. A floating boom (2), set across the inlet to the Mill Race diverted the largest floating debris carried by the river, before the flow passed through the fish screen (3) with an inter bar spacing of 14mm as agreed with the local river officer.

A footpath passes over the mill race at (4) and for safety an additional "Kinder Gidder" (child screen), rack was fitted immediately upstream of the access platform for the sluice gate at (5). A grass by-pass spillway was planned but not installed during this project at (6) to carry any surplus water safely around the HPM installation at (7).

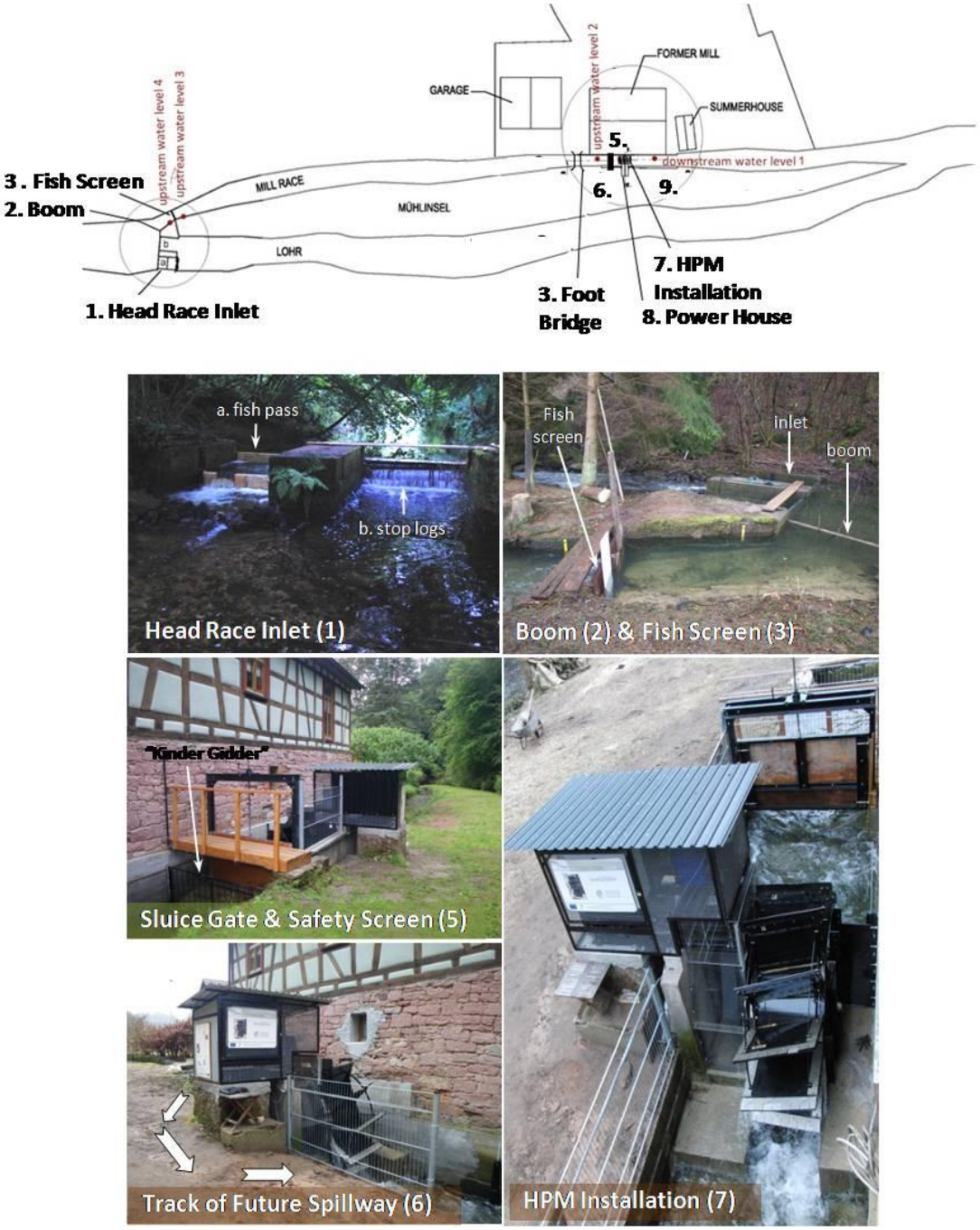

Figure 4.6: General Layout of Partenstein Mill Scheme.

The fixed ratio gearbox, generator and inverter were safely installed above flood level in the power-house (8), with power lines fed into the Mill House for metering and grid connection. For performance testing, water level measurement stations were set up at the positions shown, while flow measurements were carried out using a temporary weir

at (9) or propeller traverses conducted in the leat, immediately downstream of the stone bridge at (4).

4.3.3 Hydraulic Design

Basic HPM theory enabled the peak power output of the device to be estimated from the given design flow, while model test data reported in Linton (2009) was used to estimate the performance speed range for the device using Froude scaling laws (Figure 4.7).

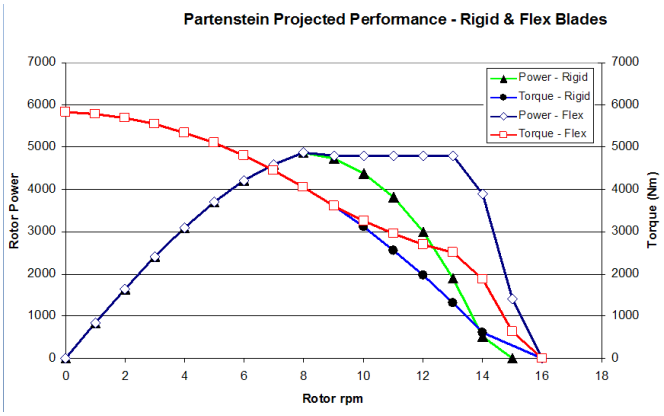

Figure 4.7: EstimatedHPM Performance Curve

These model tests were also used as a basis for setting rotor and installation geometry, with proportions of blade to hub diameter ratio, the ratio of rotor width to channel width, and shoe geometry being maintained between model and prototype as far as possible. However, the practicalities of the installation and need to simplify manufacture, forced some compromises in geometry, shown visually in Figure 4.8, with model geometry (*left*) compared with Prototype geometry (*right*), presented at the same scale. These compromises were:

1. The blade to hub diameter ratio used in the prototype corresponds with reduced model rotor diameters tested by Linton (2009), and are 30% smaller than the original Senior model wheel.
2. The prototype rotor is 1/3 of the width of the model and was selected to produce peak power at the design flow rate with a shaft speed of 10 rpm.
3. The moderate helical twist of the model blade was replaced with flat, untwisted blades inclined at 15° to the rotor shaft axis to simplify fabrication.
4. Basic HPM theory assumes that the downstream water level is tangential to the bottom surface of the hub tube. However, model tests suggested that higher power outputs could be achieved with downstream water levels at 70% of blade length, and since no data was available regarding the variations of downstream levels in high water conditions, rotor axis height was set so that the lower surface of the hub tube was 200mm above nominal downstream water level.

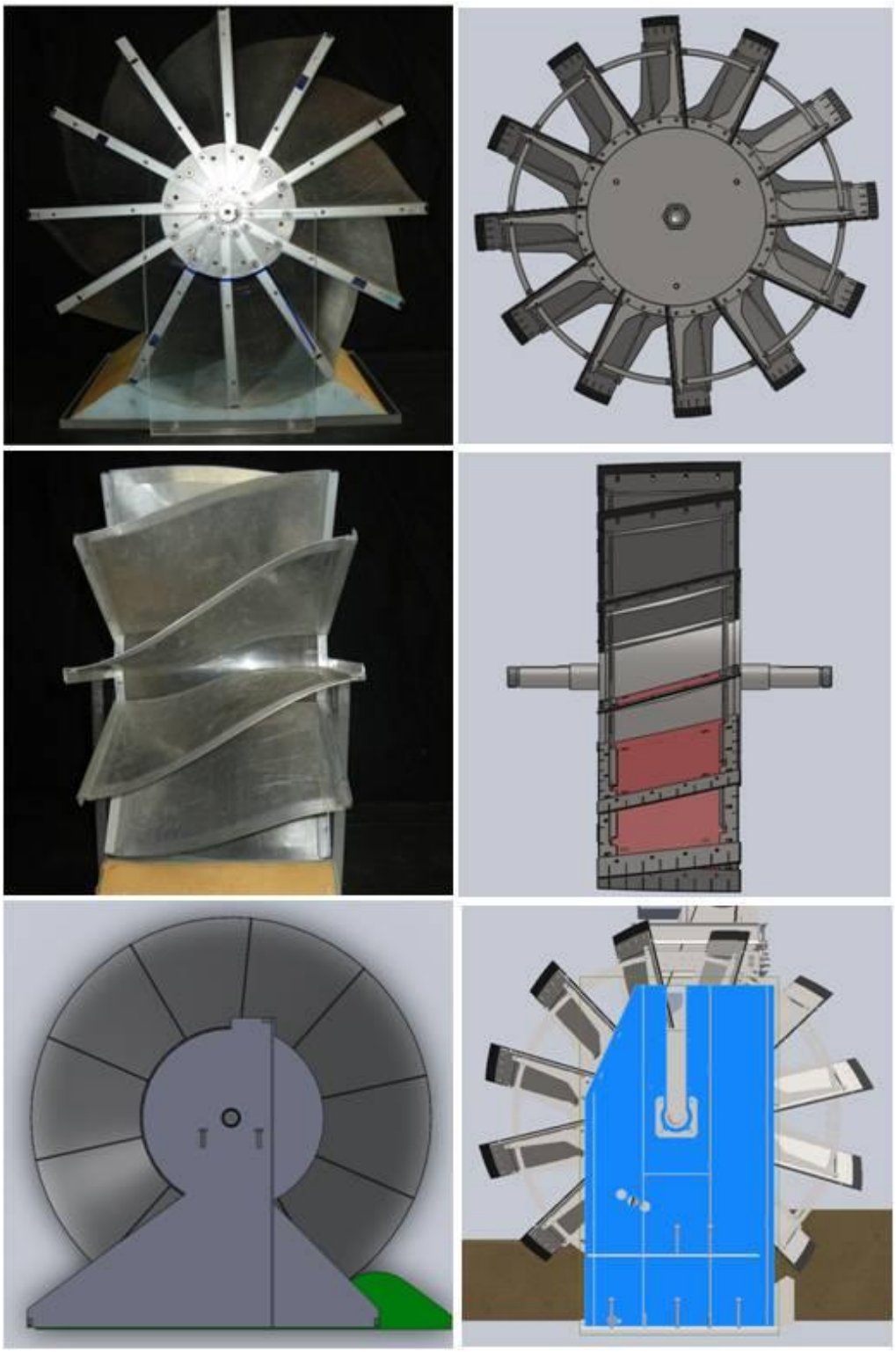

Figure 4.8: Model Geometry *(left),* **compared with Prototype Geometry** *(right)* – Blade lengths *(top),* Rotor widths and blade twist *(middle),* Side plate profiles *(lower)*

5. Model tests had shown that the shape of sidewalls have a significant impact on HPM performance. However, while initial prototype designs replicated the asymmetry of the model test installation faithfully, the side plates were simplified into symmetrical forms to increase structural strength and reduce manufacturing costs for the final unit.

Each of these compromises in hydraulic design was to impact machine behaviour to some extent as reported in later sections of this report.

4.3.4 Mechanical Design of the HPM

The overall dimensions of the HPM installation are shown in the schematic of Figure 4.9 which also illustrates how this machine was designed to fit around the existing structure in the water channel.

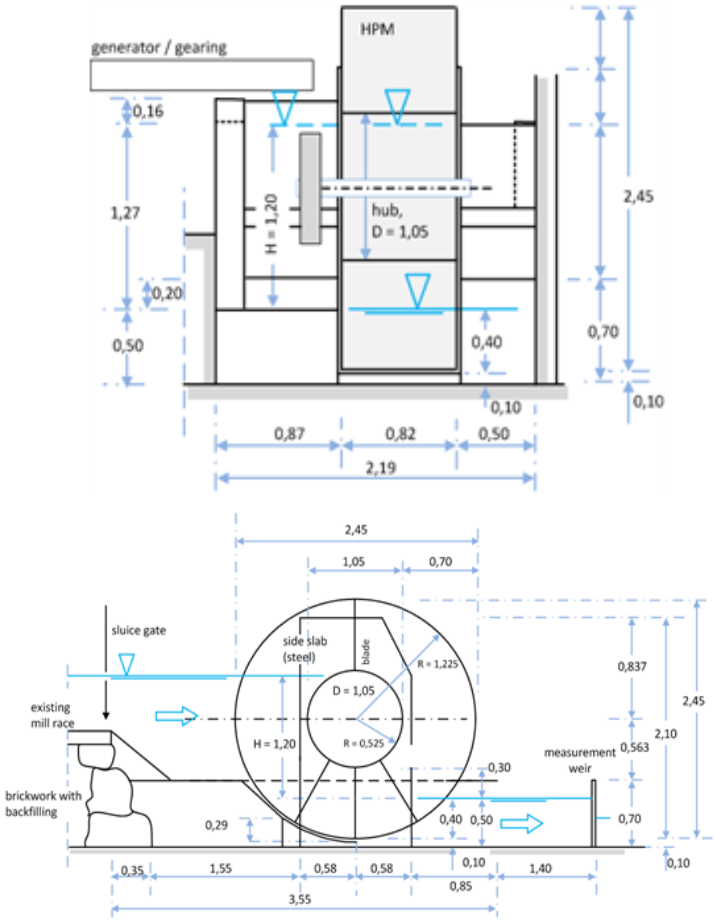

Figure 4.9: Leading Dimensions of the HPM Installation at Partenstein. showing view from downstream (*top*) & side elevation (*bottom*) – All dimensions in meters

The design used a series of bolt together, pre-fabricated assemblies to form the wheel and support structure without exceeding weight limitations. Extensive use of laser cutting technology enabled elements to be accurately assembled during fabrication and in the field, registering against alignment holes laser cut to positional accuracies of $^{+}/_{-}$ 0.05 mm. The rotor assembly is shown at the fabrication shop prior to final welding in Figure 4.10a.

The rotor was supported on a fabricated assembly consisting of side plates and shoe profile. This assembly transferred all mechanical loads from the rotor into the concrete foundations of the installation as well as forming the walls of the flow passageways through the machine.

The assembly was bolted together onto a pre-cast concrete base slab and braced to support and align the form-work for the reinforced concrete side "panniers". All loads from the installation were reacted by the mass of this concrete, with no mechanical shear connection required to the pre-existing masonry structure (Figure 4.10b). The addition of steel-plate 'Stub Weirs', used to seal the channel either side of the machine , and so direct all flow through it, completed the fixed structure of the installation.

Wheel loads were transferred from the Hub Tube fabrication (weighing 350Kg), to the side plate structure through housed bearing units bolted to the side plate assemblies (Figure 4.10c). Blade fabrications were bolted to the Hub Tube, both to keep the weight of the assembly manageable and to permit alternative blade designs to be fitted at a future date. Loads imposed on the bolts by the blades were reduced by the use of 'Snub Ties' which acted as tie bars allowing forces imposed on an individual cell to be supported by adjacent blade elements (Figure 4.10d).

Figure 4.10: HPM Design
a. Rotor during Fabrication, b. Side plates & panniers, c. Hub and Blade, d. Snub Ties

Model tests had demonstrated that water leakage around the rotor would have an important impact on performance and, in order to minimize this whilst accommodating build tolerances,

adjustable seal units were fitted to the side and edges of each blade, and to the periphery of the hub tube (Figure 4.11a).

The detail of the blade seals was quite carefully contrived, and is shown in Figure 4.11b. The position of these seals was adjusted on installation to take up the nominal build clearance between the rotor and surrounding fixed structure of 10mm.

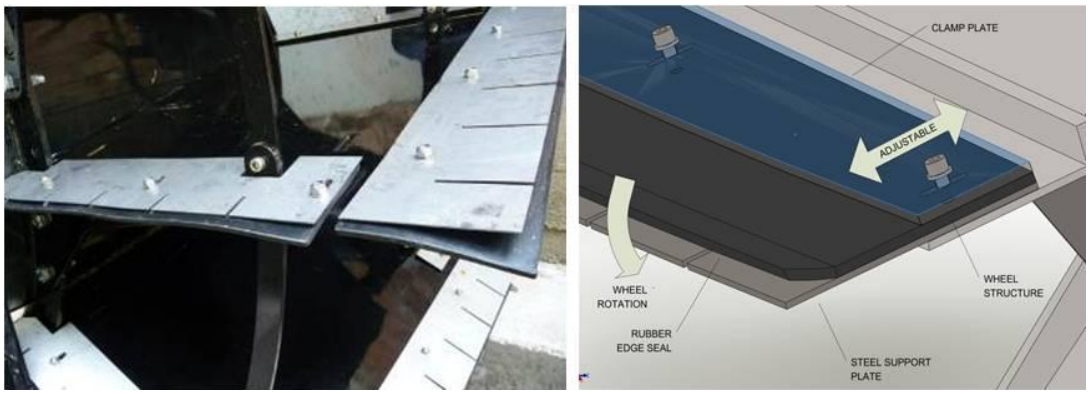

Figure 4.11: Blade Seal details: a. Assembled Seals, b. Adjustment & Function

The fabric reinforced flexible rubber seals were designed to bear against the shoe and side plate during rotation, deflecting away from tight spots on contact, but wearing in over time, to give a close running fit with minimal additional friction. The stainless steel support plate had two functions. First, it supported the rubber seal against pressure loads. To be effective, the maximum unsupported length of seal at the outer edge of rotation was limited to the thickness of the seal material itself (in this case 6mm); - any more could result in water pressure pushing the seal past the blade increasing both leakage and friction. Secondly, the support plate protected the wheel from damage due to debris in the flow. Should an object become jammed in the wheel, the fingers of the support plate were designed to yield, allowing rotation to continue and localizing any damage to an easily repaired component. Frequently, repair consisted of no more than bending the finger element back into position, following removal of the obstruction.

4.3.5 Power Take Off and Control

4.3.5.1 Design Parameters

The Power output characteristics of the test HPM presented a number of difficulties for the design of the power take-off (PTO), system:

1. Shaft Torque was very high, due to the slow rotational speeds of the device, reaching a peak value of 7500Nm when the rotor was stationary.
2. Rotational Speed of the unit varied in proportion to the volume flow rate passing through the wheel. Since for test purposes, operation was required over as wide a speed range as possible, an ideal PTO design would permit a rotor speed range from 0 to 25 rpm.
3. Variations of rotor speed as each blade passed through the bottom section of the wheel rotation, were noted by Senior (2009). However the magnitude of this speed variation, and any accompanying changes to shaft torque were unknown, with no data indicating how this "ripple" effect might vary with speed of rotation. This put an unknown, cyclic variation on top of the already high steady state loadings assumed with implications for the fatigue life of transmission components.
4. The Duty Cycle for hydropower equipment is demanding with 24 hour operation at full load anticipated for considerable periods of time. The design intent for the project was to produce an HPM installation capable of sustained operation after performance testing was complete. Duty cycle is also a function of the characteristics of the connected load – in this case an inverter controlled generator – and interactions between the load and prime mover under certain flow conditions proved to be an important source of additional transmission load (reported in Chapter 6).

4.3.5.2 Transmission Design

The transmission design had to fulfill the following functions:

1. Transmit the very high torque output from the wheel successfully to the generator.

2. Increase the speed of rotation from the wheel sufficiently to permit an “off the shelf ” generator to be used.
3. Transfer the axis of rotation from the wheel output shaft (below upstream water level), to a point well above high water level to protect the generator from possible flood damage.

Several alternative transmission designs were considered and are summarized in Figure 4.12.

The integral generator gearbox combination (Figure 4.12a), is potentially a very robust design solution. However, for this application it was rejected due to the limited speed range that could be accommodated, high initial costs, and the limited space available to the side of the HPM to accommodate the 600Kg unit.

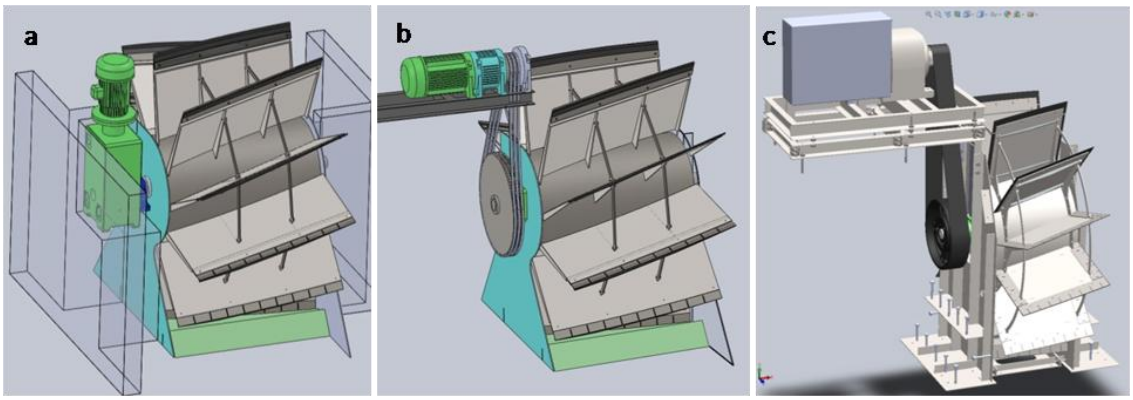

Figure 4.12: Alternative Transmission Designs: a. Integrated Generator-Gearbox, b. Triplex Chain Drive, c. HTD Toothed Belt Drive

The chain drive (Figure 4.12b), was rejected over concerns regarding costs, the environmental impact and maintenance overhead associated with providing greased lubrication to the chain, and concerns over the noise generated by such drives.

A high torque drive (HDT), synchronous belt drive was finally selected as the best compromise between cost, performance and ease of modifying velocity ratios as performance testing progressed. Belt loads were reacted internally between the side plate and generator support frames using tie plates, while belt tensioning and pulley alignment were carried out using a series of jacking screws (Figure 4.12c).

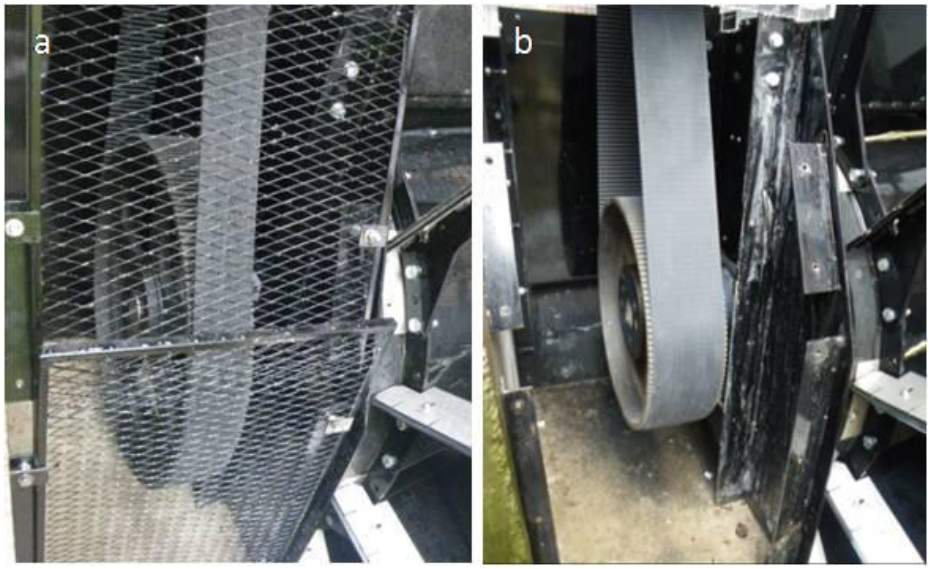

Figure 4.13: The two belt drives used: a. 1:5 ratio, 115mm belt (September 2011 tests). b. 1:3.6 ratio, 160mm belt (fitted January 2012).

The belt formed the first stage of the transmission system, turning a 5:1 fixed ratio gearbox, driving a low speed, permanent magnet, variable speed generator via a flexible coupling. Two belt ratios were employed during tests in order to cover the necessary speed range to develop the complete performance curve, due to generator operating speed limits (see below); a 1:5 belt ratio for all tests in 2011 reduced to 1:3.6 to enable higher wheel speed to be used for all tests carried out in 2012 (Figures 4.13a and 4.13b).

4.3.5.3 Electrical Generation and Control

The generation and control system had to be capable of operation in two different modes: direct manual control over a wide range of preset speeds during performance testing, and sustained autonomous operation extracting the maximum available power from the flow for grid connected electricity generation. This latter requirement was by far the most demanding, and a block diagram of the electrical system used is shown in Figure 4.14 while the complete generator sub assembly, mounted on its supporting frame is shown in Figure 4.15.

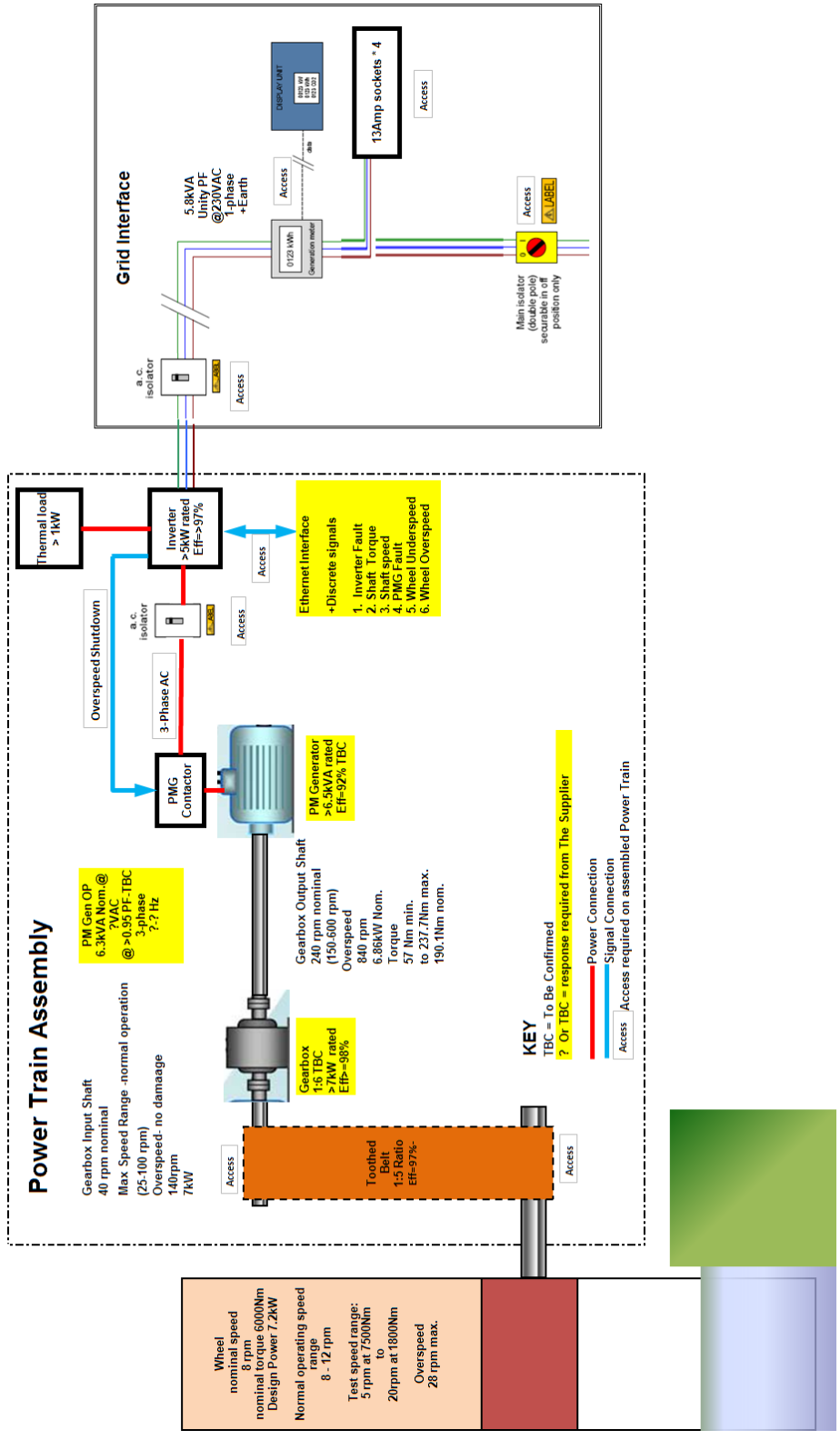

Figure 4.14: HPM Control System

Figure 4.15: The Generator Sub Assembly. a. at the factory, b. During installation

To achieve the required very wide speed range, a low speed, permanent magnet generator was employed. However, in practice, the speed of the generator had to be restricted between upper and lower limits: very low generator speed (<30 rpm), resulted in high currents in the generator, and the danger of heat damage to windings and insulation, while at generator speeds above 300rpm, output voltages exceeded the insulation rating of 600V for the inverter input. A Siemens Step 7 PLC controller monitored the system and disconnected the generator should operation occur outside these limits. This controller also engaged ballast resistors to control peak currents occurring during the start up process.

Start up and shut down were both manual operations due to the absence of a fully automated sluice gate control (caused by budget restrictions), and the sluice had to be manually closed following automatic disconnection of the generator since the HPM would at this stage be freewheeling. This proved to be a serious compromise for practical generation, particularly given the high diurnal flow variations experienced at this particular site. The conditioning of electricity for grid supply was carried out using an Ingateam 6.0LT Inverter system originally designed for wind turbine installations (Figure 4.16). This unit controlled connection / disconnection to the grid automatically ensuring compliance with local grid connection standards. In addition, it had the inbuilt capacity to accept a performance power curve for the specific device being controlled, enabling the unit to ensure load was applied more efficiently, to

achieve maximum power output at any given speed. An optimising algorithm also appeared to be incorporated within the device, which periodically allowed rotor speed to vary as the system attempted to detect whether a higher power output could be sustained from the prevailing conditions.

However, variations in downstream water level, and therefore net head, changed the operating characteristics of the machine significantly – effectively requiring a different power curve to be used for each operating head condition. This limitation gave rise to several practical operational problems with the installation, also reported in Chapter 5.

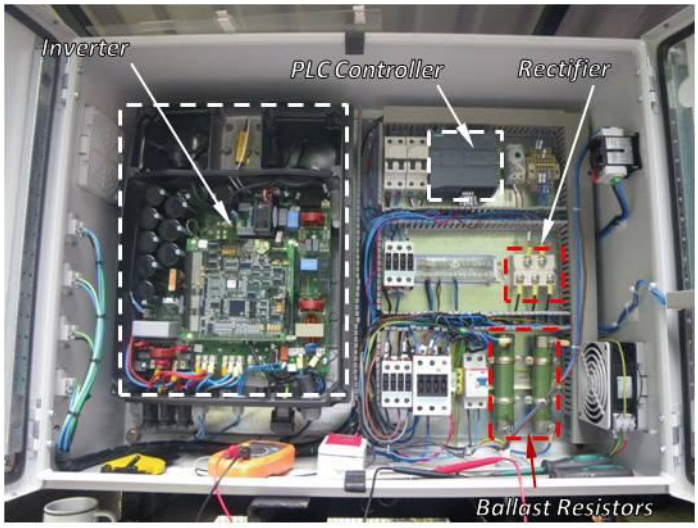

Figure 4.16: Inverter *(cover removed)* **& Control System.**

4.3.6 Ancillary Equipment

In a complete micro-hydro system, ancillary equipment can have a significant impact on both costs and ease of operation of the installation (ESHA, 2004). The brief descriptions of designs used at Partenstein presented here illustrate this point, and also highlight the areas in which these designs need to be improved for reliable future operations.

4.3.6.1 Sluice Gate

To keep costs low, a simple sluice gate was fabricated using marine ply as the facing material, reinforced with steel channel (Figure 4.17). To ensure "man portability", the unit was prefabricated for in situ assembly into a pre-existing step contained in the existing masonry. The basic fabrication and seal system worked well, although the hydraulics of the location chosen presented a considerable disruption to the flow (reported particularly in the Scale model tests of chapter 9).

Operation of this gate was performed manually using a “Rising Stem” design accessed via a small timber platform. As alluded to above, manual operation was a compromise – a fully automatic open and close function of the sluice is required for fully autonomous operation of the HPM and is considered essential to all future installations.

Figure 4.17: Sluice Gate, with marine ply blade, channel stiffeners and access platform.

4.3.6.2 Fish Screen

For expediency, the fish-screen was located at the former location of a sluice gate, close to the inlet of the mill race (Figure 4.18).

Figure 4.18: The Fish Screen. (left). Viewed from upstream, (right). Grill sections and support structure.

The support structure for the screen was designed to resist full static pressure loads occurring should the narrow, 14mm spacing between blades become blocked. This was a regular occurrence during autumn operation where leaves carried down by the river, required manual cleaning of the fish screen every 20 minutes or so. This screen was also undersized for the prevailing conditions, with approach velocities rather too high to comply with UK standards due to its location within the mill race channel, rather than at the mouth of the inlet.

In addition the rather crude design of this fish screen resulted in higher than necessary head drops across it – particularly at high flow rates, and sections of the screen needed to be removed to achieve the flow rates necessary during high rotor speed tests (Chapter 6).

4.3.6.3 Fish Pass

While a fish pass is usually a mandatory feature of micro-hydro installations and mill reactivation projects, an unusual requirement for the Partenstein project was that the fish pass had to be removable so as not to impede the passage of the very high winter flow rates.

The design employed (Figure 4.19), was a rather crude embodiment of a "slot and pool" fish-pass, intended to function at a minimum flow rate of 70 litres per second (Armstrong et.al. 2010). The steps of the pass themselves, were constructed from timber sections, supported by steel channels bolted to the existing masonry walls of the piers.

Although this design was sufficient for temporary test purposes, a better design is required for long-term operation, both in terms of the fish species catered for and for ease of removal in high-water conditions.

Figure 4.19: The Fish Pass. *(left)* from downstream, *(centre)* from upstream over one step, *(right)* one baffle.

An installation based on a Super Active Baffle design (Figure 4.20), appears to offer the best all round compromise, since it has been shown to be passable for all fish species, and lends itself to pre-fabrication into a removable form. The hydraulic design required for a fixed fish pass installation, that is able to accommodate winter flows with no increase in backwater levels, is not a trivial design problem although further consideration is

beyond the scope of the present work.

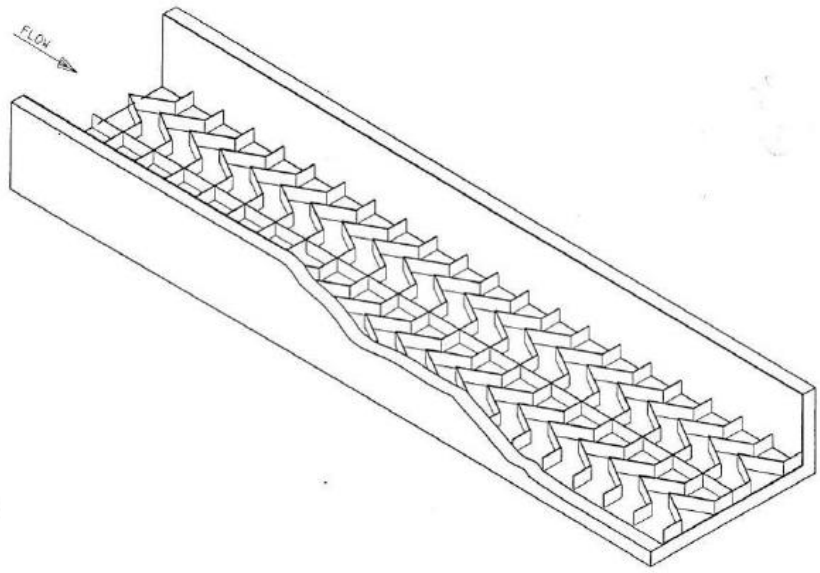

Figure 4.20: Larinier Super Active Baffle Fish Pass *(Environment Agency, 2010)*

4.4 Installation Costs

Project costs for the Partenstein Installation are summarised in Table 4.2 and Figure 4.21.

Note that these are direct costs and refer to the one off prototype machine hence care should be taken in applying these values to future projects for the following reasons:

1. The prototype installation had a number of shortcomings which must be addressed in future applications, notably the lack of an automatic gate (estimated €6500 additional cost), and control system (estimate €6,000 additional cost).

Item	Partenstein Cost (€)	Future Project (€)
Machine	11500	11500
Power Take Off	18300	24300
Civil Works	7800	7800
Fish and Safety Screens	2000	2000
Installation	4000	4000
Sluice Gate	0	6500
Totals:	43600	56100

Table 4.2: Summary of Project Costs

2. Values for the machine, installation, fish and safety screens are costs, not prices, with no allowance for operating overheads, design or profit which would normal result in a considerable mark up in commercial projects.

Nevertheless, this cost data is useful and leads to some interesting observations. First the cost of civil engineering works is very low, reflecting the substantial advantage in redeveloping sites where water control structures are already present and in good condition. Second, the direct cost of the machine itself is comparatively low, particularly taking note of the fact that this represents the costs for a one-off experimental prototype. The third observation is however, more significant: the cost of the power take off is substantial and if the modifications recommended above were included, would amount to 55% of the project total. This may prove to be an inherent flaw in the first generation HPM concept – the low cost of the machine appears to be negated by the complexity of harnessing the very low, variable speed mechanical output from the device and needs to be addressed in future design iterations.

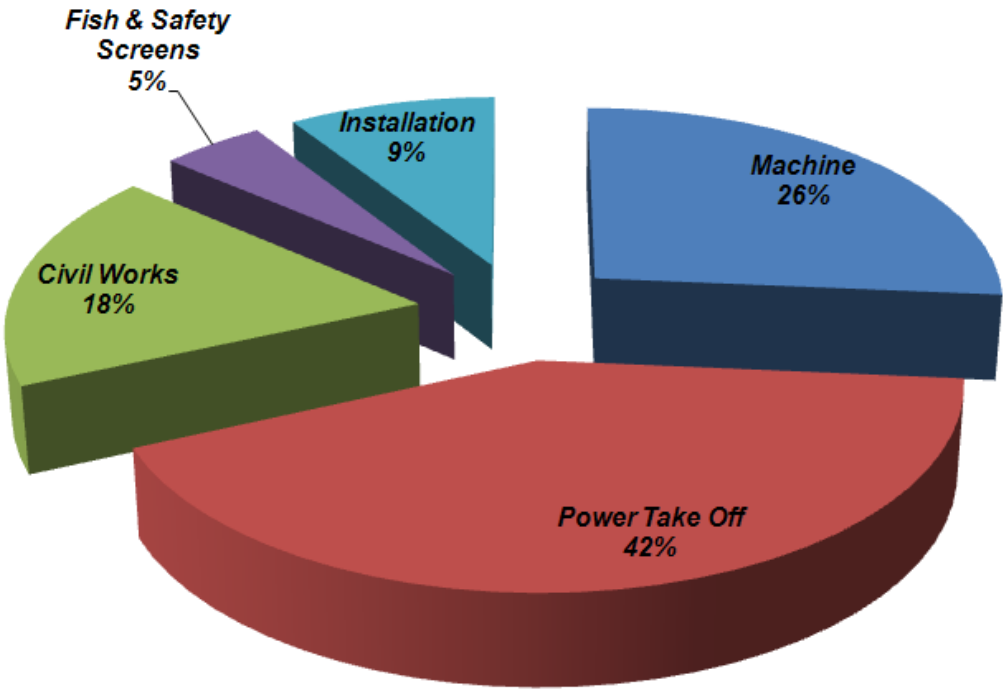

Figure 4.21: Summary of Project Costs

Chapter 5: Performance Testing Methods

5.1 Flow Measurement Techniques

Accurate flow measurement, under the less than perfect operating conditions experienced during field trials, is challenging and difficult, especially if dedicated flow measurement structures are not available.

In the case of HPM performance testing, accurate flow measurements are particularly important in the calculation of machine efficiency since peak values occur at low flow rates where measurement errors are likely to be proportionately most significant.

Three different flow measurement methods were employed for the Partenstein tests, to allow for comparison of results and better containment of errors, with varying degrees of success.

Figure 5. 1: General view of HPM installation September 2011 *(above),* Detail of Measurement Weir *(below)*

5.1.1 Sharp Crested Weir

A temporary, sharp crested weir was placed downstream of the test unit during early tests (Figure 5.1). The height of the weir crest above zero datum was established through survey measurements, and the depth of water upstream of the weir read during tests, using the water level station at MP1 (see below). Flow passing over the weir was then calculated using the standard equations contained in ISO 1438:2008

$$Q = \frac{2}{3} Cd.be.\sqrt{2.g}.h^{2/3} \qquad (5.1)$$

Where:

Q = Volume Flow Rate (m^3/s)

Cd = Discharge Coefficient (from standard tables according to geometry of weir installation)

be = Effective width (derived from coefficients relating weir and channel widths)

h = height of surface of flow above the weir crest.

However, a number of practical problems were encountered with this method:

1. Since the weir installation was temporary, it was not possible to ensure that leakage flows by-passing the weir due to incomplete sealing with the channel walls, were eliminated, distorting results at low flow rates.
2. The HPM produced significant turbulence and waves in the water surface immediately upstream of the weir. This both increased the difficulty in accurately reading water depths, and distorted flow calculations as waves broke over the weir crest during operation, with weir readings becoming impractical at HPM rotor speeds greater than 5 rpm.
3. Recommended measurement weir geometry is laid down in international standards and must be strictly adhered to if standard discharge coefficients are to be applied reliably; this was not possible in this test installation and flow calculation errors may result.
4. An additional problem in this installation was that the presence of the measurement weir raised the operating downstream water level of the HPM significantly, altering the expected test condition for the device with interesting and unexpected results reported in chapter 6.

Early performance tests using weir flow measurements produced a wide scatter in results, apparently underestimating flow rates and consequently machine efficiency was over estimated.

5.1.2 Velocity Meters

A horizontal axis propeller meter (Ott-KleinflugrlTyp C2), was used to conduct a velocity survey for a series of performance tests carried out in January 2012 (Figure 5.2). The test section chosen was immediately downstream of the stone bridge across the mill stream with an approximately rectangular channel cross section and concrete plastered walls.

Figure 5.2: Velocity Measurement Equipment used for January 2012 Performance Tests

Four measurement stations were used across the width of the channel with measurements taken at 20%, 40% and 80% of water depth as required. In all, 22 different flow conditions were measured by S. Schneider of Darmstadt University (Figure 5.3), who also carried out the numerical integration to convert these velocity measurement to flow rates. While the non uniform shape of the test section could give rise to some measurement errors, the large number of width and depth stations used should have kept these to a minimum. However, measurement errors will be higher at low rotational speeds due to the low velocities occurring in the channel at very low flow rates, while results obtained at maximum operating speeds need to be treated with some caution as steady state flow conditions were hard to maintain over the time period required to complete a full set of measurements.

Figure 5.3: a. Velocity Measurement Test section. b. Velocity measurements being carried out by S. Schneider, TU Darmstadt

Nevertheless, this method was taken as the "gold standard" against which all other flow

measurements were compared and, while somewhat slow in operation, was used to calibrate flow estimates derived from rotor speed for subsequent comparison of performance tests.

5.1.3 HPM Rotor Speed

From basic theory and model test data (Senior 2009 & Linton 2010), it has been shown that the HPM is a positive displacement machine, where the flow rate passing through the device is directly proportional to the rotational speed of the rotor. Distortions in this linear speed / flow relationship occur at very low and very high rotor speeds. When the rotor is stationary, leakage around the hub and blade seals allows a small flow to pass through the device leading to an underestimation of flow at low rotational speeds. At higher rotor speeds, turbulence produced by blades entering the upstream flow, causes increasing levels of air to be entrapped in the rotor, reducing the fill ratio of the device and leading to an over estimation of flow.

However, provided an independent flow measurement method is used to calibrate the rotor for these non-linearities, within normal operational limits, flow estimation based on wheel speed offered a straight forward and consistent measurement method that was available for all test conditions.

Sources of errors associated with this measurement method include errors in wheel speed measurement, changes in leakage rates through the rotor due to the movements of seal elements and variations of operating head across the rotor.

5.2 Water Level Measurements

Direct reading measurement scales were fixed vertically to the side walls of the channel at four locations in the millrace; MP1- 2 meters downstream of the HPM, MP2- 2 meters upstream of the sluice (Figure 5.4), MP3- 0.5 meters downstream of the fish screen and MP4 -on the wall of the masonry pier at the inlet to the millrace.

The heights of each scale were established through survey above the zero reference datum of the installation which was taken to be the height of the upper surface of the shoe of the HPM at the Bottom Dead Centre (BDC), the results of which are summarised in Figure 5.5.

Figure 5.4: The Water Level Measurement Station at MP2, Upstream of the "Kinder Gidder" and HPM

Problems in direct reading of the scales were encountered at some flow conditions due to the highly turbulent flow conditions in the flume immediately upstream of the rotor and the generation of surface waves on both sides of the HPM.

The amplitude of waves was judged by eye, (using binoculars where necessary to increase resolution), and mean values recorded for performance calculations. However, the potential for reading errors remained high. Stilling tubes and float gauges were trialed, but proved to be unreliable given the constraints imposed by field conditions, and the high turbulence levels experienced particularly in the "plenum" immediately upstream of the rotor.

The most consistent readings were obtained with gauges MP1 and MP2, although since MP2 was positioned upstream of the "kinder gidder" safety screen, care had to taken to ensure this was clear of debris prior to the running of each test to avoid head drop errors.

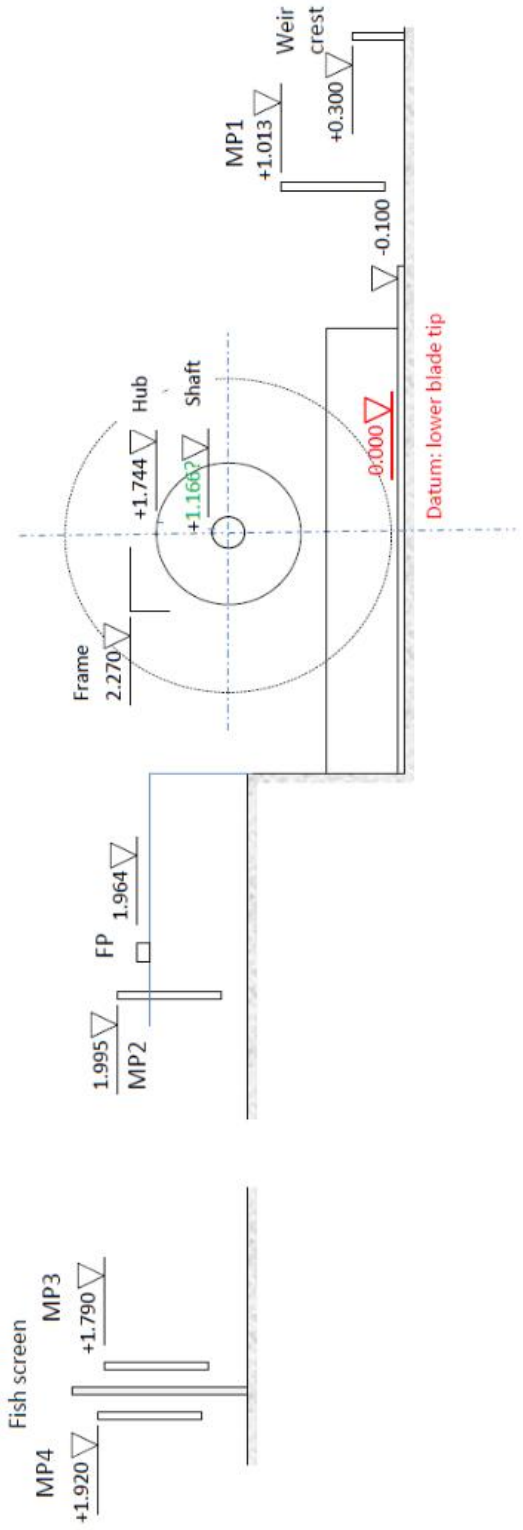

Figure 5.5: Survey Levels of water measurement scales. Note zero reading at all stations is at the top of scale.

5.3 Power Measurement

5.3.1 Electrical Output

Irrespective of the method of load control employed (see below), for each test condition, electrical power output was calculated based on current and voltage readings. In all cases, these measurements were taken on the DC side of the full wave rectifier fed directly by the three phase output of the generator. Due to the high voltages involved, voltage measurement probes were hard wired to the rectifier output terminals, while current readings were taken using a current clamp meter (Figure 5.6).

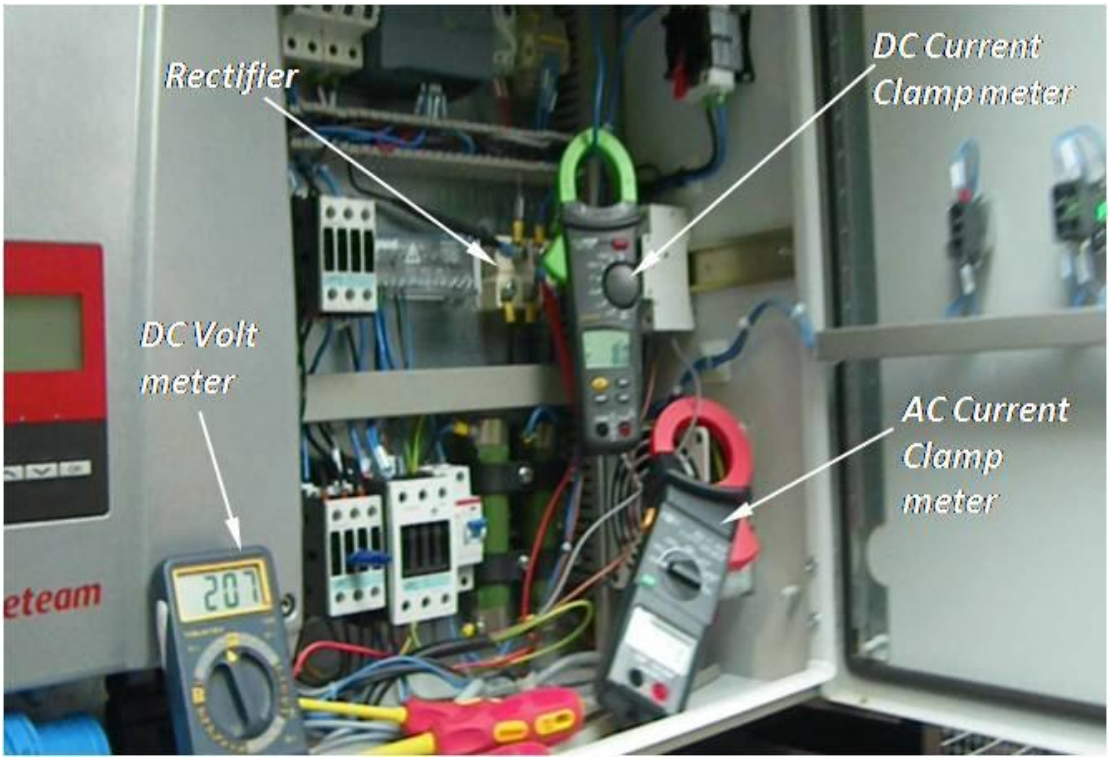

Figure 5.6: Set up for electrical power measurements

A second clamp meter was applied across one of the AC inputs from the generator to monitor winding currents, to ensure safe current levels were not exceeded during low speed rotor tests.

Where variations in voltage and current occurred during readings, mean values were estimated and recorded.

5.3.2 Rotor Speed

Wheel speeds were measured using a stop watch to record the time taken for 10 revolutions of the HPM, repeated as necessary to obtain reliable results. While this method was simple, quick and reliable, it was not possible to measure variations in rotor speed occurring during rotation. Qualitative estimates of speed variation had to be made from video recordings where available.

5.4 Performance Test Methods

The maximum flow rates and water levels available for performance testing were dependent on prevailing river conditions during test periods. Some adjustment of upstream water level was possible using the stop logs in the inlet head-works, but downstream water depth was directly linked to river levels and therefore beyond the control of experimenters. Essentially, river conditions dictated two separate blocks of testing: low water testing in the autumn of 2011 where a shortage of water limited maximum rotor speeds to around 6 rpm and high water testing carried out in early 2012, where high river flows combined with a change in belt drive gearing ratio, allowed rotor speeds to be controlled at up to 17rpm.

Two methods of applying load to the system were employed during performance testing:

5.4.1 Inverter Control

During these tests, the power curve of the Inverter was used to directly control rotor operation. The available flow to the HPM was controlled by throttling the flow into the millstream through partial blocking of the fish screen (Figurer 5.7), and allowing the Inverter to bring the HPM speed to a steady state.

This generally took around 5 minutes to achieve and, provided the inverter power curve was updated to match the available head produced by river conditions during the test, upstream water level entering the HPM could be controlled within 5mm of a target value. In effect, these were “constant level” tests; HPM speed was a by-product of the inverter control system seeking to maintain constant loading of the system and could not be set directly.

In addition, under inverter control, rotor speeds had to be maintained within the operating limits described in Chapter 4, by the PLC control unit, restricting the range of HPM speeds that could be tested.

Figure 5.7: Using the Fish Screen to throttle inlet flow during Inverter control tests.

5.4.2 Load Bank Control

A more direct means of controlling rotor speed was achieved by connecting an external resistance load bank to the test output of the control cabinet. This modification to the original control system design enabled the rectified DC output from the generator to be directly connected across a series of variable resistors. Electrical load could be varied to directly control rotor speed, with power output converted into waste heat. The test circuit was protected by a series of current limiting breakers and cut out switches to ensure safe operation, and the apparatus used for this test is shown in Figure 5.8.

The following technique was developed for these tests:

the HPM was first started with a minimum resistance load, to control initial peak rotor speeds. With no throttling of the flow, the electrical load was increased until steady state was achieved, adjusting applied resistance as necessary to achieve the desired test condition. Care had to be taken with this method to ensure steady state conditions were achieved before measurements were taken. In addition, care was needed in applying

and removing resistance loads, to prevent safe operating conditions being exceeded. Sudden removal of load could result in generator over-speed, producing dangerously high voltages; too sudden an addition of resistance could cause the generator speed to drop, resulting in excess currents. Although the test circuit contained safety breakers and fuses to protect the system, considerable operator care was required, and the incremental application or removal of *small* resistance loads was essential. For tests carried out in January & February 2012, the inverter was able to apply more load than the available load bank for low speed rotor tests, hence a combination of loading techniques were used to develop the complete power curve.

Figure 5.8: Test set up for Load Bank Control.

5.5 Observation of Rotor Behaviour

In addition to the performance test measurements already described, extensive video filming of the HPM at each performance test condition was carried out. Footage was shot of both upstream and downstream rotor behaviour at both full and slow motion speeds in an attempt to gain insights into the hydraulic phenomena occurring. The sound track to this video record also proved useful in the qualitative measurement of noise output from both the hydraulics of the HPM itself and the interaction with the power take off.

5.6 Estimation and measurement of loss factors.

In order to estimate shaft power and the hydraulic efficiency of the machine, some means of estimating hydraulic, mechanical, and electrical loss factors were required. Comprehensive measurement of these loss factors was not possible given the constraints of the field tests.

However, basic measurements were used wherever possible as a basis for estimating

losses throughout the performance curve, as described below.

5.6.1 Hydraulic Losses – Leakage.

Measurement of leakage flow occurring across the rotor was carried out following the practice of model testing by Linton (2009), at zero rotational speed.

With blade and hub seals carefully adjusted to give minimum running clearances, rotation of the rotor was prevented with wooden chocks, setting one blade vertically at bottom dead centre of rotation. Water was then fed to the upstream side of the rotor and the system allowed to reach steady state before the sharp crested weir was used to measure flow. The upstream water level could be adjusted by the addition or removal of stop logs in the head race to enable leakage to be determined for several head differences across the rotor (Figure 5.9). No adjustment could be made to downstream water levels which were set by river conditions.

Figure 5.9: Leakage Flows during Static Rotor Test. Note the significant leakage past the hub seals

However, this technique had several drawbacks: first, given the very low flow rates involved with leakage flows (15 to 30 litres per second typically), inaccuracies in measurements obtained from the weir readings had a high impact on leakage results. Second, it was found that the blade and hub seal positions moved very quickly after

adjustment, opening out considerably after a few hours of HPM operation, altering the leakage flow rate.

A compromise solution was adopted for estimating leakage by extrapolating flow data obtained using propeller velocity measurements, to derive flow at zero rotor speed (presented in Chapter 6). The flow measurements taken during the test series in January 2012, following 36 hours of continuous operation after the seals were repaired and adjusted, were taken to be representative of all tests carried out in this installation in the absence of better data.

5.6.2 Friction and Transmission Energy Losses

The principle sources of mechanical energy losses in the machine and transmission system are:

1. Friction between the blade and hub seals of the rotor and the surrounding fixed structure.

2. The torque required to turn the toothed belt and gearbox against their internal friction.

3. The torque required to turn the generator against internal bearing friction, air resistance of the rotor ('windage') and the force required to overcome resistance of the permanent magnets ("cogging" forces).

4. The torque required to accelerate the system against the inferred inertia of the generator and gearbox at unsteady speeds.

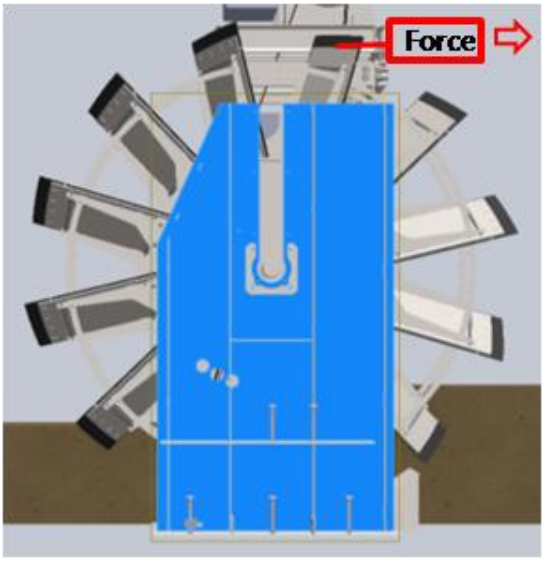

Figure 5.10: Measurement of rotor friction force

For this project, mechanical losses were estimated using the following assumptions:

- Forces and torques arising from sources 1 & 2 are independent of rotor speed and remain constant.
- Losses arising from source 3 are included in the efficiency curve for the generator.
- Rotor performance is assumed to be measured at steady state with no accelerations of the system occurring.

This latter assumption is a significant compromise, particularly at low flow rates where rotor speed fluctuations were clearly evident.

5.6.2.1 Rotor Friction Test Method

A very crude test was carried out applying force to one blade of the wheel / transmission / generator system without water present. A force meter was used to applied load tangentially to one blade edge at top dead centre and the force required to achieve a steady rotation recorded (Figure 5.10). The speed corresponded approximately to 4rpm of the wheel and tests were repeated a number of times to obtain average force values, summarized in Table 5.1.

Differing test conditions, including changes in belt drive ratio, removal of the coupling between the generator and gearbox and differing conditions of the seals enabled good estimates to be obtained for losses due to each component in the system. In particular it was important to separate losses occurring on the wheel side of the belt transmission (which do not change with belt ratio), and those arising from the gearbox and generator, to enable data sets from 2011 (belt ratio 5.05:1) and 2012 (belt ratio 3.6:1) to be compared.

Data Set No.	Date of Test	Conditions	Belt Ratio	Gearbox Ratio	Radius Arm (m)	Average Measured Force (N)	Torque (Nm)	Comments
1	**28/07/11**	Rotor+ Gbox + Generator. 1 month after seal fitting	**5.05**	**4.989**	**1.102**	**410**	**451.8**	
2	**17/02/12**	Hub + Blade Seals retracted, generator uncoupled	**3.6**	**4.989**	**1.2**	**153.7**	**184.4**	
3	**17/02/12**	As for test 2 with generator connected	**3.6**	**4.989**	**1.2**	**283.3**	**339.9**	Rotor torque to drive generator = 339.9 – 184.4
4	**21/02/12**	Blade & Hub seals tight, dry rotor, generator disconnected	**3.6**	**4.989**	**1.2**	**243.6**	**292.3**	Not representative. Note test 4 & 5 show how quickly friction reduces on running
5	**25/02/12**	Run for 36 hours to allow seals to settle. Generator disconnected	**3.6**	**4.989**	**1.2**	**197.8**	**197.8**	
Derived Summary Data:		**Rotor Friction Torque = 129.4 Nm**			**Gearbox Friction Torque = 19.7 Nm**			

Table 5.1: Summary of Rotor and Transmission Torque Required to Over-come Friction.

The same gearbox with a fixed ratio of 4.989:1 was used for all tests and one revolution of the HPM resulted in 25.2 revolutions of the generator for tests carried out in 2011, while in results for 2012 tests one revolution of the HPM resulted in 18 revolutions of the generator. This had to be taken into account for both mechanical and generator losses when seeking to extract Shaft Power outputs to allow differing performance test sets to be compared.

The mechanical power losses were calculated as follows:

$$PL_{rotor} = \omega RFT \qquad (5.2)$$

$$PL_{gearbox} = \omega . VR_{belt} . VR_{Gbox} . GFT \qquad (5.3)$$

where:

PLrotor= the power lost by the rotor, *PLgearbox* = the power lost by the gearbox

ω = Rotor Speed (radians/second), *RFT* = Rotor Friction Torque = 129.6 Nm

VR_{belt} = belt velocity ratio, VR_{Gbox} = Gearbox Velocity Ratio,

GFT = Gearbox Friction Torque = 19.7 Nm

5.6.2 Electrical Losses

Factory test data was provided by Permagsa for the variable speed generator (Datos 300-225 generador 2011), from which the variation of generator efficiency over the operating speed range could be estimated.

Since all electrical power measurements were taken directly from the Generator / rectifier side of the system, Inverter efficiency was not a factor in calculating the Hydraulic efficiency for the rotor, although this has also been presented alongside the generator efficiency curve in Figure 5.11 to enable overall "water to wire" efficiencies to be assessed. Note how electrical energy losses are very high below generator speeds of 70rpm, and efficiency of the electrical system never exceeds 90% across the whole operating range.

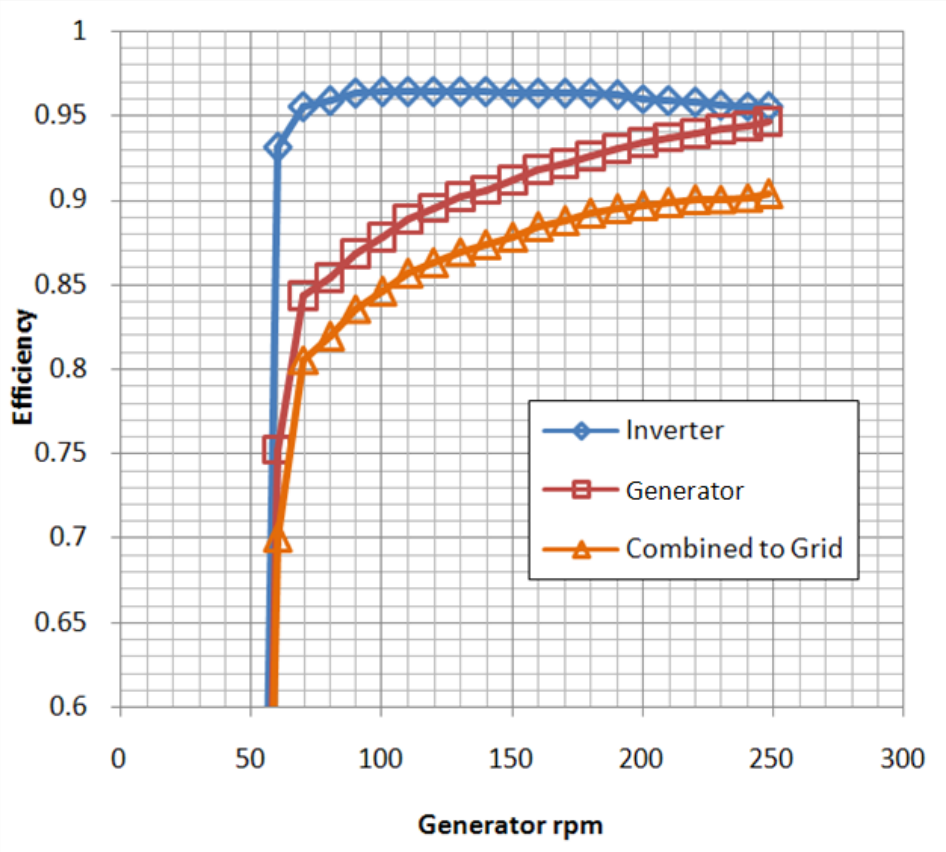

Figure 5.11: Variation of Electrical Efficiency with Generator Speed

Chapter 6: Field Test Results and Observations

6.1 Field Test Conditions

6.1.1 Overview

Performance testing was concentrated into three test periods due to the availability of equipment and suitable river flow rates. The nominal operating conditions for each test series are summarised in Table 6.1, while complete performance measures for all test conditions are presented in Table 6.2 at the end of this chapter. A brief description of each test condition follows.

Test Series Reference	Dates of Tests	Test Description	Control method	Upstream Water Surface Elevation (mm)	Down-stream Water Surface Elevation mean (mm)
9/11 Prototype	16-17/09/11	September 2011 tests: Low river flows. Weir raised downstream water level	Load Bank	1605	414
9/11 Reduced Head Prototype	17/09/11	September 2011 tests: reduced upstream level. Weir raised downstream	Load Bank	1472	461
1/12A Prototype	10-13/01/12	January 2012 tests at high water levels	Load Bank & Inverter	1656	374
1/12 Reduced Head Prototype	17/10/12	Upstream water level reduced	Load Bank & Inverter	1553	348
2/12 Prototype	29/02/12	Low downstream water levels	Inverter	1605	248

Table 6.1: Summary of Prototype Field Test Conditions

6.1.2 The 9/11 Test Series.

These tests were conducted on the 16th and 17th September 2011, when flows in the river Lohr were low. This limited the sustainable speed of HPM rotation to a maximum of 6 rpm and for these tests an external load bank was used to control rotor speed directly. Variations in stop log positions allowed two groups of inlet water levels to be compared although the control of water levels during testing, using this method, was not precise. Two additional factors unique to this test series should be noted. First, the belt drive used, as described in chapter5, hada step up speed ratio of 5.05:1, permitting the generator to turn significantly faster with each revolution of the HPM than in later tests. This allowed slower sustainable rotor speeds to be tested, and also, due to the higher generator speeds attained, increased overall electrical system efficiency compared to later test series. Secondly, a sharp crested weir was fitted downstream of the HPM for flow measurement as described in chapter 5. This weir raised the level of water leaving the HPM by 300mm, changing the prevailing operating condition of the test.

6.1.2 The 1/12 Test Series.

High water levels were available in the river when this test series was carried out between the 10th – 13th January 2012. This permitted power measurements to be carried out across the whole operating range of the HPM, using an external load bank to directly control rotor speed. The belt speed ratio for this and subsequent tests was reduced to 3.6:1,which by limiting generator rotation and output voltage, enabled higher HPM speed conditions to be measured safely. No downstream weir was present, with water levels at the exit to the HPM set by prevailing river conditions. Upstream water levels were again adjusted using stop logs to allow different input conditions to be examined, while a velocity flow meter was used for flow measurements for all tests in this series.

6.1.3 The 2/12 Test

This final series of tests, were conducted between the 24th – 29th February 2012. The load bank was not available for these experiments and the HPM was operated under direct inverter control, throttling the input flow at the fish screen as described in Chapter 5, to set the rotor speed. Flow measurements for these tests were estimated from wheel speed, using the calibrations previously described and, with no

measurement weir fitted, exit water levels were again set by the prevailing river conditions.

6.2 Observations of Machine Behaviour

6.2.1 Inlet Channel Flows

The constriction of the mill race through the "Kinder Gidder" safety screen and the sluice gate-sill, combined with the rapid changes in channel section occurring in the rotor plenum, produced considerable variations in inlet flow velocity, resulting in significant turbulence losses (Figure 6.1).

Figure 6.1: Inlet Turbulence at 11.6 rpm – a. Safety screen and gate with plenum visible beyond, b. head drop across safety screen = 20mm, c. Extreme turbulence in Plenum

These turbulence flow conditions prevented definitive measurements of water surface elevations being taken but, the sparse data collected suggested that a net head loss of between 40 and 80 mm may have occurred, representing up to 7% of available head at the nominal 1.2 meter design condition. Note that since all performance calculations are based on elevations measured between gauges MP1 and MP2, these inlet head losses have been incorporated into machine efficiency estimates – giving pessimistic values for the HPM performance.

Clearly greater attention should be given to the design of the inflow area in future installations to minimise losses in this region.

6.2.2 Rotor Cell Filling and Blade Entry

The basic operating principle of the HPM assumes that, at slow rotor speeds, the blade inclination angle is sufficient to allow water to enter from the side of the machine to complete cell filling with minimal turbulence and air entrapment. This mode of operation was observed at rotor speeds below 4 rpm, as shown in the picture sequence of Figure 6.2.

Figure 6.2: Cell Side Filling at 3.7 rpm – fill progresses left to right, Note the creation of asymmetric flow in plenum.

However as rotor speeds increased above 4 rpm, this fill mechanism began to break down. The rotation was too fast to permit side filling of the blades to propagate across the full width of the rotor, with flow increasingly entering the rotor across the outside edge of the blade, resulting in a rise in both air entrapment and turbulence (Figure 6.3).

Figure 6.3: Cell Side Filling at 5.7 rpm – initial blade splash is high, forming a steep wave front on the left hand inlet side of the cell. High turbulence is evident as water enters from three sides of the blade.

Another important effect of blade entry is shown in Figure 6.4, which shows the localised reduction in water surface elevation in the wake of the blade at the slightly higher rotor speed of 6.3 rpm. Blade entry has formed a 'hole' in the water surface,

partly due to the sudden impact of the blade on entry at the upstream surface, and partly due to the bluff body drag of the flat blade being drawn through the water. The depth of this depression marked in the Figure, is estimated from the length of snub tie visible in the shot as 360mm, and is likely to result in a substantial reduction in pressure head over the power extraction section of blade rotation.

By the time rotor speeds reach 9 rpm, the side filling mechanism accounts for only 40% of the volume of cell filling, with the remaining fluid entering over the other blade edges while increased turbulence, air entrapment and blade splash become evident. Blade splash has two components: the first occurs across the width of the rotor, induced by the blade inclination angle.

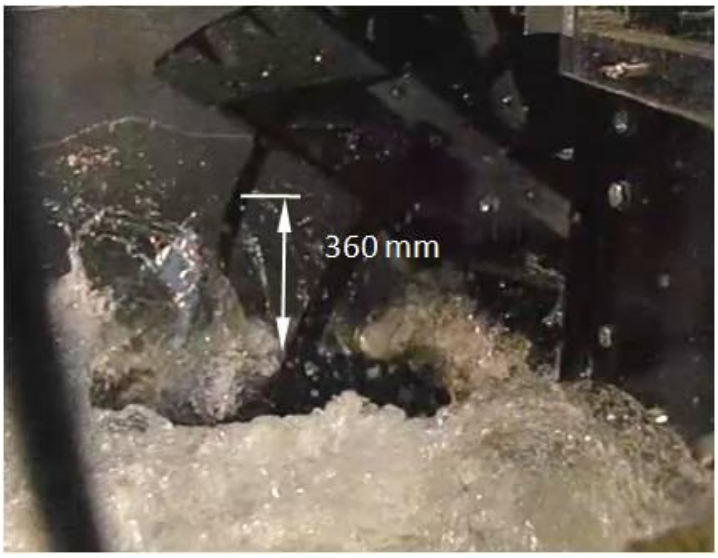

Figure 6.4: Local surface depression following blade entry at 6.3rpm

The second component is produced by the advance of the blade as the rotor revolves, imparting an upstream acceleration, following contact with the water surface, in opposition to the momentum of the incoming flow. This second component is likely to reduce at lower input water levels, as indicated by the two test conditions shown in Figure 6.5.

Figure 6.5: Blade splash compared for differing water depths at rotor speeds of 9 rpm: The deeper water condition is on the left.

The violence of the energy loss due to this momentum change is shown in Figure 6.6 where the rotor is turning at 10.6 rpm, while the sluice gate is being operated prior to shut down. Although this rotor speed is very close to the peak power output for the machine, blade splash and noise became unacceptable for prolonged operation, and the speed of the machine had to be limited as described in the next section.

Figure 6.6: The violence of blade splash (shown here at 10.6rpm), made prolonged operation of the machine hazardous, and generation speeds were limited to below 6rpm as a consequence

Blade entry also acted on the flow to produce strong re-circulating currents and wave patterns upstream of the rotor in the plenum, (Figure 6.7). This recirculation is caused principally by the sideways component of velocity induced on blade entry by the blade angle, deflecting off the side wall and combining with the incoming flow. While this circulation is always present, its velocity and intensity changes with blade passing, indicating losses are present due to turbulence and accelerations in substantial bodies of water.

As rotor speeds increase further, blade splash appears to reach a limit after which there seems to be no further increase in magnitude with increasing HPM speed. This may be due to the high turbulence resulting in increasing levels of air entrapment in the surrounding flow, and a decrease in the fill ratio of individual cells.

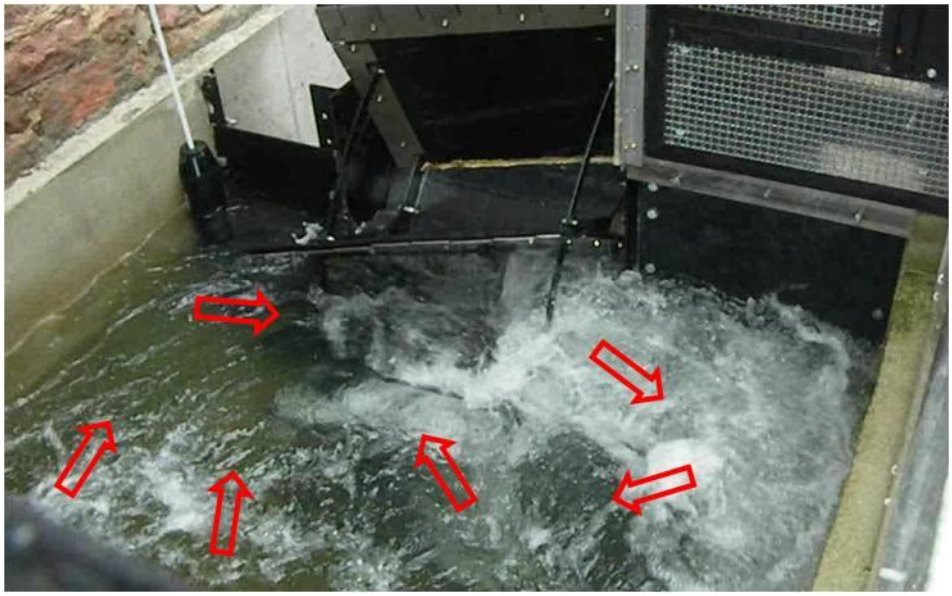

Figure 6.7: Re-circulating flow caused by blade entry at 6.7 rpm: flow enters from the bottom of the picture, entering the rotor from the left. The inclined blade angle contacting the water accelerates some flow from the right hand side of the HPM.

In these field tests, it was only possible to observe *surface* turbulence and splash directly. However, it is important to investigate whether overall rotor drag follows similar patterns, as seems likely, and to what extent such losses can be reduced by alternative blade geometry or rotor architectures. This became an important objective of the laboratory scale test programme described from chapter 8 following.

6.2.3 Rotor Noise Production

The high noise levels produced by the prototype HPM resulted in an unexpected operational constraint on the installation for sustained electricity generation, with rotor speeds limited to below 5 rpm to keep sound output to acceptable levels. This noise generation appeared to have two main contributing factors: the rotor hydraulics, described here, and interactions with the control and generator system described in section 6.2.6.

6.2.3.1 Blade Splash

Significant noise outputs resulted from the turbulent blade entry and splash already described. This proved to be highly directional in nature and since the majority of living accommodation in the mill was located downstream of the rotor, noise from this source had a low impact for this installation. However, the levels of water splashed onto the mill walls at higher rotor speeds was a serious cause for concern to the mill owner and was a further limitation on practical operating speed.

6.2.3.2 Hub Venting

At all operational speeds, a very pronounced suction sound was heard emanating from the rotor and apparently coinciding with the emptying of each cell on the downstream side. This linkage was demonstrated by the qualitative test shown in Figure 6.8, where the exit to the HPM was partially blocked to slow down the rate at which water could leave the cell. With the rate of emptying reduced, a significant reduction in noise output resulted.

This appeared to be due to the compromised side plate geometry used for this installation, preventing air from entering the cell as each blade passed the downstream edge of the shoe profile and water was released by the rising blade. With no alternative flow path, air was drawn into the cell via the narrow gaps between the hub seals at high velocity, resulting in significant production of noise. Vent holes were added to the side plates, but only partially alleviated the problem since they could not be placed in the ideal position due to surrounding structure.

Cell venting behaviour is also likely to have a strong influence on both the variation of rotor efficiency with downstream water levels and variations in rotor output speed during cell emptying, described in later sections of this report. A fundamental change

to rotor and installation geometry will be required to eliminate these problems entirely from operation of the prototype HPM.

Figure 6.8: Ventilation Reduction Test: an angled weir was added to the end of the side panniers to raise local water levels and reduce the speed of cell emptying.
(photo: Jurgen Kunkel)

6.2.4 Exit Flow

Flow leaving the HPM was constrained by the sidewalls of the concrete panniers that formed the basic structure of the unit (Figure 6.9). Considerable variation in the velocity of this flow was observed during cell emptying, particularly at lower rotational speeds, resulting in wave generation downstream of the machine (a). At low water levels and moderate rotor speeds a hydraulic jump formed, usually at the abrupt transition of channel width occurring at the end of the pannier section. However, stable jump formation was rare, and appeared more often as transient behaviour during the cell emptying cycle (b). Higher flow rates and water depths eliminated jump formation entirely producing a jet like spout of fast flowing water accompanied by wave generation and turbulence (c).

Figure 6.9: Exit Flow Close to the wheel: a. wave formation driven by large variation in flow velocity (5.7 rpm), b. stable hydraulic jump formation at end of panniers (10.5 rpm), c. water spout produced at high flow rates (13.9rpm).

Wheel exit flows produced marked asymmetry in tail race water conditions, particularly at high flow rates (Figure 6.10), generating waves and large areas of turbulent re-circulating flow. This behaviour helps to explain why flow measurements using a downstream weir were prone to error – channel conditions are far from uniform.

Figure 6.10: Turbulent and asymmetric flow conditions in the exit channel: wheel speed is 8.4 rpm

Performance tests revealed a strong relationship between downstream water level and HPM efficiency. However, the presence of standing waves and turbulence indicate that further losses are produced which an improved exit channel geometry, particularly between the end of the panniers and full downstream channel width, may reduce.

6.2.5 Rotor Speed Variations

The lack of instrumentation to enable rotor speed and shaft torque variations to be recorded over time was a serious oversight in the design of this test installation. It became apparent from observation of the field test unit that considerable variations in speed occurred as each blade passed through the device. These fluctuations became more pronounced at lower rotor speeds and during low head operation indicating that power extraction and cell emptying were likely to be the primary driving mechanisms, rather than drag losses due to upstream blade entry. Speed variations were observed with the generator under external load bank control indicating that this represented a fundamental property of the rotor hydraulics.

However, using inverter control during low speed, low head operation resulted in very pronounced speed excursions, indicating that some interaction between the hydraulics of the rotor and the generator control system was taking place. This interaction was implicated in the subsequent failure of the PTO belt drive reported below.

6.2.6 PTO and Control System Behaviour

The Ingateam 6000 TL inverter used to control this test installation was a compromise design solution based on available equipment. This unit is widely used to control wind turbine applications, but its use in hydropower installations is comparatively rare. The technical risk was further increased by the lack of knowledge regarding the predicted characteristics of the HPM to be controlled.

A number of installation teething problems were encountered during the project. These included premature failure of the generator shaft encoder used to feed generator speed data to the PLC controller, early problems with Inverter software and premature failure of the first belt drive due to incorrect belt tensioning during installation.

However, three serious flaws in the control system became apparent over the test period of the HPM:

1. Inverter control of electrical load produced a harsh mechanical vibration in the generator and transmission. Tests were carried out with the generator controlled by the external resistance load bank and repeated under inverter control for identical operating conditions of the HPM. Operation was relatively smooth and quiet with the load bank, but under inverter control, vibration levels were found to be much higher, indicating a problem with the internal control algorithm. An upgrade to the inverter software made some improvement to the situation, but the combination of very high applied loads at low, variable and fluctuating speeds, proved to be beyond the control capability of the inverter system as installed. The operating speed range of the rotor was limited to 6 rpm to keep noise levels within acceptable limits.

2. The control system could only accommodate a single power curve, therefore, was only able to exert accurate control of the rotor over a narrow head range. Under conditions that matched the control curve, good rotor speed regulation and excellent maintenance of upstream water levels was achieved, as demonstrated during the 2/12 inverter tests. However, with changing weather conditions, downstream water levels deviated significantly from the control curve values. The system registered a deviation of power output occurring at a given speed and following its hill-climbing algorithm, varied rotation in search of a new sustainable operating point on the power curve. This effect seemed to be particularly pronounced if excess power (compared with the control curve values), was produced at a given speed, due to the higher heads occurring across the rotor. Under these circumstances, very large rotor speed variations occurred as the control system sought a new operating speed, corresponding to this higher power output.

   However, since the high power output was caused by the excess operating

head due to a fall in *downstream* water level, rather than excess flow resulting in an increase in *upstream* depth, a higher rotor speed could not be sustained. As the higher speed rotor consumed more water than could be supplied by the river flow conditions, water levels in the head race fell resulting in a lower power output. This led, in turn, to the control system "hunting" about the operating condition, with almost continuous rotor speed changes, resulting in disturbing and fluctuating noise levels from both the hydraulics of the wheel and mechanical vibration of the PTO.

3. A low speed resonance condition was inadvertently established during sustained operation of the HPM for electricity generation. Following performance testing, the rotor speed was restricted to 3.5 rpm in order to reduce noise output and the power control curve of the inverter modified accordingly. In an attempt to reduce cell ventilation noise (as described previously), a temporary weir was added by the mill owner, across the exit channel at the end of the concrete panniers, to slow the rate of cell emptying. While this did reduce ventilation noise, it had the side effect of reducing effective operating head across the rotor, reducing both the speed of rotation and power output of the machine. As already shown, such hydraulic conditions would result in large speed variations of the rotor with the passing of each blade. However, this combined with the control system characteristics to produce a resonance condition resulting in very abrupt changes in rotor speed and imposing very high cyclic forces on the transmission.

   Two features of the PTO may have contributed to this resonance condition. Inverter induced vibrations reported above, imply that the basic control algorithm was poorly matched to the electro-mechanical drive train of the HPM. In addition, the belt drive and jack–screw mounting of the PTO sub frame introduced low stiffness elements into the transmission, resulting in large deflections under the high torque loads imposed by the HPM at these very low operating speeds. Not surprisingly, this resonance condition imposed an excessive duty factor on the belt drive, resulting in failure of the

belt element after three weeks of near continuous operation. This occurred despite the load rating for the belt being over twice the predicted maximum torque produced by the HPM under design conditions.

Clearly, the design of the PTO system for an HPM is not a trivial engineering problem and will be a crucial factor in determining both the operational reliability of the device and the cost of future installations. However, the focus of this report is on understanding the fundamental hydraulic behaviour of the HPM rotor and, while the hydraulic mechanisms forcing rotor speed variations will be investigated, further consideration of resonance phenomena in the control system of the field trial unit, is beyond the scope of the present work.

6.3 Performance Test Results

6.3.1 Flow Measurements

Since flow measurements have a very significant impact on derived values for rotor efficiency, establishing a consistent measurement method to permit realistic comparison between the various test conditions was essential. Results obtained using the three different flow measurement techniques are compared in Figure 6.11.

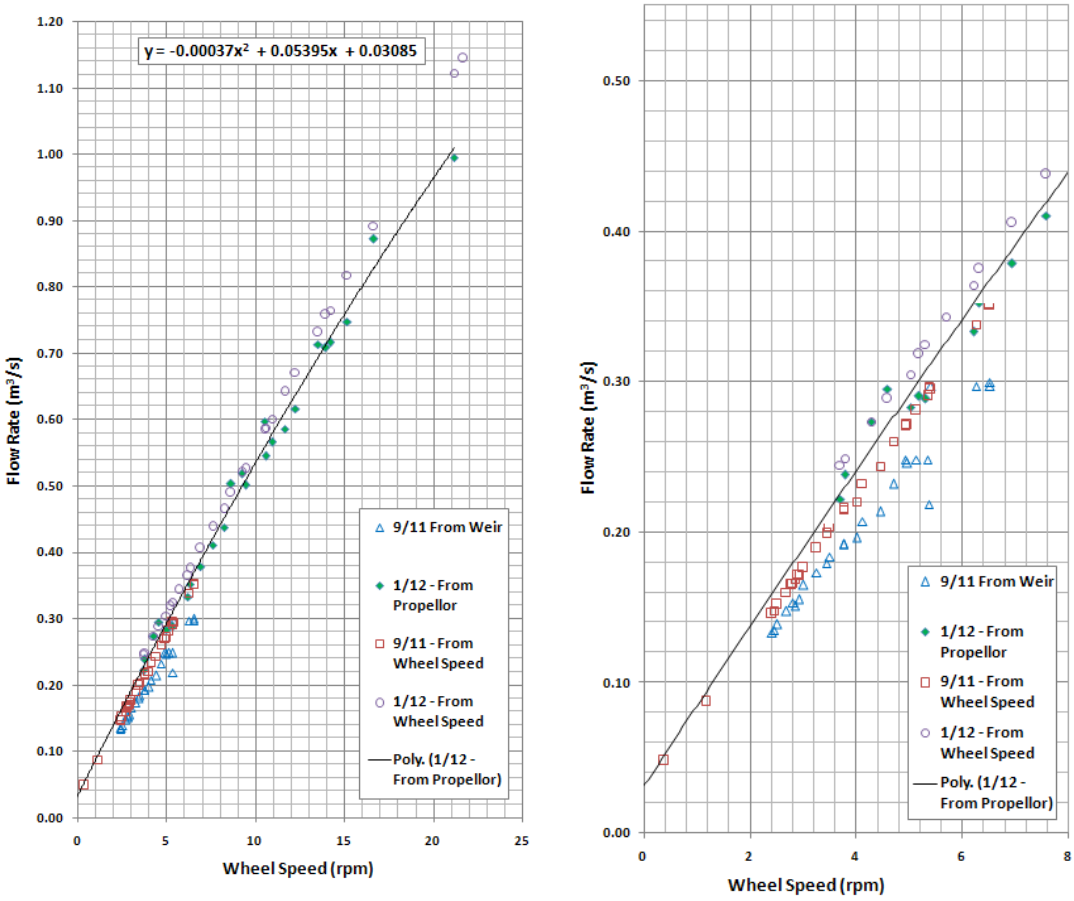

Figure 6.11: Comparison of Flow Measurement Techniques:
overall flow rates (*left*), detail of low flow region (*right)*

Weir flow measurements appear to significantly underestimate flow rates, compared with the other methods, therefore leading to over optimistic calculations for HPM efficiency. Flow estimates derived from rotor speed and propeller velocity measurements show very good agreement at low rotational speeds. However, as

increased rotor rpm produce higher levels of turbulence and air entrapment, flow estimates based on rotor speed, become increasingly unreliable, over-estimating flows compared to propeller velocity measurements.

In order to establish a consistent, means of flow estimation that could be used across all data sets, the equation for the polynomial curve fitted through the propeller tests was employed, to enable flow to be calculated directly from recorded rotor speeds. The weakness of this method is that it assumed the leakage rate occurring during the propeller flow tests in January 2012, could be applied to all other test conditions. However, due to the concerns regarding the reliability of leakage measurements made when the rotor was stationary described in chapter 4, this represents a reasonable compromise, and indeed the only viable methodology that can be applied across all field test conditions.

Therefore, for all test cases, flow through the rotor is calculated from:

$$Q = - 0.00037.\ rpm^2 + 0.05395.rpm + 0.03085 \qquad (6\text{-}1)$$

Where:Q= Volume Flow Rate (m^3/s), rpm = wheel speed (revolutions per minute)

The constant term '0.03085', represents the leakage flow rate assumed to apply at all test conditions to which this flow calculation is applied.

6.3.2 Power Output

The measurements obtained for all of the performance tests undertaken are summarised in Table 6.2, presented at the end of this chapter.

Electrical Power output measurements obtained for all test conditions are shown in Figure 6.12, plotted against the DC voltage reading for the generator. This voltage is directly proportional to generator speed and is plotted here since it represents the "raw" data form before data is processed or estimated loss factors applied. The effect of different belt ratios can be clearly seen in the off-set of the 9/11 results compared to later data-sets.

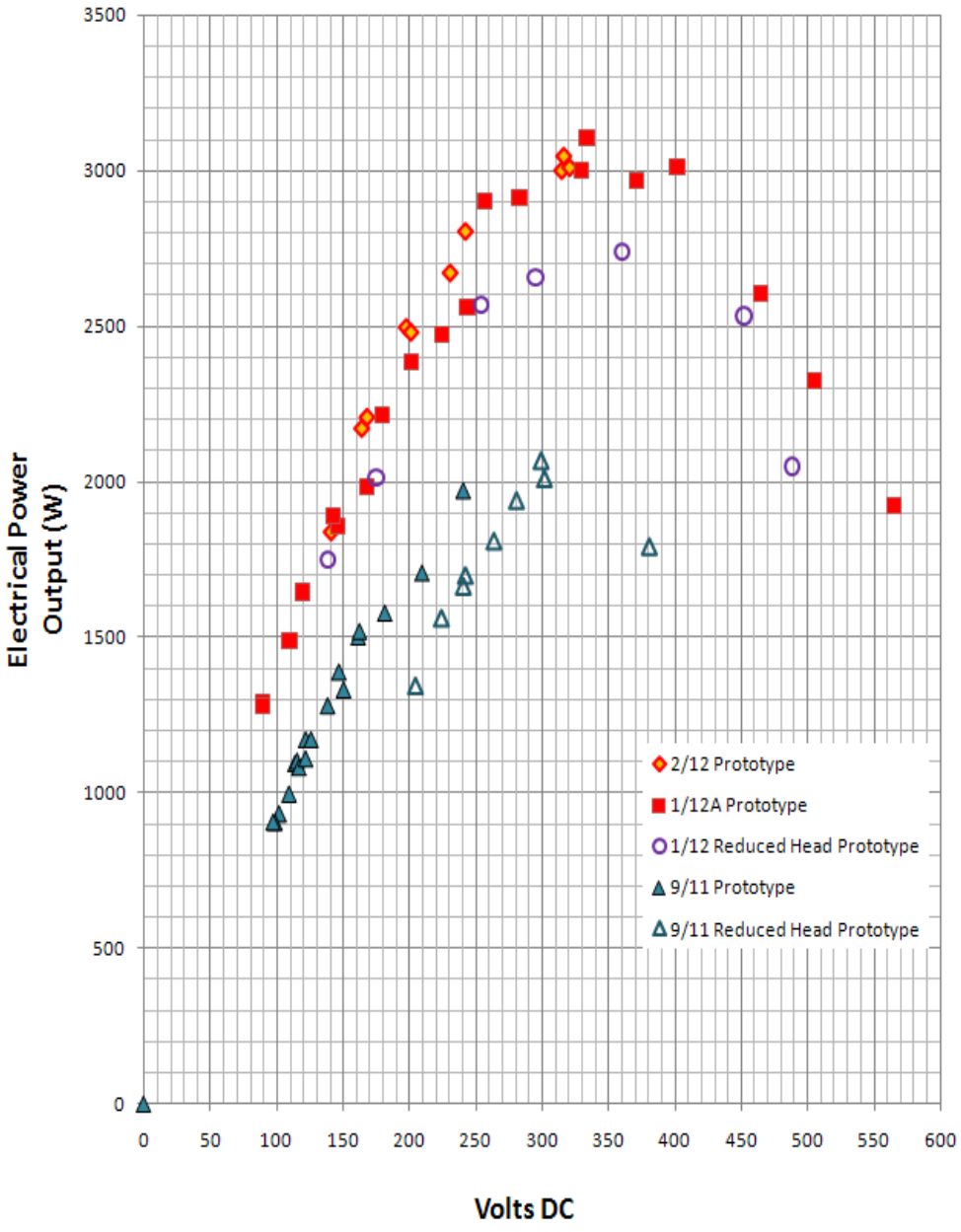

Figure 6.12: Raw data plots for all prototype test conditions

Applying suitable corrections for generator and mechanical losses enables the Shaft Power output for the machine to be calculated and Figure 6.13 compares Shaft Power for all test conditions.

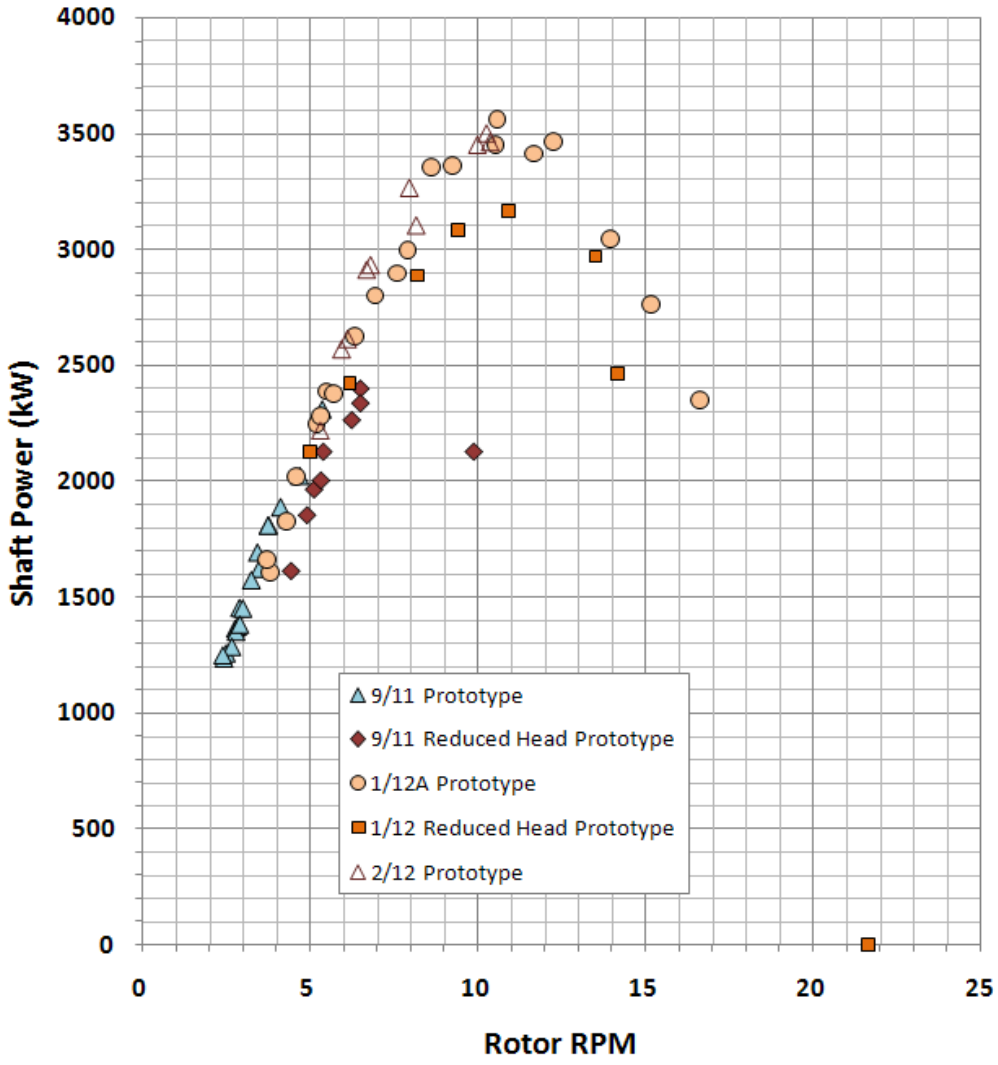

Figure 6.13: Shaft Power variation with Rotor Speed – all prototype tests

Shaft Power is paramaterised using the maximum shaft power output measured for a given test condition (Figure 6.14). Since the 9/11 test series was too limited to include the maximum power condition in that range of measurements, Pmax for these tests is estimated from the 1/12 data set, factored to account for head differences between the two test conditions.

In the figure, P/Pmax is plotted against rotor speed (a), and also against Q/Qmax-theoretical (b), for comparison. Peak power output occurs at a rotor speed of 11 rpm, which is slightly above the estimated design speed of 10 rpm corresponding to the 0.635m³/s design flow rate. However, with a shaft power of under 3.6kW, power output is substantially below the 5kW power output anticipated for this site.

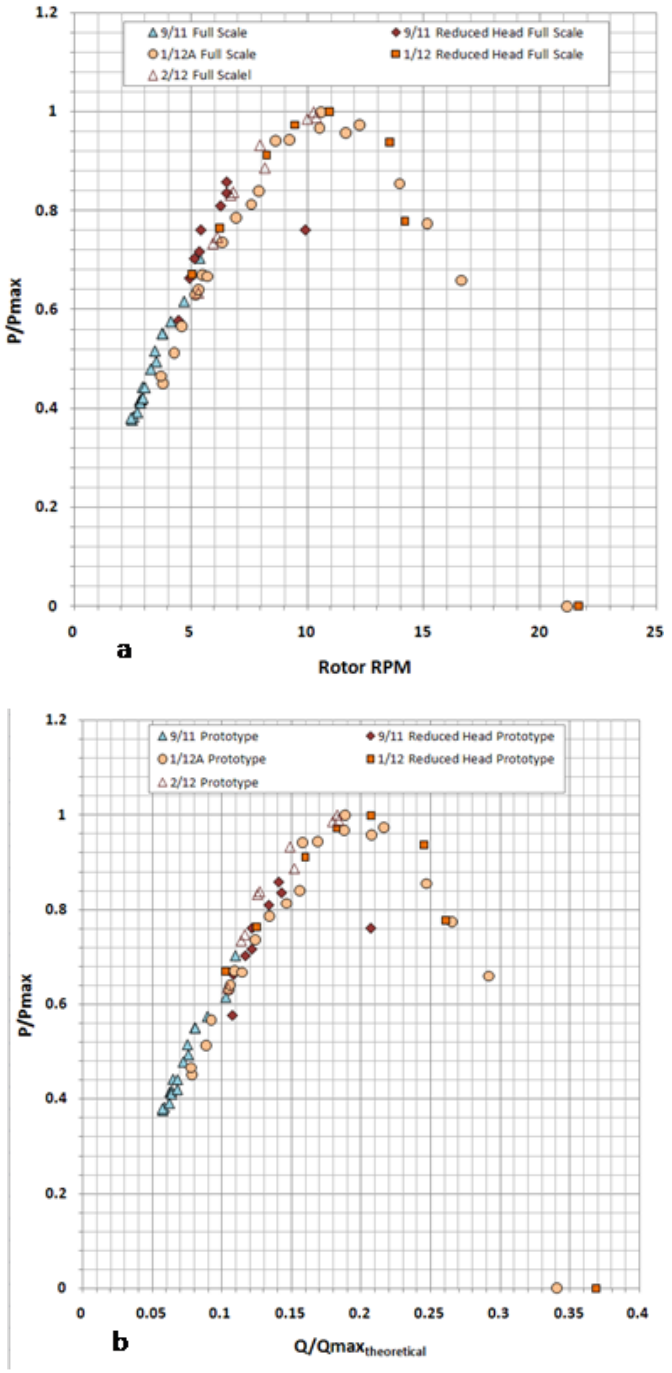

Figure 6.14: Non Dimensionalised Performance parameters – all Prototype tests

6.3.3 Efficiency

The HPM efficiency based on the measured electrical power output for all test series is shown against rotor speed in Figure 6.15a and represents the overall water to wire efficiency for the machine based on measured gross flows.

There appears to be a 10% mismatch in efficiency between the 9/11 and 1/12 datasets which was initially assumed to be due to changes in mechanical losses and generator efficiency caused by the different belt ratios used for these tests.

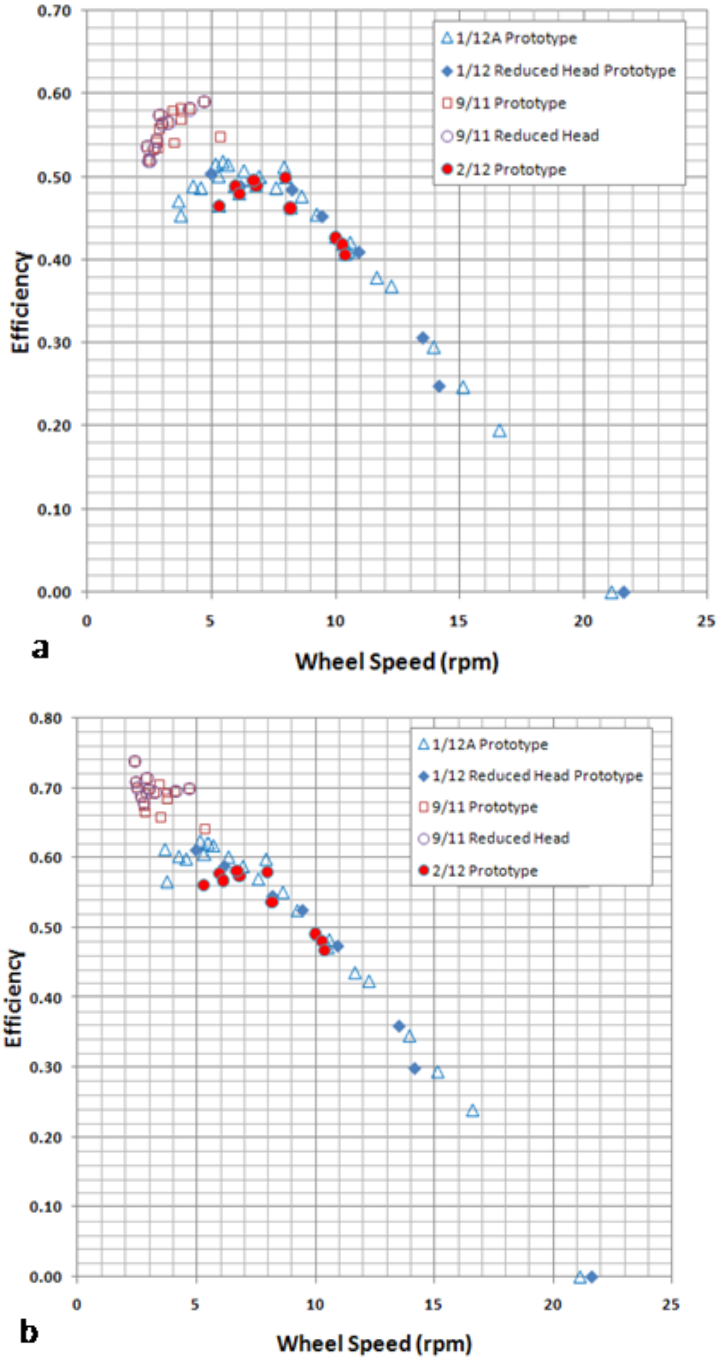

Figure 6.15: HPM Efficiency: a. Water to wire efficiency from measured flow, b. Hydraulic efficiency based on Shaft Power and net flow

However, these changes are taken into account to produce the efficiency curve of Figure 6.15b. This curve is based on derived shaft power and should be a true 'hydraulic efficiency' based on the net flow through the machine excluding leakage. However, the

pronounced down turn in data points at the lowest rotor speeds suggests that some leakage effects may still be present due to uncertainties in leakage flow estimates. Neglecting the impact of leakage errors, figure 6.15b shows an 8% difference in peak efficiency value between the 1/12 and 9/11 data sets. There is considerably more scatter in shaft power based efficiency results which may indicate inaccuracies in interpolating generator efficiency data, and extrapolating flow data at the very low rotor speeds involved.

However, a hydraulic property of the HPM does appear to be displayed here, further explained by Figure 6.16.

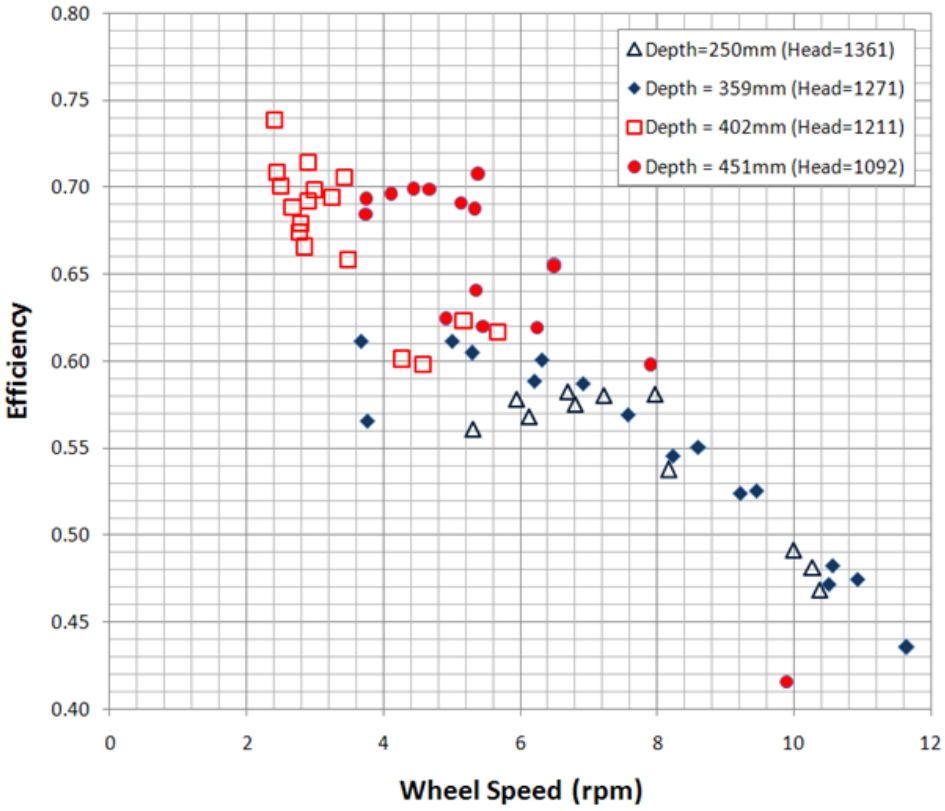

Figure 6.16: Shaft Efficiency grouped according to downstream water level

Here data points from all test series have been re-ordered and grouped according to the average downstream water elevations. Once again these are 'hydraulic' efficiencies, based on net flow with leakage excluded. Although considerable scatter in data

remains, the downstream water levels relative to the blade length and hub diameter appear to have quite a powerful effect on HPM efficiency.

Basic HPM theory assumes the downstream water levels are tangential to the bottom surface of the hub tube, resulting in no change of velocity as flow leaves the rotor. This is not the case with the field trial unit and, since water levels within the cell must fall as the cell empties, a loss of the remaining potential energy of the fluid, combined with losses due to acceleration of the exit flow, must result in lower over-all rotor efficiencies. In addition, the suction effect observed in the rotor caused by the lack of cell ventilation during cell emptying, may constitute a significant energy loss, judging by the volume of noise emitted and the apparent strong impact on rotor speed.

This impact of exit water level on wheel performance is analysed in chapter 7 and a modification to basic HPM theory is suggested.

Model tests reported in later chapters of this report present the direct measurement of the forces and cell pressures at model scale occurring during cell emptying and while the detail of the processes involved are complex, represents a useful contribution to knowledge.

6.3.4 Power and Efficiency

Peak values for hydraulic efficiency of around 70% have been achieved from the prototype installation, despite the faults with the installation already identified. However, quoting peak efficiencies can be misleading since they correspond to low rotor speeds at which power outputs are generally low. For practical applications, efficiencies over the normal operating range of the installation are more important and two methods of representing this variation of efficiency and power are presented below.

Figure 6.17 shows the variation of both P/Pmax and Hydraulic Efficiency with rotor speed for the 1/12A Prototype test condition. Peak efficiency of 68% occurs at 64% of peak power at a rotor speed of 5 rpm, while efficiency falls to 50% when peak power is produced at 10 rpm.

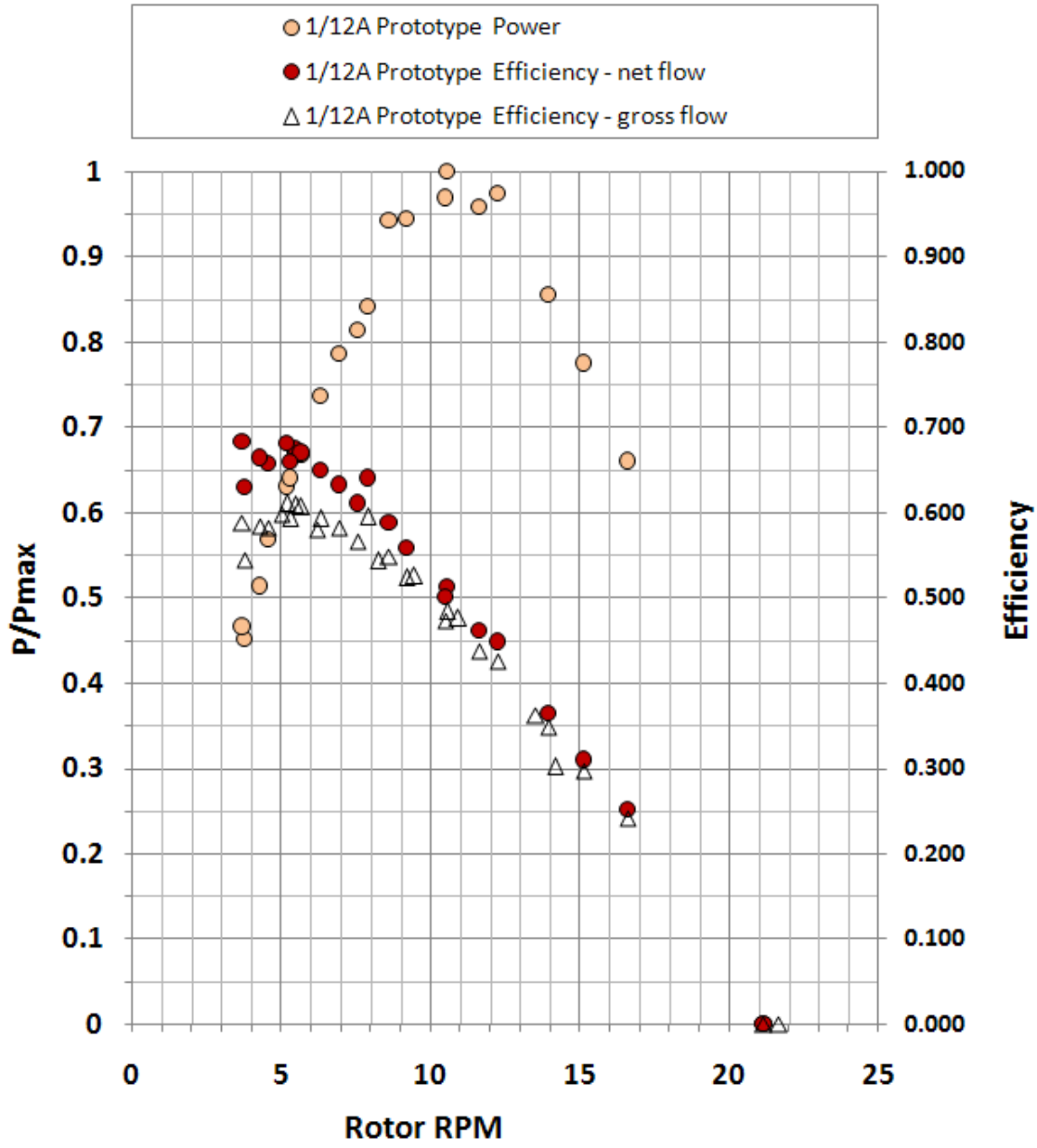

Figure 6.17: Power & Efficiency Variation with Rotor Speed

The decline in efficiency from the peak value is almost linear to the free wheel condition at 21 rpm. Also presented on this curve is efficiency based on gross flow which clearly shows the impact of leakage particularly at low speeds.

Similar information is presented in Figure 6.18, but this time plotting P/Pmax directly against Efficiency in the manner used by Gotoh (2000), which makes it slightly easier to interpret the power / efficiency trade off to be made in selecting the operating range for this machine.

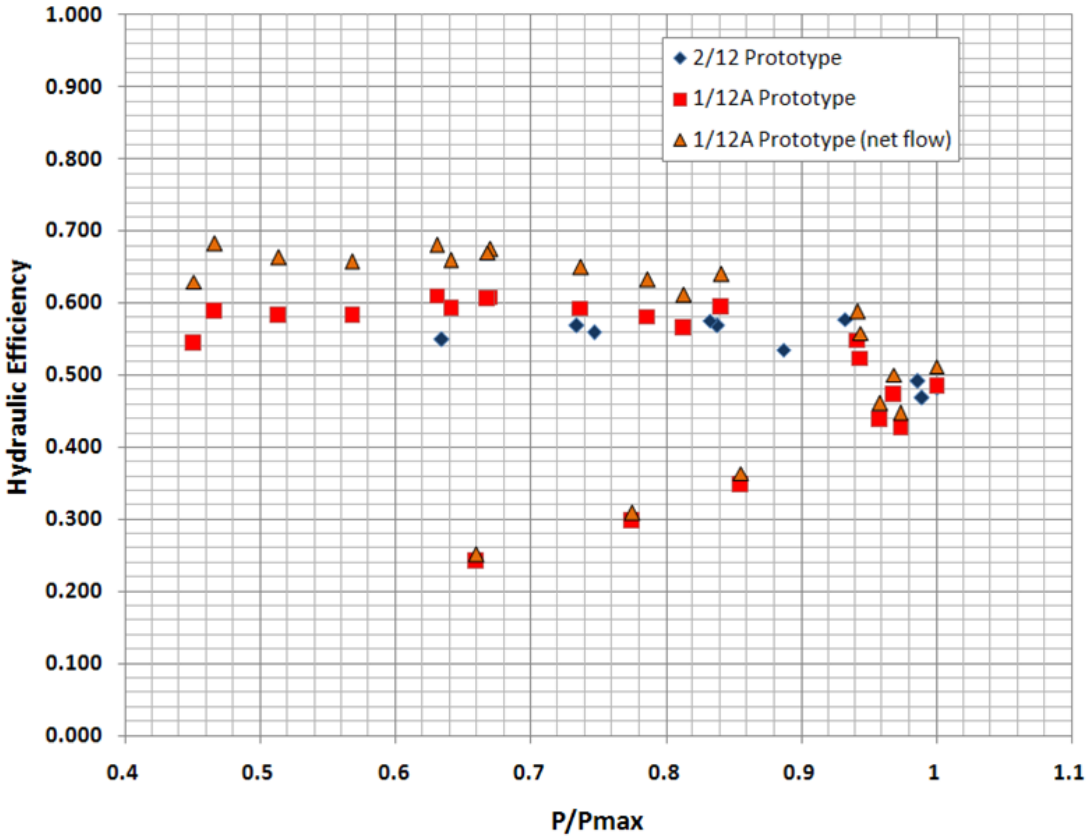

Figure 6.18: The direct comparison of Parametric Power with Efficiency

The impact of leakage on efficiency is also demonstrated in this plot. Leakage accounts for 8 – 10% of peak efficiency values, although it has a negligible effect once rotor speeds reach peak power and above.

6.4 Estimation of Measurement Errors

The assumptions used to derive shaft power output and flow rates from the measured data have already been described in some detail in chapter 5. We will not attempt to account for underlying flaws in any of these assumptions since insufficient data is available, but, instead, will concentrate on quantifiable errors arising through the

measurement process in the key areas of Power Output, Measured Head, and Flow Rate.

For brevity, the impact of these errors will be considered at the 1/12A operating condition only – although a similar level of impact will be present at all test conditions.

6.4.1 Power Output Errors

Reading errors in the measurement of electrical power output are small; good instrument resolution and the 'averaging' technique employed to record fluctuations in current and voltage readings result in errors of +/- 10 Watts.

For the generator efficiency derived from manufacturers' tests, we assume a constant error of 1%. Due to the assumptions required to estimate friction losses in the rotor and gearbox, no sensible additional estimation of reading errors can be made.

6.4.2 Measured Head Errors

Water level readings contain potential errors due to reference level setting, scale resolution and difficulties in making readings in turbulent flow conditions. There errors are quantified as follows:

Reference level error: +/- 5 mm

Scale resolution error: +/- 10 mm

Turbulence reading error: +/- 10 mm

This gives a total error of +/- 25 mm which, for the 1/12A test condition, represents 2% of the measured head resulting in a pro-rata error in the energy content of the flow.

6.4.3 Flow Rate

From the literature, flow rate measurements based on propeller readings are likely to contain errors of around 5% for carefully conducted experiments under good conditions (ISO 8363, 1997).

As described above, a range of leakage flow rates could be applied to these experiments and, due to the importance of this parameter, these are considered separately in later chapters and will not be included in the basic flow errors described here.

6.4.4 Impact of Errors on Performance Curves

The impact of measurement errors on performance graphing is shown in Figure 6.19. Power measurement errors have a negligible effect on P/Pmax values since errors in values tend to cancel each other out. However, the impact on efficiency is potentially very significant as shown by the error bars applied to the gross efficiency data points, amounting to +/- 7 to 8% error across the operating range. For clarity, error bars have not been applied to the net flow efficiency curve although a similar range of values will occur.

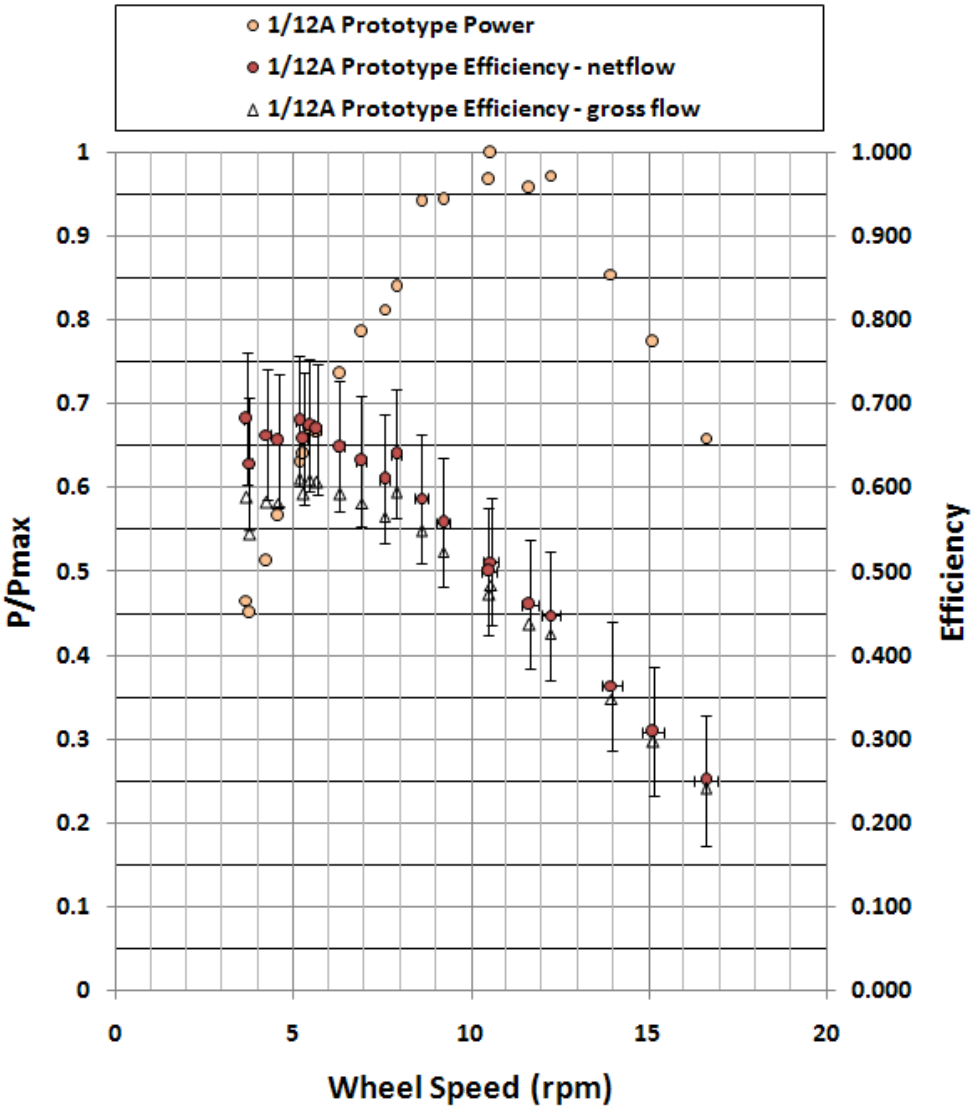

Figure 6.19: The impact of Measurement Errors on Performance Plots

6.5 Summary

This chapter has presented very detailed observations from trial operation of the HPM Prototype installation.

In particular the high levels of turbulence at moderate rotor speeds, sensitivity of the machine to variations in river conditions and generation of noise during the cell emptying process have resulted in significant limitations in operation.

Having due regard to the range of potential errors inherent in these measurements, performance tests suggest a very strong linkage between downstream water levels and peak machine efficiency. However, thus far no comparison with Classical HPM theory has been made and so chapter 7 will begin with this correlation before going on to further analyse performance results and evaluate overall machine capability.

Test Date	Test Time	Wheel time for 1 revolution (s)	Wheel rpm	Electrical Power (Ahead of inverter)	Generator efficiency	Power lost to friction and Transmission (W)	Shaft Power (W)	Elevation 'MP2' (mm)	Elevation MP1 (mm)	Head Drop MP2-MP1(mm)	Datum Wheel Flow (m3/s)	Efficiency Qdiff	Efficiency Qdiff
29/02/2012	11:54	11.29	5.31444	1840	0.87	112	2219	1535	193	1342	0.3006	0.465	0.561
	12:22	10.09	5.94648	2173	0.89	125	2570	1585	223	1362	0.3328	0.489	0.578
	12:40	9.79	6.1287	2209	0.89	129	2614	1615	243	1372	0.3420	0.480	0.568
	13:06	8.81	6.81044	2498	0.90	143	2933	1640	258	1382	0.3763	0.490	0.575
	13:20	7.34	8.17439	2674	0.91	172	3105	1610	283	1327	0.4439	0.463	0.537
	13:40	7.53	7.96813	2807	0.91	167	3266	1585	263	1322	0.4337	0.499	0.581
	14:05	6	10	3003	0.93	210	3453	1610	263	1347	0.5319	0.427	0.491
	14:16	5.84	10.274	3049.4	0.93	216	3502	1625	263	1362	0.5449	0.419	0.481
	14:30	5.78	10.3806	3012.7	0.93	218	3464	1625	253	1372	0.5499	0.407	0.468
	14:55	8.96	6.69643	2482.35	0.90	141	2913	1615	238	1377	0.3706	0.496	0.582
10/01/2012	03:00		7.9	2562	0.91	166	2994	1635	448	1187	0.4304	0.511	0.597
11/01/2012	01:00	10.57	5.67644	1982.4	0.88	119	2378	1625	393	1232	0.3191	0.514	0.617
	01:45	11.6	5.17241	1854.2	0.87	109	2245	1645	393	1252	0.2933	0.515	0.623
	02:20	13.1	4.58015	1644	0.85	96	2021	1705	393	1312	0.2627	0.486	0.598
	03:25	14.05	4.27046	1485	0.85	90	1828	1650	393	1257	0.2466	0.488	0.601
	03:50	15.9	3.77358	1287	0.84	79	1605	1695	383	1312	0.2206	0.453	0.565
12/01/2012	11:30	16.28	3.6855	1278	0.81	77	1661	1635	353	1282	0.2160	0.470	0.611
	01:10	11.31	5.30504	1887.6	0.87	111	2281	1650	368	1282	0.3001	0.500	0.604
	01:40	9.5	6.31579	2214	0.89	133	2624	1635	368	1267	0.3515	0.507	0.601
	02:35	7.92	7.57576	2475	0.90	159	2897	1615	363	1252	0.4144	0.486	0.569
	03:05	8.66	6.92841	2383.6	0.90	145	2800	1635	363	1272	0.3822	0.500	0.587
	03:25	5.676	10.5708	3106.2	0.93	222	3562	1720	373	1347	0.5589	0.421	0.482
	04:00	4.9	12.2449	3015	0.94	257	3466	1690	378	1312	0.6365	0.368	0.423
	04:20	2.836	21.1566	0	0.00	444		1690	378	1312	1.0120	0.000	0.000

Table 6.2 – Part 1: Full Summary of Prototype Test Results

Test Date	Test Time	Wheel time for 1 revolution (s)	Wheel rpm	Electrical Power (Ahead of inverter)	Generator efficiency	Power lost to friction and Transmission (W)	Shaft Power (W)	Elevation 'MP2' (mm)	Elevation MP1 (mm)	Head Drop MP2-MP1(mm)	Datum Wheel Flow (m3/s)	Efficiency Qdiff	Efficiency Qdiff
13/01/2012	11:00	6.97	8.60832	2904.1	0.92	181	3355	1690	353	1337	0.4650	0.476	0.550
	11:25	6.508	9.21942	2914.9	0.92	193	3360	1675	353	1322	0.4946	0.454	0.524
	11:50	5.708	10.5116	3003	0.93	221	3450	1690	348	1342	0.5561	0.410	0.471
	12:25	5.15	11.6505	2968	0.94	244	3412	1665	353	1312	0.6092	0.379	0.435
	01:15	4.3	13.9535	2604	0.95	293	3045	1635	373	1262	0.7134	0.295	0.345
	01:30	3.61	16.6205	1921	0.96	349	2350	1575	363	1212	0.8288	0.195	0.238
	01:45	3.962	15.1439	2323	0.95	318	2760	1625	373	1252	0.7656	0.247	0.294
Reduced head tests	02:10	5.488	10.9329	2736	0.93	229	3165	1545	363	1182	0.5759	0.410	0.474
	02:50	6.35	9.44882	2655	0.92	198	3079	1545	363	1182	0.5056	0.453	0.525
	03:30	7.288	8.23271	2565.4	0.95	173	2885	1570	363	1207	0.4467	0.485	0.545
	03:50	11.97	5.01253	1751.4	0.87	105	2123	1595	353	1242	0.2850	0.504	0.611
	04:03	9.67	6.20476	2012.5	0.88	130	2419	1575	363	1212	0.3459	0.489	0.588
	04:40	4.436	13.5257	2531.2	0.94	284	2967	1565	353	1212	0.6944	0.307	0.359
	04:00	4.23	14.1844	2049.6	0.95	298	2464	1515	353	1162	0.7237	0.248	0.299
free wheel		2.77	21.6606	0	0.00	455		1515	353	1162	1.0314	0.000	0.000
24/02/2012	01:55	8.31	7.22022	2721.9	0.90	152	3170	1677	273	1404	0.3968	0.498	0.580
16/09/2011		157	0.38217	0		9		1720	303	1417	0.0381	0.000	0.000
		52	1.15385	0		28		1717	323	1394	0.0804	0.000	0.000
	12.31	21.62	2.77521	1094.4	0.84	67	1364	1638	408	1229.5	0.1678	0.541	0.674
September Tests 2011	12.3	20.69	2.89995	1171.2	0.85	70	1453	1640	413	1227	0.1745	0.558	0.692
	12.5	21.12	2.84091	1103.025	0.85	68	1373	1625	398	1227	0.1713	0.535	0.666
	1.47	15.97	3.75704	1501.95	0.87	90	1810	1653	426	1227	0.2198	0.568	0.684
	1.05pm	17.2	3.48837	1331.925	0.87	84	1623	1625	403	1222	0.2056	0.540	0.658
	1.21	11.2	5.35714	1972.1	0.90	128	2310	1665	451	1214	0.3027	0.547	0.641
	2.45	16.01	3.74766	1519.375	0.88	90	1809	1645	432	1213.5	0.2193	0.582	0.693
	2.5	17.49	3.43053	1389.15	0.86	82	1693	1623	416	1207	0.2026	0.579	0.706

Table 6.2 – Part 2: Full Summary of Prototype Test Results

Test Date	Test Time	Wheel time for 1 revolution (s)	Wheel rpm	Electrical Power (Ahead of inverter)	Generator efficiency	Power lost to friction and Transmission (W)	Shaft Power (W)	Elevation 'MP2' (mm)	Elevation MP1 (mm)	Head Drop MP2-MP1(mm)	Datum Wheel Flow (m3/s)	Efficiency Qdiff	Efficiency Qdiff
17/09/2011	1.21	21.45	2.7972	1082.25	0.84	67	1350	1600	401	1199.5	0.1690	0.544	0.679
	1.12	18.46	3.25027	1281.125	0.86	78	1573	1610	413	1197	0.1931	0.565	0.694
	1.3	23.92	2.50836	933.3	0.78	60	1258	1585	393	1192	0.1536	0.520	0.700
	1.35	24.57	2.442	905.85	0.77	59	1235	1580	396	1184.5	0.1500	0.520	0.708
	1.15	20.02	2.997	1171.8	0.85	72	1451	1600	421	1179.5	0.1796	0.564	0.698
	1.26	22.43	2.67499	996.45	0.82	64	1286	1575	403	1172	0.1625	0.533	0.688
	1.45	24.96	2.40385	906.75	0.76	58	1249	1555	391	1164.5	0.1480	0.536	0.739
	2.55	14.57	4.11805	1579.05	0.88	99	1888	1590	431	1159.5	0.2387	0.582	0.696
	3.45	20.63	2.90839	1110.2	0.85	70	1382	1540	413	1127	0.1749	0.574	0.714
	2.57	12.8	4.6875	1707.425	0.89	112	2023	1545	446	1099.5	0.2683	0.590	0.699
	2.1	12.2	4.91803	1560.275	0.90	118	1856	1525	443	1082	0.2802	0.525	0.624
	5.35	9.6	6.25	1938.9	0.92	150	2267	1545	473	1072	0.3482	0.530	0.619
	4.45	9.22	6.50759	2066.55	0.92	156	2402	1505	468	1037	0.3611	0.563	0.654
	4.15	9.22	6.50759	2008.3	0.92	156	2339	1470	463	1007	0.3611	0.563	0.656
	4.47	11.11	5.40054	1808.4	0.90	129	2130	1475	468	1007	0.3050	0.600	0.707
	4.52	11.7	5.12821	1662.9	0.90	123	1967	1445	448	997	0.2910	0.584	0.691
	3.04	11.25	5.33333	1697.5	0.90	128	2006	1440	453	987	0.3015	0.581	0.687
	4.55	13.5	4.44444	1342.75	0.89	107	1615	1350	428	922	0.2557	0.581	0.698
	3.35	6.07	9.88468	1790.7	0.95	237	2130	1495	503	992	0.5264	0.350	0.416

Table 6.2 – Part 3: Full Summary of Prototype Test Results

Chapter 7: Analysis and Review of Field Trials

7.1 Comparison with Classical Theory:

7.1.1 Modifications required for prototype

The simplified geometry and water levels assumed in the classical theory are quite different from that of the prototype machine and some modifications to the basic analysis are required if valid comparisons are to be made.

While the assumption of a 2 dimensional machine will be retained, the differences in downstream water levels shown in figure 7.1 between prototype and theory must be accounted for in the basic equations as described below.

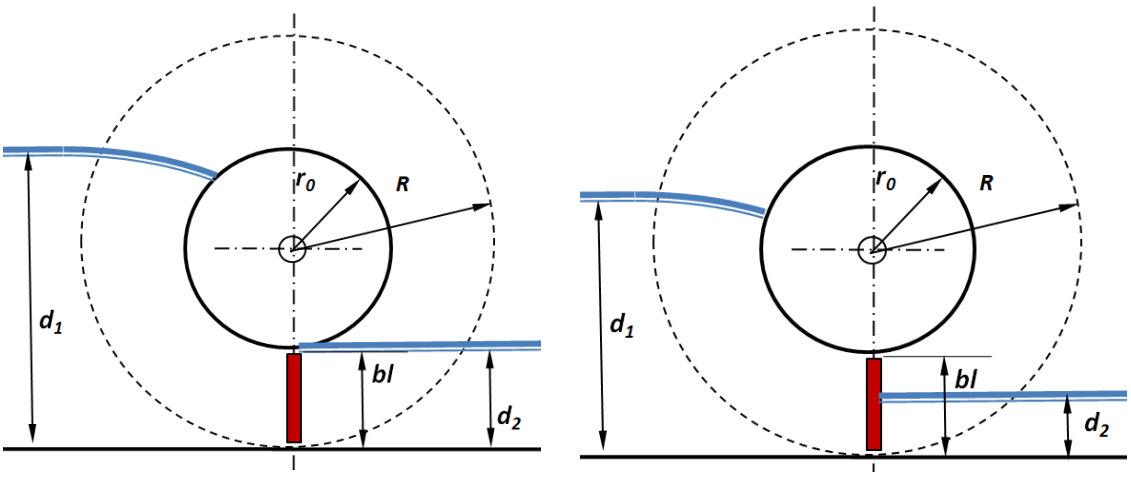

Figure 7.1: Geometry differences between theoretical geometry *(left)* and Prototype *(right)*

7.7.1.1 Blade Force

The deviations from theoretical water levels modify both blade force and ideal power output expected from the prototype machine.

The force on the blade caused by water pressure in the ideal machine was given in chapter 3 by equation 3.8. Correcting this equation for a machine of width 'W_T' gives:

$$F_p = W_T \rho g b l (d_1 - d_2 - \Delta h_1) \qquad (7.1)$$

However, for the lower downstream water level in the prototype machine, the average pressure on the upstream side of the blade becomes:

$$p_u = \rho g \left(d_1 - \Delta h_1 - \frac{bl}{2} \right) \tag{7.2}$$

Giving a blade force due to upstream pressure of:

$$F_{up} = W_T bl \rho g \left(d_1 - \Delta h_1 - \frac{bl}{2} \right) \tag{7.3}$$

The expression for blade force due to downstream pressure remains unaltered as:

$$F_{pdown} = \frac{\rho g}{2} W_T {d_2}^2 \tag{7.4}$$

Giving the net force on the blade due to water pressure as:

$$F_{pnet} = W_T \rho g \left[bl \left(d_1 - \Delta h_1 - \frac{bl}{2} \right) - \frac{{d_2}^2}{2} \right] \tag{7.5}$$

7.7.1.2 Flow Rate

Since the blade structure has a significant volume in the prototype machine, this must be allowed for in the calculation of volume flow rate.

We define 'Vol_{blade}' as the volume displaced by the structure of a single blade assembly in the prototype rotor, obtained from the 3D CAD model of the unit.

The blade has a mean radius from the axis of rotation of the machine of 'r_{mean}':

$$r_{mean} = r_0 + \frac{bl}{2} \tag{7.6}$$

For a machine with 'N' blades rotating at 'n' revolutions per second, the net flow passing through the machine is:

$$Q_{net} = 2\pi n r_{mean} bl W_T - nNVol_{blade} \tag{7.7}$$

Leakage flow and gross flow are calculated as before.

7.7.1.3 Velocity and Power

In basic theory, ideal power output is calculated as the product of blade force and downstream velocity V_2. In the prototype unit, the velocity of the centre of the blade is used:

$$V_T = \omega r_{mean} \tag{7.8}$$

where: ω = angular velocity of the rotor (radians/s)

This is related to the V_2 by the continuity equation:

$$V_2 = V_T \frac{bl}{d_2} \tag{7.9}$$

7.1.2 Comparison with 1/12A Data Set

Since the 1/12A test series produced the most complete performance curve, it will be used for theory comparisons. This test set also has the advantage that propeller flow measurements are available, which allows leakage flows to be based on measurements rather than estimated values.

Parametric performance values are compared with a best fit curve from adapted theory in Figure 7.2. All losses (including acceleration) are represented by a turbulence loss coefficient of 2.9. No adjustment in leakage flows has been made to aid curve fitting.

On first glance the fit between theory and data for P/Pmax appears reasonable, with theory over-estimating efficiency by some 18%. However, parametric power comparisons can be misleading since while the 'spread' of the power curve can be compared easily, these plots tend to disguise deviations in absolute power values.

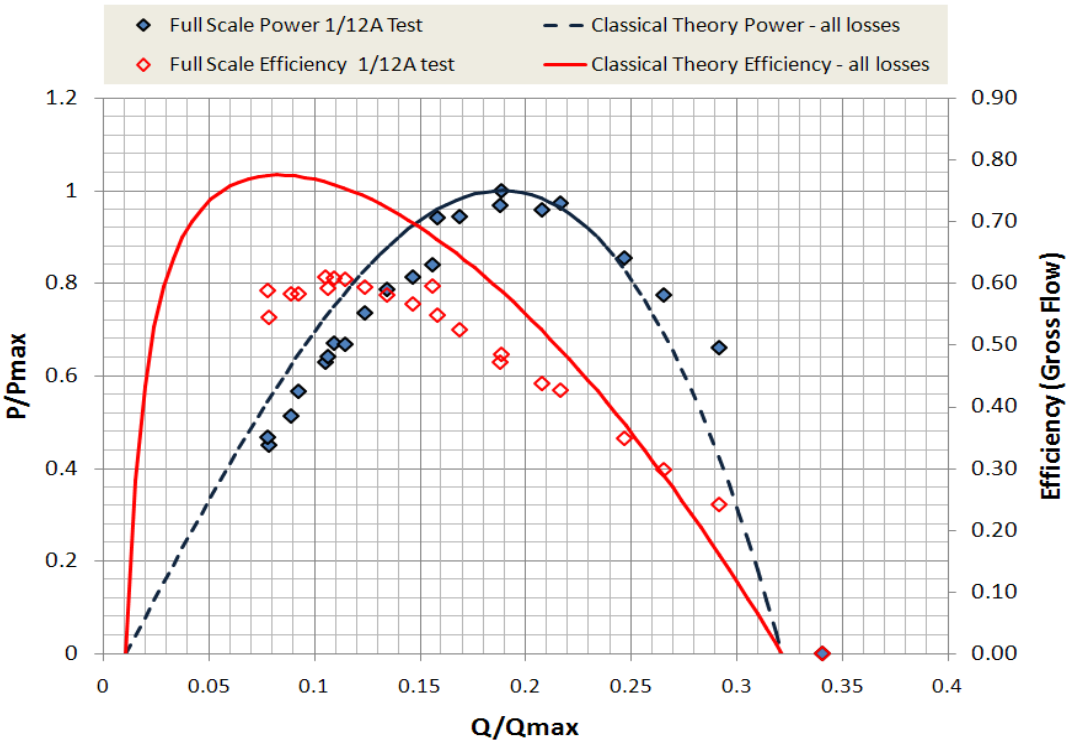

Figure 7.2: Parametric Comparison of 1/12A Test Data and Theory

This is very clearly illustrated in Figure 7.3 where absolute values for shaft power and efficiency are plotted against prototype wheel speed.

From this figure classical theory appears to give a poorer match with measured data. Increasing the turbulence loss coefficient any further to reduce power output reduces the spread of the power curve to unrealistic levels although the general shape of the curves is represented to some degree.

There are two possible causes for this large deviation between theory and measurements: the first could be due to errors created by applying 2 dimensional theory to a 3 dimensional machine; the second could be due to additional factors present in the prototype not accounted for by basic theory.

Both of these issues are addressed in the new theory developed in the following sections.

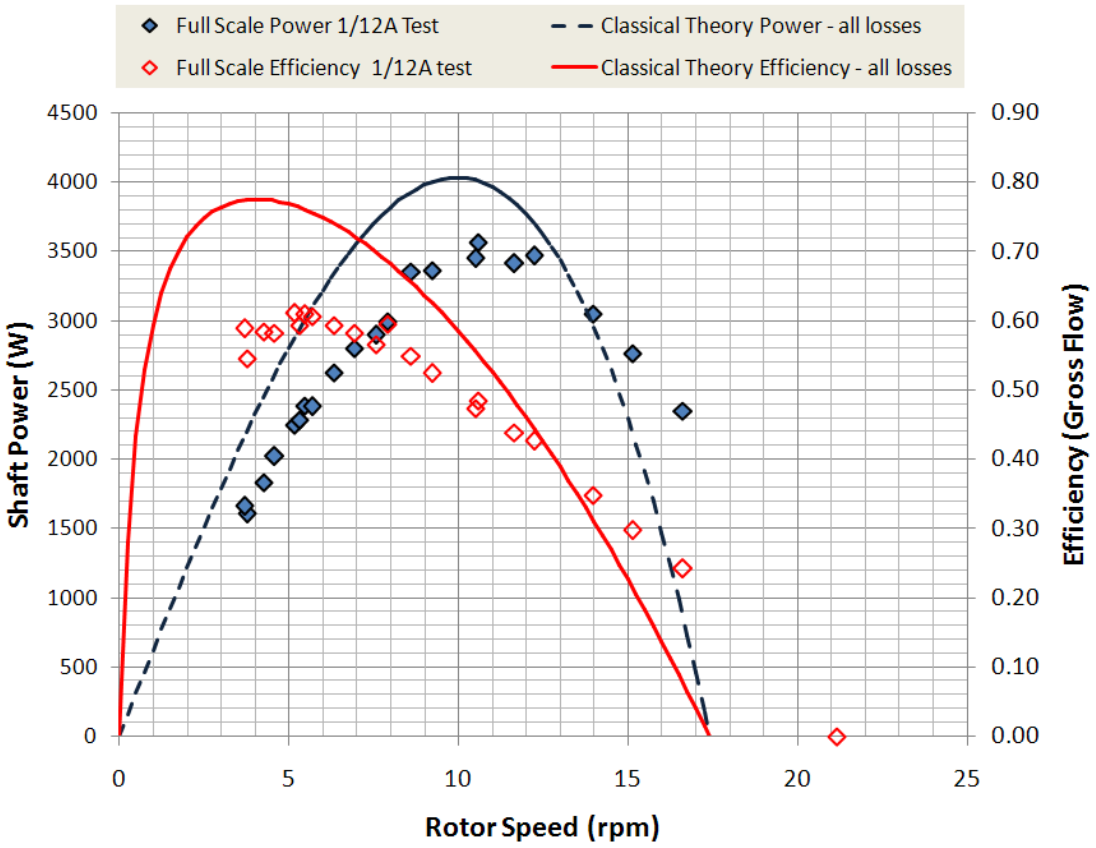

Figure 7.3: Absolute Comparisons of 1/12A Test Data and Theory

7.2 HPM 3-D Theory

7.2.1 Geometry

The full three-dimensional geometry of the prototype is shown in Figure 7.4 and the potential complexity required by a full analysis is immediately apparent. In particular the width of the downstream channel (W3) means that the water level at the machine exit (d2) cannot be calculated directly and an iterative solution technique is required.

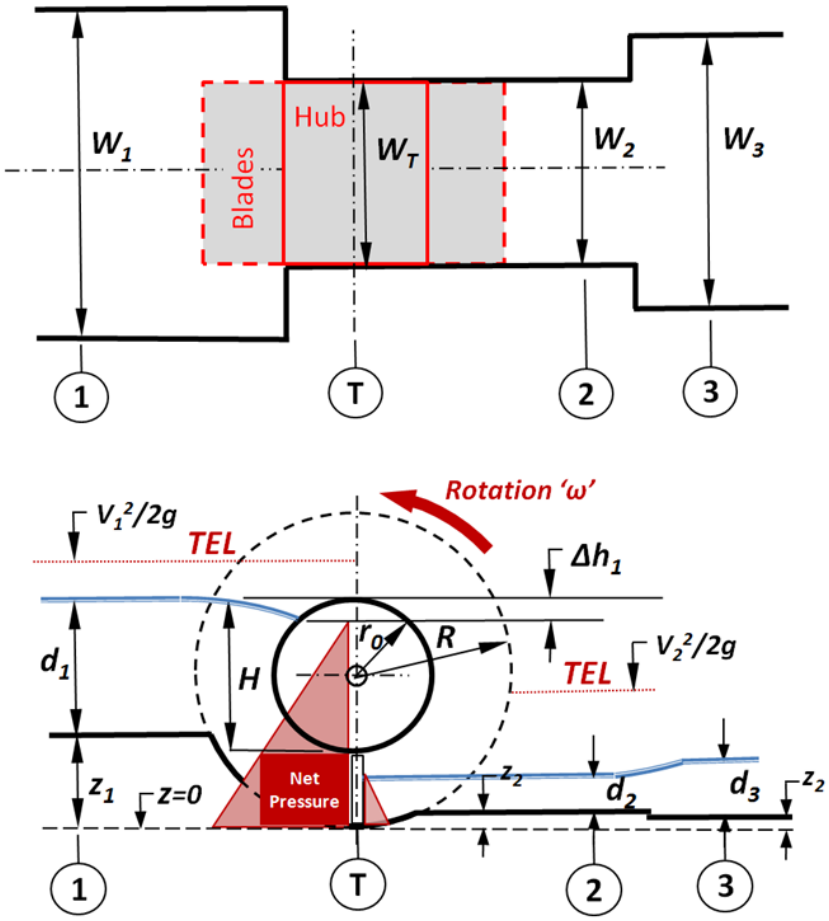

Figure 7.4: Complexity of Prototype Installation Geometry

The complexity of such a solution does not aid the current study of fundamental machine behaviour and, in the present work, the simplified intermediate installation geometry shown in Figure 7.5 will be considered. Eliminating the increase in downstream width enables direct calculation of exit water depth, while neglecting

variations in channel floor elevations simplifies the algebra considerably.

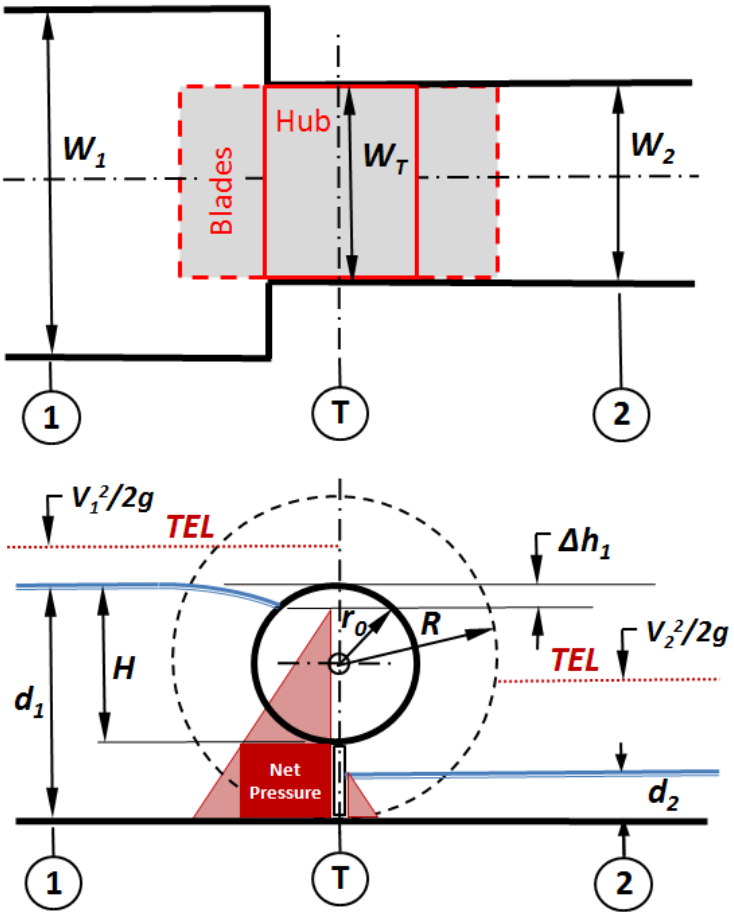

Figure 7.5: Simplified 3D Installation Geometry

7.2.2 Continuity Equations

Flow volumes through the three stations shown in figure 7.5 are linked by continuity:

$$Q_{gross} = V_1 d_1 W_1 = V_T b l W_T = V_2 d_2 W_T \qquad (7.10)$$

Re-arranging to express all velocities in terms of the blade speed 'V_T':

$$V_1 = V_T \left(\frac{b l W_T}{d_1 W_1}\right) \qquad (7.11)$$

$$V_2 = V_T \left(\frac{blW_T}{d_2 W_T}\right) = V_T \frac{bl}{d_2} \tag{7.12}$$

7.2.3 Head Drop due to Flow

Applying the energy equation between stations 1 and T gives:

$$\Delta h_1 = \frac{V_T^2 - V_1^2}{2g} = \frac{V_T^2}{2g}\left[1 - \left(\frac{blW_T}{d_1 W_1}\right)^2\right] \tag{7.13}$$

7.2.4 Pressure Forces on the Blade

The contribution to overall blade forces made by individual pressure components are detailed, along with the notation used in this analysis, in Figure 7.6.

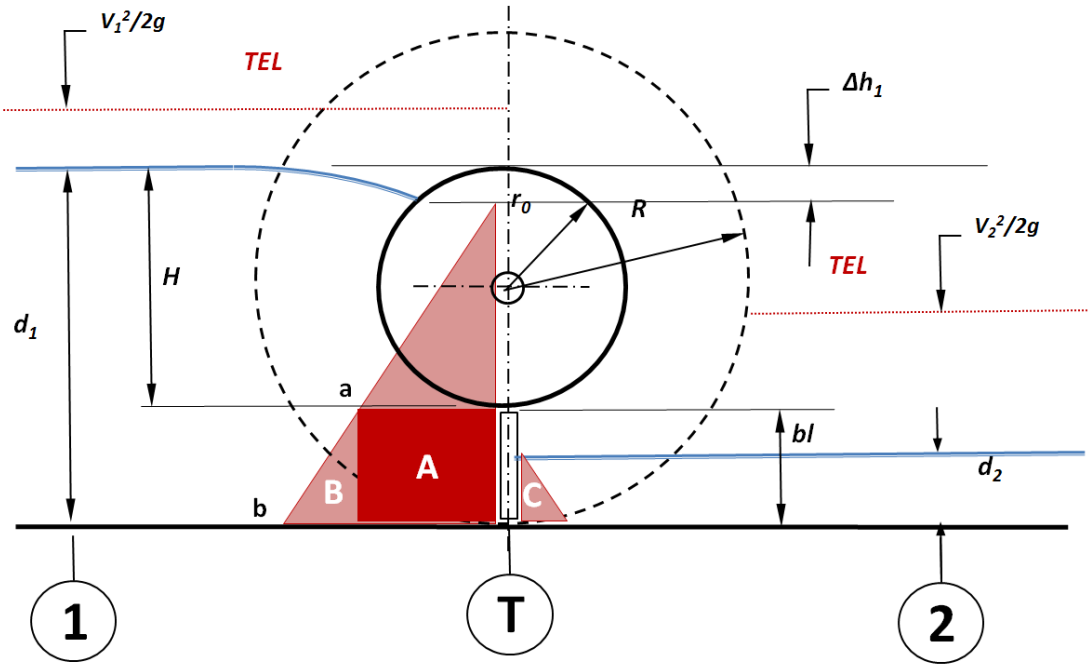

Figure 7.6: Blade Force Pressure Components

As can be seen, calculation of blade forces is more complex than in classical analysis and the centroid distances of each pressure area from the rotor axis becomes significant.

In this analysis the torque arising from each pressure component will be equated rather than the simple blade forces used in classical theory.

The pressure at points 'a', 'b' and 'c' in figure 7.6 are given by:

$$p_a = \rho g(d_1 - \Delta h_1 - bl) \tag{7.14}$$

$$p_b = \rho g(d_1 - \Delta h_1) \tag{7.15}$$

$$p_c = \rho g d_2 \tag{7.16}$$

The blade force arising from pressure area 'A' is:

$$BF_A = \rho g(d_1 - \Delta h_1 - bl)blW_T \tag{7.17}$$

The centroid radius of area 'A' is r_{mean} so torque due to area 'A' is:

$$T_{FA} = r_{mean}BF_A \tag{7.18}$$

The blade force arising from pressure area 'B' is:

$$BF_B = \frac{\rho g}{2}W_T bl^2 \tag{7.19}$$

And centroid radius 'cr_B' of area 'B' is:

$$cr_B = r_0 + \frac{2}{3}bl \tag{7.20}$$

Giving a torque due to area 'B' of:

$$T_{FB} = \left(r_0 + \frac{2}{3}bl\right)BF_B \tag{7.21}$$

The blade force arising from pressure area 'C' is:

$$BF_C = \frac{\rho g}{2}{d_2}^2 \tag{7.22}$$

And centroid radius 'cr_C' of area 'C' is:

$$cr_C = r_0 + bl - \frac{1}{3}d_2 \tag{7.23}$$

Giving a torque due to area 'C' of:

$$T_{FC} = \left(r_0 + bl - \frac{1}{3}d_2\right) BF_C \tag{7.24}$$

7.2.5 Total 'ideal' torque and power

Total torque due to blade pressure forces is:

$$T_{ideal} = T_{FA} + T_{FB} - T_{FC} \tag{7.25}$$

And the resulting power output:

$$P_{ideal3D} = \omega T_{ideal} \tag{7.26}$$

7.2.6 Turbulence Losses

For convenience in this analysis we redefine 3-dimensional turbulence losses in terms of rotor blade velocity only:

$$F_{turb3D} = \frac{1}{2} C_{T3D} bl\rho W_T {V_T}^2 \tag{7.27}$$

Where C_{T3D} is the empirical loss coefficient for the three dimensional machine.

This is a compromise made to make it easier to relate turbulence losses to blade geometry in later chapters. However it does have the draw-back that exit flow losses related to the omitted V_2 term may not be so well represented resulting in an over estimate of turbulence energy loss at high rotor speeds. This makes little difference at prototype scale, but may be more significant at the higher speeds of equivalent model tests.

7.2.7 Inflow Acceleration

Due to the mismatch in water depths either side of the blade at bottom dead centre of rotation, head losses due to acceleration are conveniently considered in two stages. The inflow acceleration considered here, analyses the speed change between the upstream water channel and working section of the machine. The outflow acceleration covering velocity changes as water leaves the cell to the exit channel will be considered in the next section.

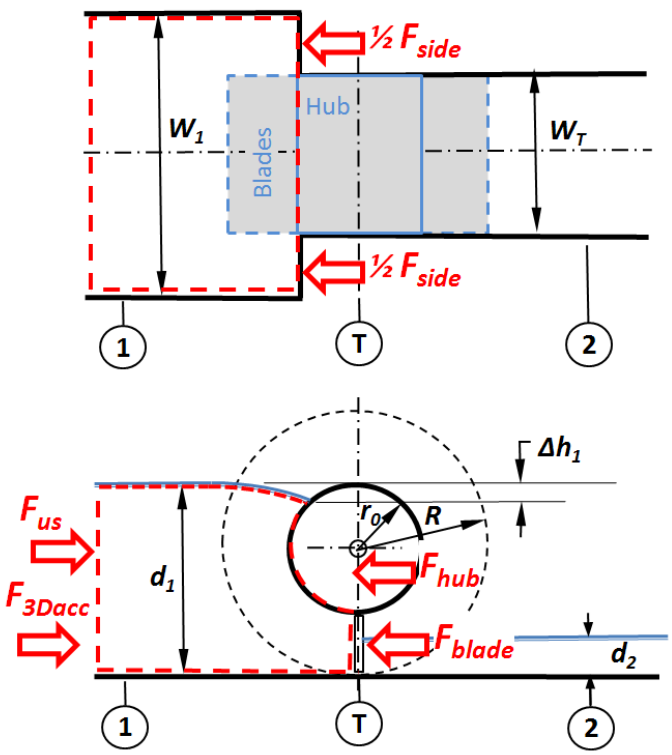

Figure 7.7: Inflow Acceleration Control Volume

Consider the control volume covering the flow entering the machine shown in Figure 7.7.

The boundaries extend between the wetted surfaces of the upstream channel, upstream surfaces of the blade and hub and the free surface of the inflowing water.

External forces arise from the hydrostatic pressure upstream, and reactions of blade hub and side plates of the installation.

By inspection these forces are as follows:

$$F_{us} = \frac{\rho g}{2} W_1 {d_1}^2 \tag{7.28}$$

$$F_{hub} = \frac{\rho g}{2} W_T (d_1 - \Delta h_1 - bl)^2 \tag{7.29}$$

$$F_{side} = \frac{\rho g}{2} (d_1 - \Delta h_1)^2 (W_1 - W_T) \tag{7.30}$$

To calculate the reaction force on the upstream face of the blade, it is convenient to calculate an 'average' pressure over the blade surface from equations 7.14 & 7.15:

$$p_{bav} = \frac{P_a + P_b}{2} = \frac{\rho g}{2}(2d_1 - 2\Delta h_1 - bl) \qquad (7.31)$$

$$F_{blade} = \rho g W_T bl\left(d_1 - \Delta h_1 - \frac{bl}{2}\right) \qquad (7.32)$$

Applying the momentum theorem:

$$\sum F_x = \rho Q(v_T - v_1)$$

And recalling that: $V_1 = V_T\left(\frac{blW_T}{d_1 W_1}\right)$ gives:

$$F_{3Dacc} = F_{hub} + F_{blade} + F_{side} - F_{us} + Q\rho V_T\left(1 - \frac{blW_T}{d_1 W_1}\right) \qquad (7.33)$$

As for the previous theory, this loss of head due to acceleration is represented by a force applied at the centroid of the blade, resulting in a torque opposing rotation of:

$$T_{acc} = r_{mean} F_{3Dacc} \qquad (7.34)$$

7.2.8 Exit flow acceleration

The acceleration of the exit flow that occurs during cell emptying is analysed using the control volume of Figure 7.8.

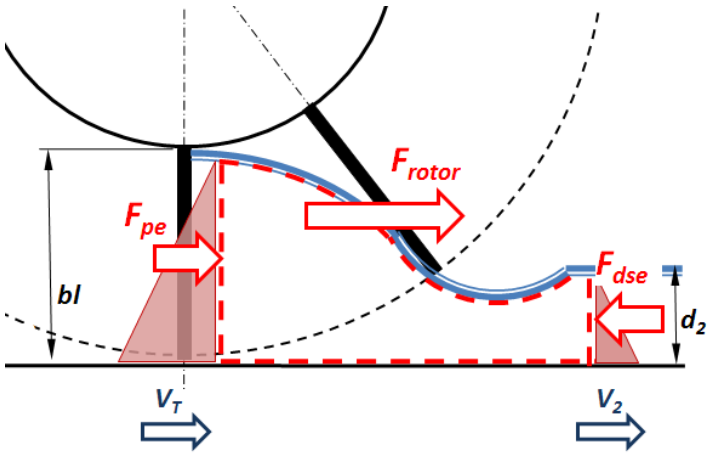

Figure 7.8 Exit Flow Acceleration Control Volume

The figure shows the approximate behaviour of fluid as an individual cell empties. The control volume is offset from the downstream surface of the blade to allow a hydrostatic

pressure distribution to be assumed.

The remaining boundaries are the floor of the exit channel, the free surface of the exit flow and downstream station 2. Two key assumptions are made in this analysis:

1. The free surface of the exit flow is fully vented to atmosphere.
2. Pressure forces acting on the rotor blades are combined with the acceleration force to give a single quantity 'F_{rotor}'.

The external forces are calculated as follows:

$$F_{pe} = \frac{\rho g}{2} bl^2 W_T \tag{7.35}$$

$$F_{dse} = \frac{\rho g}{2} {d_2}^2 W_T \tag{7.36}$$

Applying the momentum theorem gives:

$$F_{rotor} + F_{pe} - F_{dse} = Q\rho(V_2 - V_T) \tag{7.37}$$

Therefore:

$$F_{rotor} = Q\rho(V_2 - V_T) + \frac{\rho g W_T}{2}\left({d_2}^2 - bl^2\right) \tag{7.38}$$

Using continuity, we can make the substitutions:

$V_2 = \frac{blV_T}{d_2}$ and $V_T = \frac{Q}{blW_T}$ into equation 7.38, giving the result:

$$F_{rotor} = \frac{Q^2\rho}{blW_T}\left(\frac{bl}{d_2} - 1\right) + \frac{\rho g W_T}{2}\left({d_2}^2 - bl^2\right) \tag{7.39}$$

Since power is the product of velocity and force, the power loss due to exit acceleration is:

$$P_{exit} = \frac{Q^3\rho}{bl^2{W_T}^2}\left(\frac{bl}{d_2} - 1\right) + \frac{\rho g Q}{2bl}\left({d_2}^2 - bl^2\right) \tag{7.40}$$

Equation 7.40 is a potentially important result since it appears to explain how

downstream water levels relative to the setting of the rotor hub, impact power output. This acceleration term disappears as exit water levels approach the depth of the blade and therefore, the bottom of the hub tube, suggesting that a significant proportion of exit flow losses are completely independent of the cell suction effects observed in chapter 6. While additional suction losses are analysed below, equation 7.40 shows that exit acceleration losses are inevitable for the current HPM prototype installation even if every measure is taken to ensure the free entry of air into the cell during the emptying process.

7.2.9 Unvented Cell Losses

Initially we will consider the machine for the extreme case where no air is deemed to enter the cell via the blade and hub seals. For the analysis we assume**:**

- No flow leaves the cell until the blades rotate past the extent of the side plate and channel walls at which point ventilation of the cell takes place.
- We define the angle of rotation of the mid-point of the cell at which ventilation can take place as 'ϕ_{vent}' which is determined from the 3D CAD model of the installation. For a given geometry, this angle remains constant for all operating conditions and at all scales.
- After the cell rotates past 'ϕ_{vent}' we assume that the cell is instantly vented with the free surface at all points in the cell at atmospheric pressure.

We will consider two loss mechanisms here: the first due to the increase in potential energy of the cell contents as machine rotation increases their elevation and, the second due to changes in acceleration loss occurring during the subsequent draining process.

7.2.9.1 Elevation Loss

If no fluid leaves the cell, the potential energy of the cell increases as rotation progresses. We assume that energy is furnished by the rotor acting on the cell contents as a discrete mass of fluid. The rotation at the point of venting is shown in Figure 7.9.

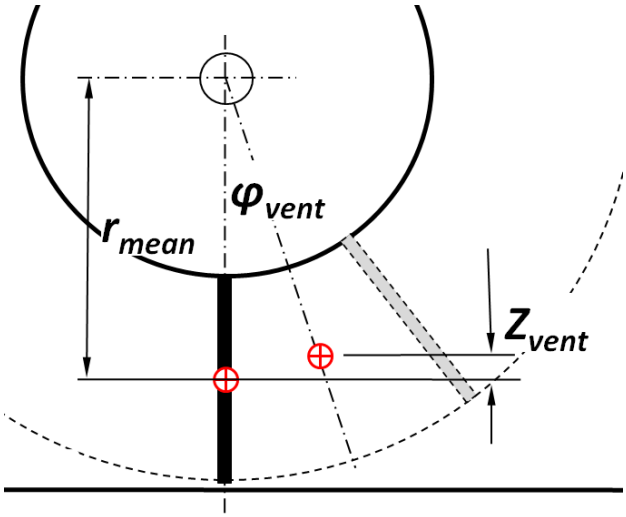

Figure 7.9Unvented Cell Elevation

For this unit:

$$\emptyset_{vent} = 30° \tag{7.41}$$

So:

$$Z_{vent} = r_{mean}[1 - \cos(\emptyset_{vent})] \tag{7.42}$$

From basic physics, 'work' is the product of force and distance, while 'power' is the rate at which that work is done and is the product of force and velocity. Applying this to the cell contents, the power lost to the system due to elevation increase is:

$$P_{zvent} = Q\rho g Z_{vent} \tag{7.43}$$

$$P_{zvent} = Q\rho g r_{mean}[1 - \cos(\emptyset_{vent})] \tag{7.44}$$

7.2.9.2 Unvented Acceleration Loss

The delay in cell emptying caused by the lack of cell ventilation requires some modification to the control volume of Figure 7.8, as shown in Figure 7.10.

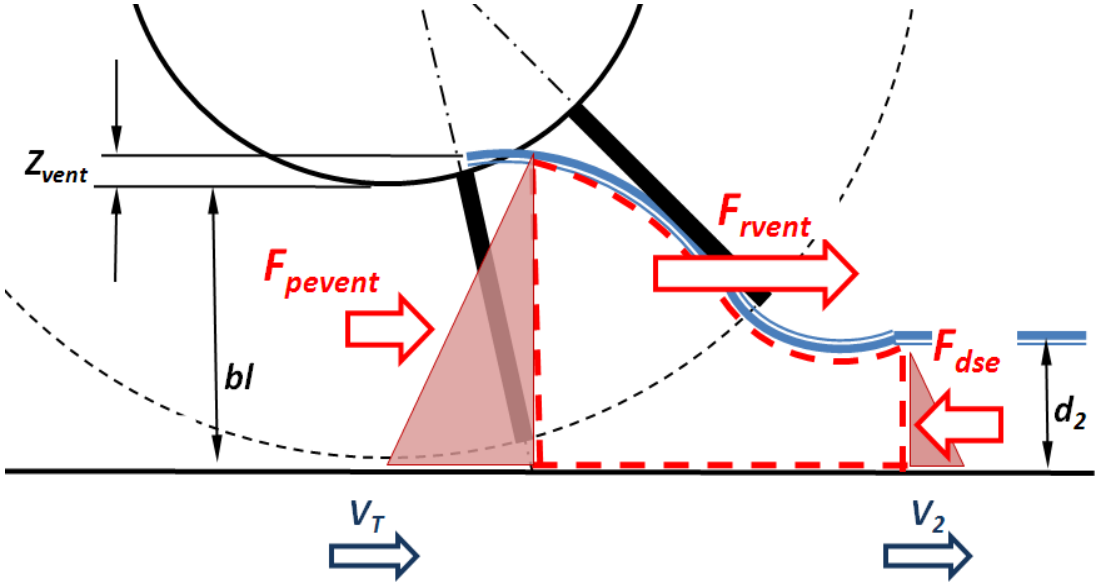

Figure 7.10 Unvented Acceleration Control Volume

The external forces are calculated as follows:

$$F_{pevent} = \frac{\rho g}{2}(bl + Z_{vent})^2 W_T \qquad (7.45)$$

As before:

$$F_{dse} = \frac{\rho g}{2} {d_2}^2 W_T \qquad (7.46)$$

Applying the momentum theorem and making the same substitutions for V_2 and V_T as above gives:

$$F_{rvent} = \frac{Q^2 \rho}{blW_T}\left(\frac{bl}{d_2} - 1\right) + \frac{\rho g W_T}{2}\left({d_2}^2 - (bl + Z_{vent})^2\right) \qquad (7.47)$$

which is equal to:

$$F_{rvent} = \frac{Q^2\rho}{blW_T}\left(\frac{bl}{d_2} - 1\right) + \frac{\rho g W_T}{2}\left(\left({d_2}^2 - bl\ \ ^2\right) - \left({Z_{vent}}^2 - 2blZ_{vent}\right)\right) \quad (7.48)$$

Comparing equation 7.48 with 7.39 it is clear that the net *increase* in acceleration force caused by this lack of cell ventilation is:

$$\Delta F_{rvent} = +\frac{\rho g W_T}{2}\left({Z_{vent}}^2 - 2blZ_{vent}\right) \quad (7.49)$$

The change in acceleration power loss due to lack of ventilation is given by:

$$\Delta P_{exitvent} = \frac{\rho g Q}{2bl} Z_{vent}(Z_{vent} - 2bl) \quad (7.50)$$

The *additional* power loss due to fully unvented cell is:

$$P_{unvent} = (P_{zvent} + \Delta P_{exitvent}) \quad (7.51)$$

7.2.10 Losses due to partial ventilation

So far we have analysed two extremes for cell exit losses; that of a fully ventilated cell where fluid may freely leave the rotor and that of a fully sealed cell where no fluid may leave the machine before the side ventilation areas are opened by the advancing blade.

In practice, judging from the observations of chapter 6, some air clearly enters the cell prior to ϕ_{vent} being reached and therefore a portion of the cell contents must be able to leave.

This makes the losses of equation 7.51 too pessimistic and some correction is required.

The actual hydraulic processes occurring during cell emptying are complex and will be discussed in later chapters. However, a simplified approximation to energy loss estimates developed above will be applied here.

It seems likely that the entry of air into the cell will put a limit on the volume flow rate of water leaving the rotor. It is also likely that this inflowing air will reach a 'terminal velocity' as it passes through the narrow gaps between the fixed structure and blade and

hub seals, due to friction and viscosity losses.

We assume therefore that the restriction of in-flow air produces a constant flow-rate of water leaving the rotor prior to ϕ_{vent}. i.e.

$$Q_{drain} = constant \tag{7.52}$$

The volume of fluid able to leave the cell before ϕ_{vent} is reached depends on the rotor speed:

$$V_{drain} = Q_{drain} \frac{\varphi_{vent}}{\omega} \tag{7.53}$$

Let the volume of fluid contained in the cell be 'V_{cell}'.

The fraction of cell fluid that is able to drain is:

$$\frac{V_{drain}}{V_{cell}} = \frac{Q_{drain}}{V_{cell}} \frac{\varphi_{vent}}{\omega} \tag{7.54}$$

We define the parameter:

$$CDQ = \frac{Q_{drain}}{V_{cell}} \tag{7.55}$$

Note that for very low rotor speeds, cell contents will drain completely before ϕ_{vent} is reached, in which case we assume that the exit losses of equation 7.40 only, are applied, with no additional ventilation loss added.

However, as rotor speed increases, the proportion of cell contents able to drain decreases, and the additional unvented cell losses of equation 7.51 are assumed to apply to the remainder.

$$P_{partial} = \left(1 - CDQ \frac{\varphi_{vent}}{\omega}\right)(P_{zvent} + \Delta P_{exitvent}) \tag{7.56}$$

While this equation gives a means of estimating the impact of inadequate cell ventilation on HPM performance, it is a little inelegant and needs to be treated with some caution. In particular it should be noted that:

1. At low rotor speeds, the quantity in the first bracket of equation 7.56, may yield a negative value which is a meaningless result. Therefore to harmonise with our previously stated assumptions, ventilation losses are deemed not too apply at

such low speeds. This will almost certainly lead to an over-estimation of performance at rotor speeds below peak efficiency.

2. The parameter 'CDQ' is not dimensionless, but has units of '1/s' and scaling laws must be applied to this value when using this theory to compare model & prototype geometry.

Nevertheless, the above theory gives at least a starting point in modelling cell ventilation losses and all of the foregoing is compared with prototype measurements in the next section.

7.3 New Theory Compared with Prototype Data

7.3.1 The 1/12A Data Set

To give the most unforgiving comparison between measured data and theory, absolute values for Shaft Power and gross flow Efficiency are plotted against rotor speed in Figures 7.11 and 7.12 respectively.

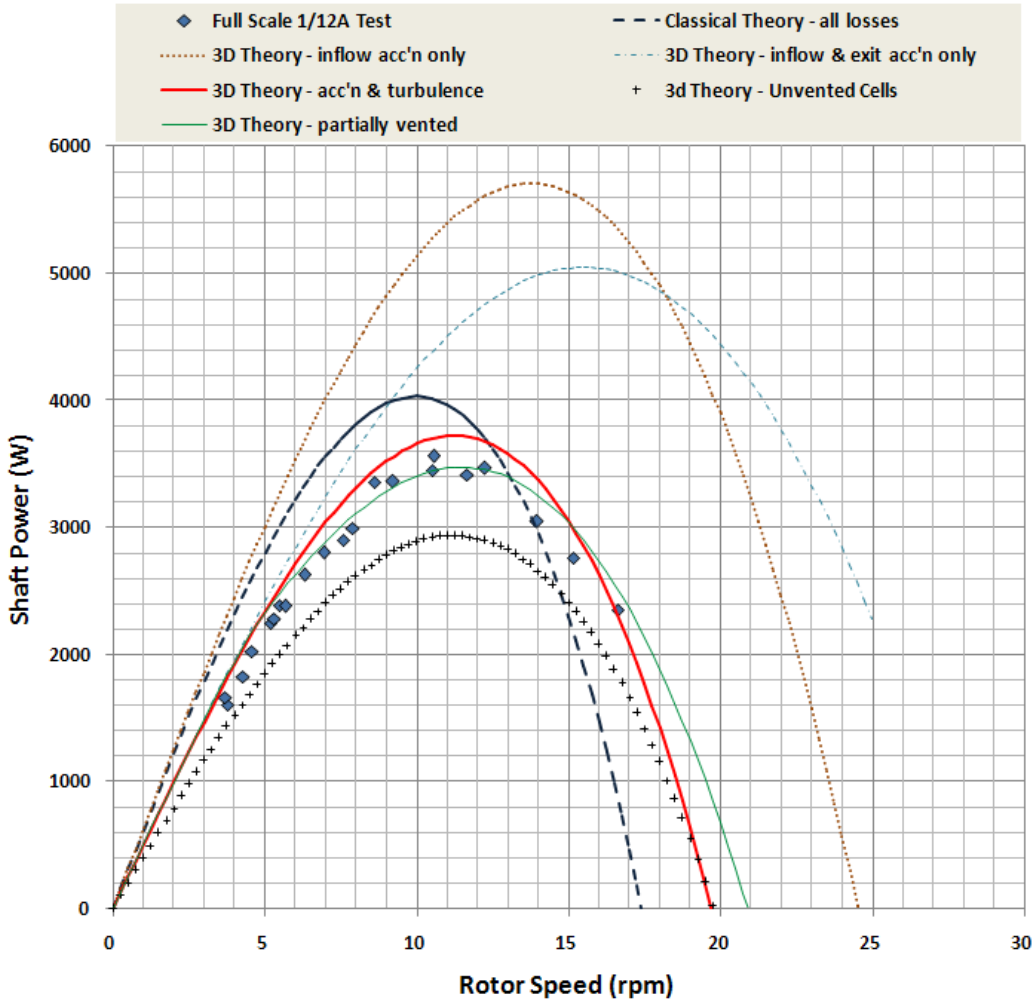

Figure 7.11: Comparison of Measured Power with theory – 1/12A Data Set

Each figure plots the effect of theoretical loss components separately to indicate their cumulative impact on performance. Using the measured value of QL0=0.031 m^3/s and selecting C_{t3D}=2.65, the Shaft Power predicted by 3D Theory (which excludes any ventilation loss), shows quite good agreement with data across the operating range.

However, power output is generally over-estimated with a maximum error of around 5%. As anticipated in the previous section, applying the full energy loss for an unvented cell is much too pessimistic but, putting CDQ=0.9 combined with Cdturb =1.4, enables a good fit to be obtained between partially vented power predictions and prototype measurements.

Similar trends are observed in the efficiency curve in Figure 7.12, with 3D Theory for a fully vented cell giving some over-estimation of efficiency across the operating range.

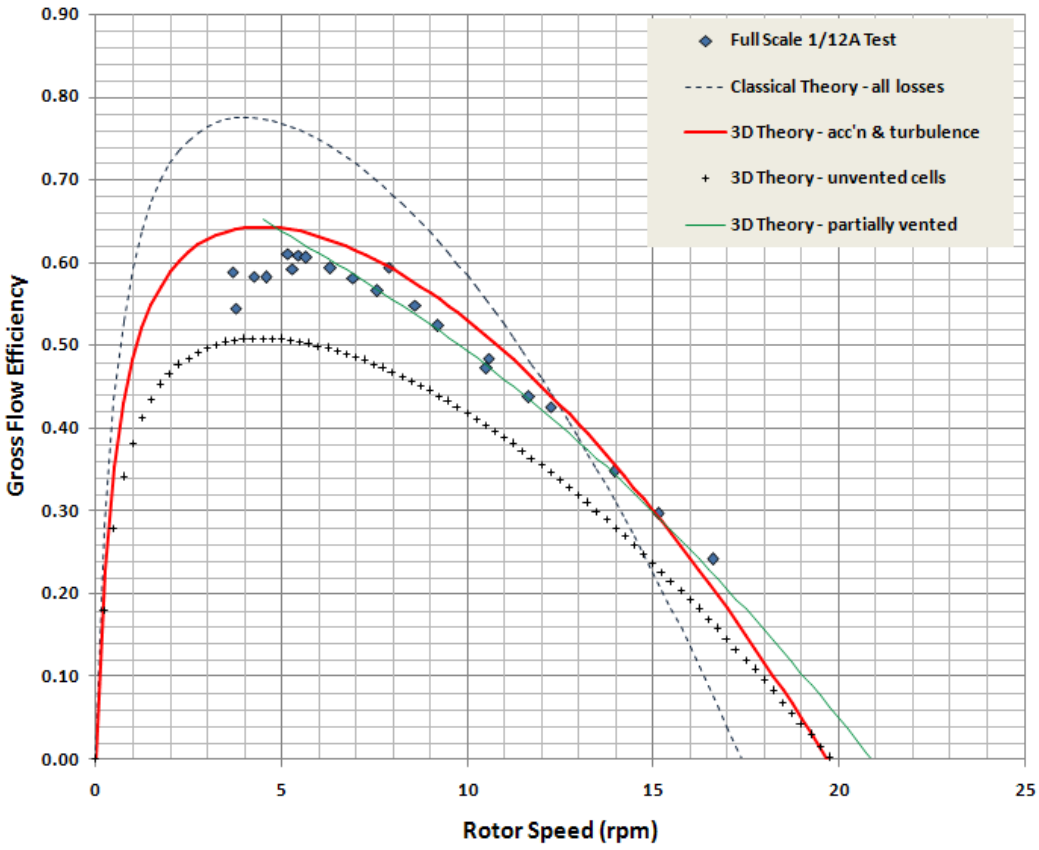

Figure 7.12: Comparison of Measured Efficiency with theory – 1/12A Data Set

Partially vented theory gives a good match with measured efficiency above about 5 rpm; this is hardly surprising given that an additional empirical factor is now present to aid adjustment. However, the much closer match between the theory and the almost linear decline in measured efficiency in the higher operating band is encouraging. Below 5 rpm, the assumption that losses due to poor ventilation do not apply, implicit in the

approximation of equation 7.56, is clearly wrong and some loss mechanism must be present, thus far not included in the system of equations.

The situation is further complicated by the difficulty in estimating leakage flows and mechanical losses which dominate power output in this operating range. Performance measurements are therefore also most prone to error at these very low rotor speeds.

The potential impact of leakage losses is investigated further in the parametric performance plot of Figure 7.13.

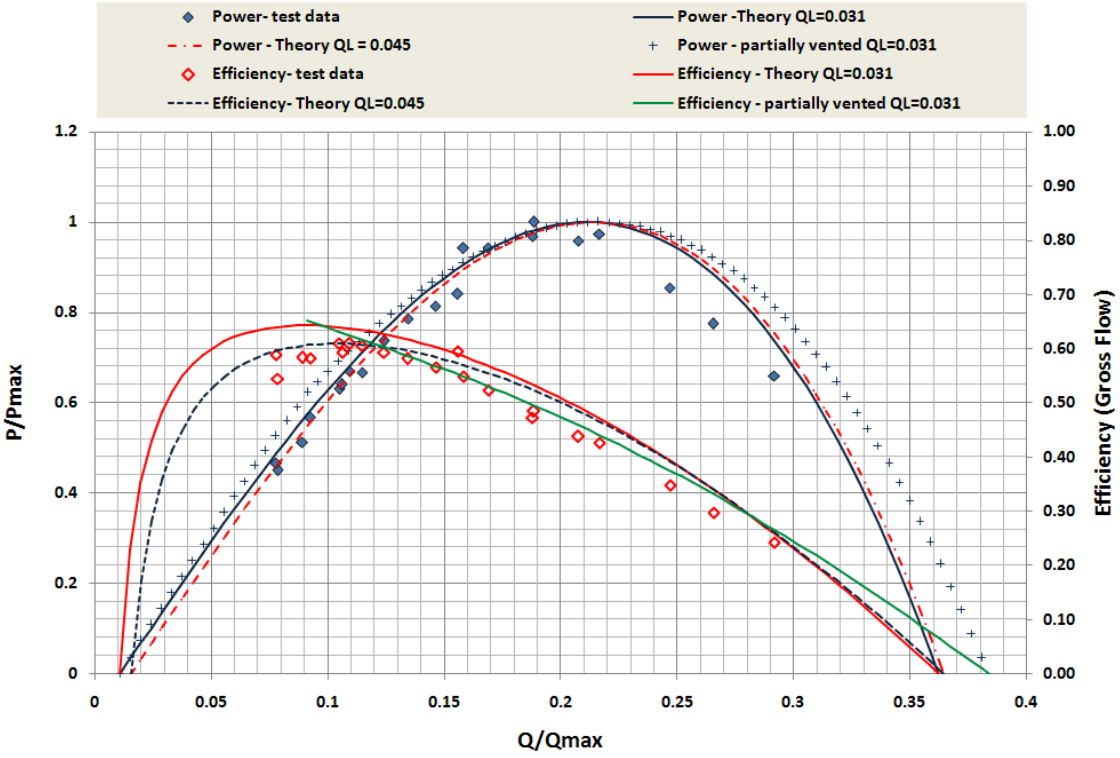

Figure 7.13: Impact of Leakage Flow to Parametric Performance – 1/12A Data Set

In this graph, 3D Theory has been added with leakage increased to a value of QL0 of 0.045 m^3/s. This is used in combination with a revised value for C_{t3D} of 2.5. These altered parameters give an improved fit between theory and data, which is superior to partially vented theory at maximum efficiency and below. However, above maximum efficiency, partially vented theory still gives a better match to the form of the measured data.

This graph illustrates the sensitivity to deviations in leakage flows, whether through measurement error, or calculation of performance predictions. The arbitrary increase of leakage flow from 31 litres per second to 45 litres per second, while representing a 50% increase in leakage, amounts to less than a 2% loss of total flow through the machine at peak power. Such a small deviation is well within the realistic range of measurement error for this prototype, yet has a significant impact on both the value of peak efficiency and the form of the curve in this region. We therefore have to be a little careful not to place too much confidence in the absolute values obtained by these fine 'adjustments' to theory in the peak efficiency region.

Although peak efficiency for these machines is invariably quoted in the literature, a more reliable measure may be to compare efficiency at peak power output, where leakage has a much smaller impact. This has the added attraction of reflecting real world machine operation more effectively; a mill owner sells power, not efficiency and, if water conditions permit, will always seek to operate the machine at its maximum power output.

7.3.2 The 9/11 Data Set

The range of data points collected during the 9/11 measurements covers a very small portion of the overall operating range for the machine. However, since these measurements represent the deepest downstream water levels tested, comparison with the 3D theory is important if any confidence is to be placed in the modelling of exit acceleration losses; the corresponding parametric performance comparisons are presented in Figure 7.14. For clarity, data is only compared with 3D Theory in this figure, since measurements do not extend into the region for which Partially Vented Theory is effective.

Once again, the sensitivity of the analysis to leakage flow is demonstrated with an additional plot, where a low leakage of 0.016 m^3/s is used, while keeping the turbulence loss coefficient value constant at 2.65.

This modification puts the theory through the measured data and may be justified since this data set was collected immediately after machine hub and blade seals were reset following repair. Low leakage rates may therefore have been present in the machine for

these tests, although as noted in previous chapters, leakage rate would have increased substantially over the following 36 hours.

Insufficient data was collected to enable the efficiencies at peak power to be compared.

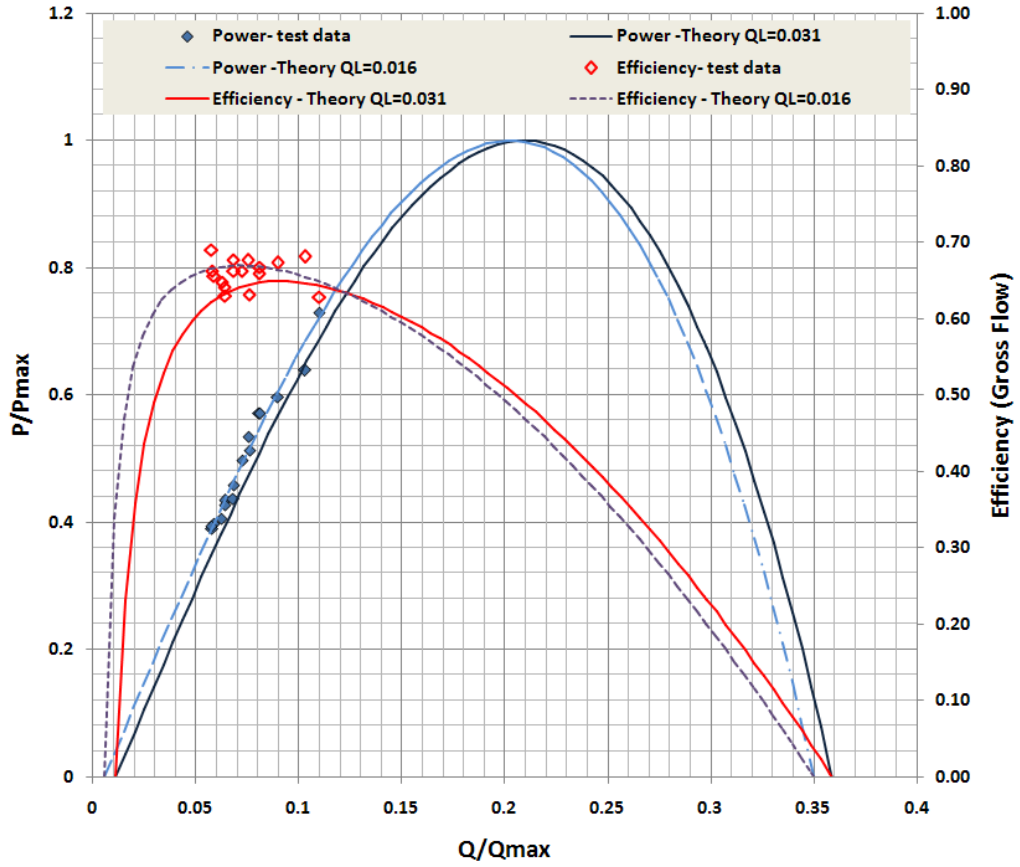

Figure 7.14: Comparison of Parametric Performance Measures with 3D Theory – 9/11 Data Set

7.3.3 Initial Conclusions

In HYLOW internal reports covering these prototype tests (Schneider et.al, 2012) some doubts were cast over the validity of Prototype test data, due to the poor fit with Classical Theory, the relatively constant values of efficiency measured around the peak value and the near linear decline in efficiency at higher rotor speeds. Since these features of the efficiency curve were not predicted by classical theory, the report

suggested that measurements were unreliable and needed to be treated with caution.

This work suggests that such a conclusion was wrong. The above figures show that the theory developed in this chapter accounts very well for the shape of the efficiency curve for both 9/11 and 1/12 test conditions and gives a far better fit to absolute power output values than the theory previously available. This reinforces confidence in both the new theory and the accuracy of the prototype test results themselves.

Despite the significant effect of assumed leakage rates, we can conclude that the new 3D and partial cell ventilation theories presented in this chapter appear to successfully model both the form and magnitude of the performance curve for the HPM prototype and represent one of the most useful contributions to knowledge made by this present work. In particular, the new theory accounts convincingly for the sensitivity of the HPM to variations in downstream water levels observed in the previous chapter, and accounts for the energy losses associated with cell venting observations – at least for medium to high operating speeds.

7.4 Overall engineering assessment of Prototype Unit

7.4.1 Performance

The Peak efficiency of the prototype device at around 70% was good considering that an undeveloped unit was being trialled. However, the performance at peak power output was less impressive and machine efficiency does not compare well with competing devices in this operating range.

Figure 7.15 shows the relative importance of energy losses incorporated into the 3D Theory and Partial Vent Theory for the 1/12A test condition. Values of P/Pmax were obtained by calculating the power from each energy source in terms of the peak power output achieved by the machine. The figure represents a useful visualization tool to help identify where performance gains are most likely to be achieved in future HPM designs.

Acceleration losses at the exit are larger than those at the inflow, up to about 0.2 Qmax, emphasizing the importance of selecting the correct blade length and hub diameter to match both site head and *downstream* water conditions. Suction losses are also significant at high speeds – emphasizing the importance of ensuring that shoe, blade

and side plate geometries allow the unrestricted flow of air into the cell as soon as cell emptying is started.

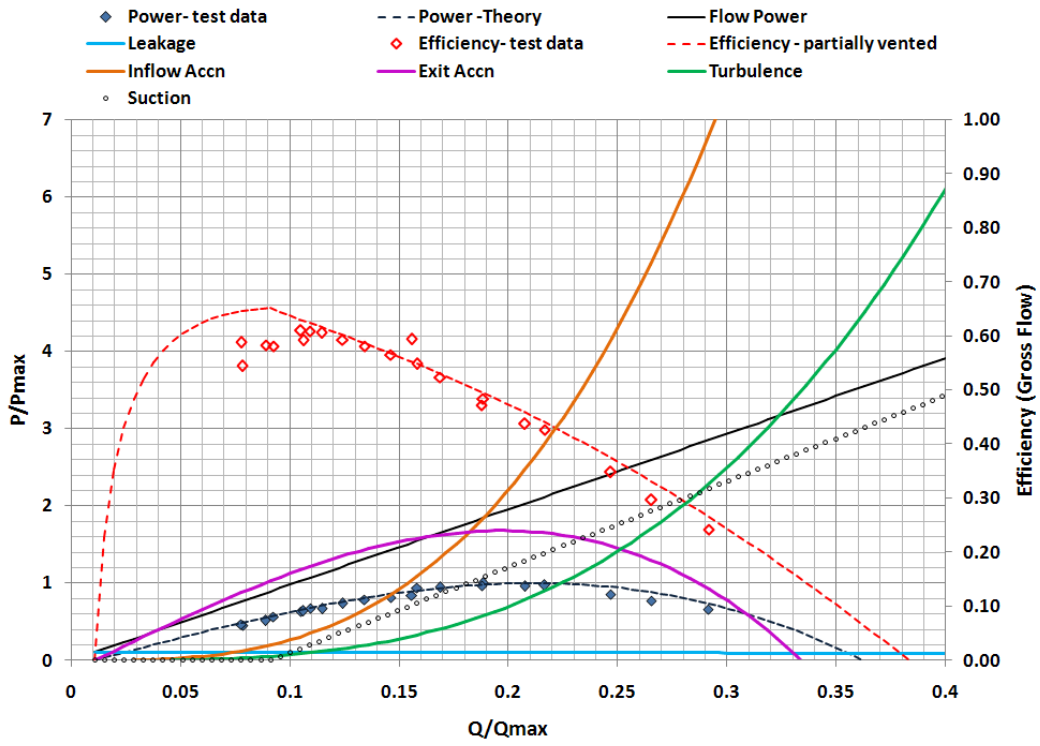

Figure 7.15: Theoretical Loss Components – 1/12A Geometry and Levels

Above peak power, inflow acceleration losses are dominant while turbulence losses continue to increase. While there is some scope to reduce turbulence losses with improvements in the basic HPM design, the scope to reduce acceleration losses with the current concept is limited and alternative approaches may need to be considered.

7.4.2 Costs

The cost of installation of this unit was high for the power output achieved although this was principally due to the cost and complexity of the power take off system required.

The Power take off design required by the HPM is challenging, the cost and complexity of which has been under-estimated by previous workers (Senior et al. 2009). This complexity arises from the following:

1. The variable speed of the machine required to accommodate changes in river flow rates demands that variable speed generators and control systems are used. These are considerably more complex and expensive than the fixed speed units more commonly found in micro hydro installations and upon which previous cost claims for the HPM were based (Senior et. al. 2008).
2. The very wide range of this variable speed, 1rpm for summer flows, 10 rpm for winter conditions, is difficult to accommodate electronically or mechanically in a single simple system.
3. The very low speeds of the rotor with very high torque outputs require a large gearbox and /or a variable low speed generator to be used, both of which carry significant energy loss and cost penalties.
4. The variability of torque occurring during each *cycle* of rotation, particularly at the lower operating speeds required to achieve high efficiencies, adds considerably to the sophistication of the transmission and control system required. Such cyclic variations put very high fatigue loads on power take off components and demand rapid control responses beyond the capacity of most low cost commercial products.

7.4.3 Environmental Impact

The wider environmental assessment of the HPM installation on river ecology in terms of hazard to aquatic life forms and sediment transport was beyond the scope of the current research and is not considered here. However, operation of the machine was found to have 'quality of life' impacts in the immediate vicinity of the mill through the generation of noise which represented a very real limitation on machine operation.

The contributing factors in noise generation were:

1. Impact forces and splash on blade entry to the upstream water. Splash was as significant as noise generation in curtailing operating speed since continual wetting of surrounding structures was unacceptable.
2. The 'suction' sound produced during cell emptying was an unexpected hydraulic effect.
3. Control system noise which was a product of both the high cyclic speed variations (possibly linked to 2 above) and the 'hunting' of the control system in response to changing operating conditions. Noise from this source could be heard at night over a radius of 400 meters or more.

It is anticipated that, once the causes of these effects are better understood, careful design of the machine and control system should enable these sources of noise to be minimized or eliminated from future designs.

7.4.4 Engineering driven areas for development

For the HPM concept to develop into a viable micro hydro power technology, the foregoing assessments suggest that efforts to improve the hydraulic performance of the device should be concentrated in the following areas:

1. Improvements to basic hydraulic efficiency.
   - Development of rotor and blade shapes must be carried out to significantly reduce blade drag and splash on the upstream side of rotation.
   - The suction effect must be eliminated through appropriate design, both to remove the noise irritation it produces and to improve performance. It is possible that eliminating this effect may also help reduce speed variations during rotation of the machine which is highly desirable.

2. Investigate alternative HPM concepts to reduce PTO cost and complexity.

   - The efficient operating speed of the HPM needs to be increased from the current 4-10 rpm to the region of 20 – 40 rpm, if realistic system costs are to be achieved. This implies rotor designs that exploit, to some degree, the kinetic energy of the flow in addition to the primary static

pressure energy exchange currently employed. It also implies design of installations to minimize losses at higher water velocities.

- The wide range of HPM speed variation needs to be addressed. The use of split rotors akin to Cross Flow Turbine practice is suggested. A rotor split into two sections sized to accept 1/3 & 2/3 of the design flow rate, with an appropriate inlet control, would reduce operating speed range to one third of the current levels. This, combined with a higher basic rotor speed, should permit the use of low cost variable speed transmission elements in conjunction with fixed speed generator and control systems.

7.5 Implications for the model test programme

Within the scope of the present work, it was not possible to investigate the full range of HPM developments recommended above. However, three distinct areas of work were identified for the model test programme. These were:

1. Scale Performance tests – the exact repetition of field trial tests at laboratory scale to investigate to what extent full scale behaviours are represented and to enable direct assessments of scale effects to be carried out.
2. Performance Improvement tests – to investigate how efficiency of the device can be improved based around modifications to the existing rotor and installation design
3. Detailed Rotor Energy exchange tests – designed to directly observe and measure interactions of the rotor with the fluid during rotation.

Chapter 8: Model Scaling, Test Apparatus & Experimental Methods

8.1 Model Scaling

8.1.1 Hydraulic Similarity

The relationship between the measured performance of model and full scale test units is governed by the laws of ***hydraulic similarity*** (Hamill, 2006).

In the ideal model we would seek to achieve:

- *Geometric Similarity* – with the model physically reproducing to scale the features of the full scale machine to a high degree of fidelity.
- *Dynamic Similarity* – with the model faithfully reproducing to scale the forces experienced within the prototype unit.
- *Kinematic Similarity* – with the model reproducing to scale the velocities and directions of flow experienced within the prototype under the test conditions investigated.

In practice, due to the complexity of hydraulic phenomena it is impossible to achieve similarity between model and prototype in all respects and some compromises need to be made. These compromises must result in some deviations in measured behaviour between model and prototype known as 'Scale Effects'. However, if the model tests are well designed these scale effects should be minimized.

In the present work, we are also interested in whether the simplifications in hydraulic behaviour assumed in HPM theory neglect phenomena which in themselves are effected by scale. If such factors are present, we would expect the accuracy of performance predictions to alter between prototype and model units significantly. If such factors are not present, theory should be comparable across the scales.

8.1.2 Geometric Similarity

In the review of Chapter 3, the importance of geometric similarity to hydrostatic machine performance comparisons was highlighted.

The linear scale between prototype and model is given by:

$$X = \frac{L_p}{L_m} \tag{8.1}$$

Where: X is the scale, L refers to length measurements and the subscripts 'p' and 'm' refer to the prototype and model respectively.

Due to the availability of test flumes, the maximum size of model that could be accommodated corresponded to a value of X equal to 6. However, surface roughness particularly in the flow channels was not scaled and no attempt was made to match the undulating bed of the prototype mill race.

8.1.3 Dynamic Similarity – matching Froude number

The HPM is an open-channel device where the presence of the free surface and the fundamental driving forces for the machine are governed by the relationship of inertial forces to gravity forces. In such circumstances *Froude Similarity* is most often applied (Heller, 2011). Froude Number 'F', is given by:

$$F = \sqrt{\left[\frac{inertial\ force}{gravity\ force}\right]} = \sqrt{\left(\frac{V}{gL}\right)} \tag{8.2}$$

where:

V is mean velocity, g is the acceleration due to gravity and L is a characteristic length.

The physics behind machine losses were largely unknown at the time of designing the test installation. If they were dominated by viscosity effects, Reynolds number (inertia force and viscous force) would become important. However, friction in turbulent flows is independent of Reynolds number and, since turbulent conditions were clearly present during normal operation, viscosity effects were likely to be small. The exception to this might be at very low operating speeds where turbulence is low. Scale effects are therefore likely to be most significant at the lowest machine flow rates – having a disproportionately greater effect at model scale compared with the prototype unit.

8.1.4 Velocity & Time scaling arising from Froude Similarity

Froude similarity between model and prototype imply the following ratio of velocities:

$$F_m = F_p \Rightarrow \frac{V_m}{\sqrt{gL_m}} = \frac{V_p}{\sqrt{gL_p}} \tag{8.3}$$

$$\frac{V_m}{V_p} = \sqrt{\frac{L_m}{L_p}} \Rightarrow V_m = V_p\sqrt{\frac{L_m}{L_p}} \tag{8.4}$$

For the scale ratio X= 6 used for these tests:

$$V_m = V_p\sqrt{\frac{1}{6}} = 0.408V_p \tag{8.5}$$

Thus a 1/6th scale model actually experiences real world velocities around 40% of the prototype unit. This resulted in the formation of critical inlet flow conditions in early model tests which choked the inlet flow. This was, not observed in the prototype unit and the distortion of inlet channel depth away from true scale was required in order to ensure correct functioning of the laboratory machine.

Since velocity has units of length 'L' divided by time 'T' equation 8.4 can be re-written as:

$$T_m = T_p\sqrt{\frac{L_m}{L_p}} \tag{8.6}$$

Since from equation 8.1: $X = \frac{L_p}{L_m} = 6$

$$T_m = T_p\sqrt{\frac{1}{6}} \tag{8.7}$$

Therefore in the current test programme, it is useful in comparing the rotational speed of model and prototype units to note that:

$$rpm_p = 2.45rpm_m \tag{8.8}$$

and, when reviewing video records to be aware that similar time scaling needs to be applied to the playback frame-rates employed.

8.2 The Test Flume

8.2.1 Lay-out and flow control

The leading dimensions for the flume originally constructed by Senior and used for all subsequent small scale model experiments is shown in Figure 8.1.

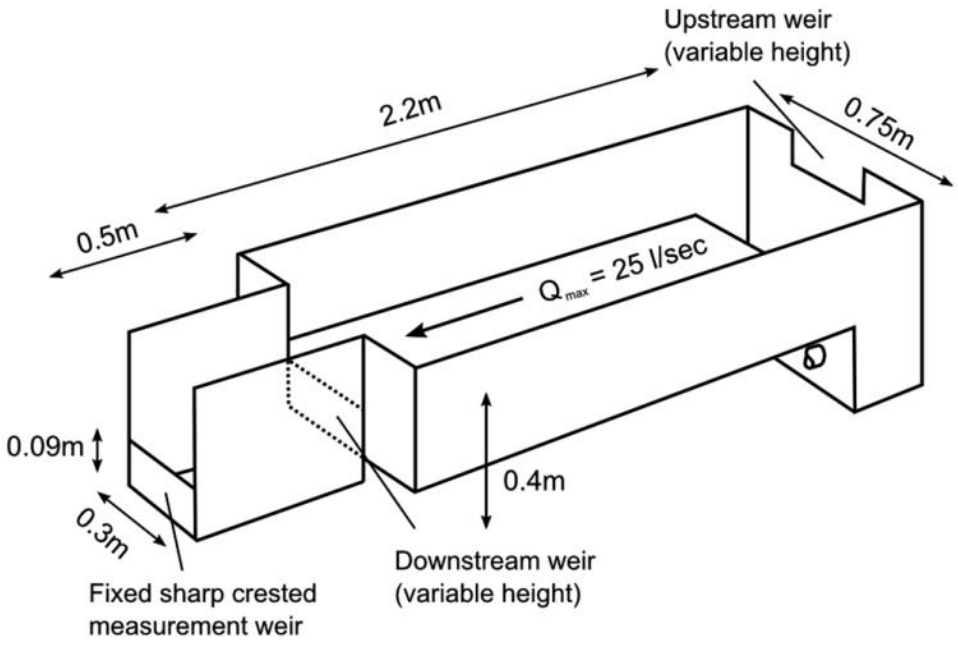

Figure 8.1: General dimensions of Test Flume*(Senior, 2009)*

For the present work several modifications were carried out to the basic flume, including the addition of a flow straightening honeycomb section at the inlet, and new universal mountings for the rotor supports. Gross flow control in the flume was achieved using a variable speed pump, with fine flow and level control achieved upstream using an adjustable weir. This spilled water into a by-pass channel which directed surplus flow away from the working section for direct return to the pump reservoir (shown schematically in Figure 8.2). Downstream water levels were maintained with an adjustable weir, upstream of the measurement channel.

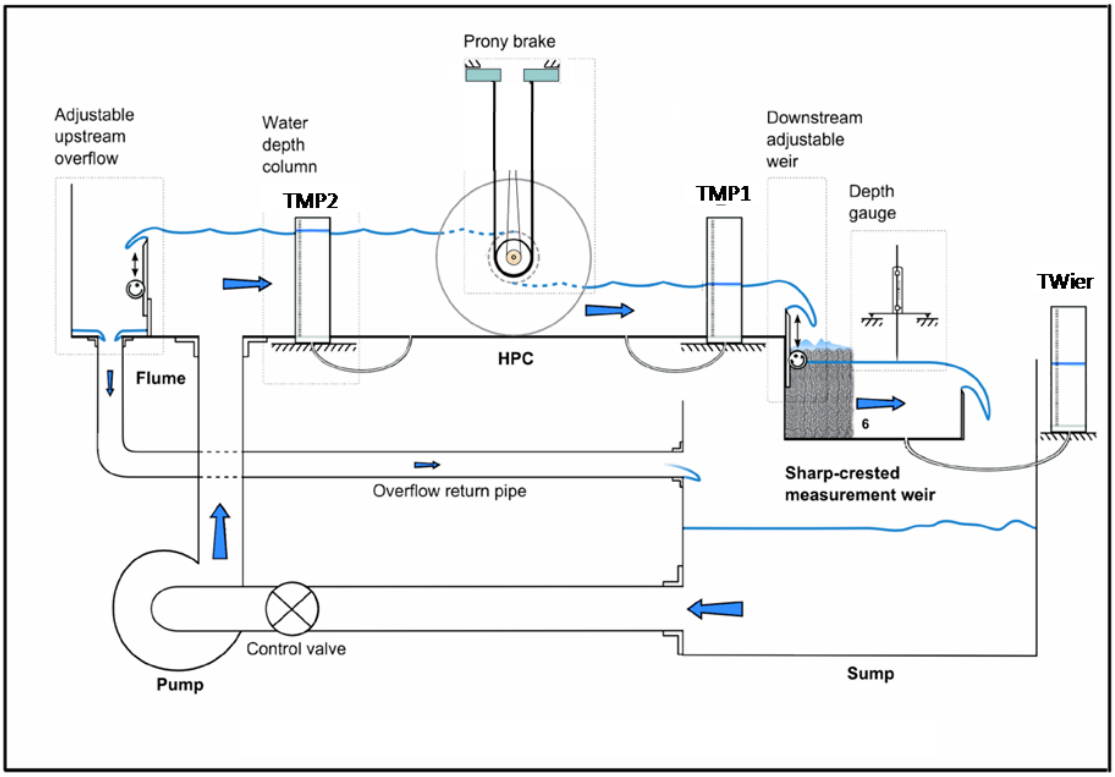

Figure 8.2: Schematic of model test flume flow controls and level measurements
(after Senior, 2009)

8.2.2 Water Level and Discharge Measurement

Water levels were measured using fixed scales attached to the walls of the flow channel. This replicated the positioning of field test unit measures and was supplemented with pressure taps along the centre-line of the channel floor at the same stations as the wall scales. These pressure taps fed into stilling tubes TMP1 & TMP2 where depths were read directly by steel rule.

In order to improve resolution at lower operating speeds, flow measurements were carried out using a triangular-notch thin-plate weir, set up in accordance to ISO 1438:2008. The leading dimensions of this flow measurement installation are defined in Figure 8.3 and summarized in table 8.1. Due to space limitations, the length of the discharge channel was insufficient to avoid the formation of surface waves at higher flow rates and 'wave mat' material was employed at the head of the measurement section to maintain as even a velocity distribution as possible across all test conditions.

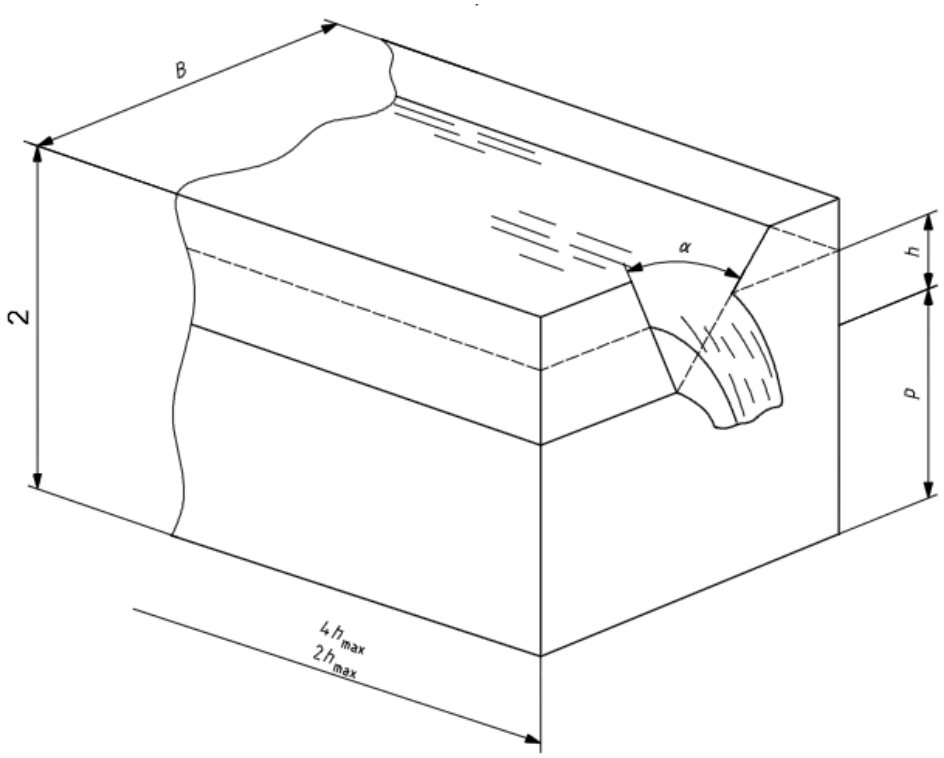

Key
1 upstream face of weir plate
2 head measurement section

Figure 8.3: Discharge Weir definitions *(ISO 1438:2008)*

Channel Width 'B' (m)	Weir crest height above floor 'p' (m)	Distance to upstream gauge station (m)	Notch angle 'α' (radians)	Measured head above crest 'h' (m)
0.3	0.0954	0.28	π/2	0.0067 – 0.151

Table 8.1: Discharge Weir leading dimensions

A series of floor pressure taps were combined and led into a stilling tube (TWier), where water surface elevations were measured using a vernier surface gauge.

Discharge was calculated using the Kindsvater-Shen formula:

$$Q = C_d \frac{8}{15} \tan\frac{\alpha}{2} \sqrt{2g}\, h_e^{\,5/12} \qquad (8.9)$$

where:

C_d is the coefficient of discharge read off from calibration curves contained in ISO 1438:2008 for each test condition which are reproduced in Figure 8.3.

h_e is the effective head calculated from:

$$h_e = h + k_h \qquad (8.10)$$

where:

h is the measured head above the weir crest

k_h is an experimental correction factor to compensate for surface tension and viscosity. For notch weirs where $\alpha=\pi/2$, k_h has been shown to have a constant value of 0.00085m over the range of conditions covered by Figure 8.4.

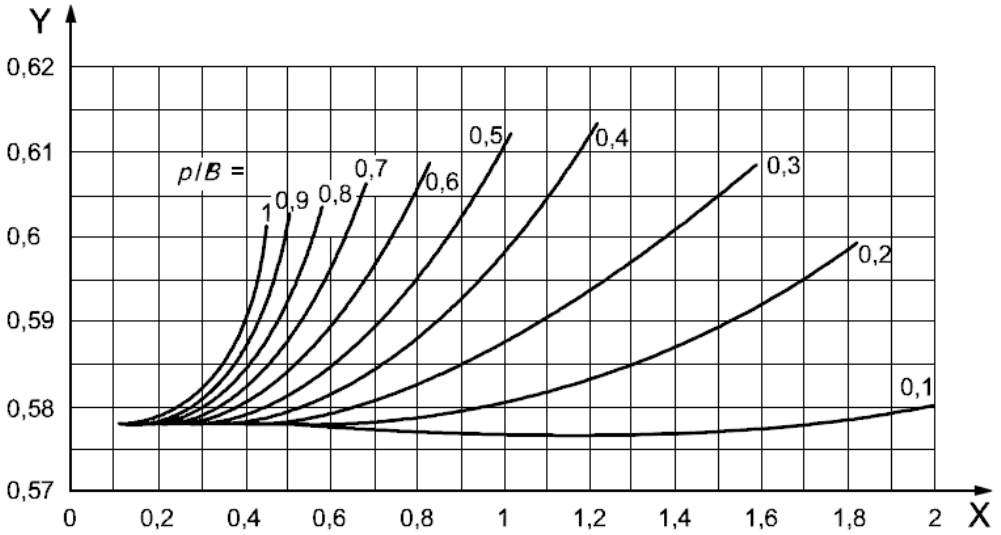

Key

X value of $\frac{h}{p}$

Y value of C_d

Figure 8.4: Coefficient of discharge, C_d (α=90°), *(ISO 1438:2008)*

8.3 Flume Installation

8.3.1 Installation Model

Inlet and water exit channels were formed from a combination of Perspex panels for the walls and polystyrene foam for the channel beds, which were initially accurately scaled from the prototype installation. However following early testing, the inlet channel floor was lowered substantially to avoid the inlet choking phenomena alluded to above (Figure 8.5).

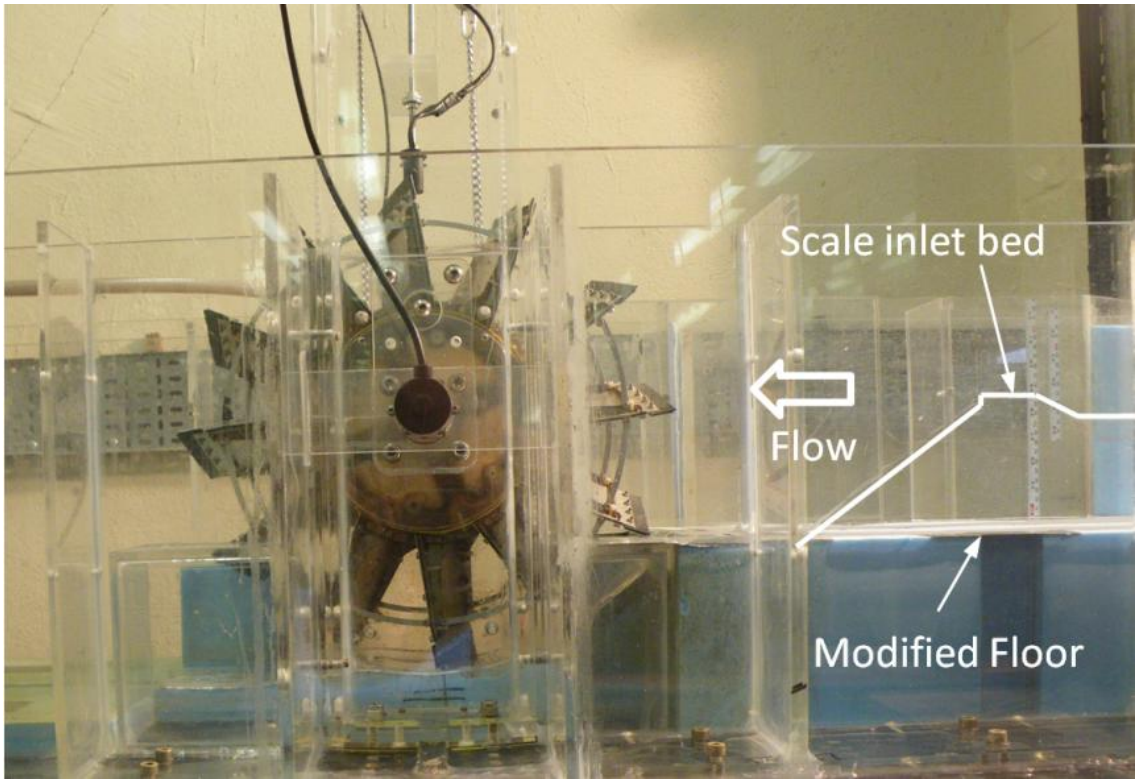

Figure 8.5: Non scale modification to inlet Channel floor

8.3.2 Machine Output Torque Measurement

To enable the variation of HPM output torque during rotation to be monitored, a Proney brake was set up using two load cells to react belt forces. Brake loads were applied using straining screws (Figure 8.6).

A leather belt was used to apply friction, acting directly onto a 100mm diameter plain pulley attached to the HPM shaft, running in air. To avoid low speed resonance problems, the length of the relatively flexible leather was kept to a minimum, with steel

chains used to connect the belt to the measurement load cells.

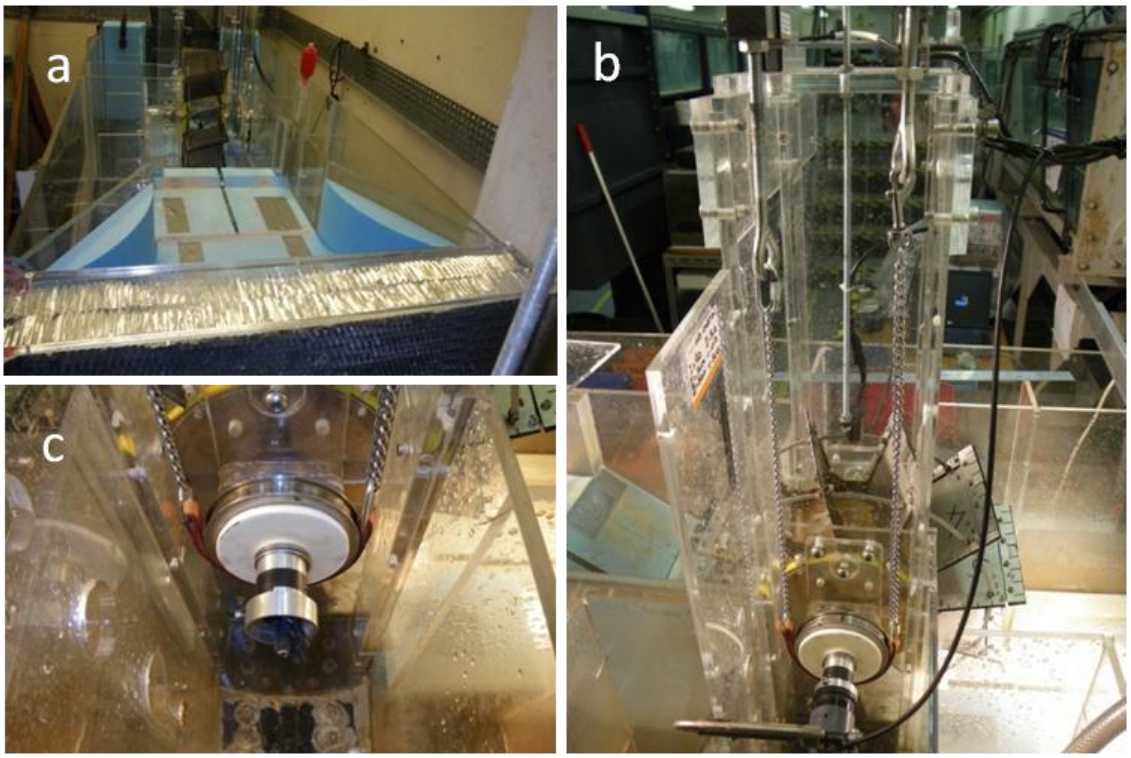

Figure 8.6: Model Test Flume Details: a. Flow straightener and inlet, b. Universal rotor mount and Proney brake, c. Friction belt

Early attempts to use a less stiff friction belt arrangement resulted in heavy resonance problems particularly at low rotor speeds, mimicking the PTO resonance conditions experienced on the prototype unit.

Output signals from the load cells were conditioned using a strain gauge amplifier and signal conditioning unit, before being read by a PC using a National Instruments USB-6210 DAQ unit, controlled using 'Labview' Software. All other time varying data collected from rotor mounted instruments were conditioned, read and controlled using this hardware and software combination. The data collection rate of the available DAQ unit was limited to a maximum sample rate of 64 Hz which was adequate for lower rotor speeds but proved marginal for higher flow rate conditions.

8.4 Rotor Installation

8.4.1 Rotor Construction

The 1/6 scale rotor is shown during construction in Figure 8.7 and consists of a water tight central hub, containing instrumentation, to which blade assemblies are connected. Components for this model were laser cut from the same CAD geometry files used for the field trial prototype to ensure accurate scaling.

Figure 8.7: Scale model rotor during assembly

8.4.2 Rotor Sensors

Two pieces of instrumentation were fitted inside the rotor itself, details of which are shown in Figure 8.8.

A pressure transducer was mounted through the casing of the hub, positioned to read

the pressures at the centre-line of the rotor in the middle of one cell (a).

One pair of blade ribs was modified to accommodate strain gauges bonded and sealed to protect from water damage. These blades were arranged in a single bridge circuit to enable the combined bending moment across the blade, to be measured (b). Signals from the Hub pressure and strain gauge transducer were fed along the centre of the hub shaft through a mercury slip ring to allow signals to be read with the minimum addition of electrical noise (c).

Rotor speed was measured using a Baumer BHK optical shaft encoder mounted externally to the Rotor output shaft, having a resolution of 1200 pulses per revolution. A Honeywell Gear tooth, Hall-effect sensor model 1GT101D was mounted to the support structure working in combination with a magnet fixed to a blade assembly to give a reference signal corresponding to the top dead centre of rotation of the HPM (Figure 8.9). This acted as a synchronisation signal from which phase angles of all other signals could be calculated.

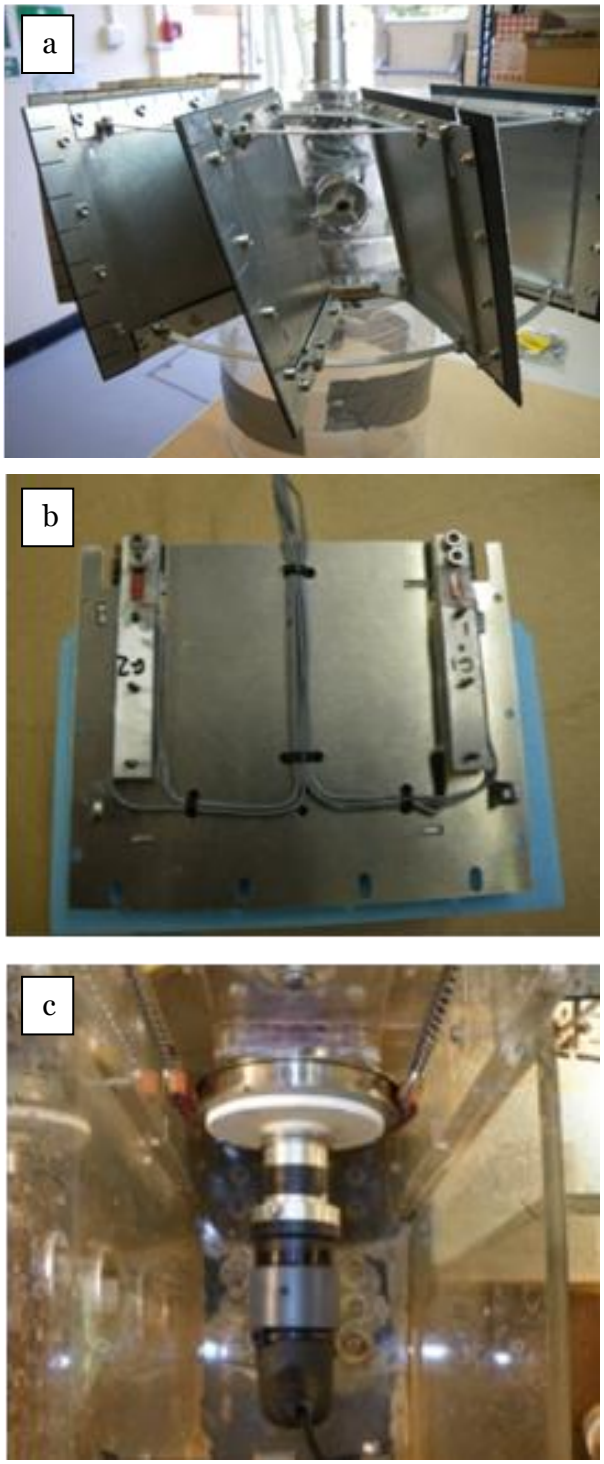

Figure 8.8: Detail of Rotor Mounted Sensors: a. Hub Pressure transducer, b. strain gauge installation, c. Mercury slip ring attached to output shaft

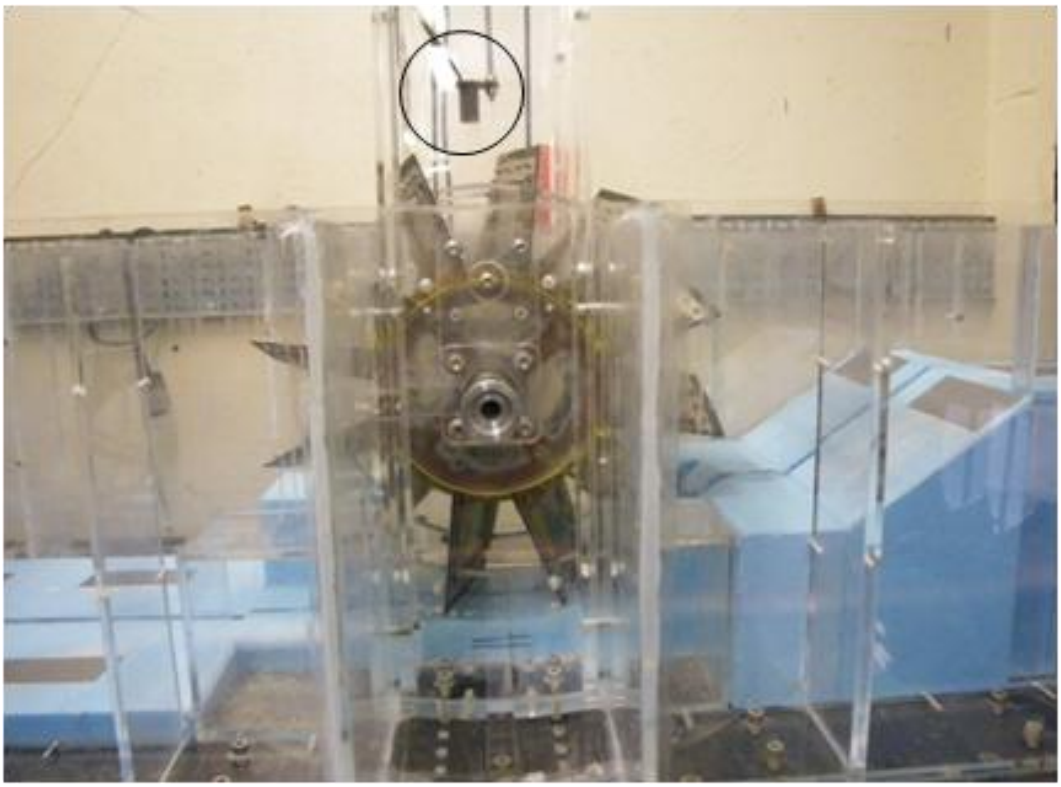

Figure 8.9: Side view of wheel installation. The Hall-effect sensor is circled.

8.5 Calibration Methods

8.5.1 Water Level Readings

With the flume sealed at each end, water was added to achieve a constant reference level either side of the rotor, from which relative readings and height above reference zero for the model could be directly measured. A similar technique was used to set the reference height of the stilling tube to the weir crest height used for flow measurements.

Prior to each test series, pressure tap lines were purged of air. This was achieved by filling stilling tubes to above the level of the flume side walls and leaving the apparatus to reach a steady level after driving entrapped air out of the system.

8.5.2 Hub Pressure Sensor

Following on from the water level calibrations described above, the sealed flume was again used for hub pressure transducer calibration. With flume water levels held at a

steady level, the wheel was rotated incrementally and instrument voltages recorded for each setting. The depth of the transducer tap point below water was calculated and plotted against voltage readings to obtain the transducer calibration (Figure 8.10). This process was repeated periodically and the calibration factors for this transducer found to be very stable giving high confidence in the results produced. However, the instrumentation system did suffer from some zero drift during the course of several hours testing. This was eliminated from the final results during the post processing of raw data by correcting the zero offset to bring the instrument gauge pressure reading to zero at top dead centre of rotation for each test series.

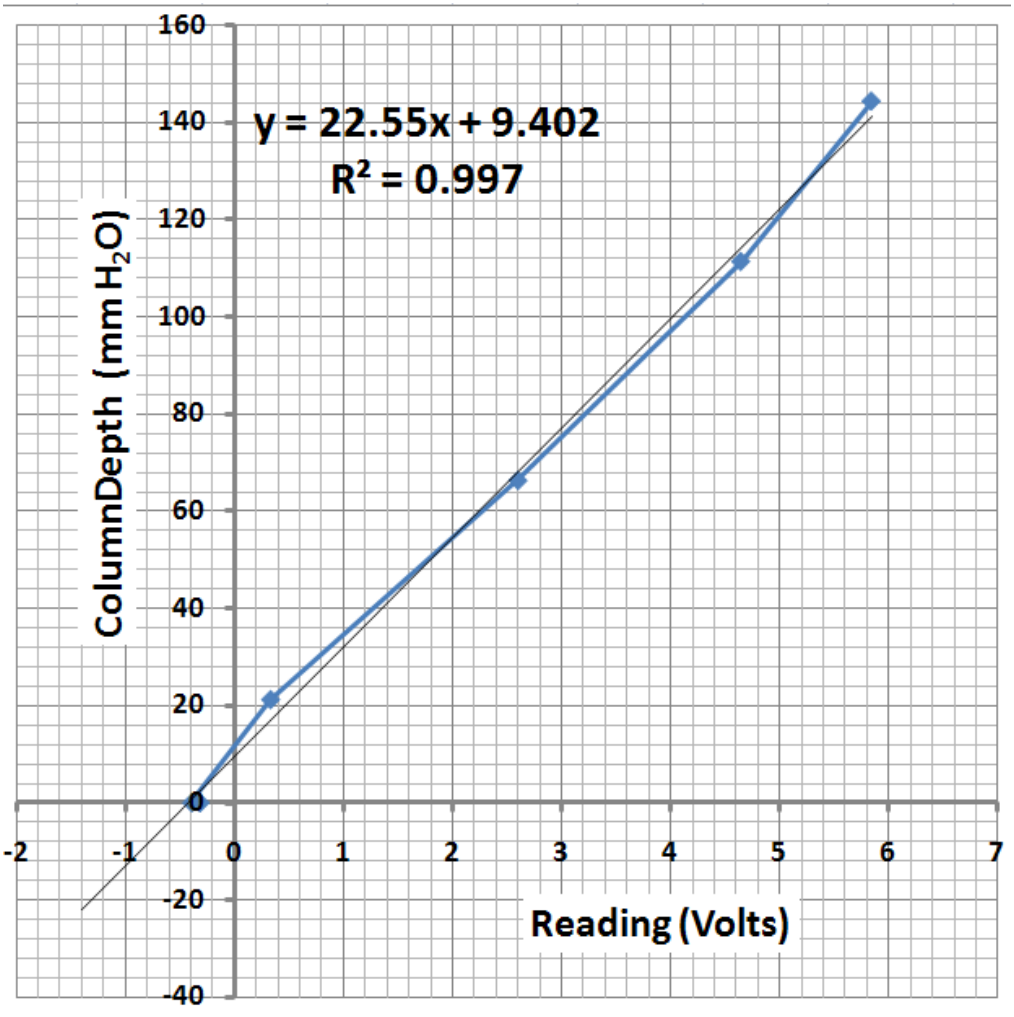

Figure 8.10: Typical Hub Pressure Sensor Calibration Curve

8.5.3 Strain Gauged Blade

The strain gauge readings showed considerable variation in calibration factors over time and a full calibration was carried out at the start of each test session. The rotor was first locked with the strain gauged blade horizontal (Figure 8.11 top). Masses were then progressively applied at a fixed position on the blade and calculated bending moments about the centre of the strain gauge positions compared with voltage outputs read by the DAQ unit. These values were recorded for both load addition and removal, and plotted to enable gauge factor and zero offsets to be extracted. As with the hub pressure transducer, zero drift in the readings was corrected for during post processing by assuming bending moments were zero with the blade at top dead centre. This also corrected for the mass of the blade unit itself.

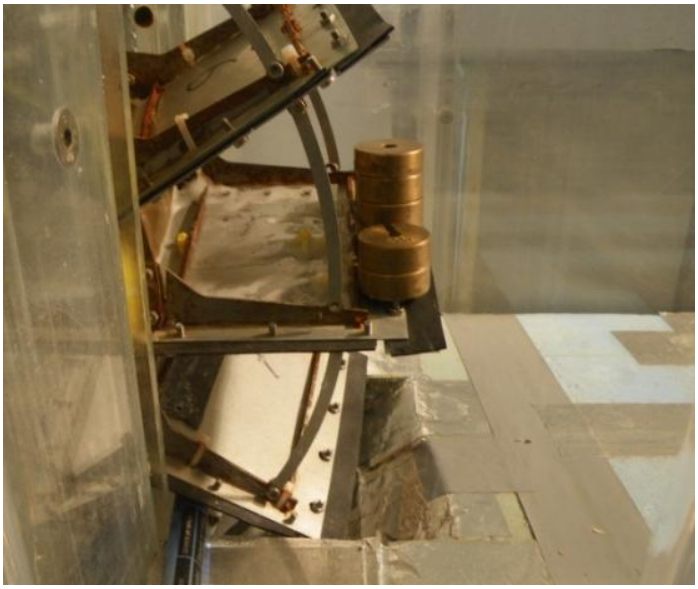

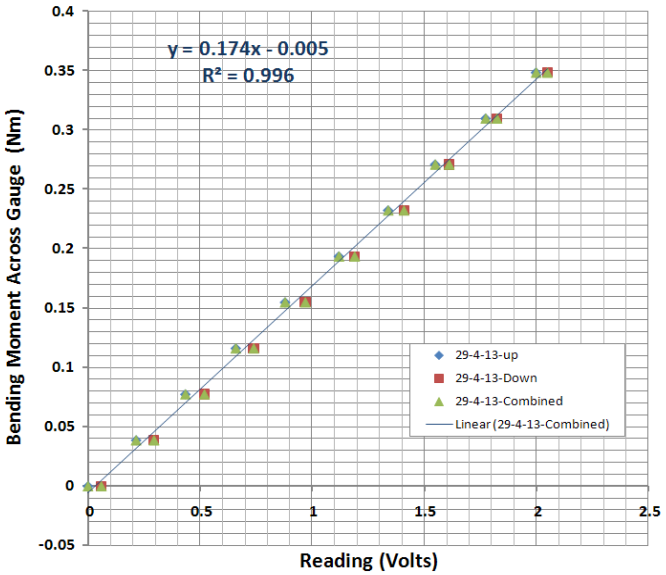

Figure 8.11: Strain Gauged Blade Calibration method & typical curve

8.5.4 Load Cells

Loads cells were calibrated at the start of each day's testing. With the friction belt completely slack, fixed masses were applied at the loading point of the load cell, and output voltages read through the DAQ unit. These were recorded as load was applied

and removed. The results were plotted to allow calibration factors to be calculated. The signals from these transducers proved to be very stable, with little drift in zero reading and no change in gauge factor over the test period.

8.6 Experimental Methods

8.6.1 Performance Testing

Performance testing of the rotor followed a similar methodology for all experiments reported in this work and a view of the test rig during a typical test, is shown in Figure 8.12, viewed from upstream of the rotor.

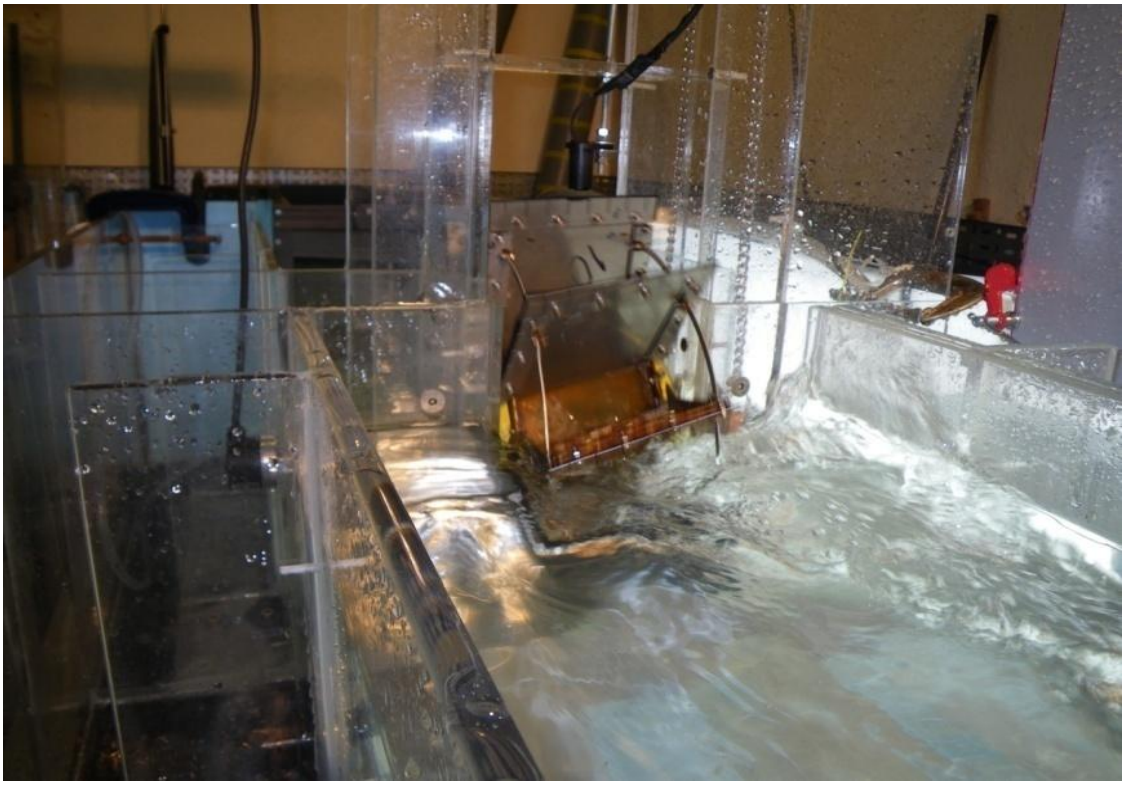

Figure 8.12: The Flume during a typical Performance Test

All test series adopted the following routine:

Test sessions began with the calibration of sensors described above, followed by the purging of air from pressure tap lines. After purging, care was taken to ensure

minimum water levels were maintained over the pressure tap points to prevent the re-entry of air.

In setting up performance test series, it was found easiest to start with the highest rotor speed condition first, collect measurements, and then progressively add load to the Proney brake to establish the next slower test point. In this way, test data was built up efficiently to cover the whole performance speed range for the model.

Load was applied to the Proney brake by adjusting straining screws on the load cells, until the approximate test speed was achieved. Pump flow rate and inlet and exit weir positions were adjusted to produce the desired water levels. These were adjusted progressively alongside brake load until the target rotor speed and water levels achieved. Care had to be taken in setting up test conditions since the adjustment of each control frequently resulted in the need to re-adjust others and, following each change in conditions, flume flow took several minutes to reach a steady state.

Great care had to be taken to ensure the water levels in both the flume and the stilling tubes attained steady state before readings were taken. Depending on condition, this could be as long as 30 minutes. Once steady state had been achieved, DAQ unit measurements were recorded while stilling tube levels were read and recorded manually. A video survey of the test condition was then carried out, with a slow motion camera mounted at a fixed position perpendicular to the working section of the rotor to ensure video data could be readily compared between test conditions. Any unusual behaviour of the model was also noted.

8.6.2 Modifications for alternate model Test Series

The above apparatus and test methods were adopted for both Scale performance testing and detailed rotor energy exchange experiments.

For performance improvement testing experimental techniques remained unchanged although alterations were carried out in the construction of the rotors themselves. For clarity, these modifications will be described at the start of the relevant sections reporting the results of these trials.

8.6.3 Estimation of Leakage

Following the practice established during prototype testing, leakage flows were estimated by extrapolating plots of rotor speed vs. measure flow to give the discharge when the rotor was stationary. This was found to be more consistent than attempting to measure leakage rates with the rotor held stationary, since measurement errors were high with such low flow volumes and water levels across the weir were better maintained within the range of values for which the ISO discharge coefficients were valid.

8.6.4 Estimation of Rotor Friction

Rotor friction losses in the model were estimated using the same method adopted for the prototype unit. With the Proney brake belt completely slack, a force meter was attached to the periphery of the rotor via a cable. The horizontal force required to establish slow, steady rotation was measured and recorded (Figure 8.13). This exercise was repeated several times to enable a consistent average to be obtained and rotors were wetted prior to each test to keep blade friction levels realistic.

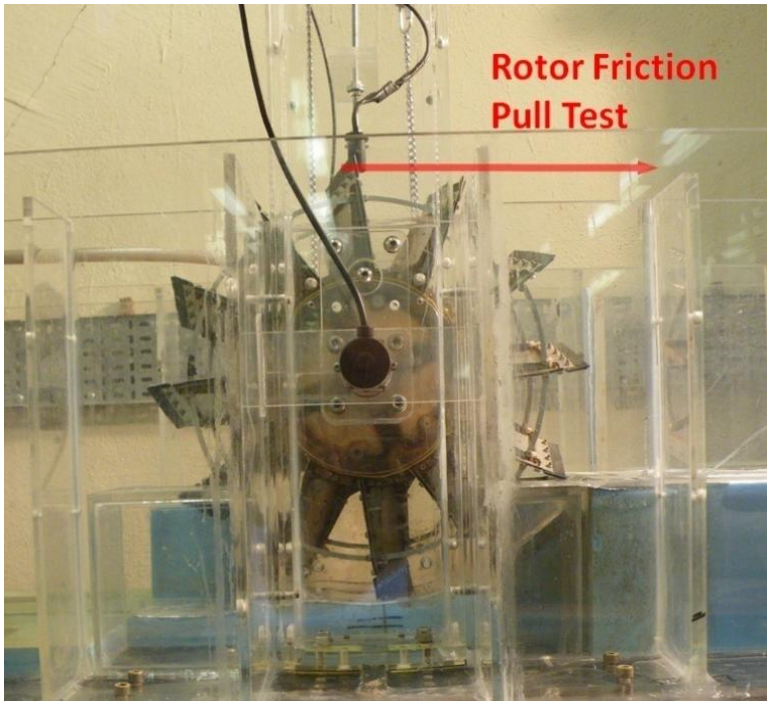

Figure 8.13: Estimation of Model Rotor Friction

These tests effectively measured the friction due to the slip ring, shaft seals and bearings and were repeated at the start of each model test series.

Chapter 9: Performance Test Results & Analysis

Introduction & Navigation

A wide number of test conditions and detail experiments on scale model HPM machines have been carried out which are presented in the next two chapters.

The results of performance tests are presented in this chapter while 'time series' data and video observations are used in chapter 10 to study the detailed interaction between the rotor and the fluid passing through it during operation.

Since a large number of experiments are described here, this chapter is divided into 3 main sections to make this information more manageable.

Section 1 summarises the test conditions used, details correction methods required to flow and torque measurements, and then presents parametric measures used to better compare model and prototype performance.

Section2 presents the scale reproduction of prototype field tests to identify the presence of potential scale effects. The effectiveness of theory applied at the two scales is also investigated.

Section 3 presents tests investigating the effect of modifications to the model designed to improve performance. In the process, useful deductions regarding energy loss mechanisms are made.

9.1 Section 1: Test Conditions & Measures

9.1.1 Summary of Test Conditions

The water levels used throughout this test programme are summarized in Table 9.1, which, for convenience, presents both prototype and model water surface elevations. For detail performance comparisons, both the 9/11 and 1/12 test conditions were used following the practice established in Chapter 7. For rotor modification and rotor-fluid interaction experiments, the 1/12 test condition only was studied since it represents the most comprehensive source of prototype data.

Table 9.1: Summary of Model Test Conditions

Test Reference	Description	Upstream Surface Elevation (m above 'Z' datum)		Downstream Surface Elevation (m above 'Z' datum)		Nominal Head across rotor (m)	
		Prototype	Model	Prototype	Model	Prototype	Model
9/11	September 2011 test: Low river flows, weir raises downstream water levels	1.605	0.268	0.414	0.069	1.191	0.199
9/11 Reduced Head	September 2011 Test: Reduced Upstream water levels. Weir raised downstream water levels.	1.472	0.245	0.461	0.077	1.011	0.168
1/12A	January 2012 tests: high water levels & no downstream weir fitted.	1.656	0.276	0.374	0.062	1.282	0.214
1/12 Reduced Head	January 2012 Tests with reduced upstream levels	1.553	0.259	0.348	0.058	1.205	0.201
2/12	February 2013 Inverter tests with low downstream water levels	1.605	0.268	0.248	0.041	1.357	0.227

During the 'Deep Water' tests to be described in Section 2, several downstream water levels were applied while upstream water elevations were maintained at the 1/12 test level. These test conditions are summarized in Table 9.2 alongside the 1/12 test condition for comparison.

Test Reference	Blade – Depth ratio (bl/d2)	Upstream Surface Elevation (m)	Downstream Surface Elevation (m)	Nominal Head across rotor (m)
1/12A	0.53	0.276	0.062	0.214
DS-105	0.90	0.276	0.105	0.171
DS-125	1.07	0.276	0.125	0.151

Table 9.2: Summary of 'Deep Water' Test Conditions

9.1.2 Model & Flume Behaviour

In line with the observations of Heller (2011), we need to be alert to the possibility of potential sources of error that may be present when comparing results between scale models and full size prototypes. The 'model effects' relating to the distortion of the inflow depth have already been described in chapter 8 and will not be repeated here.

'Measurement effects' caused by differences between prototype and model measurement techniques may have been introduced in these experiments. In general, far more measurements were attempted in the model tests than were possible with the prototype. However, because of this, several refinements to model data were applied that were unavailable when prototype measurements were collected.

9.1.2.1 Leakage Flows

Following normal practice, leakage flow rates were estimated from both flow measurements carried out on stationary rotors, and by extrapolation of speed-flow rate curves. Stopped rotor tests in the past have been carried out for differing upstream water levels. However, during the present work, experiments were also conducted with variations in downstream water conditions, with upstream water levels being maintained at a constant level. As can be seen from Figure 9.1, downstream water level had an appreciable effect on leakage flow – an effect entirely consistent with modeling

leakage as flow through a submerged orifice (Senior, 2009), but not one previously allowed for in prototype measurements.

This will have most impact on machine operation at slow speeds and in the calculation and comparison of peak efficiencies. For model tests reported in this chapter leakage flows were estimated exclusively by extrapolating the speed/flow-rate curve for each operating condition and, therefore this variation in leakage flow is accounted for.

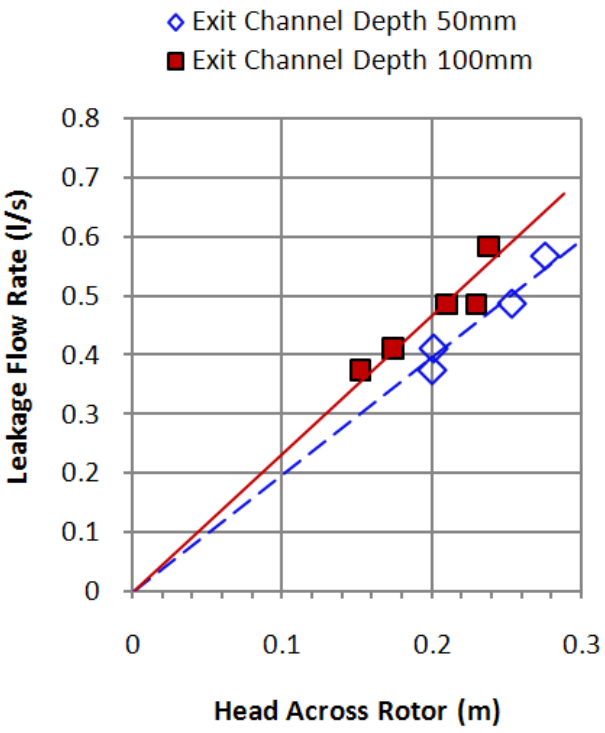

Figure 9.1: Variations in Leakage Flow due to Downstream water levels

The effect is somewhat mitigated by comparing true hydraulic efficiency based on net flow rates between model and prototype data sets, although since net flows must themselves be calculated using leakage estimates, some error may remain.

9.1.2.2 Flow Rate Corrections

In early performance tests, insufficient time was allowed for water levels in the weir-measurement tube to settle before readings were taken. This affected a series of scale performance tests before a better experimental technique was applied. This can be seen by comparing the speed/flow-rate curves for later experiments (Figure 9.2), with those obtained from early tests (Figure 9.3).

In Figure 9.2, the variation of flow rate with wheel speed is very linear over a good portion of the operating range, and deviation only occurs at higher speeds as turbulence and air entrapment reduces the fill ratio achieved by individual cells.

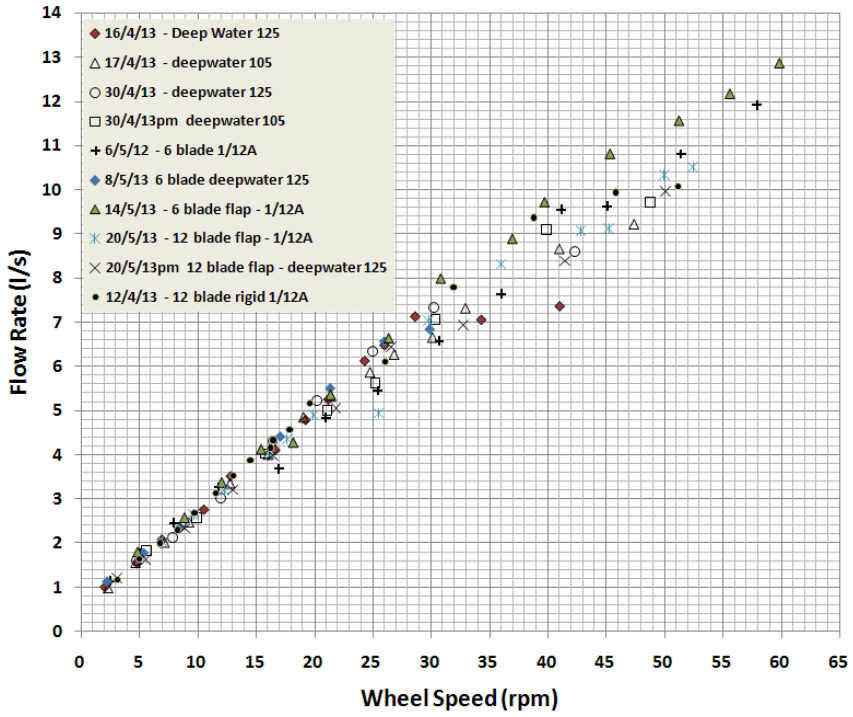

Figure 9.2: Speed-Flow Curves for Later Tests

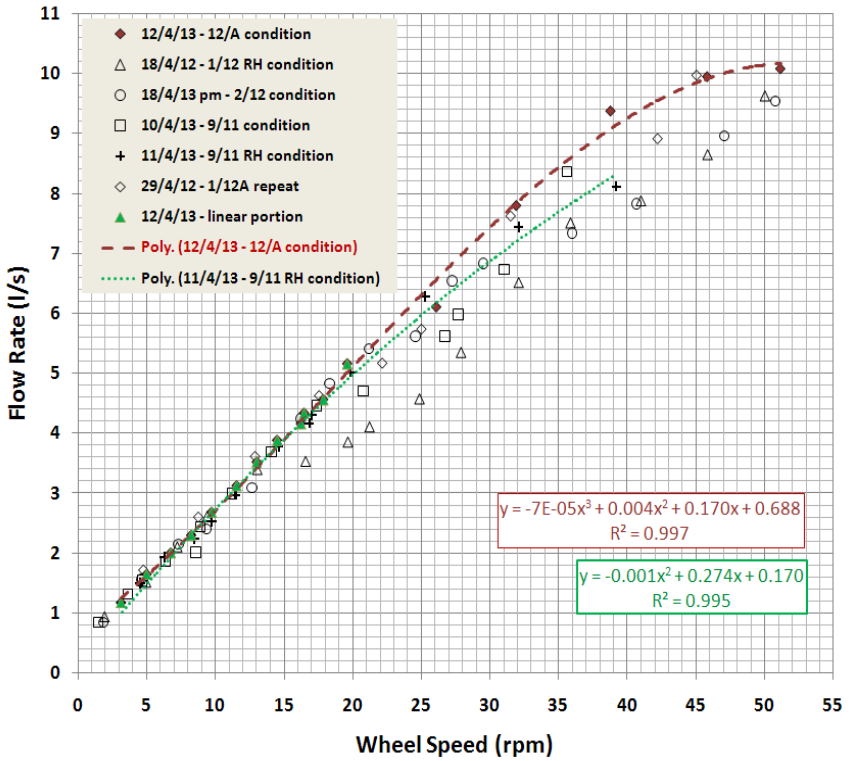

Figure 9.3: Speed-Flow Curves Errors in Early Tests

However, in the 9/11 and 1/12 Reduced Head data sets in Figure 9.3, there is a clear deviation from this expected behaviour, consistent with the poor measurement technique used. Since time limitations precluded the repetition of these tests, corrections were applied to individual data points to restore a linear flow rate variation consistent with later experiments. The resulting flow rates used in subsequent performance calculations are shown in Figure 9.4. While this manipulation of measured readings is not ideal, the overall impact on accuracy should be small, although the potential for distortion of results to the 9/11 data set in particular needs to be noted.

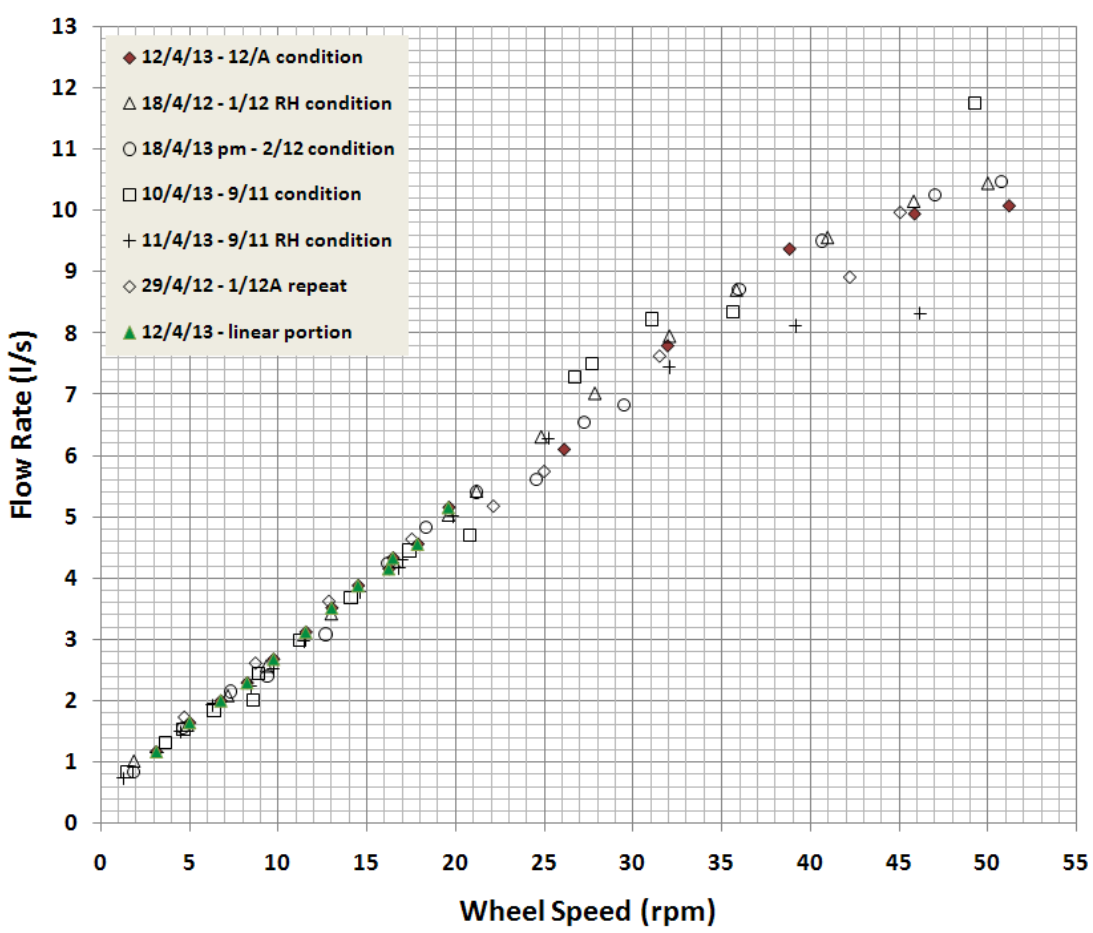

Figure 9.4: Speed-Flow Curves with Corrections

9.1.2.3 'Rubbing Torque' Corrections

The only method available for estimating mechanical friction losses in the prototype unit was by low speed pull tests as described in chapter 5. This technique was also employed for the model tests, but, since time series data for load cell forces and shaft angles were available from the rotor instrumentation, an additional correction for 'rubbing torque' could be applied.

A typical plot of the variation occurring in the output rotor torque during one revolution of the machine is presented in the annotated graphic of Figure 9.5.

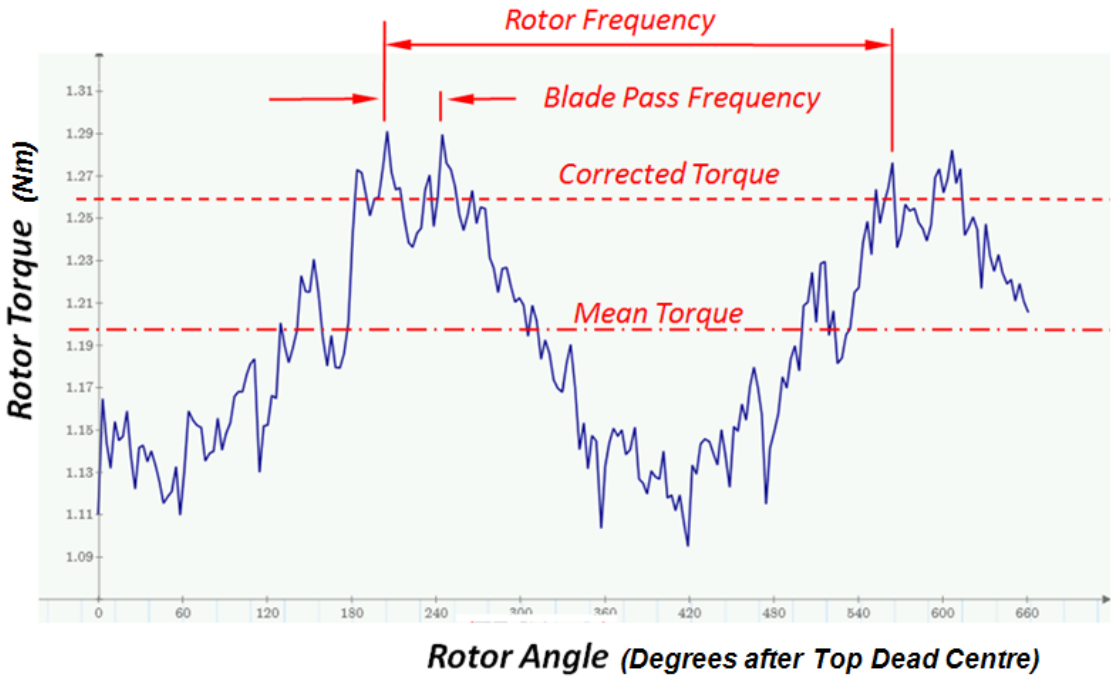

Figure 9.5: Variation in Output Torque During Rotation - 'Rubbing Torque' Correction

The characteristic torque variation due to individual blades passing through the machine can be seen at a pitch angle of 30 degrees, corresponding to the angle between cells in a 12 blade rotor. This will be described in more detail in later sections of this chapter, but of interest here is the clear, underlying sinusoidal variation in torque that is produced over one revolution. Since this variation is so regular, it can only be due to variations in the mechanical losses of the rotor itself and not through more random hydraulic effects.

There are several possible causes, including out of balance forces in the rotor or small eccentricities in the Proney brake pulley. However, it is more likely that changes in friction caused by seals making contact with part of the fixed structure during rotation are being measured here.

Since friction can only contribute a loss of torque and never a gain, the assumption that the true torque value is measured at the peak of the sine wave variation enables a correction to be made to the mean torque values produced by the processing software. This is done graphically by examining the torque variation at each test point and manually estimating the correction offset required. Although this is laborious, in practice offset values are remarkably consistent for a given data set, and offsets can be averaged to minimize estimation errors.

Torque measurements obtained from rotor pull tests are still applied since these account for friction losses in the slip ring, bearings and shaft seals which occur before the output torque is measured. While there is some risk that an element of blade seal friction may also be included in pull test data, the overall error is thought to be small.

While offering an essential improvement to model test accuracy, no equivalent data is available to apply similar corrections to the prototype measurements even though similar torque variations were certainly present in the field trial unit. Model corrections typically add 2 – 4% to mean torque measurements and we may therefore expect some discrepancy to be apparent in model and prototype performance comparisons.

9.1.2.4 General Observed Behaviour

The general behaviour of flows around the model during performance testing appeared to replicate qualitative observations for the prototype unit very closely giving good confidence that kinematic similarity had been achieved. Blade impact, cell filling, exit flow and even ventilation noise were all found to be replicated by the model and will be described in detail in Section 4 of this chapter.

9.1.3 Parametric Performance Comparisons

So far in this thesis, parametric comparisons between data sets have been carried out using P/Pmax and Q/Qmax in combination with both gross-flow and net-flow efficiencies. These are convenient parameters which fit well with HPM theory and will continue to be used in this chapter.

However, theory shows that machine efficiency will change for a rotor operating at differing heads. This implies that these parametric measures can only be used to compare equivalent operating conditions, resulting in different power and efficiency curves for each combination of water levels encountered.

The ideal parameters for comparison of data would enable all operating conditions for rotors of similar geometry to be considered on a single set of curves and, for this, we will consider the parameters employed in general hydraulic machine design.

Dimensional analysis for generic hydraulic machines acting on a fluid between different water levels, yields the following non-dimensional groupings after the application of the Buckingham '$\boldsymbol{\Pi}$' theorem. This is standard working presented in may texts and will not be replicated here, but the non-dimensional groupings are:

the *flow or discharge coefficient*:

$$\Pi_1 = \frac{Q}{nD^3} \tag{9.1}$$

the *head coefficient*:

$$\Pi_2 = \frac{gH}{n^2D^2} \tag{9.2}$$

and the *power coefficient*:

$$\Pi_3 = \frac{P}{\rho n^3 D^5} \tag{9.3}$$

where: Q is the volume flow rate (m³/s), n is the number of revolutions per second made by the machine (1/s), g is the acceleration due to gravity, H is the head absorbed by the machine (m), P is the Power output of the device (W), D is the outside diameter of the machine and ρ is the density of the fluid (Kg/m³).

It is also useful to note that these coefficients can be used directly to obtain *efficiency (η)* for the machine, since:

$$\frac{\Pi_3}{\Pi_1 \Pi_2} = \frac{P}{\rho Q g H} = \eta \qquad (9\text{-}4)$$

For geometrically similar machines operating under equivalent hydraulic conditions, these parameters should be independent of unit size and scale. Deviations in operating conditions will cause scattering of results, while the presence of scale effects should result in a divergence between the trend of the plots, obtained from the two machine sizes – a useful aid in the identification of scale effects carried out in Section 2.

9.2 Section 2: Scale Performance Tests

9.2.1 Performance Comparison of all Test Conditions

Performance measurements obtained from all scale tests are compared directly with the corresponding prototype results in Figure 9.6 using P/Pmax and Q/Qmax parameters.

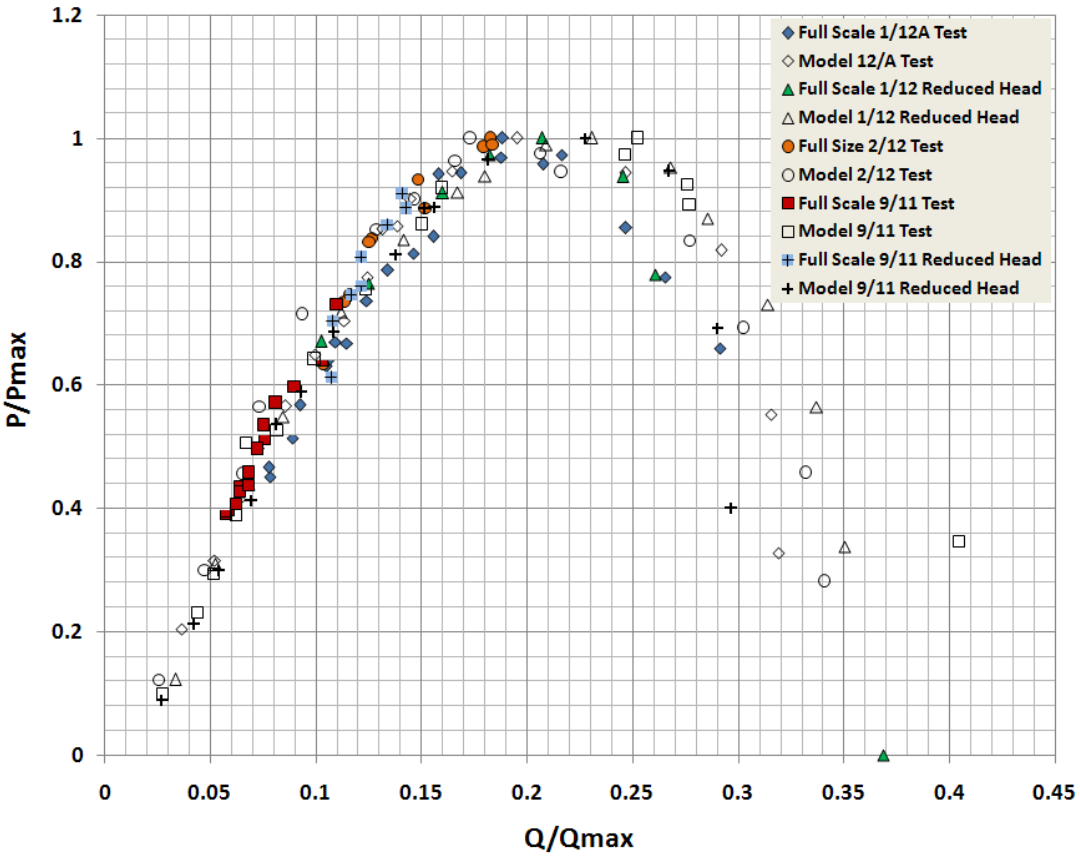

Figure 9.6: Parametric Power Comparison between Prototype and Scale Model Tests

Correlation between results for the two machine scales appears to be generally good up to 0.2 Qmax which corresponds to peak power output. However, above this level only 2 prototype data sets are available which show that the model outperforms the prototype machine significantly. However, comparison of Gross Flow Efficiencies (Figure 9.7), appears to show good agreement with the model for the 1/12A data set for the whole range of available prototype data, up to 0.29 Qmax. While the model apparently out-performs the prototype for most test conditions above 0.2 Qmax, correlation of model

and prototype data for the 1/12A data set remains consistent. Of note in the figure is the apparent anomaly between model and prototype results for the 9/11 Reduced Head test condition.

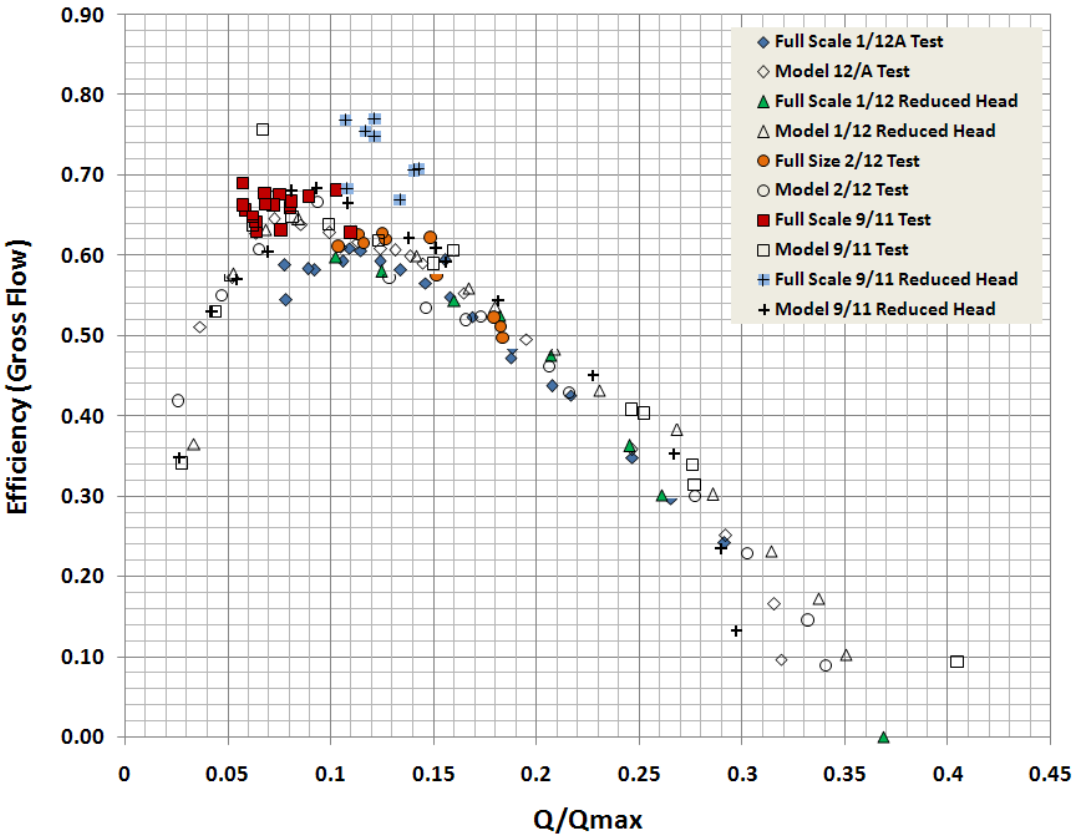

Figure 9.7: Gross Flow Efficiency Comparison between Prototype and Model Test

The explanation for this is contained in Figure 9.8 where Net Flow Efficiencies for all data sets are presented. Once efficiencies are corrected for leakage flow rates, model tests once again out-perform their prototype counterparts by about 3%. This may partly be accounted for by the more refined measurement techniques used in the model tests described in Section 1.

However, theory indicates that net flow efficiencies for HPMs should increase as flow rates fall as portrayed by the model test points in the figure. The residual down turn in data for the 2/12 and 1/12A prototype results may indicate that leakage flows have been

underestimated in these test conditions and not be fully accounted for in the net flow correction.

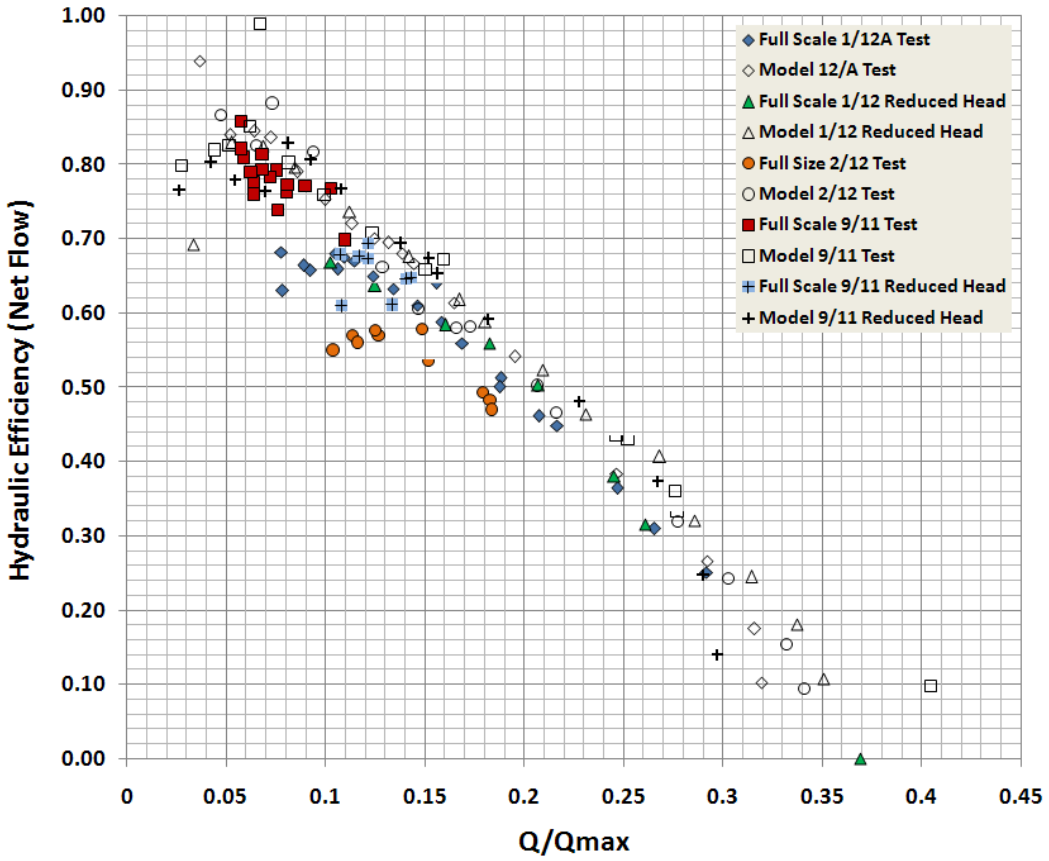

Figure 9.8: Net Flow Efficiency Comparisons between Prototype and Model Tests

We have to be careful not to read too much into these data comparisons – a 3% discrepancy puts readings well within the practical margin of error for these experimental measurements and overall agreement between test scales appears to be very good, although with the proviso of some significant deviation at higher flows.

9.2.2 Hydraulic Parameter Comparisons

To try and clarify whether scale effects are present, all model and prototype test data were compared using generic hydraulic machine coefficients. It is useful to note that values for all of these coefficients decrease with increasing rotor speeds for these machines.

Power and Head Coefficients are plotted against each other in Figure 9.9. Graph 'a' shows the full range of operating conditions covered by tests, while graph 'b' focuses on the higher speed ranges at which most data points are clustered.

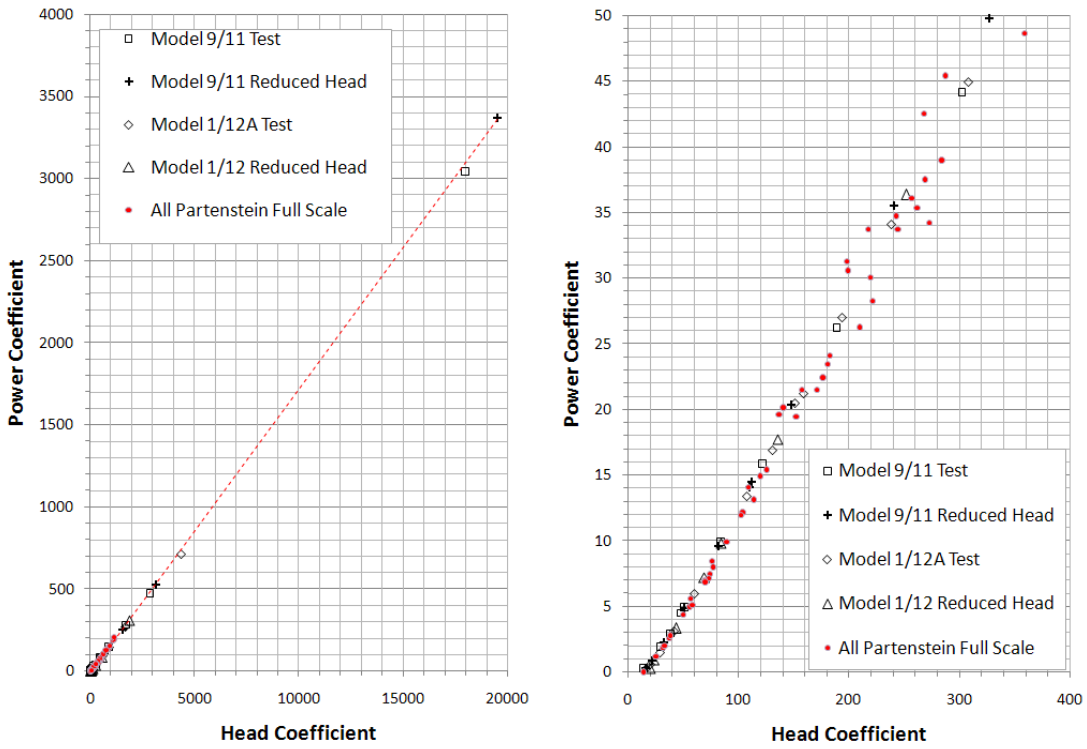

a. b.

Figure 9.9: Comparison of Power and Head coefficients: a. Full range of tests, b. clustered data range

While some scatter is evident in Prototype readings corresponding to low rotor speeds, data is well clustered around a linear trend with no discernable deviation in gradient or offset between model and full scale. Power and Head coefficients are considered therefore to show very good agreement across the scales.

The situation is less clear when the flow coefficient is introduced to the comparisons as shown in Figure 9.10. Since prototype flow rates were all estimated from a single speed-flow curve (as reported in chapter 6) these points show a high level of congruence, clustered along a clearly defined curve. Model test data show a much higher level of scatter reflecting the greater variability and inherent difficulty in obtaining accurate flow rate measurements at lab scale. However, this scattering appears to be along the

same curve as the full scale results.

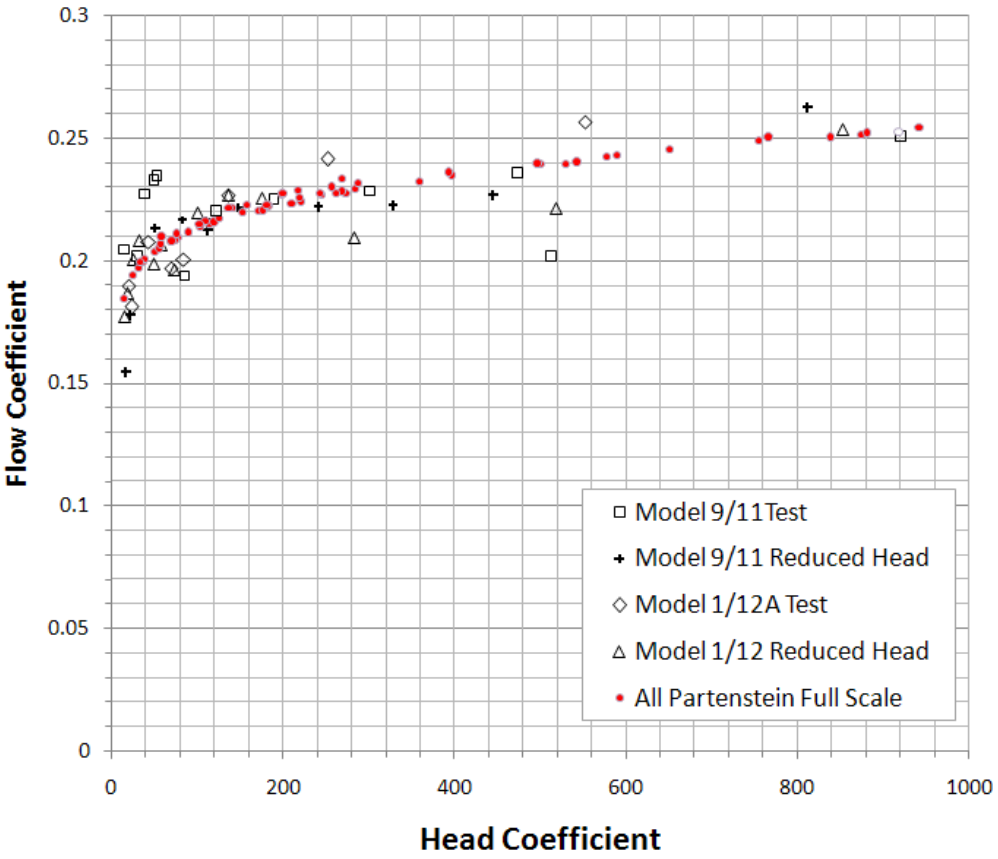

Figure 9.10: Variation of Flow Coefficient with Head Coefficient

The situation is clarified by comparing model and prototype data for just the 1/12A test condition as shown in Figure 9.11. This reduces scatter considerably, with very good congruence between scales across the whole operating range. There may be some hint of divergence for Head Coefficient values below 20, equating to the highest rotor test speeds although data points are too sparse to enable any firm deductions to be made.

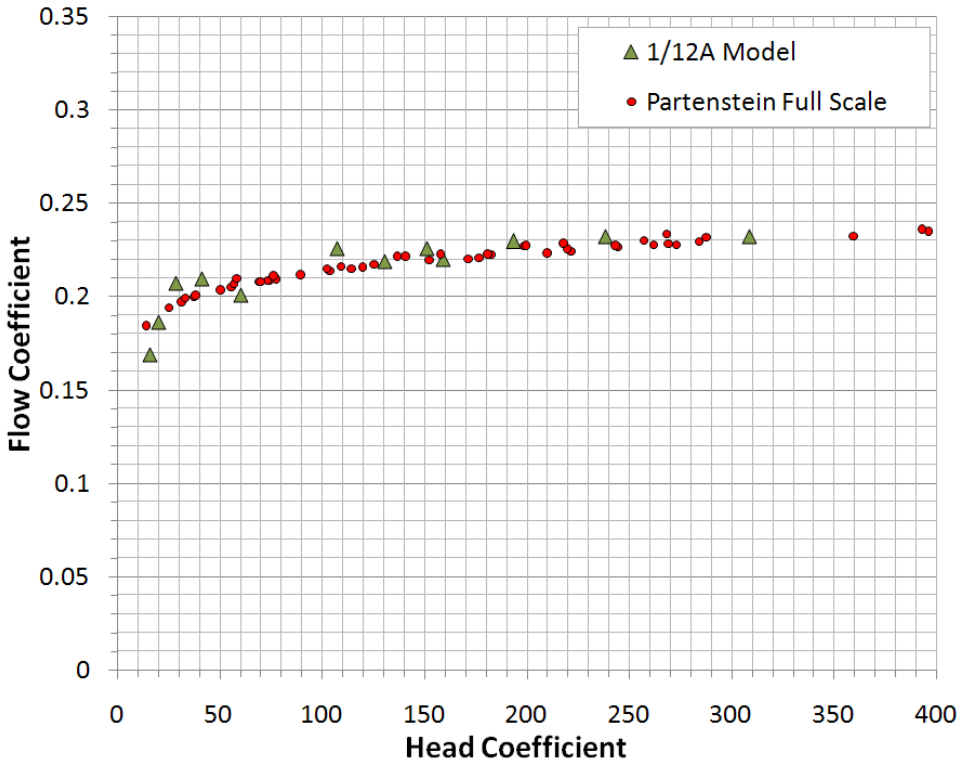

Figure 9.11: Parametric Comparison of 1/12A Condition at Model & Prototype Scales

9.2.3 Further Comparison of 1/12A Test Condition: Theory and Data

Since the 1/12A test condition offers the most complete performance curve from the prototype device, these results are examined in more detail in this section. In particular performance parameters have been calculated using both full scale and model geometries with power and gross efficiencies from theory, model and prototype compared in Figure 9.12.

Theoretical plots obtained from 3D Theory, excluding ventilation effects are also included in the figure for reference.

Several points are worth noting from this figure:

1. As observed above, agreement between model and prototype data is generally good, although deviations occur at higher flow rates.

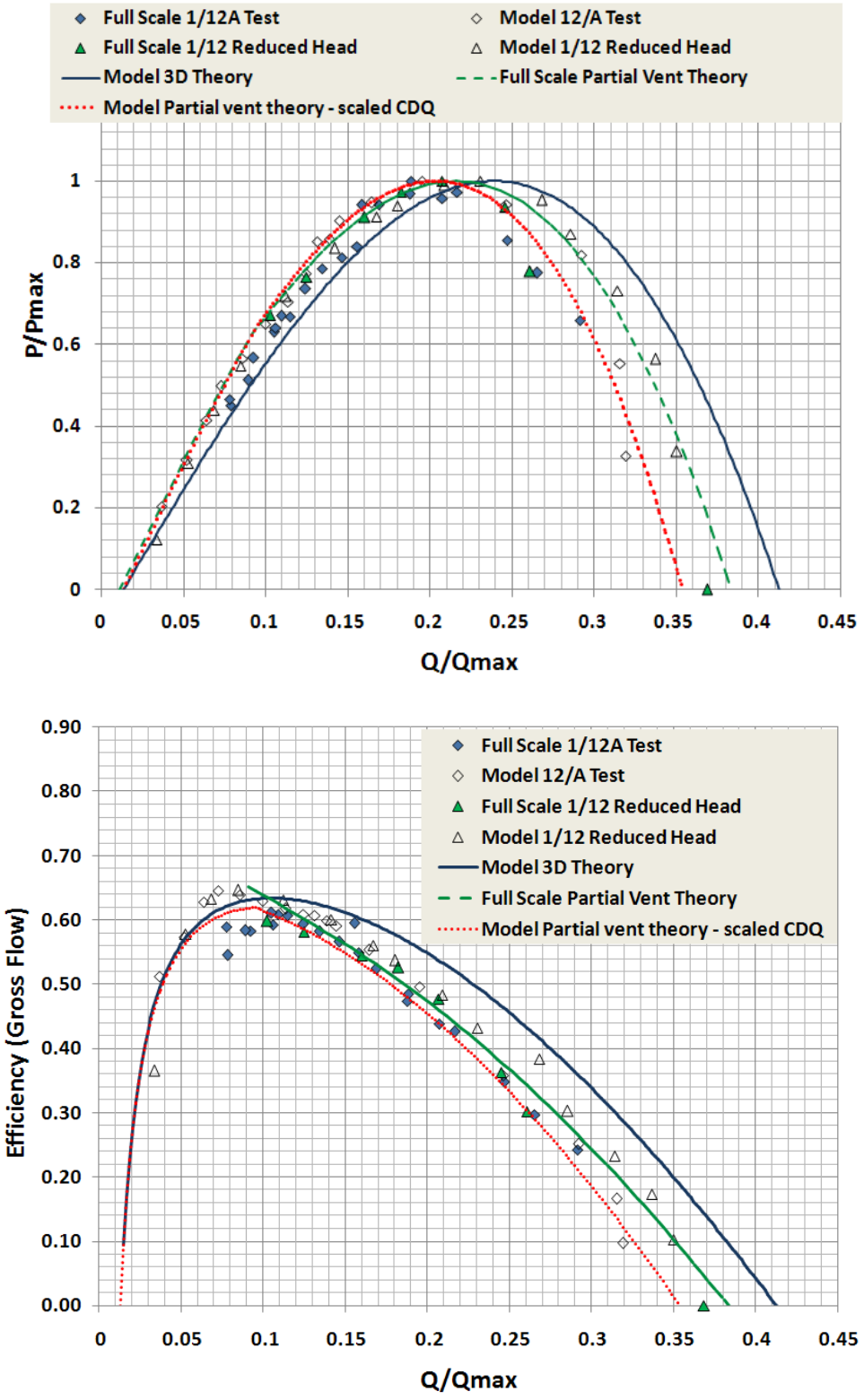

Figure 9.12: Theory and Data compared at Model &Prototype Scales

2. Both partial vent theories give a better fit to data below Pmax at both scales, than the basic 3D theory indicating that ventilation losses are both present and well represented at both model and prototype scales.

3. There is some apparent discrepancy between calculations based on model geometry compared with full scale theory above Pmax. However, this is accounted for by the presence of higher than true scale leakage flow rates in the model tests (Table 9.3). This was caused by opening up blade seal clearances in an effort to reduce friction losses to which the model was particularly sensitive. Estimated leakage represents 2.8% of the maximum measured flow-rate at prototype scale, but this increases to 4.3% of maximum measured flow in the laboratory tests and this variation in leakage has a noticeable impact in power and efficiency curves throughout the flow range.

Prototype Measured (l/s)	Froude Scaled (l/s)	Model Measured (l/s)	Model as % of Scaled
31	0.352	0.436	124%

Table 9.3: Comparison of Leakage Flow Rates for 1/12A Test Condition

So far, prediction of parametric values by partial vent theory appears to be good with little observable variation between the scales. However, prediction of absolute measured values by theory is less convincing as portrayed by the curves in Figure 9.13. Efficiencies predicted by theory *(Figure 9.13 upper)* under-estimate measured values above rotor speeds of 30 rpm, with shaft power predictions *(Figure 9.13 lower),* showing a similar trend.

No such under-estimate was made in shaft power by partial vent theory at prototype scale reported in Chapter 7, where very good agreement with measured data was achieved across the operating range.

Something unexpected is occurring here and there are several possible explanations to be considered:

1. Errors in the model measurements, for example an over correction for friction or leakage losses, may be present in the readings – although since peak power is well predicted by theory, this is unlikely.

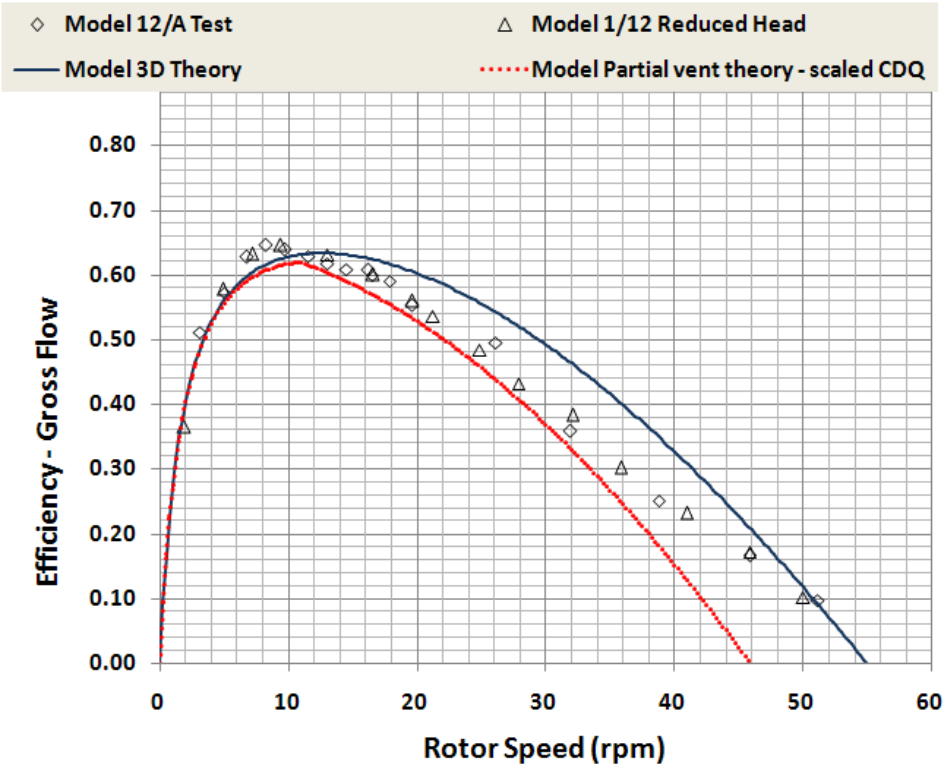

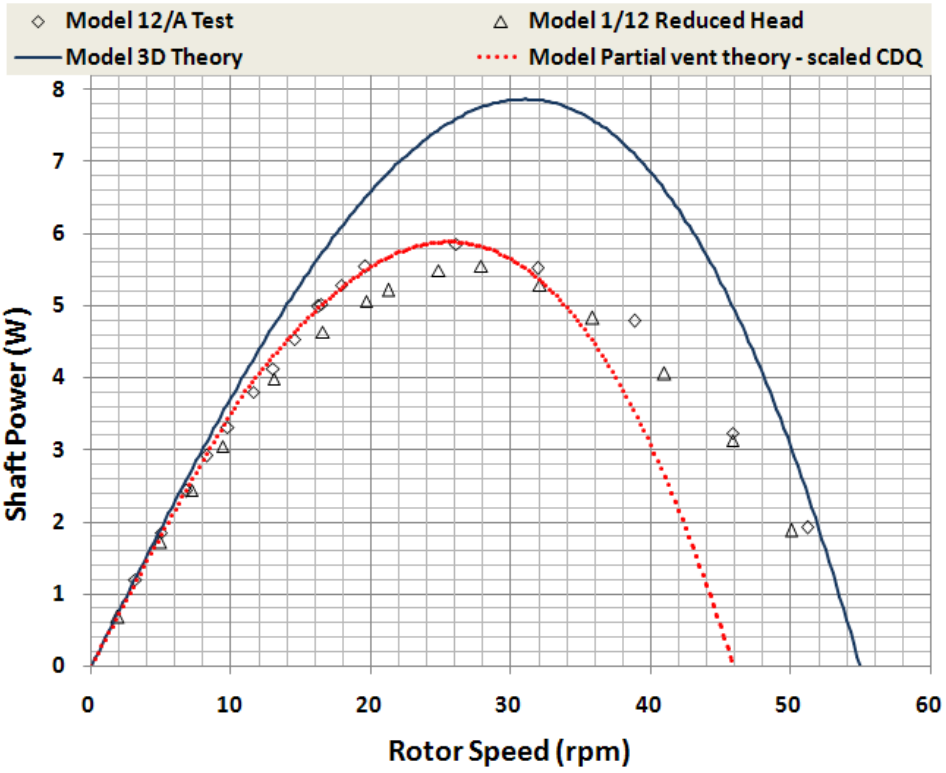

Figure 9.13: Absolute Measured Values Compared with Theory 1/12A Condition, Model Scale

2. A scaling error may be present in one or more of the parametric constants employed by the theory. While Froude scaling was applied to the 'CDQ' values (since it has units of 1/s), the dimensionless 'C_{T3D}' coefficient was left unaltered. Since this coefficient effectively incorporates all energy losses not explicitly analysed elsewhere in the theory, it seems possible that at least one loss mechanism is present that is affected by scale.

3. The presence of an energy exchange mechanism completely omitted from the theory the impact of which went unnoticed during prototype trials but has become apparent over the extended range of measurements possible at model scale. Note that this is not necessarily the result of scale but may actually be the product of a *measurement effect* since so little data could be collected in the high flow region of operation during prototype testing.

The above observations are important since they relate to a potential flaw in the modeling of HPM behaviour by *the theory*, and do NOT represent *Scale Effects* to be applied in the comparison of measurements between model and Prototype test units.

Energy exchange mechanisms will be considered further in Chapter 10 where Rotor-Fluid interaction experiments are presented and possible future refinements to theory are suggested in Chapter 11.

9.2.4 Conclusions from Section 2

1. Based on the preceding direct comparison of model and prototype data obtained from equivalent operating conditions, we can conclude at this stage that, within the margin of measurement errors, *no significant scale effects appear to be present* over most of the operating range.

2. While some divergence between model and prototype data is present at flow rates above 0.29 Qmax, it is unclear if this is due to experimental variation or the presence of a scale effect in this performance region.

3. Some error in predicting Shaft Power at model scale has been found in the theory, not apparent at Prototype scale, suggesting the presence of at least one additional energy exchange mechanism not currently included in the mathematical model. This will be further studied in later sections of this work.

9.3 Section 3: Performance Improvement Testing

9.3.1 Deep Water Testing

9.3.1.1 Scaled Rigid Rotor

The theory developed in Chapter 7 indicates that downstream water level should have a significant effect on HPM performance. However, since an increase in blade submergence inevitably leads to an increase in blade area in contact with downstream water, losses due to blade drag are also likely to increase. The optimum setting of the wheel relative to exit fluid levels is likely to be a compromise between these two effects.

To study this trade-off, a series of 'Deep Water' tests were carried out. In order to isolate performance changes due to downstream conditions, upstream water levels were maintained constant for each test, thus keeping the inflow acceleration and upstream blade drag contributions to overall rotor losses consistent. The resultant change in head across the rotor was readily accounted for by theory.

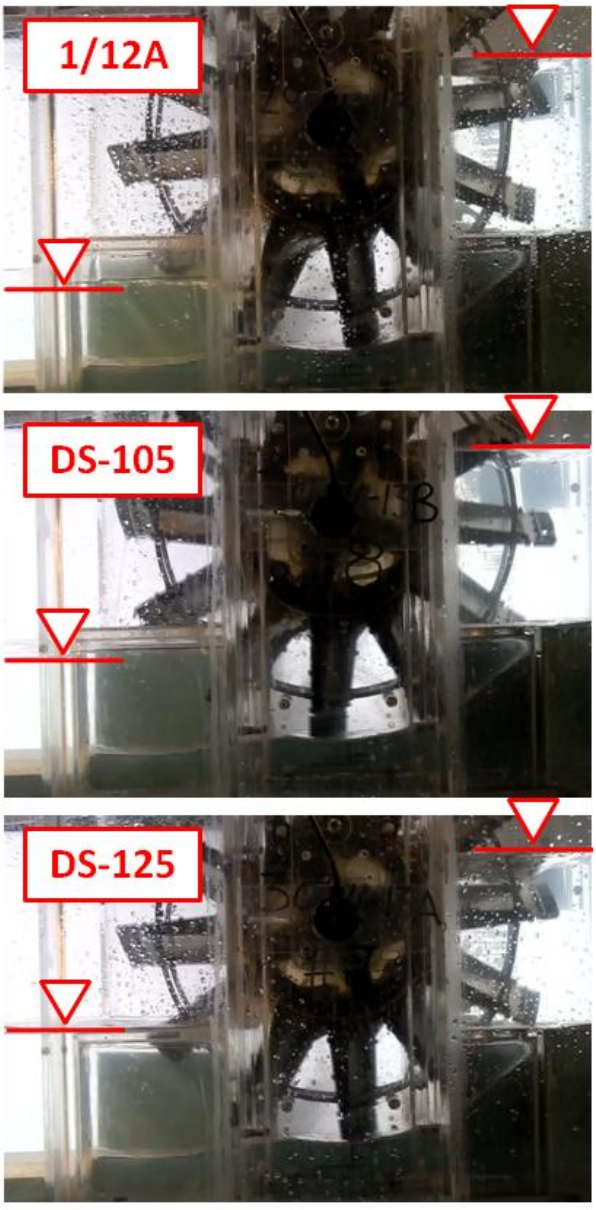

Figure 9.14: Deep Water Test Conditions

The three water levels investigated (as detailed in Table 9.2 at the start of this chapter), are shown in Figure 9.14. The results from two separate series of experiments are presented in Figure 9.15, where parametric power and net flow efficiencies are shown in order to account for differences in leakage rates measured between test set-ups.

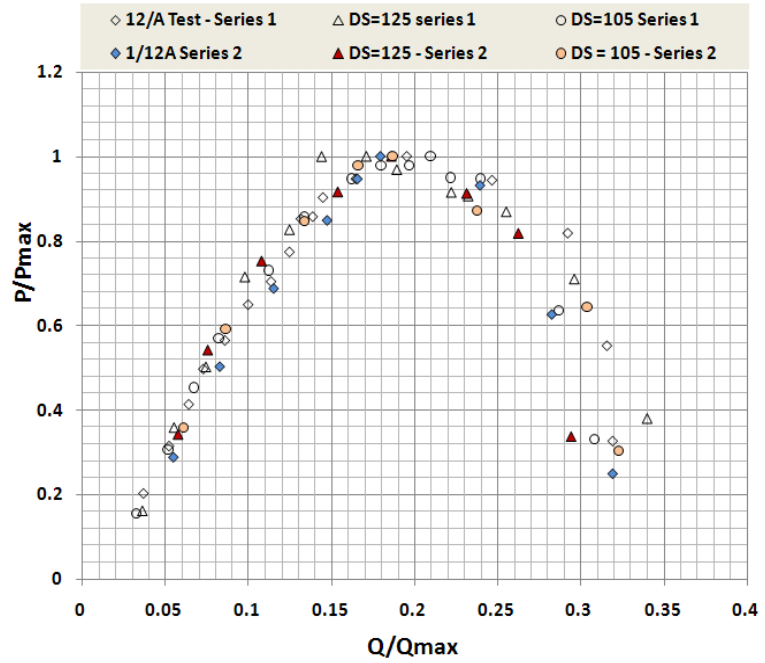

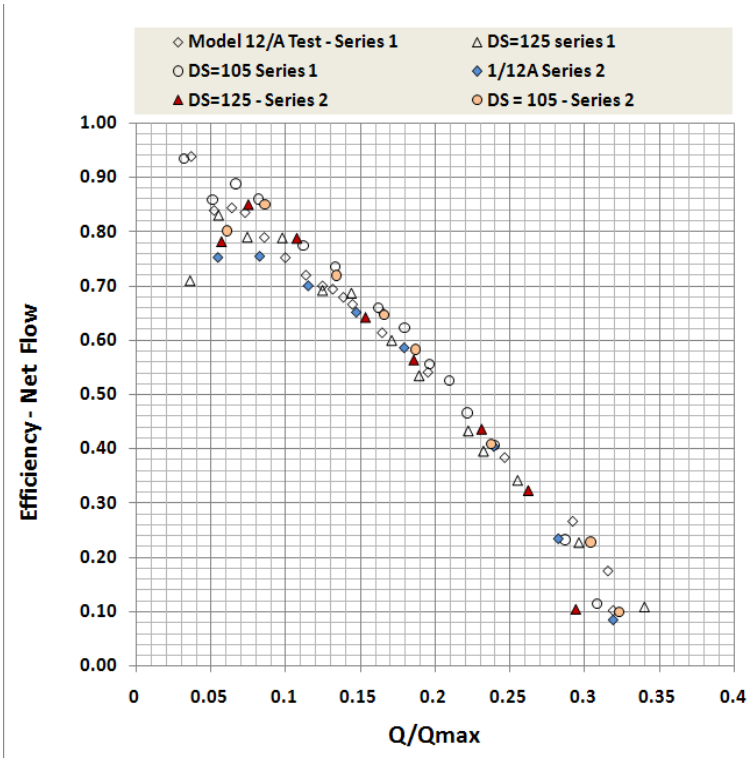

Figure 9.15: Parametric Comparison of Deep Water Test Series

As expected from theory, increasing downstream water level produces an improvement of 9-10% in peak efficiency although, interestingly, this same level of improvement is apparent in both the DS-105 and DS-125 data.

However, as flow rate increases, the DS-125 condition shows a notable reduction in both output power and efficiency, indicating an increase in some component of loss, with downstream depth.

This is shown more clearly in the comparison of absolute values between data from a single test series and theory displayed in Figure 9.16.

The form of the power curve for both the 1/12 and DS-105 conditions *(Figure 9.16 upper)* is consistent with previous test conditions and presents a reasonable fit to their corresponding theory lines. However, the shape of the DS-125 curve is quite different in form – showing a reduction in the speed at which maximum power occurs and a definite distortion from the expected profile, giving a very poor fit with its

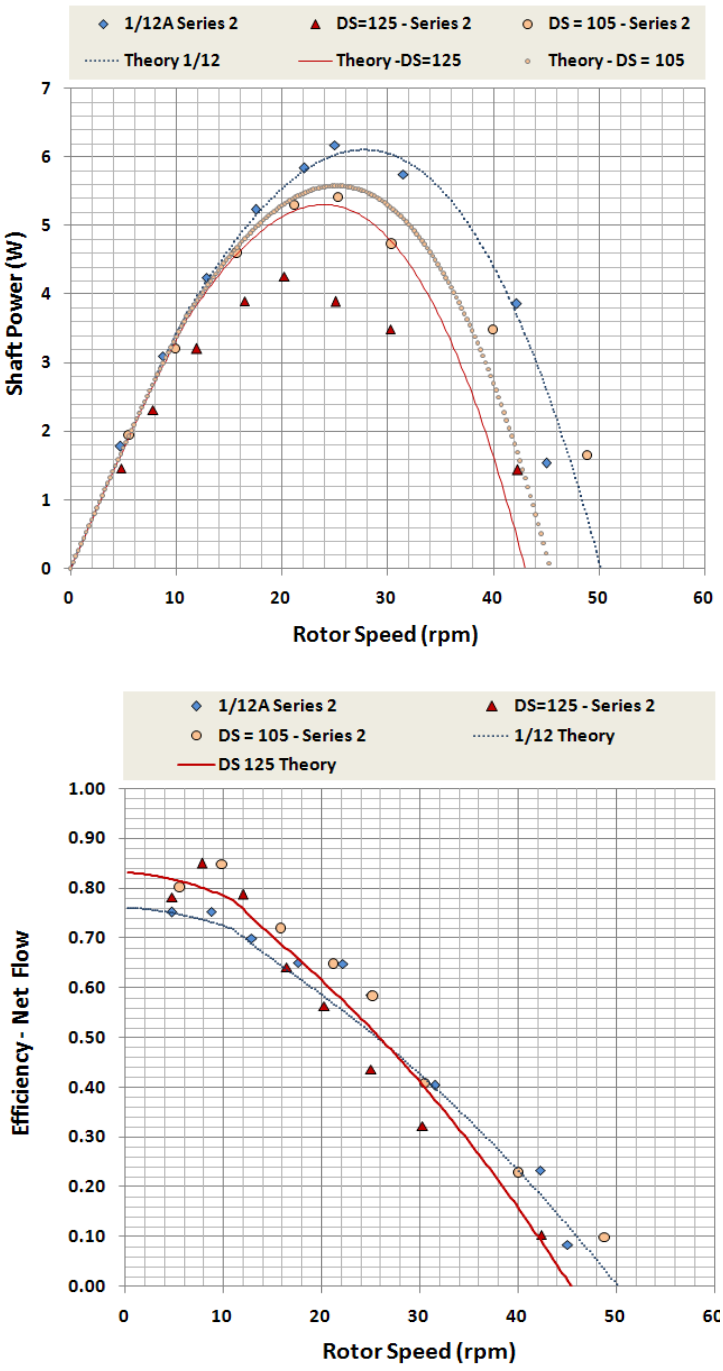

Figure 9.16: Absolute Power and Efficiency Comparisons with Theory – Deep Water Tests

theory line. Similar patterns are repeated in the net flow efficiency curve *(Figure 9.16 lower),* the DS-105 depth being able to sustain higher levels of efficiency at greater speeds that the DS-125, and with the latter data-set underperforming compared with theory above around 15 rpm.

The key is to identify the loss mechanism involved here: whether due to blade drag, turbulence or some form of acceleration loss in the exit channel. To help with this process, we will now consider deep water test results carried out with modified rotor designs described fully in a later section of this thesis. However, since these results are so pertinent to the energy loss mechanism being investigated here, they are presented below, even if slightly out of sequence in this report.

9.3.1.2 Deep Water 'Flap Wheel' Tests

The 'Flap Wheel' is a novel design concept where flexible membranes are fixed over cut outs in the blades that are able to deflect under the action of fluid forces. This deflection reduces both the drag produced as the blades pass through standing water, and permits earlier ventilation of the cell during the emptying process (Figure 9.17).

Figure 9.17: 'Flap Wheel' rotor during blade 'Deep Water' testing. Blade emerging from the downstream flow (*left*), Upper flap deflecting to provide early cell ventilation (*right*)

This concept is described in more detail in section 9.3.2 but, of interest here, is that the Flap Wheel offers a substantial reduction in drag, both at blade entry ***and exit*** from the flow. If blade drag is the primary additional loss mechanism present in the performance graph of Figure 9.16, it should have a significant impact on both power and efficiency measurements. On the other hand, if acceleration losses are dominant, the Flap Wheel modification should result in little or no improvement in efficiency, since flow rates passing through the unaltered exit channel geometry remains the same.

A direct comparison of Flap Wheel performance at the DS-125 water level is made with earlier Deep Water tests in Figure 9.18.

The change in performance made by the Flap Wheel can be clearly seen, with the shape of the power curve restored to its normal form, and efficiency

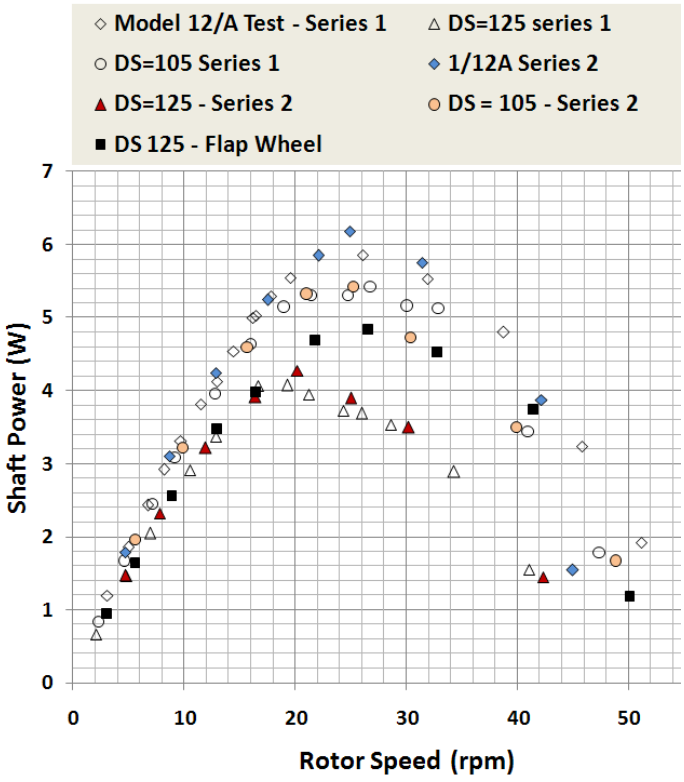

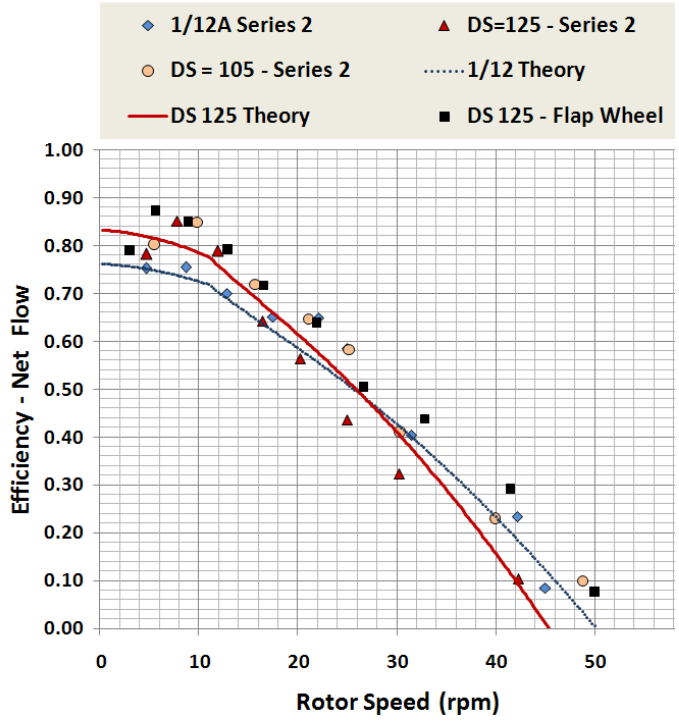

Figure 9.18: 'Flap Wheel' Rotor Performance Improvements in Deep Water Tests

matching that of the DS-105 condition at rotor speeds up to 25 rpm. Above this level, the Flap Wheel offers a substantial improvement over the scaled rigid blade rotor of DS-105.

This represents strong evidence that the additional energy losses experienced by previous DS-125 tests are the direct result of increases in blade drag caused by greater blade immersion at this condition and not through any combination of exit flow accelerations. Further, contrary to the indications of theory, this evidence suggests that with the rotor design used in the existing prototype, setting downstream water levels to produce full blade immersion will not produce the most efficient installation. A better compromise would be a blade depth setting corresponding to the DS-105 test case where 90% blade immersion is achieved.

The forgoing also indicates the need to model blade drag as a discrete loss mechanism in the theory if installation geometries are to be better optimised in future designs - a subject that will be discussed further in Chapter 10.

9.3.1.3 Deep Water 6-Blade Rotor with modified Exit Channel

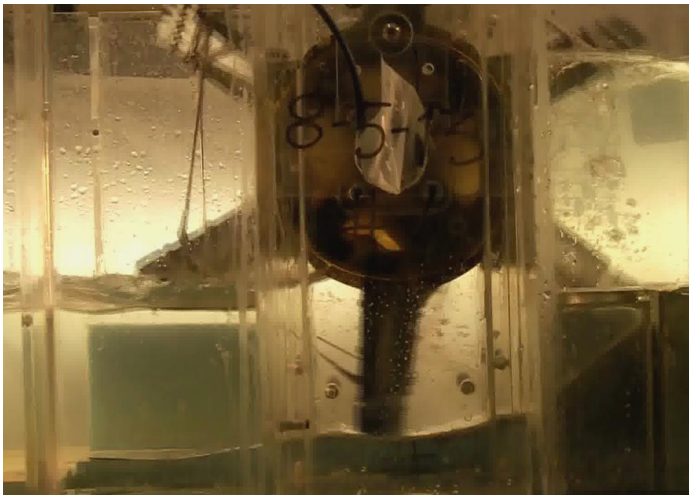

Figure 9.19: 6-Blade Rotor, DS-125 Test, with modified Exit Channel

The 6-Blade rotor is fully described in the next section, but to bring all deep water tests reporting under one heading, results from this specific experiment will be presented here. As described later, this machine consisted of 6 equidistant, rigid blades arranged around the rotor hub with minor modifications also applied to one side plate on the upstream side. Unique to this experiment was the removal of one side block in the exit channel on the leading side of the blade, intended to promote more rapid cell emptying by enabling cell fluid to escape from the side of the blade as

well as through the gap formed between the blade edge and exit channel floor (Figure 9.19).

A limited range of data was collected with the DS-125 water level only, and power and efficiency plots are compared with other deep water tests in Figure 9.20.

These limited tests have only extended up to peak power but, within this range, demonstrate useful gains in both power output and efficiency. Peak power is now close to that of the 1/12 test output despite the significant reduction in head in the DS -125 test condition, while efficiency at peak power is a respectable 60% with peak efficiency (assuming the data point is valid) topping out at 91%.

The difficulty in analysing the mechanisms behind these performance improvements, is that so many parameters have altered with this test set up, with blade drag, exit channel acceleration, cell ventilation and power stroke length all being changed. However, in later sections, general explanations for the higher performance obtained from 6 bladed rotors will be suggested.

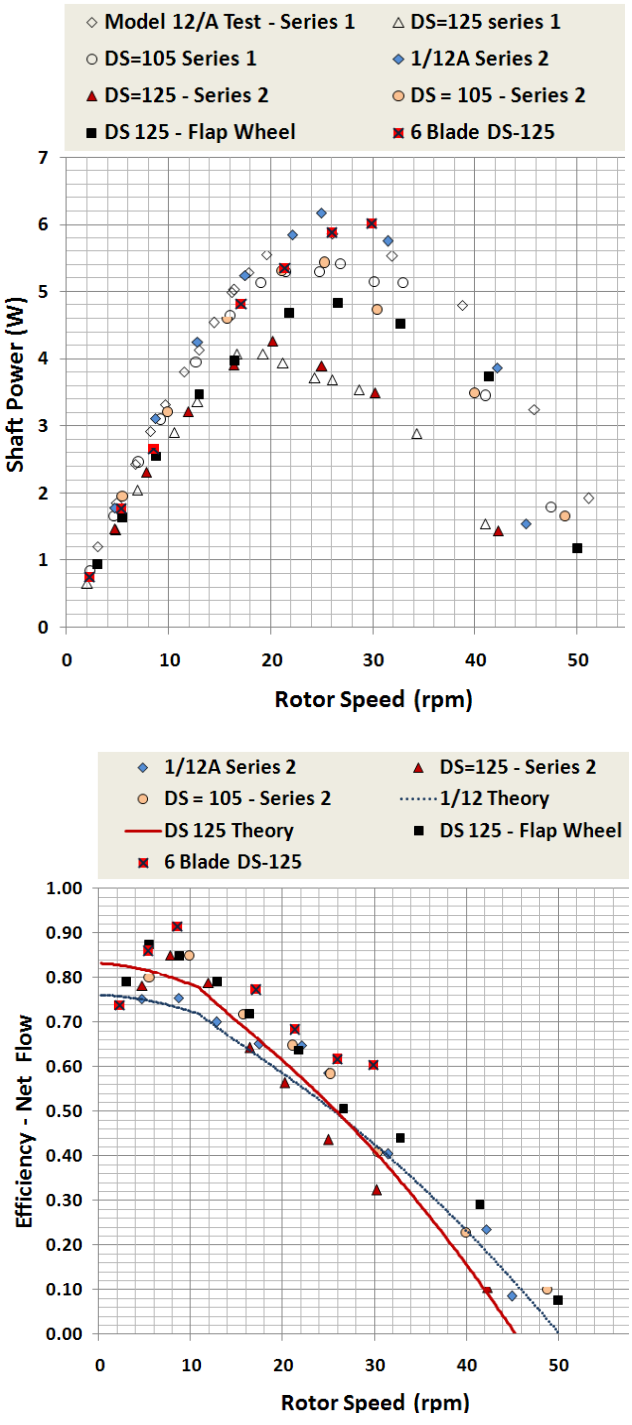

Figure 9.20: 6- Blade Rotor with Modified Exit Channel Compared with Deep Water Tests

9.3.1.4 Conclusions from the 'Deep Water' Test Series

It is useful to gather up the learning established by this quite complex series of experiments at this stage, as follows:

1. Losses caused by lack of ventilation during cell emptying have been shown to exist at both model and prototype scales and the new theory developed in Chapter 7 found to be valid.

2. As predicted by theory, ventilation losses are reduced as downstream water levels are increased.

3. However, overall machine efficiency is not necessarily improved with greater blade immersion, as blade drag forces are increased by both the greater area of blade in contact with the fluid and the greater distance that blades must travel through the exit flow.

4. Optimal setting of the rotor height relative to downstream water levels is a trade-off between these two losses.

5. The absence of blade drag as a separate loss mechanism is a serious omission in the existing theoretical model of HPM performance.

6. Significant gains in performance were obtained from the 6-Blade rotor tests, the mechanisms for which are so far unexplained.

9.3.2 Alternative Rotor Configurations

Alternative configurations of the scale model of the prototype unit were investigated to both provide further insight into the energy loss mechanisms present in these machines and to provide a sound experimental foundation on which to base any modifications to the full scale unit proposed in the future.

Two basic configurations were investigated: the 'Flap Wheel' which has already been introduced, and the '6 blade' rotor, which consisted merely of removing alternate blades from the basic unit. Both devices are described initially before moving on to present overall performance results for this complete series of experiments. For comparison, a third hybrid configuration was also tested – the 6 Blade Flap Wheel.

9.3.2.1 'Flap Wheel' Rotor

Following prototype testing, it was clear from observations that the large area of the flat blades contacting and moving through bodies of water both on entry and exit made a significant contribution to energy losses. Following on from the 'Flexible Rotor' design originated by Linton (2009), a revised arrangement of self conforming blade surfaces was developed to create the 'Flap Wheel' rotor (Figure 9.21). The key features of this development were to divide the rotor surface into two separate areas each covered by a flexible membrane fixed along the outside edge. Large areas of the blade structure were cut away to leave only a minimal lattice of metal to support the membrane when it experienced full pressure loads.

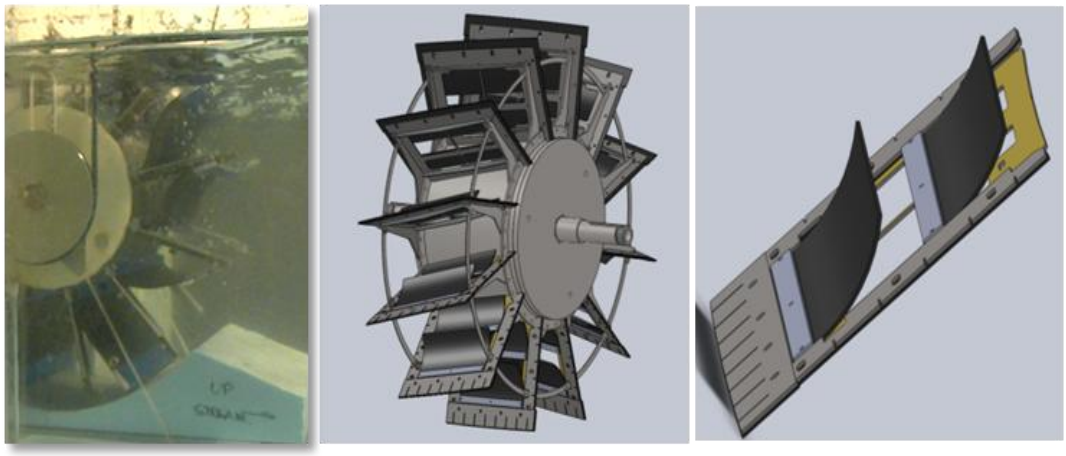

Figure 9.21: 'Flap Wheel' Concept: Original 'Flexible Rotor' under test *(left),* Partenstein Rotor adapted to flex blades *(centre),* Detail of Flap Blade modification *(right)*

The fixed edge of the membrane acted as a hinge, allowing the flaps to deflect as described previously, to minimize energy losses due to drag. Having the fixed edge on the outside of each flap enabled correct functioning to be maintained across a wide range of operating speeds, avoiding the inertia related deployment problems found in the original flexible rotor (Linton, 2009). Note that to enable free operation of the flaps, 'snub ties' were removed from the blades for all Flap Wheel rotors.

Two sets of Flap Wheel tests were carried out. The first wheel used the same 1mm thickness of nitryl rubber material for all membranes. However, for the 'modified Flap Wheel' test series, the innermost flap membranes, adjacent to the hub-tube, were modified to use a thinner 0.25 mm thick PVC material across the hinge lines. This

modification was carried out to promote early ventilation of cells during the draining process, since suction pressures were too low to enable correct opening of the 1mm thickness membrane material previously used.

9.3.2.2 6-Blade Rotor

The selection of 12 blades for HPM rotors was an entirely arbitrary decision taken by Senior, and subsequently followed by all workers in the field. However, the geometry of the shoe used in the Prototype installation created a working section in the machine extending over 60° of rotation.

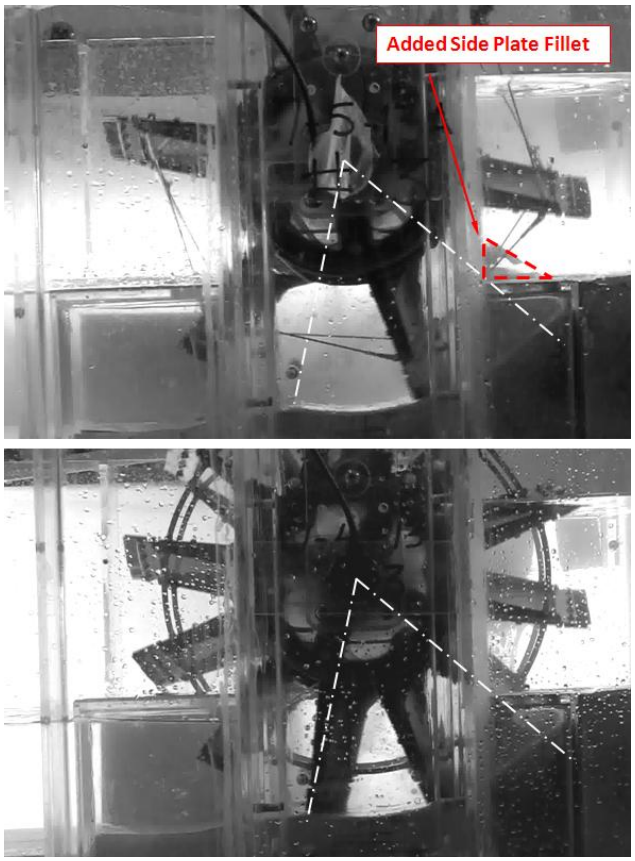

Figure 9.22: 6-Blade Rotor *(above)* compared with standard 12-Blade *Unit (below)*

It was reasoned that this additional shoe length could be exploited by reducing the number of blades in the rotor from 12 to 6 and thus doubling the length of rotation over which full up and downstream pressure differential would be exerted across the blade. This would double the length of the working stroke, and might be expected to improve operating efficiency.

This description is clarified by comparing 12 and 6 blade rotors shown in Figure 9.22. In each picture the extent of the working section, formed by a combination of shoe and side plate geometries, are marked. Two further modifications to the 6-blade installation can be seen in the figure: the lengthening of the 'snub ties' supporting adjacent blades and the profile of a side plate extension fillet, added to the side plate on the far side of the flume. This was necessary to enable the blade with its 15° inclination angle to fully seal the working section over the full 60° of rotation. In all other respects 6 and 12

blade installations were identical.

9.3.2.3 The 6-Bladed Flap Wheel

This modification should be entirely self explanatory and consisted of simply removing half of the blades from the first series Flap Wheel rotor already described. Note that the thicker 1mm membrane material was used for all flaps in this test and, therefore, inner flaps were not able to open in response to ventilation forces.

9.3.2.4 Alternate Rotor Test Observations

Detailed observations of these rotors will be described in chapter 10 of this report alongside those for the basic scaled model unit and will not be presented during the following study of machine performance measurements unless behaviours materially affected the validity of the test conditions applied.

9.3.2.5 Alternate Rotor- Direct Performance Comparisons

Direct comparisons of absolute power output from each alternate rotor configuration test, is shown in Figure 9.23. Since leakage flow rates changed significantly between the various test set ups used, *Gross* Flow Efficiencies are rather meaningless and so *Net* Flow Efficiency variation with wheel speed is shown in Figure 9.24.

All experiments were carried out using the same 1/12A test condition water levels hence the direct comparison made in the above figures is perfectly valid and useful.

The lowest power output and efficiencies were produced by the scaled model of the prototype unit, indicating that all rotor modifications offered performance improvements to some extent. The '12 Blade Flap' plot represents the first flap wheel test series, where no deflection of the inner flap to aid cell ventilation was observed at any test speed, implying that the performance improvement over the 1/12 rotor is entirely due to reductions in blade drag, both on entry and exit from the flow. As one would expect, this effect becomes increasingly significant as rotor speeds increase, but offers a modest gain of 3% in peak power.

Once the flap wheel was modified to enable opening during cell emptying, peak power is increased by around 18% compared with the base model, giving 20% efficiency improvements at higher, matching speeds. However, there is some unexpected behaviour at speeds below 25 rpm – while power outputs are consistent with the

expected curve, data points for net efficiency appear to be erratic, possibly indicating poor quality flow measurements or some unexpected variation in leakage rates. These need to be treated with some caution.

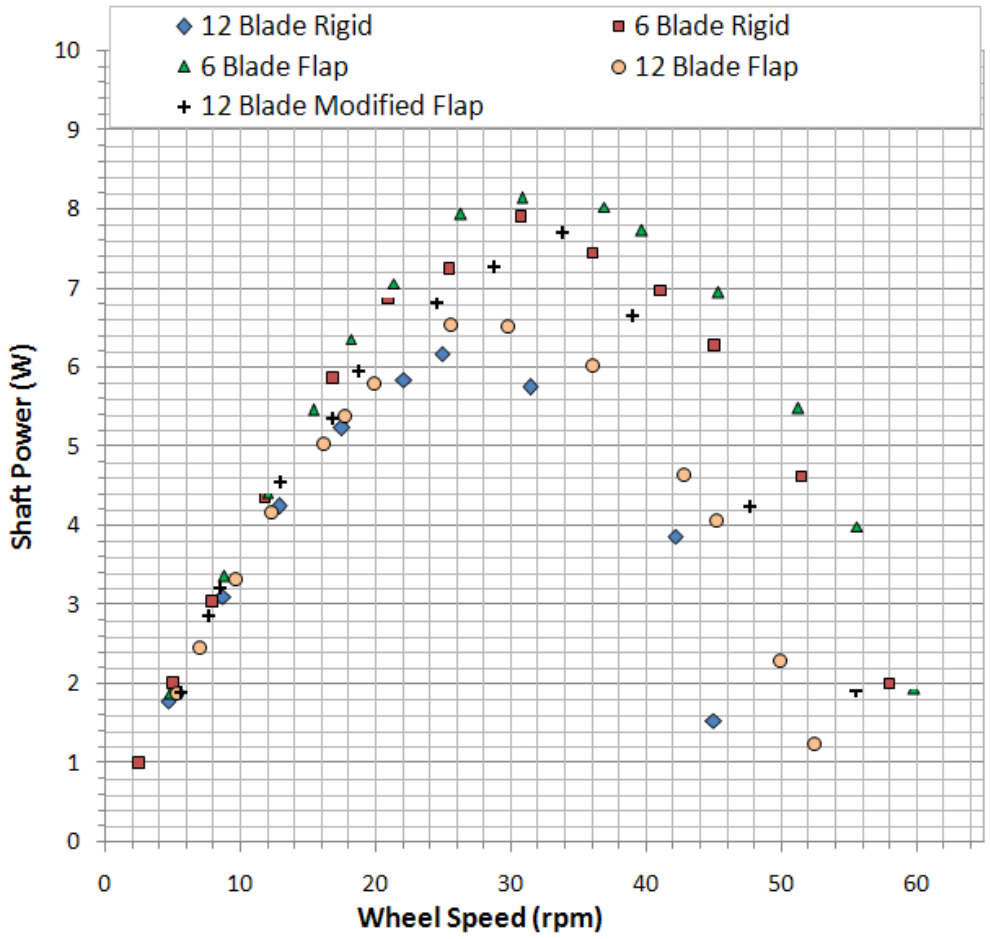

Figure 9.23: Direct Comparison of Alternate Rotor Power Outputs

Nevertheless, comparison of the two Flap Wheel models is interesting since it appears to isolate the impact of the ventilation losses on power output since the modification to the inner flap has only a small impact on overall blade drag. Assuming that the peak power gain in the first flap wheel test is due to drag reduction alone, the net loss in peak power due to inadequate cell ventilation during emptying is substantial at around 15%.

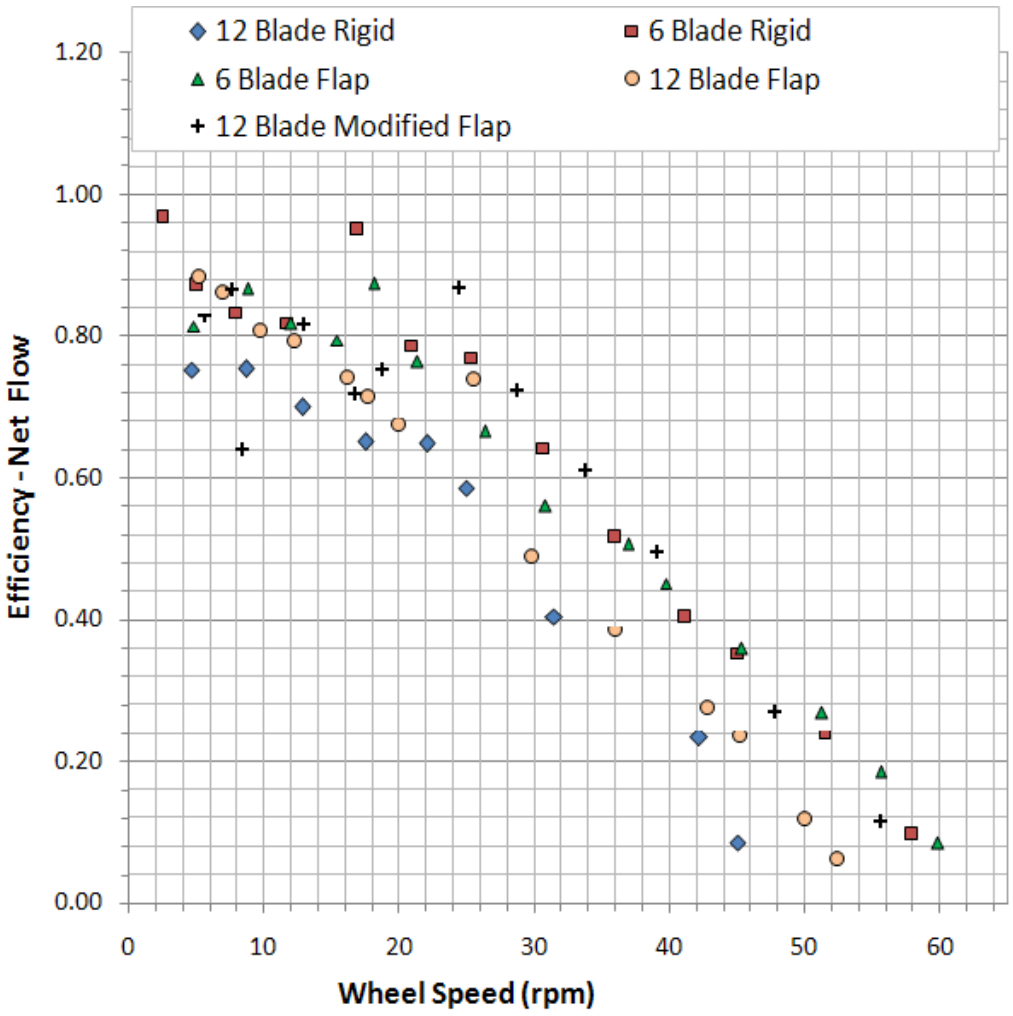

Figure 9.24: Direct Comparison of Alternate Rotor Net Efficiencies

The surprise result from this series of experiments is the very large gain in performance obtained from the 6–Blade rotor which improved peak power output by a little under 31%. If our previous deductions regarding ventilation losses are correct, something more than an improvement to what we have so far termed 'cell ventilation' has been achieved with this machine and the better match between blade pitch and working section angle appears to produce either a much more effective energy transfer mechanism, or a decrease in an energy loss mechanism, hitherto not identified.

The best absolute power output was achieved with the 6-blade flap wheel and, since this used the blades from the first flap wheel series, this further gain in efficiency can be attributed exclusively to the reduction in blade drag achieved by the flexible surfaces. This is reflected in the increasing efficiency gain with higher rotor speeds and the

modest 2.5% gain in peak power – remarkably consistent with the percentage gain already found between 12 blade rigid and flap wheel rotors.

9.3.2.6 Alternate Rotors - Parametric & Theory Comparisons

P/Pmax and Gross Efficiencies are compared against Q/Qmax in Figure 9.25.

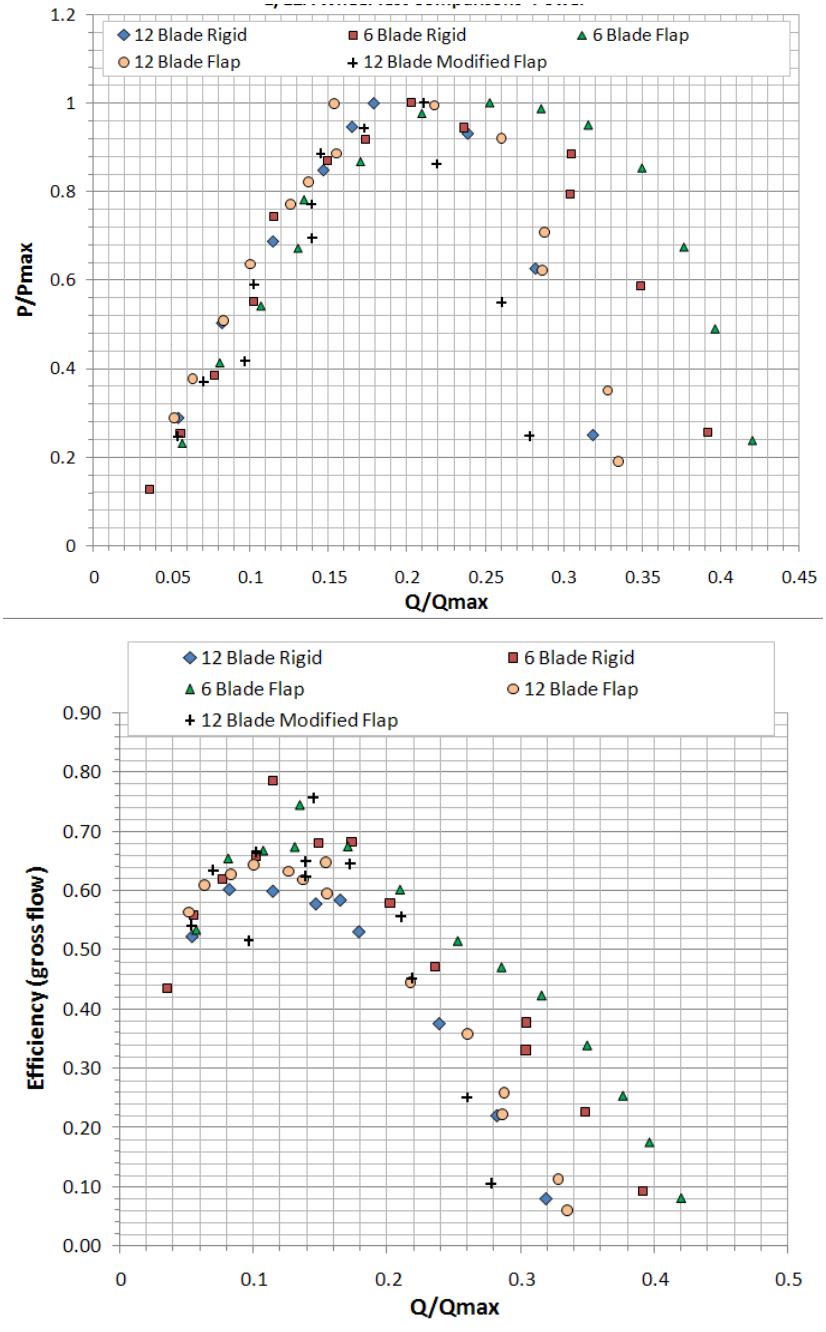

Figure 9.25: Parametric Comparison of Alternate Rotors

The power curve emphasizes the improvement gains produced by both 6-blade rotors, with the flap blade in particular, flattening and extending the range of flows over which peak power is achieved. This increases the maximum possible flow rate from 0.34 to 0.42 Qmax. In contrast, the narrow performance range of the 12 blade modified flap wheel needs some explanation.

Study of slow motion video from this rotor shows that, at rotor speeds above 40 rpm, the blade flaps become increasingly slow to close during the power stroke. This was not the case with the first flap wheel series and it appears that the early venting of the cell to reduce ventilation losses had the unintended side effect of also removing a force actively involved in the closing of the main blade flap. Thus, as speed increases, power extraction and efficiency falls dramatically limiting the maximum rotation speed significantly.

The results from all modified rotor tests are compared against 2 versions of theory in Figure 9.26: partial ventilation theory and 3D theory; these include all inlet and exit accelerations, but omit ventilation losses. The drag coefficient and leakage flow rates have been left unaltered from those of the main 1/12A rotor test of previous sections, which partially accounts for the apparent underestimating of peak efficiency values compared with these tests.

As found above, partial vent theory gives a good prediction of power output in the base rotor. This is exceeded due to the drag reduction of the first series of Flap Wheel tests, although they follow the form of the partial vent theory curve quite well.

With the ventilation gains of the modified flap and 6-Blade rotor tests, data points appear to cluster around the 3D Theory curve at least up to peak power. At this point the modified flap wheel power falls away due to the membrane operating issues already described, but the 6-Blade rigid tests continue to approximate to 3D Theory quite closely. The drag reduction produced by the 6-Blade Flap enables this rotor to significantly exceed 3D Theory predictions as rotor speeds increase.

The energy exchange mechanisms behind these performance increases will be examined in chapter 10 when detailed test observations and time series measurements from rotor instruments will be presented.

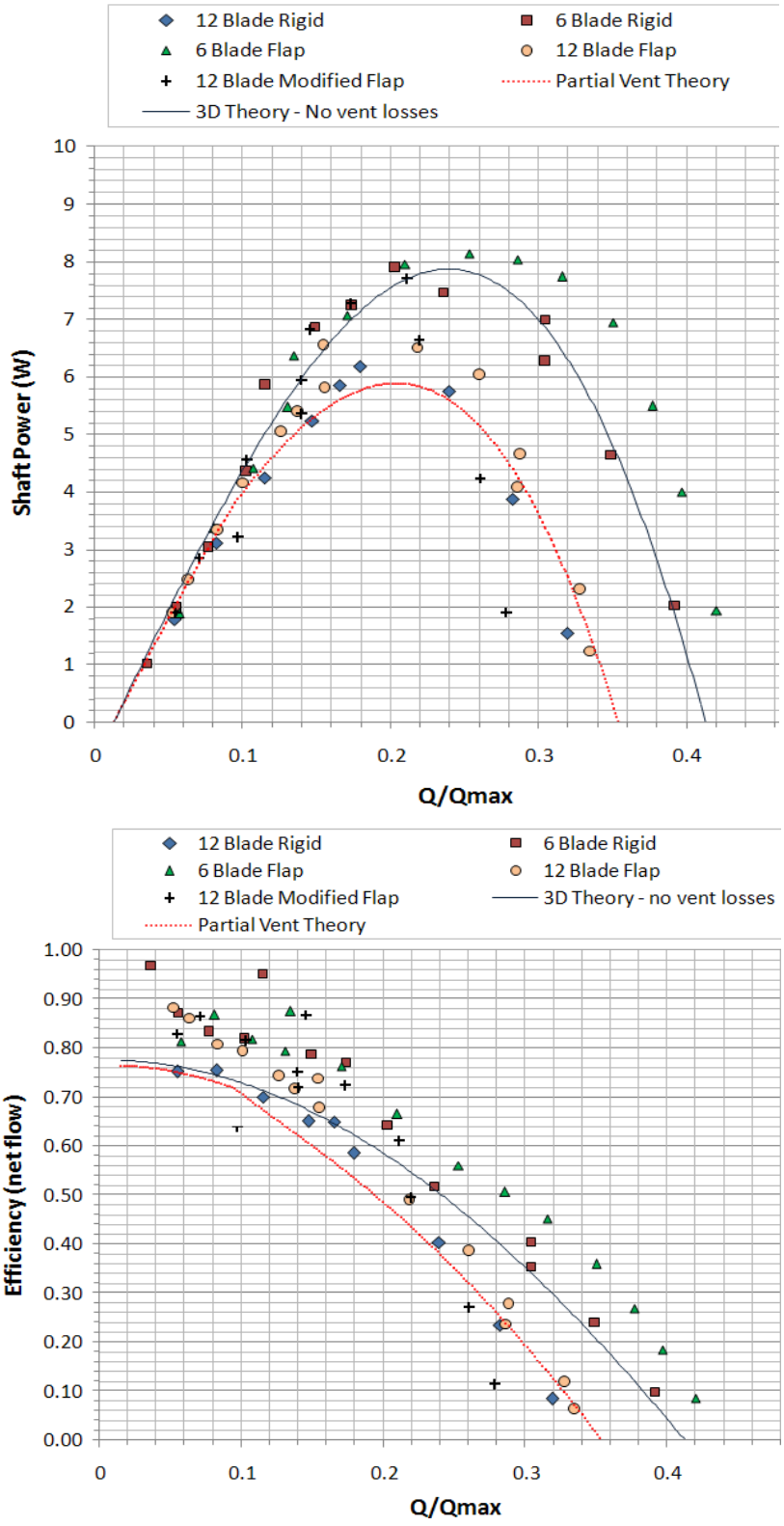

Figure 9.26: Alternate Rotor Tests Compared with Theory

9.3.3 Conclusions from Alternate Rotor Test Series

Summarising what has been learned from this series of tests, we have found the following:

1. All of the modifications to the basic rotor model resulted in significant and useful gains in power output.

2. From the flap wheel tests we observed that peak power gains due to drag reduction from the deformable blades was around 3% applied to both 12 and 6 –Blade rotors.

3. Early ventilation of the cell in the 12 Blade modified Flap Wheel tests showed that ventilation losses accounted for 15% of peak power.

4. The use of a 6-Blade rotor showed dramatic improvements in performance, boosting peak power by 31%. This suggests that a significant change in energy transfer has been produced in this rotor, which goes beyond our understanding of 'ventilation loss', so far developed.

5. Since any form of ventilation loss is omitted from the equations, 3D Theory appears to offer a good prediction of 6-Blade rotor performance.

10.1 Introduction to Rotor Processes

Based on observations of both the full-scale prototype and scale model performance tests, the detailed function of the HPM can be thought of as a number of discrete hydraulic processes. These will be briefly described here, since they provide a useful framework with which to describe and interpret rotor energy exchange observations reported in later sections of this chapter.

10.1.1 The 'Four Stroke' Analogy

In its' simplest form, an individual cell of the HPM can be considered as going through four distinct phases during each revolution of the machine and this 'Four Stroke Cycle' is summarized in the graphic of Figure 10.1.

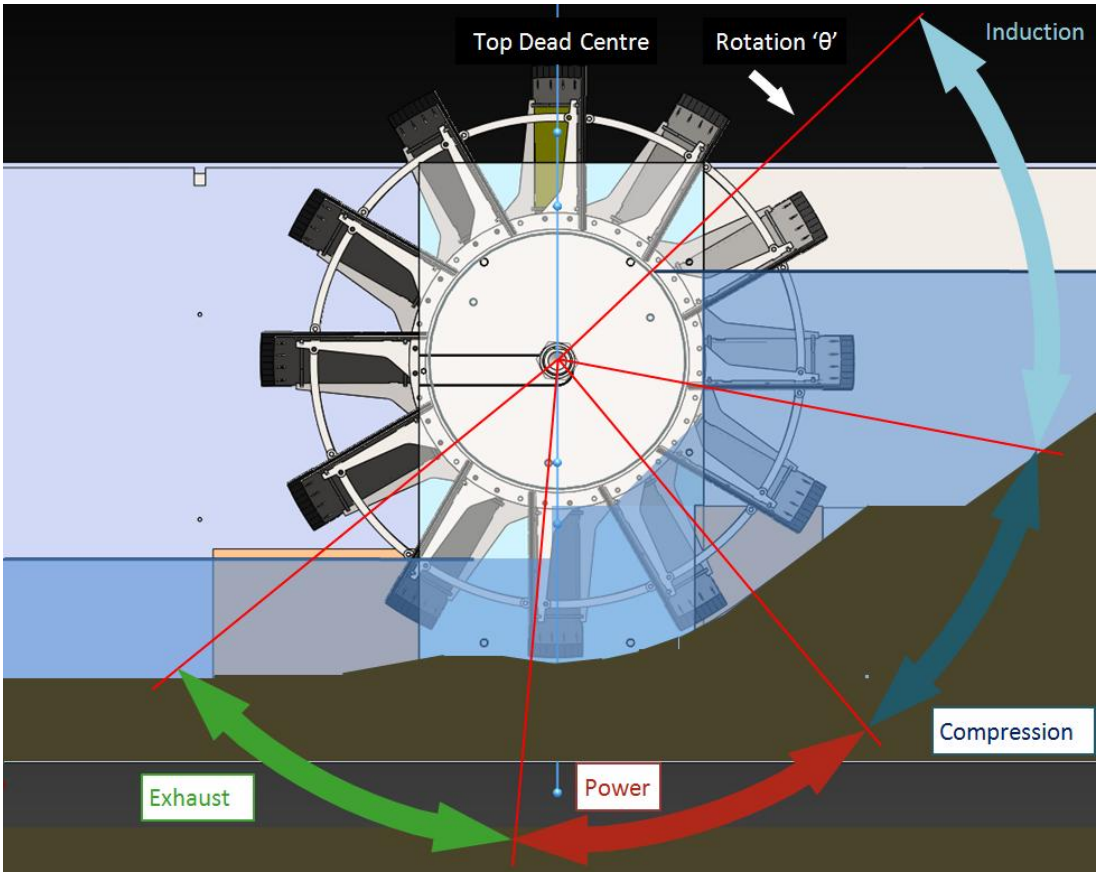

Figure 10.1: The 'Four Stroke' Phases of HPM operation

The 'Four Stroke' analogy is a useful aid to interpreting how fluid is being processed by the machine at each stage of rotation, as well as giving some hints as to the installation

geometry required in a practical design. For example, impact of the shape of the side walls and shoe is more readily understood once we realise that these features set the start and end angles for the power stroke and in effect set up the 'timing' of the machine's energy extraction processes.

Briefly the four phases consist of:

Induction: extending from first contact of the blade with the upstream surface until the following cell is completely filled with water moving at the same speed as the rotor itself.

Compression: following cell filling, further fluid mass is not added to the cell, but pressure may continue to be transmitted across the cell perimeter until rotation brings the cell into the working section of the machine and isolates its contents from the upstream water.

Power: the primary energy extraction process produced by the action of hydrostatic pressure difference acting across an individual blade in the working section.

Exhaust: once the blade passes over the edge of the shoe profile, fluid starts to be released, and cell pressure falls away quickly. The rate at which this fall in cell pressure occurs and the ease with which low pressure fluid can leave the machine both appear to have a significant effect on machine performance.

10.1.2 Cell Processes

Based on observations, we can further deduce that the 'Four Stroke' operating phases of the HPM can be subdivided into a number of discrete 'Cell Processes' during which distinct physical events are occurring. These are summarized in the graphic of Figure 10.2.

In the following sections of this chapter each of these processes will be studied first by using 'time series' measurements to quantify the magnitude of energy loss or gain associated with each process, before drawing on video survey observations to describe the physical processes occurring during these rotor-fluid interactions.

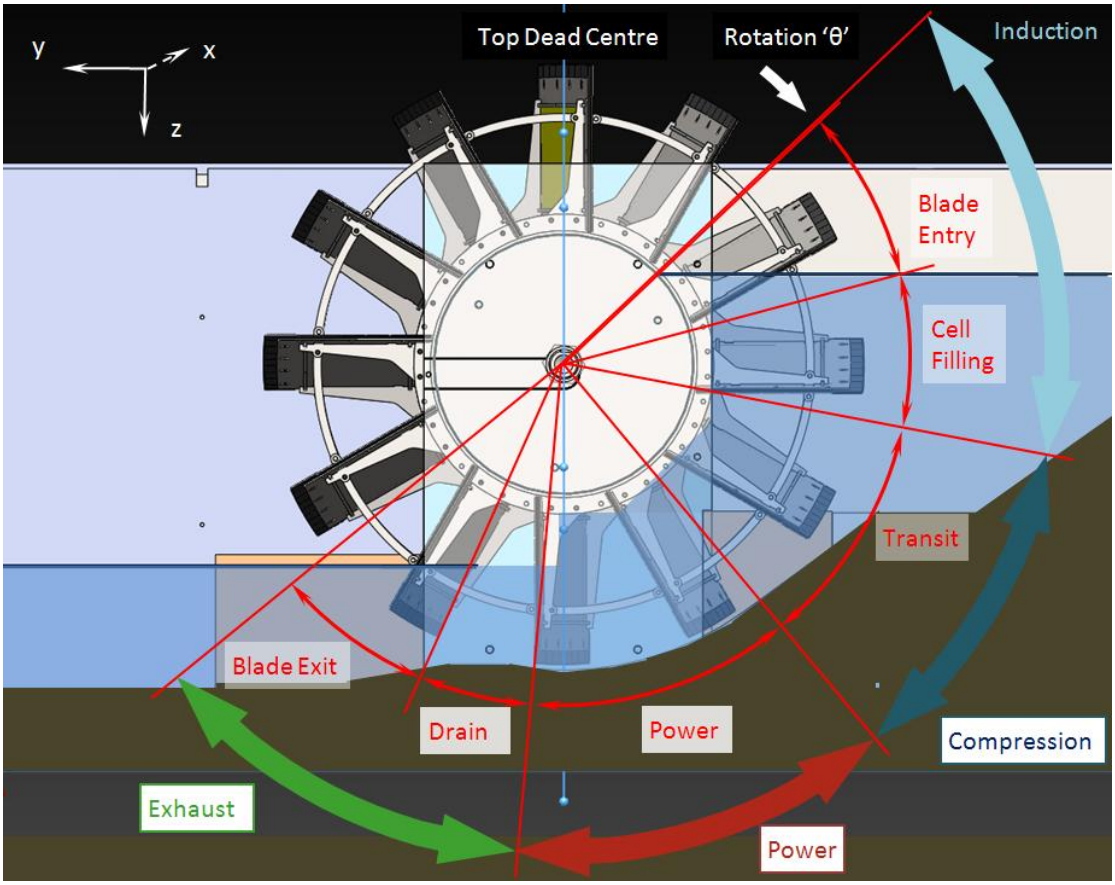

Figure 10.2: Detail 'Cell Processes' during HPM operation

10.2 'Time Series' Measurements

10.2.1 Limitations of the Data

Due to the limited rate at which data could be read using the available equipment (limited to 64Hz as described in Chapter 8), the resolution of measurements steadily reduces for rotor speeds above about 20 rpm. To preserve the sparse data collected, filtering or smoothing operations are not normally carried out, with calibration calculations applied directly to the data stream. The advantage of this is that no distortions or phase shifting of data has been introduced into the results by post processing operations; what is presented, is what was measured. The disadvantage is that for higher rotor speed plots in particular, the reader may have to look a little harder at some of the graphs and judge for themselves what trends are present in the measurements.

Because of this, the results in this section need to be regarded as ***indicative***, rather than ***definitive*** measurements, particularly as rotor speeds increase.

Nevertheless, these measurements represent, to the authors' knowledge, the first attempt anywhere, to measure forces and pressure variations occurring inside an HPM rotor during operation and as such represents a valuable contribution to knowledge, since the form of the various plots are reliable even if absolute values need to be regarded with some caution. This data enables us for the first time, to see what is actually happening within the machine, rather than merely attempting to deduce how the rotor is interacting with the fluid from performance measures and external observation.

10.2.2 Terminology

Before we compare time series data, it will be helpful to clarify the relative positions of the transducers used and the terminology we will be using to describe the position of the blades and cells being considered. The schematic in Figure 10.3 represents transducer positions for the 12 blade rotor, which has blades position at a 30 degree pitch angle. Since the pressure transducer is in the centre of the cell, its angle of rotation measured from TDC lags that of the strain gauge blade by 15°.

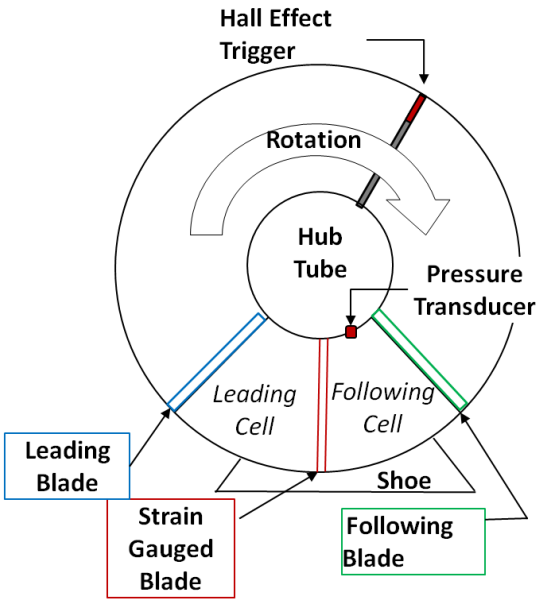

Figure 10.3: Time Series Terminology

When we consider the forces on a single blade, we need to understand that this force is impacted by the pressures in 2 cells, for which the blade under consideration forms the common dividing wall. The cell ahead of the blade rotation is termed the 'Leading Cell' while the cell behind is referred to as the 'Following Cell'. In turn, boundaries of the leading and following cells are defined by the 'Leading' and 'Following' blades, the position of which relative to the shoe and sidewall of the machine determine whether these cells are filling or draining with fluid.

10.2.3 Low Speed Blade Moment and Hub Pressure Variations

In order to eliminate as far as possible effects caused by the dynamic interaction of the rotor with the fluid, bending moment and hub pressure measurements for a very low speed rotor test condition are presented in the annotated graphic of Figure 10. 4.

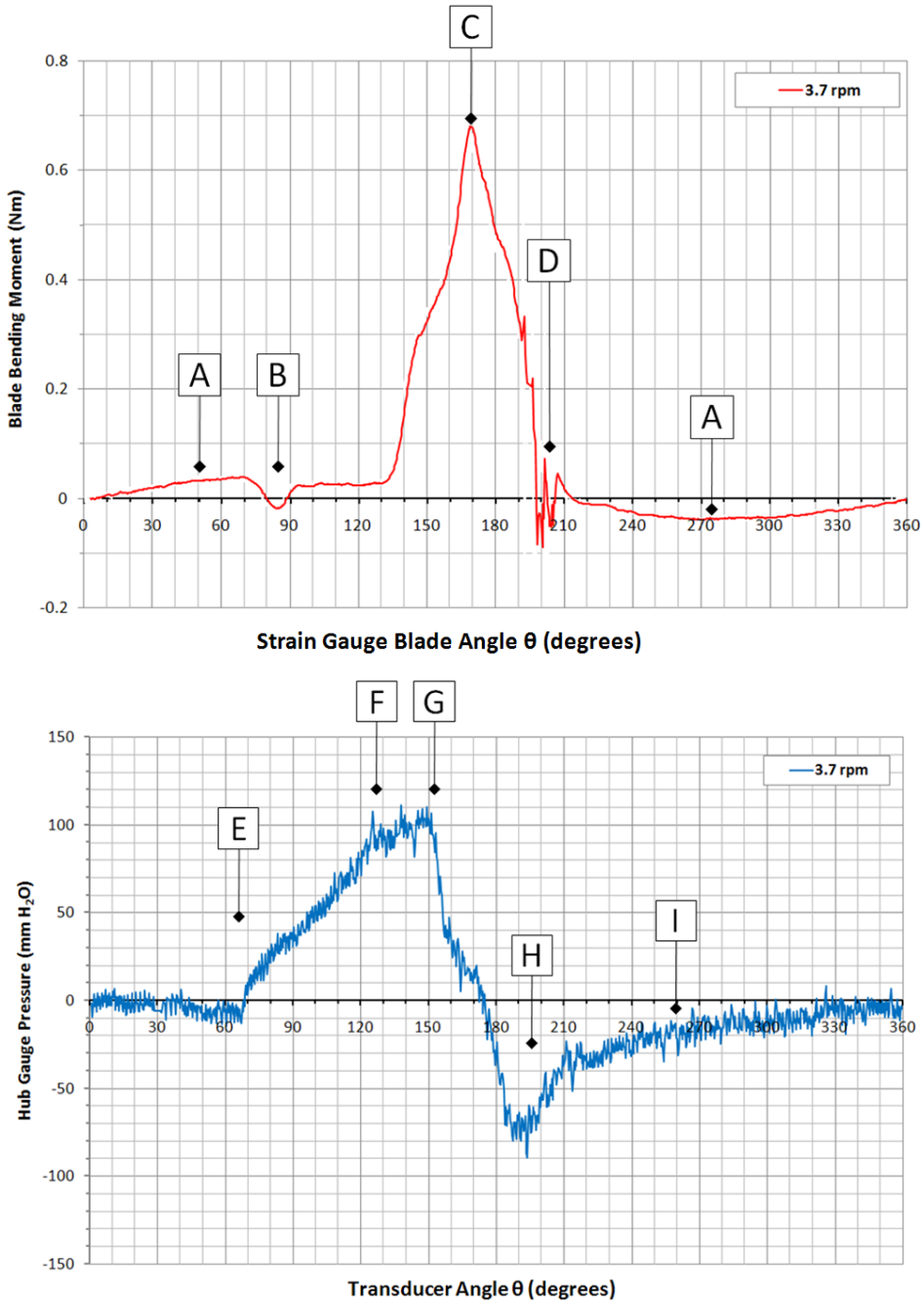

Figure 10.4: Bending moment and hub pressure variation at very low rotor speed

In this case the plots correspond to the 9/11 test water levels and for a 12 blade rotor turning at 3.7 rpm.

The key features of these plots are as follows:

Blade Bending Moment Plot *(upper graph)*

A. The strain gauges were sensitive enough to pick up the change in moment due to the weight of the individual blade – positive on the upstream side, negative downstream. This effect is corrected for in all subsequent plots.

B. Due to the very low rotor speed, blade entry and cell filling merge into the same event producing a small negative moment as the flow is accelerated locally to the blade.

C. Blade bending moments produced during the power stroke are surprisingly uneven considering the rotor speed is too low to produce significant dynamic interaction with the flow. The shape of this curve reflects the variations in pressures across the cell as the blade progresses through the working section, from the start at $\theta = 126°$, to completion of the cell draining process at $\theta = 195 - 200°$. Peak bending moment corresponds to $\theta = 170°$.

D. This discontinuity in the curve is produced by contact occurring between the strain gauged blade and the shoe, producing 'rubbing friction' as described in the previous chapter. This was the only test case for which the Strain Gauged blade was in contact in this way.

Hub Pressure Plot *(lower graph)*

E. Following contact with the water, hub pressure increases hydrostatically with rotation of the machine.

F. At the start of the working section, the following blade closes the cell fluid from upstream water, and little or no increase in pressure with further rotation is possible.

G. Pressure falls rapidly as the leading blade passes the end of the shoe profile initiating the cell draining process.

H. The lack of cell ventilation in the model set up is clear even at these very low rotor

speeds, with large negative pressures developing as insufficient air is able to enter the cell to replace outgoing fluid.

I. The negative hub pressure readings need to be treated with some caution since negative pressures are being recorded at angles for which the cell is fully vented to atmosphere and completely drained of fluid. It seems likely that some instrument hysteresis is occurring here as the transducer moves from fully submerged, positive pressure to fully drained, negative pressure very rapidly.

10.2.4 The Power Generation Mechanism

The shape of the blade bending moment plot during the power stroke is complex, and since these rotor plots are produced at very slow speeds, is almost entirely a result of the differing cell pressures existing in the cells either side of the blade.

This is shown more clearly by considering the hub pressure plot of Figure 10.5.

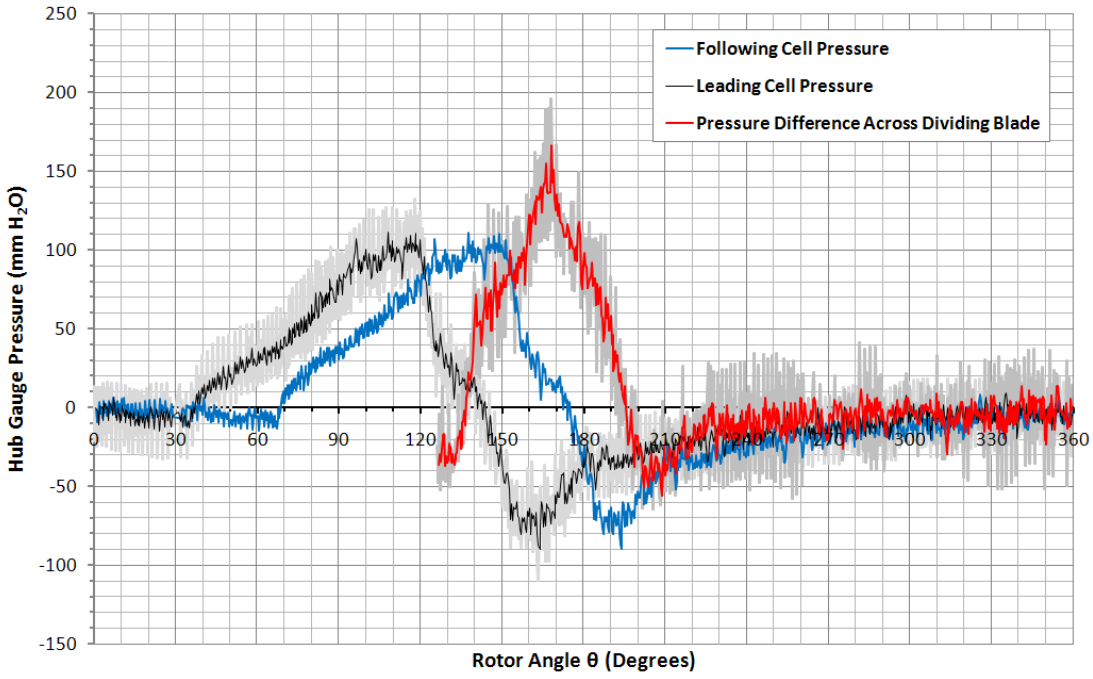

Figure 10.5: Form of Blade Bending Moment Measurements: pressure differential developed across the blade in the working section

This graph shows three pressure plots: leading and following cell pressures which are constructed from identical data, simply phase shifted by 30 degrees to account for the

differing cell positions, and a pressure difference plot, where the pressure in the leading cell is subtracted from the pressure in the following cell and plotted at the angle corresponding to the location of the blade dividing the two cells. Since this pressure difference generates no overall blade force before the blade enters the working section, the pressure difference plot is only represented from θ = 126° onwards. The original data stream included a lot of signal noise, and so 3 point moving averages have been graphed here. This explains the small discrepancy in phase angle in this graph compared with the bending moment plot of Figure 10.4.

However, comparing the pressure difference graph with the blade bending moment plotted above shows a marked similarity in shape and it is clear that the exit pressure has a significant impact on the form of the blade bending curve that goes beyond the direct energy losses due to acceleration so far considered by the theory. In fact, blade pitch, shoe length and cell emptying all have a significant effect on generating blade pressure differences during the power stroke as we shall see in a later section where 12 and 6 blade rotor measurements are compared.

10.2.5 Rotor Torque due to a Single Blade derived from Blade Bending Plots

While the variation in blade bending moment aids understanding of basic rotor behaviour, rotor torque variations would be a good deal more convenient when considering energy exchanges occurring between rotor and fluid. However, due to restrictions in the available equipment, the strain gauge blade was only able to measure bending moments occurring during operation with no data collected regarding the distribution of shear forces.

Initial blade torque estimates were based on idealising distributed blade forces to a single load acting at the centre of the blade area. This load was sized to yield the measured bending moment at the strain gauge station and torque about the shaft axis calculated accordingly.

However, a more accurate value for the torque produced at the shaft axis by an individual blade was obtained by equating the work done during a single revolution by this estimated torque, with that of the complete rotor as measured during performance

testing. This required the following assumptions to be made:

1. The true torque produced at the rotor shaft by the single blade is proportional to the estimated torque extracted from the bending moment readings as already described.

2. All blades in the rotor produce the same forces and torque about the shaft as the strain gauge blade. This implies that the work done by a single blade during one rotation will be 1/12 of the work done by the rotor as a whole for a 12 blade and 1/6 in the case of a 6-blade unit.

3. There are no speed variations in the machine with the rotor turning steadily at the mean angular velocity measured during performance testing – an assumption most prone to error at very low operating speeds.

Recognising that if the rotor angle is measured in radians, the area under the estimated torque-angle plot represents the work done by an individual blade, trapezium rule integration was carried out to obtain the total work done by a single blade over one revolution.

From the assumption of steady rotational speed, the time taken to do this work could be found from which the power contributed by a single blade to overall rotor output, could be calculated. This was compared to the corresponding single blade proportion of total rotor power measured during performance testing and any variation between the two values identified. Estimated torque values were then factored as required to produce parity with performance measures and corrected values for the 'rotor blade torque' obtained. The 'rotor blade torque' obtained in this way is compared directly with the measured blade bending moment for a 12 blade rotor at 22.1rpm at the 1/12A test condition in Figure 10.6.

Presenting data in this way is particularly useful since it gives a direct visual indication of the relative magnitude and importance of energy exchanges taking place during each cell process occurring at each phase of machine rotation. The area under the plot, but above the horizontal axis represents the energy extracted from the fluid by the rotor, while the area bounded by the plot below the horizontal axis represents energy losses.

Before we consider how the energy exchanges vary with rotor speed, it will be useful to

first compare a nominal plot with the cell processes presented at the start of this chapter.

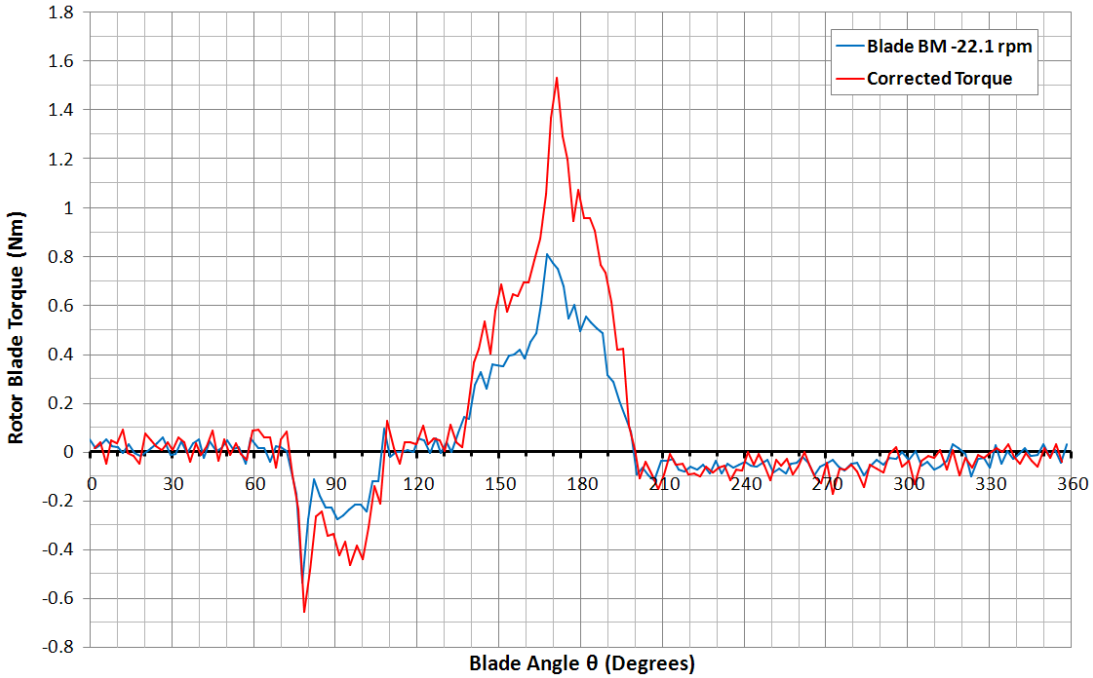

Figure 10.6: Measured blade bending moments compared with derived shaft torque for a single blade

10.2.6 Cell Processes compared with Rotor Torque Variations

The cell process notation is applied to a typical blade rotor torque plot in Figure 10.7. Once again this torque plot is for the 1/12A test condition and at 26 rpm corresponds to the maximum power output speed for the 12 blade rotor.

We will consider each process in turn:

Induction is initiated by blade entry, marked by a large negative spike in the torque curve corresponding with blade impact with the upstream water surface. This is followed by a sustained period of negative torque as cell filling takes place and local flow is accelerated to rotor speed.

During **Compression**, very little energy change occurs as cell pressure is raised hydrostatically by the increasing rotor angle during the transit phase.

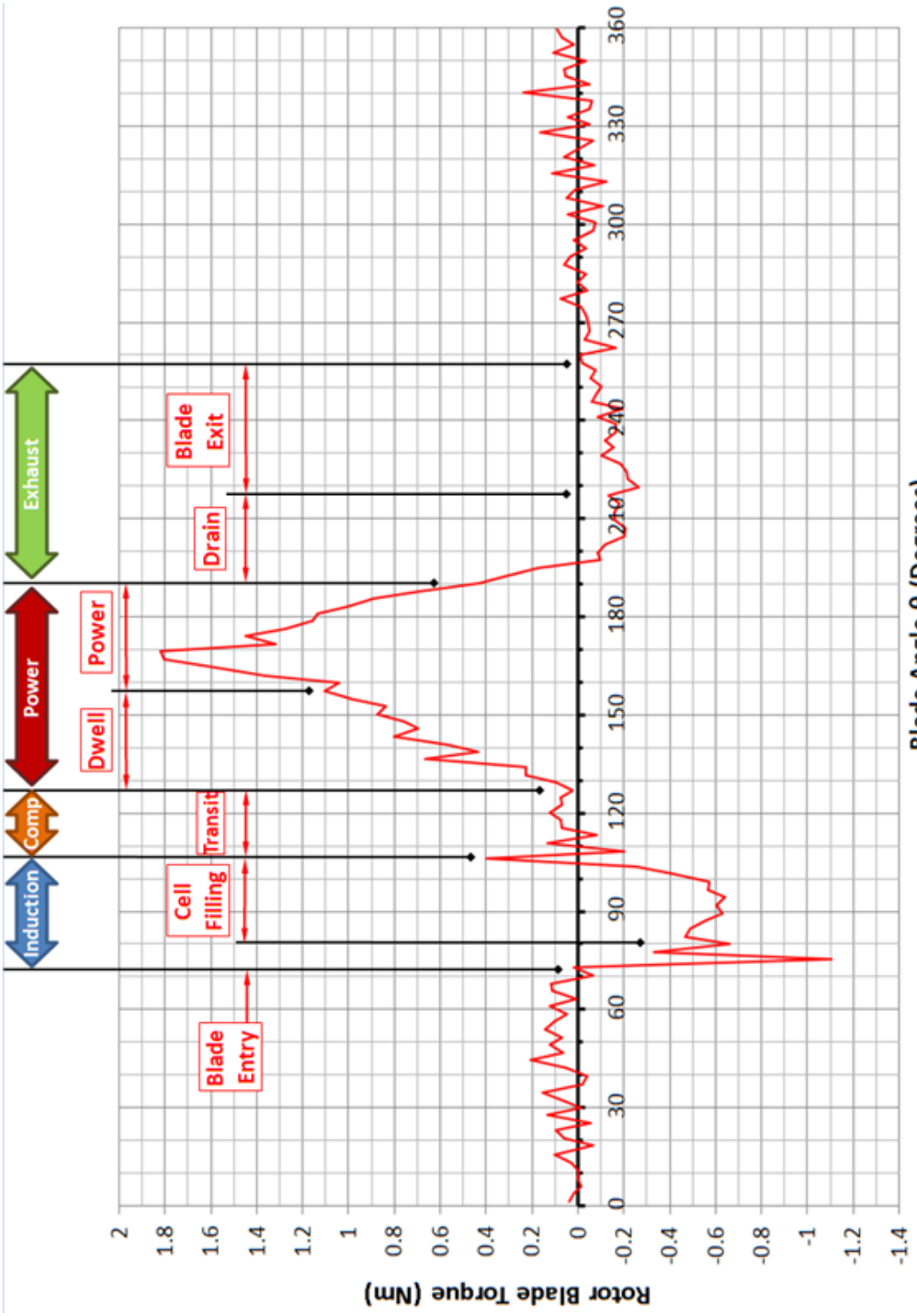

Figure 10.7: Cell Process and Torque Variations Compared

Power is extracted in two stages: the first is produced by the pressure contained in the full cell entering the working section during the dwell phase, working against the reducing pressure of the leading cell experiencing pressure loss as power is extracted during its main power stroke. The second and main power extraction stage begins as fluid is drained from the leading cell, generating full pressure difference across the blade for the first time. As we shall see later, the Power stroke is significantly different in a 6 blade rotor compared with the 12 blade device considered here, which accounts for the significant gains in performance obtained in the former device.

The **Exhaust** phase contributes some positive power extraction as fluid drains from the cell, although a significant amount of energy is lost during blade exit.

Comparing the areas under the curve we see that direct losses due to induction are very significant and represent 3 times more energy loss than those occurring during blade exit. However what is not apparent from the graph are losses due to fluid acceleration and turbulence which are experienced by the system as a loss in pressure head, and the degree to which the power extraction process is distorted due to poor cell ventilation. Both of these effects need to be deduced from other observations.

10.2.7 Variation of Torque and Hub Pressures with Speed: 12 blade rotor

The way in which hub pressure and blade torque changes as the rotor spins at different speeds across the operating range is investigated in Figure 10.8. Once again the 1/12A test condition is presented for a 12 blade rotor at three different operating speeds, corresponding approximately to peak efficiency (8.7 rpm), a little under peak power (22.1 rpm) and a high speed condition at which efficiency has fallen to approximately 20% (42.2 rpm).

First we will consider the hub pressure plots shown in the upper graph.

At the low speed maximum efficiency condition (8.7 rpm), the pressure plot displays the characteristic ‘shark fin’ profile already seen in Figure 10.4. However, as rotor speed increases, considerable distortion of this pressure curve takes place. The large pressure spikes at 90 - 100° corresponding to ‘water slamming’ contact of the following blade with the water surface. Following blade contact, turbulent conditions must be present

judging by the pressure fluctuations recorded, with very little gain in pressure now seen with increased rotation of the machine. Note the reduction in peak pressure attained compared with the low speed case – a result of head losses due to acceleration and energy losses caused by the turbulence already observed. The low data collection rate has badly affected the 42.2 rpm pressure plot which makes interpretation of the graph a little difficult and has to be treated with some caution. However, both 22.1 and 42.2 rpm curves show a more or less linear trend in the decline of pressure from $\theta \approx 150^{\circ}$ to the peak negative pressure following draining at around $\theta \approx 190 - 200^{\circ}$.

Turning our attention next to the blade torque plots in the lower graph of Figure 10.8 reveals a great deal about the changes in energy exchanges occurring at increased rotor speeds. For ease of reference, this figure is produced overleaf with the accompanying explanations presented on the facing page.

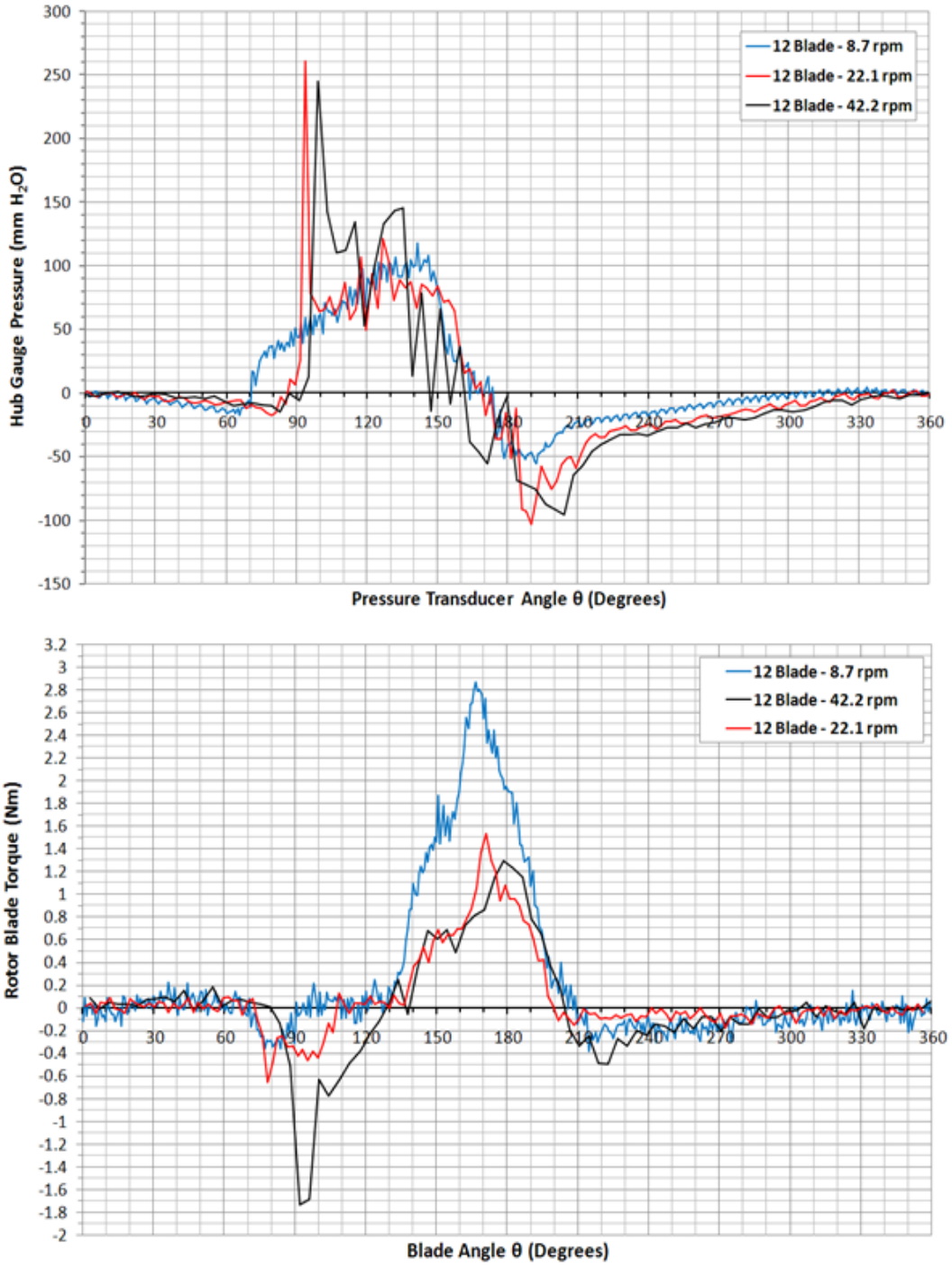

Figure 10.8: Variation of Torque and Hub Pressure with speed: 12-blade rotor

The ‘Mountain Peak’ form of the 8.7 rpm plot is already familiar from the very low speed rotor plot already shown in Figure 10.4, although the increase in speed has resulted in an increase in energy loss during cell filling between θ≈ 70 - 95° and a stronger definition in the rising torque plot of the end of the ‘Dwell’ stage of power extraction at θ≈ 150 - 160°.

Note how little energy is lost during blade exit from θ≈ 210° onwards at this low speed condition. In contrast the magnitude of energy losses during the induction phase increases significantly with rising rotor speed, with large spikes in negative torque values corresponding to blade entry and large areas of energy loss occurring during cell filling both evident in both the 22.1 and 42.2 rpm traces.

There is some ‘phase shift’ evident in the 42.2 rpm plot, with blade impact initiating some 10° of rotation later compared with the 22.1 rpm trace. This may be partly due to the low data collection rate which, depending on the exact timing of data reading compared with the hall-effect trigger at TDC could induce errors of up to 6°. This could also be partly due to alterations in the position of the water surface at high impact speeds as described from video observations in a later section.

The changes in torque during power extraction are interesting for a number of reasons. First, the reduction in peak torque values is significantly more than can be accounted for simply by the pressure reduction observed in the previous hub pressure plots, indicating some process changes may be occurring. Second, the positive area under the curve is very similar for the 22.1 and 42.2 rpm plots, suggesting that changes in power extraction are relatively stable and that decreasing efficiency for the machine at higher rotor speeds is due to increases in other energy loss mechanisms. Thirdly we note the continued presence of the ‘shoulder’ in the torque curve at θ≈ 150 - 160° as the two stage power extraction process occurring during the Dwell and Power processes continue to make their presence felt.

Finally in this section, we will compare the three torque traces during the blade exit process from θ≈ 210° onwards. A slight surprise is that energy losses at 22.1 rpm are actually lower during blade exit than for the 8.7 rpm test condition, suggesting that either a change in fluid behaviour has occurred resulting in lower energy losses or that the blade is able to extract energy from the exit flow in some way. Some energy

extraction of this form was suggested in chapter 9 during the comparison of theoretical and measured performance curves and figure 10.8 may be further evidence t for this. In contrast, exit losses are much higher for the 42.2 rpm case and as we will see from the video observation evidence presented in a later section, a number of energy transfer processes, both positive and negative, are active during the exhaust phase of HPM operation.

10.2.8 Comparison of 12 and 6 Blade Rotors

Variations in hub pressure and blade bending moments during rotation are compared between 6 and 12 blade HPM units in Figure 10.9.

The 'Shark Fin' form of the hub pressure plot *(Figure 10.9 upper)*, is similar in both devices at the low rotor speeds under consideration, although the rate of decline and magnitude of negative pressure developed, are both more pronounced in the 6 blade unit. Also absent from the 6 blade plot is the 'check' to the falling pressure gradient occurring in the 12 blade unit from $\theta \approx 155 - 180°$. This may be evidence that the cell emptying process is much less efficient for the 12 blade unit with the smaller cell sizes employed presenting a greater restriction to the exiting flow.

The contrast in blade bending moments *(Figure 10.9 lower),* between the two machines is striking. With twice the volume of fluid to be accelerated by each blade, the higher negative torques occurring between $\theta \approx 60°$ and $\theta \approx 126°$ is to be expected. What is notable is the complete loss of the 'Mountain Peak' shape from the plot during the power stroke; with full static head difference applied across the blade throughout the working section, a near constant blade force results, at much higher magnitude than the peak bending produced in the 12 blade unit. Here then is evidence of the fundamental benefit of 6 blades compared to 12 – the generation of blade force appears to be much more effective with the fewer number of blades and, while some improvements to cell emptying also appears to be present, this seems to be the dominant affect.

The near 'digital' behaviour of the blade bending moment appears to indicate the first of these explanations is valid, in which case, it would be interesting to take

measurements from a 12 blade rotor matched with a 30°shoe segment angle for comparison – sadly not covered by the present work.

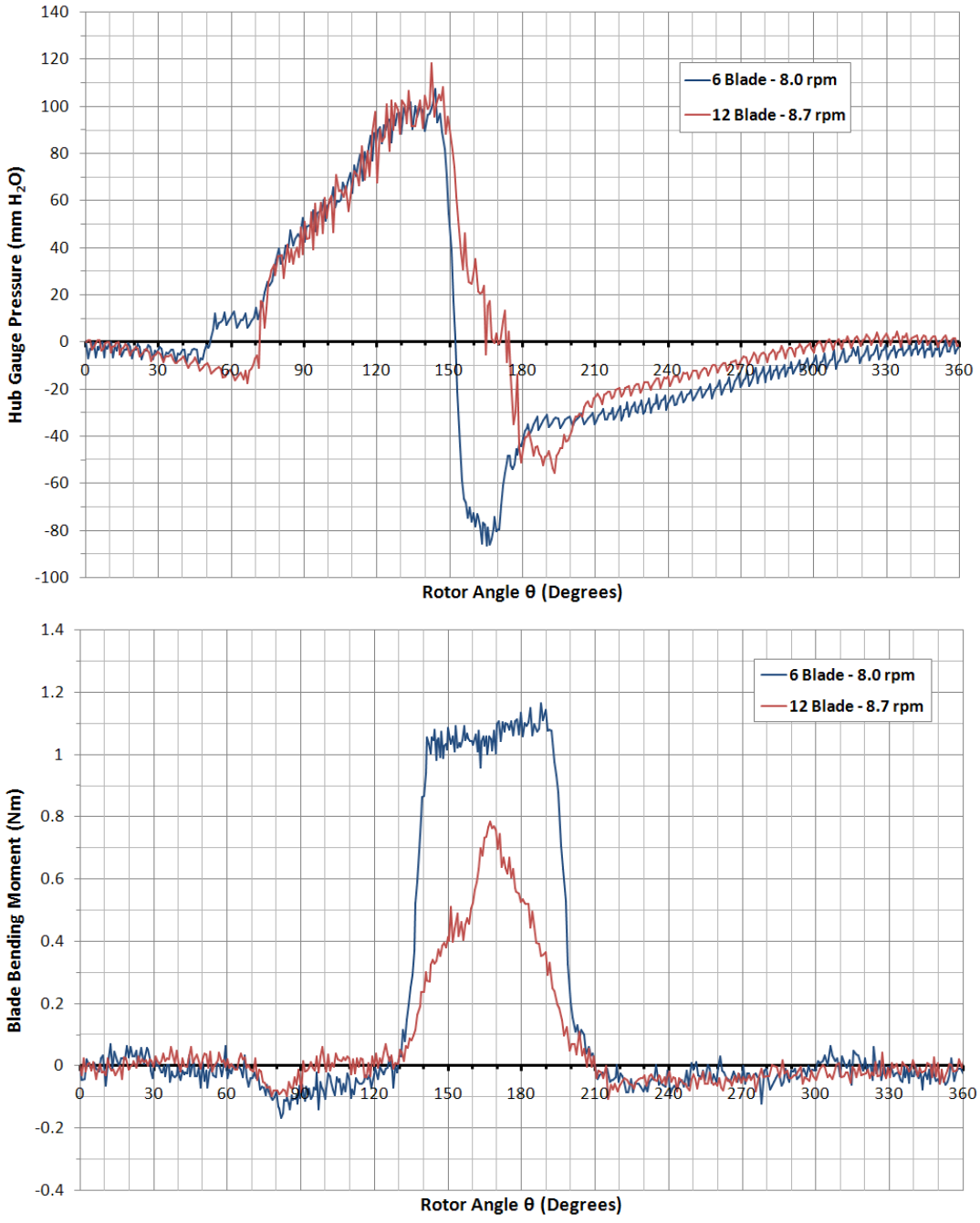

Figure 10.9: Direct Comparison of 6 and 12 Blade Rotor Characteristics

10.2.9 Variation of Torque and Hub Pressures with Speed: 6 blade rotor

Having found a fundamental difference in power extraction behaviour between the 12 and 6 blade units, the variation of 6-blade rotor characteristics with changing operating speed are presented in Figure 10.10. These curves correspond to the usual 1/12A water levels with speeds selected to approximately correspond with peak efficiency (8 rpm), a little under peak power (30.7 rpm), and a gross efficiency of ≈20% corresponding to the 45.1rpm rotor speed.

The general form of the variation of Hub Pressure plot *(Figure 10.10 upper)* with speed follows a similar general pattern to that of the 12 blade with a general decline and leveling off in measured pressures with increasing rpm. Pressure peaks following blade impact are still present and the large variation in measurements indicate that significant turbulence remains following cell filling. Negative cell pressures are more pronounced than in the 12 blade unit which fits with observations made in the previous section.

What is new are the large pressure spikes occurring around θ≈ 126° at 30.7 rpm and θ≈ 136° at 45.1 rpm, the cause for which is unclear but appears to be related to cell closing. This difference in angle between these two readings is most likely a data reading effect described previously, but the underlying cause of the pressure surges may be related to deceleration of the flow at cell closure. We may speculate that the horizontal component of velocity induced by the angled blades running parallel to the axis of rotation of the machine is brought to an abrupt stop as the cell volume enters the working section and a sharp increase in static head is the result. However, there is no other direct evidence to support this explanation and it must remain purely speculative.

The results from blade torque measurements *(Figure 10.10 lower),* exhibit a high degree of noise in the data and need to be interpreted with some caution. Having said that, we can make the following observations:

Energy losses during the induction phase are higher for both the 30.7 and 45.1 rpm test cases, than for the low speed example, although the absence of impact spikes at blade entry is puzzling and may point to transducer damage. Similarly, noise levels in the measurements make it impossible to draw any conclusions regarding energy exchanges during blade exit stage of rotation.

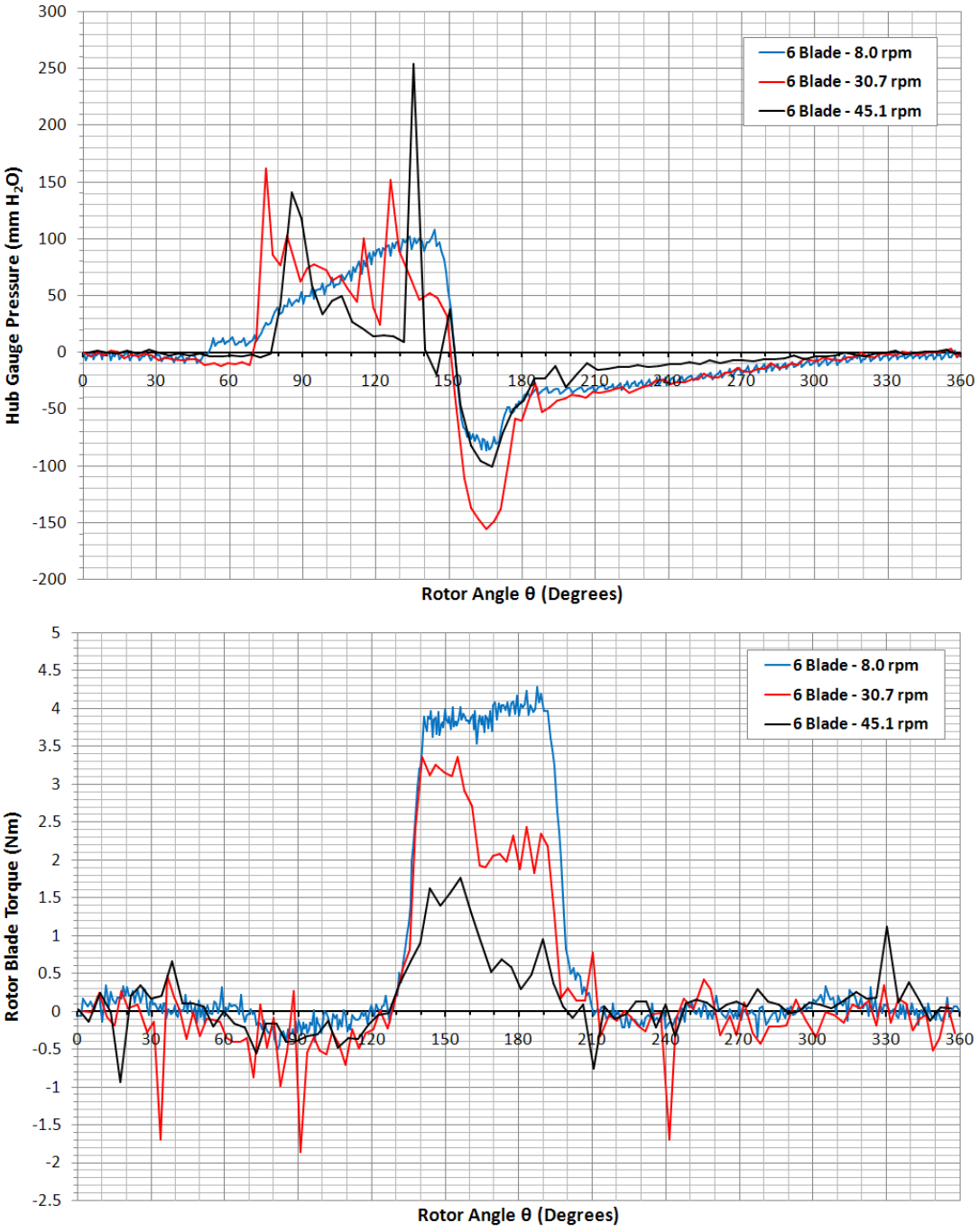

Figure 10.10: **Variation of Torque and Hub Pressure with speed: 6-blade rotor**

However, the form of the torque curves during power extraction is informative. The low speed plot is already familiar to us from the previous section. What is new is the change in form for the power stroke at higher speeds. There appear to be two distinct stages in power extraction, although blade forces are approximately constant through each of them. Maximum torque is produced during the first 20 - 30° of the power stroke, abruptly falling to a lower, but approximately constant value thereafter.

It is tempting to assign this step change to the negative cell pressure produced during cell emptying: this effect lasts for approximately 20 - 30° of rotation and would increase the effective head difference across the blade during this early stage. However, since low cell exit pressures were also present in the 8.0 rpm case, this explanation is flawed, unless the higher cell pressures during later stages of the power stroke, present in the 80 rpm data, cancel this effect out. It is possible, that the effect is related to cell emptying in some way, and the split of the power extraction process into two 30° stages does seem to indicate a geometry related process is occurring here. It is also possible that we are directly measuring the acceleration losses occurring during cell emptying. However, the exact cause of this behaviour remains unclear.

10.2.10: Speed Variations in 6-Blade and 12 blade Rotors

In previous chapters we noted the large potential performance gains that can be achieved using 6 bladed rotors compared with the 12 blade prototype. However, we also noted concerns about the magnitude of speed variations that may result from the use of a lower number of blades in the HPM.

In this section, variations in rotor speed as each blade passes through the working section of the machine are considered. Figure 10.11 shows direct traces of angular velocity variations over a single revolution for both 6 and 12 blade rotors at a range of operating speeds. Unfortunately, these readings are particularly badly affected by the lack of data reading resolution and signal noise, particularly at rotor speeds above 26 rpm.

However, below this speed, a difference in behaviour between 12 blade and 6 blade traces is apparent with very little cyclical variation seen in measurements in the scaled prototype unit. A slight offset is apparent at 180° rotation in the 8.7 rpm trace due to rubbing contact between a blade seal and the shoe.

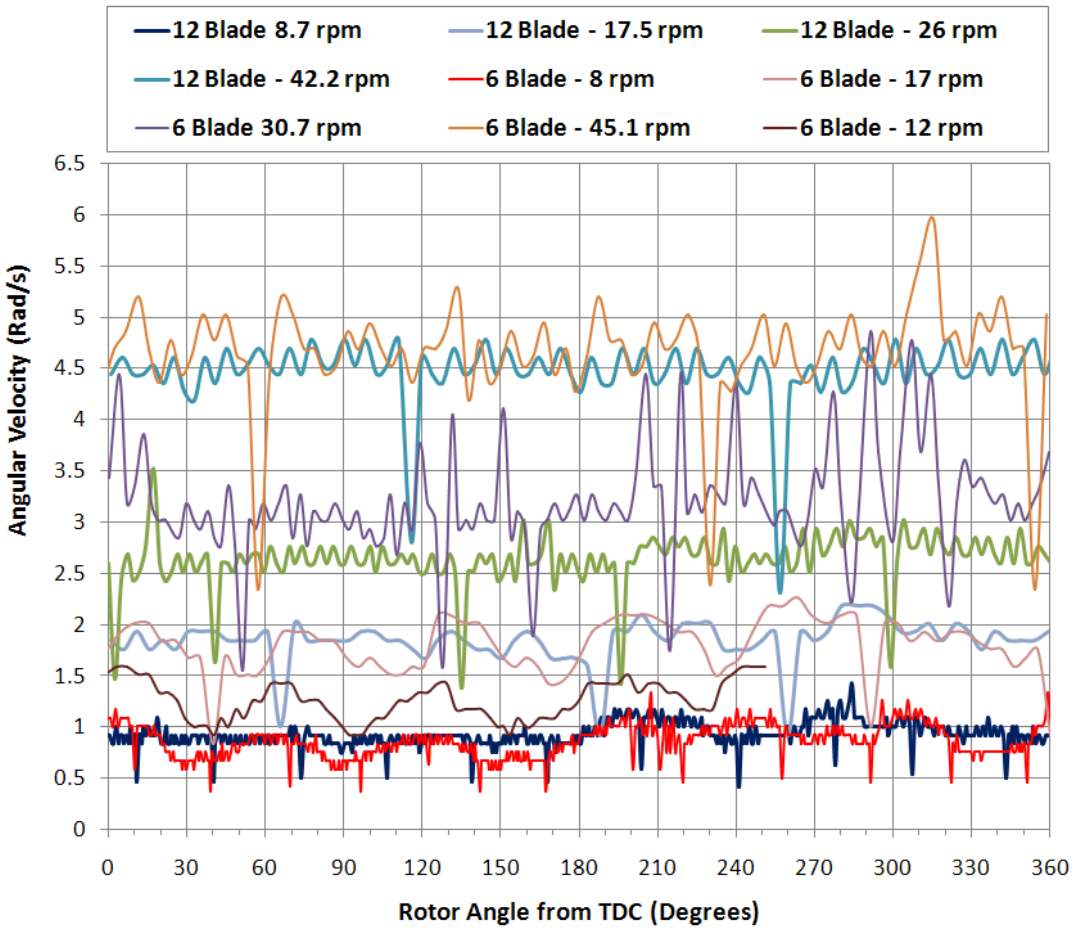

Figure 10.11: Rotor Speed Variations in 6 and 12 Blade Units

In contrast, cyclical variations with a period of 60° (corresponding to the blade pitch), are clearly present in the 6 blade traces. These seem to disappear in the rather noisy 30.7 rpm and 45.1 rpm data sets.

The 6 blade rotor traces are considered in a little more detail in Figure 10.12. In this graph, angular velocity measurements are normalised against the mean rotor speed, while to eliminate data spikes, a moving average trend line is applied through the data points. This figure enables a first estimate of the magnitude of these speed variations to be obtained: +/- 25% for 8 and 12 rpm plots, falling to +/- 17% at 17 rpm. The trace for 45 rpm is presented for comparison – all variations in this trace are due to inadequate sample rate and do not represent a pattern of altering speed.

These speed variations are large enough to be problematic to operation of practical machines and must either be attenuated through careful rotor design if low speed operation is intended, perhaps through the use of staggered blade sets or mechanical flywheels, or else the performance of the whole installation optimised to run at rotor speeds above 25 rpm.

While the quality of the data is poor, the implications of this section are important: speed variations are significant but limited to lower speed operations, and while these do not preclude the adoption of a 6 bladed rotor, they do suggest designers need to proceed with caution in this area.

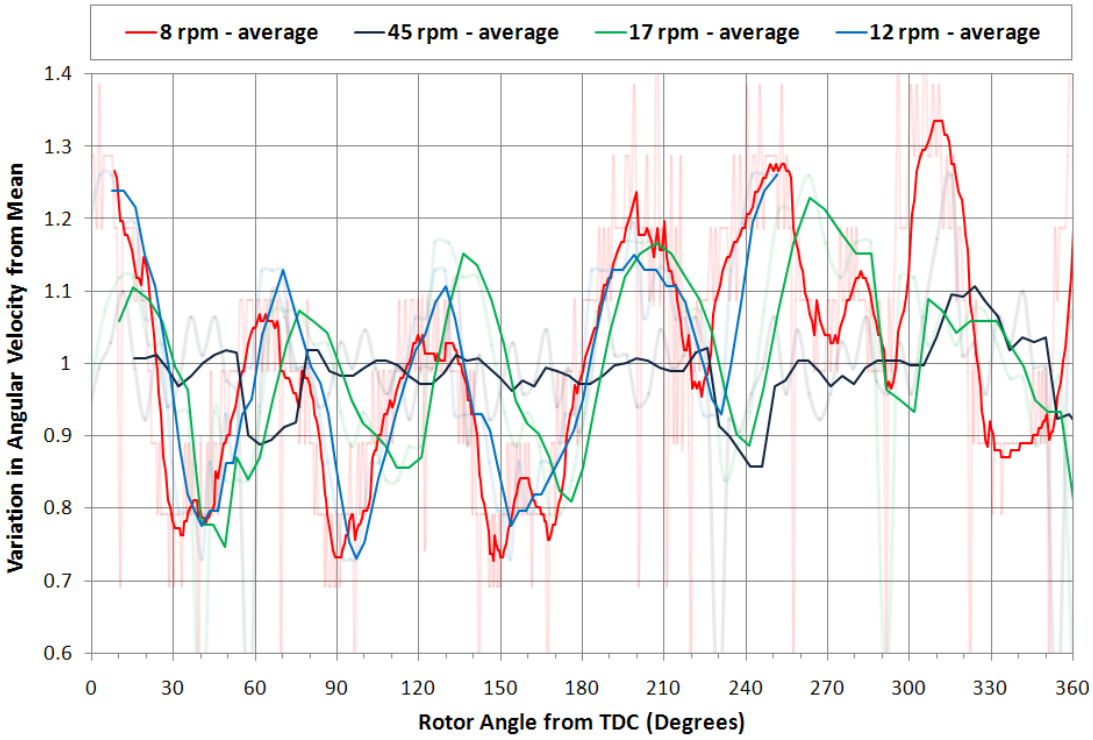

Figure 10.12: Angular Velocity Variations for 6 Blade Rotor as a Proportion of Mean Speed

10.2.11 Hub Pressure Variations with Downstream Water levels

We will conclude this presentation of time series data by using hub pressure measurements to examine variations in behaviour produced in the machine with increasing downstream water levels.

In Figure 10.13, Hub pressure measurements are compared for three different downstream water levels, corresponding to the test conditions studied in section 9.3.1.

The low speed plot, corresponding to maximum efficiency *(Figure 10.13 upper)* reveals that negative cell pressures decrease with increased water depth, although this decrease is relatively small and appears to be equivalent at both the DS-105 and DS-125 conditions. This fits with the efficiency measures already reported – the DS-105 condition offering the most overall benefit to machine efficiency.

However, the reader will recall that most of the efficiency gain was attributed in the new theory by the reduction in the acceleration required to increase the velocity of cell contents to that of the exit flows. The very modest changes in cell exit pressure measured here, also support this deduction.

The situation in the maximum power plot *(Figure 10.13 lower),* is much less clear. A zero offset error is clearly present in the 1/12A data, with pressure head readings plotted 6 – 7 mm higher than their true values. Once this discrepancy is taken into account, the 1/12A condition is very similar to the other two test cases although the scatter in the curves caused by the low data rate, mean that firm conclusions are difficult to draw. However, these measurements appear to support the findings in section 9.3.1, where efficiency gains due to increased downstream water levels were only significant at peak efficiency, becoming negligible by the time peak power output was attained.

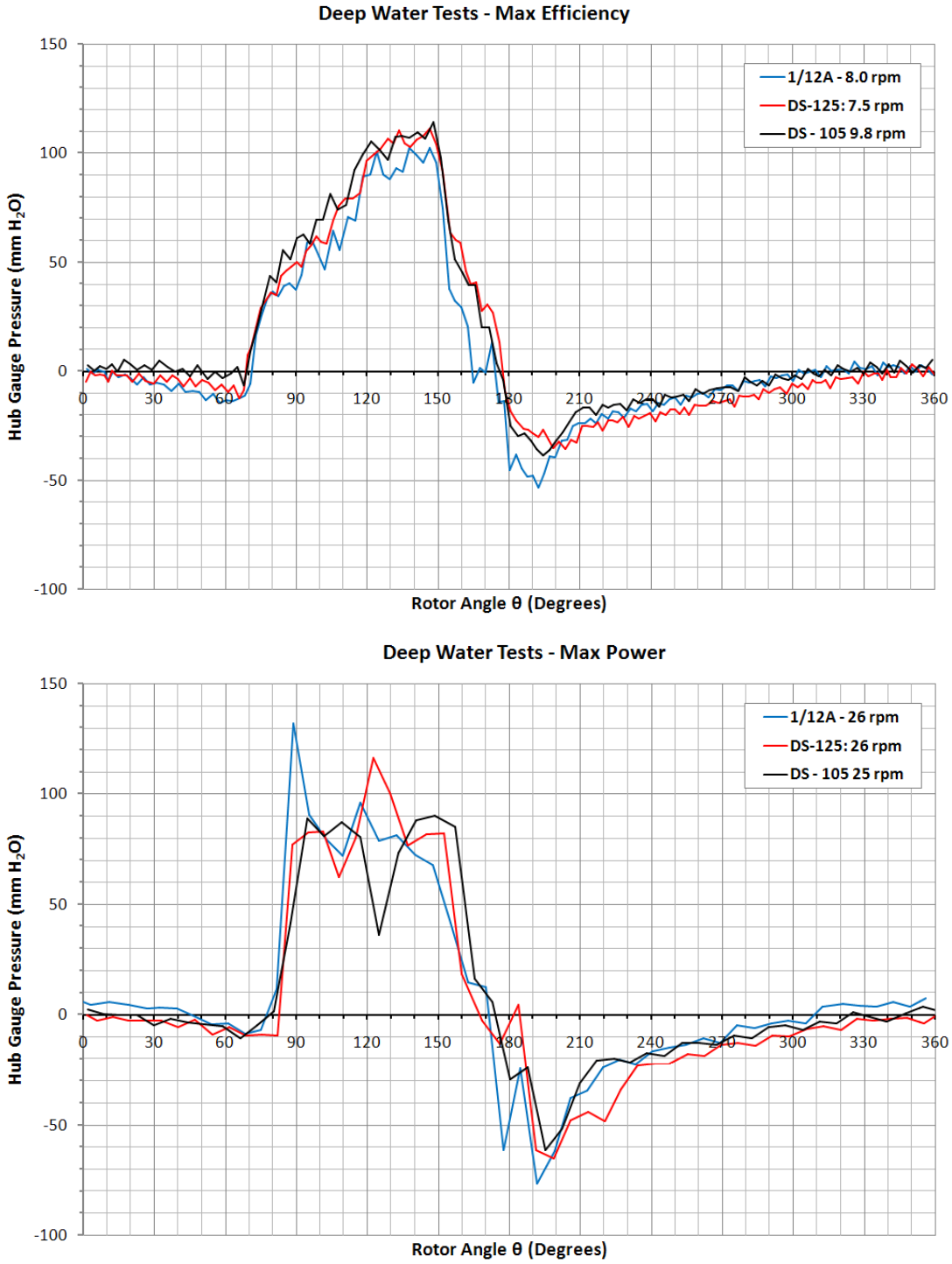

Figure 10.13: The impact on Downstream Water Level on Hub Pressure Variation

10.2.12 Summary of Time Series Data

So far in this chapter we have found the following:

1. The behaviour of the HPM can be considered as a series of discrete cell processes during which the fundamental energy exchanges during induction, compression, power and exhaust phases take place.

2. At low speeds, variations in blade forces are clearly related to changes in pressure in the cells either side of the blade in question.

3. The variation in rotor torque produced by a single blade during rotation, has been calculated and related to the cell processes already identified. The area under this torque curve gives a direct visual indication of the magnitude of energy exchanges taking place at each phase of rotation and at various rotor speeds.

4. The different power extraction behaviour has been identified for the 6 bladed rotor although the precise cause of the two stage power extraction process in these machines has not been identified.

5. Speed variations for 6 blade rotors are higher than for the 12 blade machine although this effect dies out above 26 rpm.

6. Earlier findings showing that increases in downstream water levels increase overall machine efficiency, have been confirmed.

10.3 Video Observation Studies

While time series data measures the effects of fluid-rotor interactions during rotation of the machine, identifying the underlying fluid behaviours taking place relies heavily on close observation during experiments. Video surveys were carried out alongside the performance tests already described and observations corresponding to each cell process during rotation are presented here. Where appropriate, observations from the various modified rotors are also presented for comparison, wherever the new designs significantly altered machine behaviour.

10.3.1 Blade Entry

The standard model is shown at the point of blade entry at four different rotor speeds in the picture sequence of Figure 10. 14.

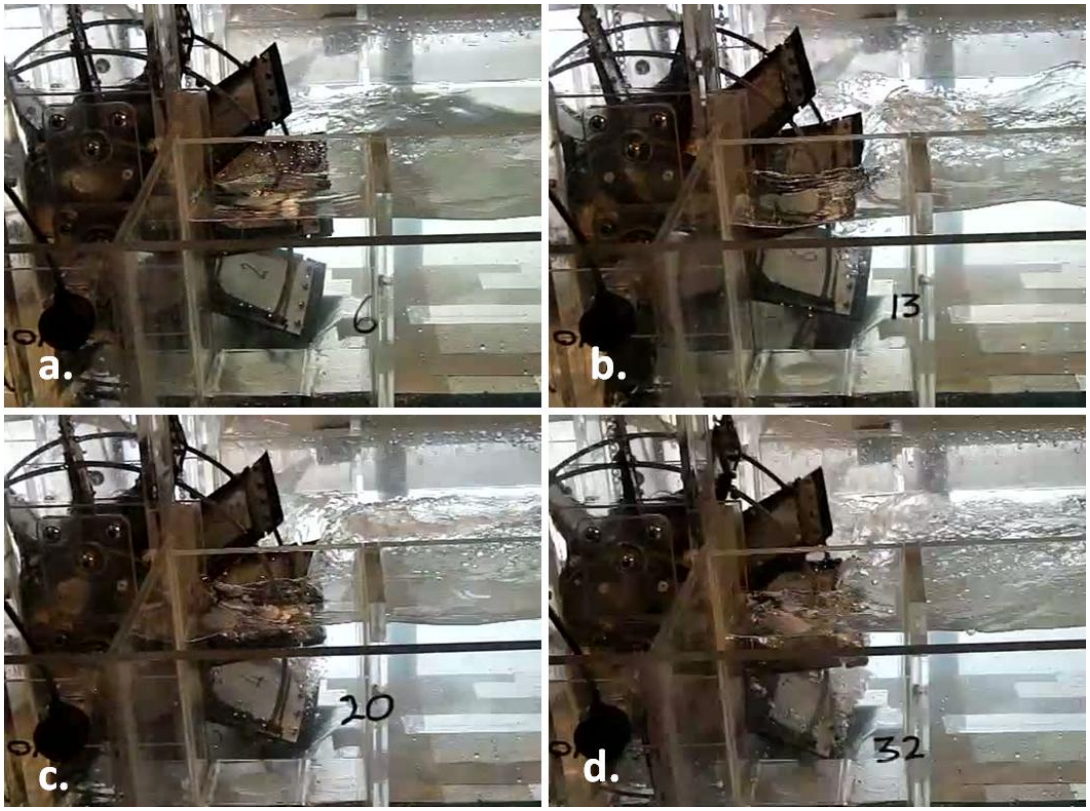

Figure 10.14: Blade Entry of the Scale Model at Differing Speeds:
a. 6 rpm, b. 13 rpm, c. 20 rpm, d. 32 rpm

There was a clear increase in energy loss on blade entry with rotor speed and, at 20 rpm and above, sufficient splash was generated to require equipment adjacent to the flume

to be splash protected. When Froude Scaling is applied, this model speed equates to 9.7 rpm at prototype scale and the levels of splash encountered compares well between laboratory scale and full size field trial experience.

However, blade impact and splash generation was far more severe with the 6 blade rotor, drenching adjacent equipment at moderate rotor speeds and creating blade impact forces large enough to cause yielding in the strain gauged blade used for force measurement (Figure 10.15 *upper*).

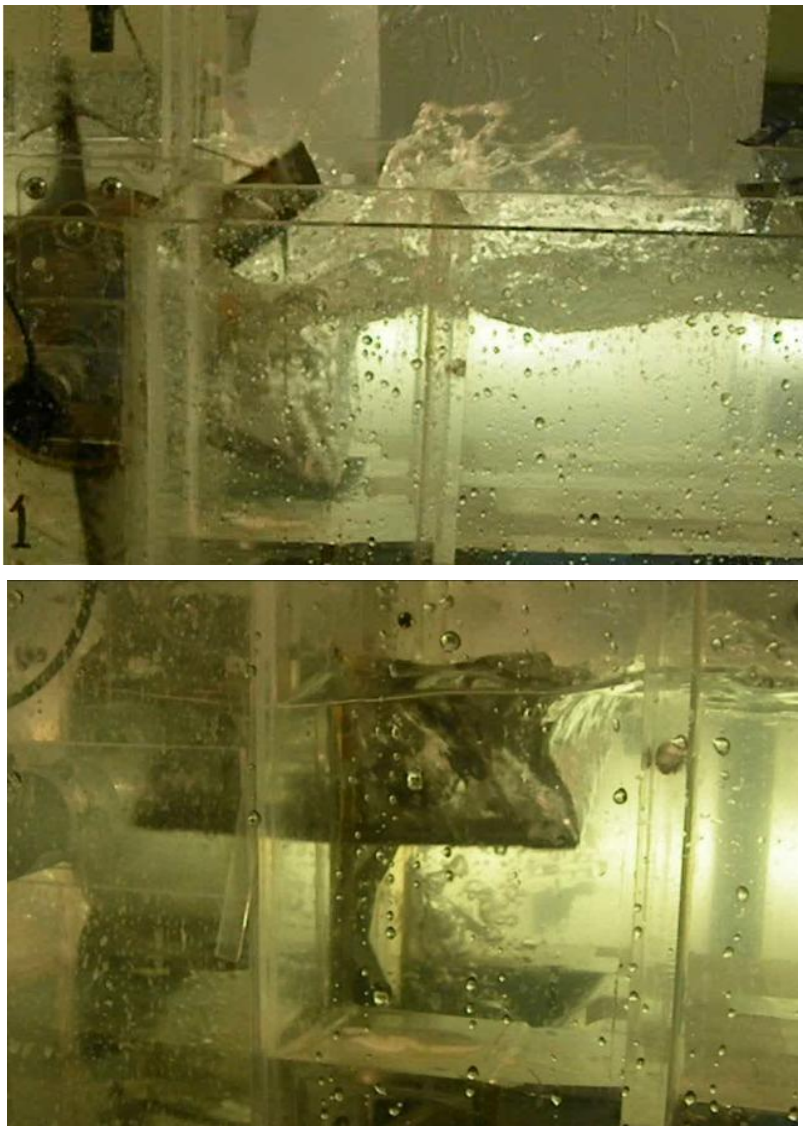

Figure 10.15: Blade impact in Alternate Rotor Designs at High rpm: 6-Blade Rotor *(upper),* 6-Blade Flap Wheel *(lower).*

The cause of this increased impact has to do with the ability of the disturbed fluid to recover to its original free surface level following the passage of each blade. On contact with the upstream water, fluid is pushed away from the blade area, creating an observable depression in the fluid surface. If there is sufficient time before the next blade strikes, water flows back into the depressed area, restoring fluid to its pre-impact levels after the blade submerges. However, in the 12 blade rotor, this time was limited and a semi-permanent depression of the blade surface was observed. Two effects are probably present here which reduced impact forces: first, the shape of the fluid surface in the depressed area results in a more gradual contact with the advancing blade and secondly, the entrapped air tends to cushion the magnitude of impact, (Gallagher & McGregor, 1986).

In the 6 blade rotor, even at relatively high rotor speeds, there is sufficient time for the surface of the fluid to be restored, resulting in the following blade encountering a relatively solid water surface. With the 6-Blade Flap Wheel rotor *(Figure 10.15 lower),* full deflection of the membranes can be seen which greatly reduces the area of blade experiencing these abrupt 'slamming' forces. This is further illustrated by the picture in Figure 10.16, taken underwater looking up at the advancing Flap Wheel blade shortly after it has made contact with the upstream water at around 15 rpm.

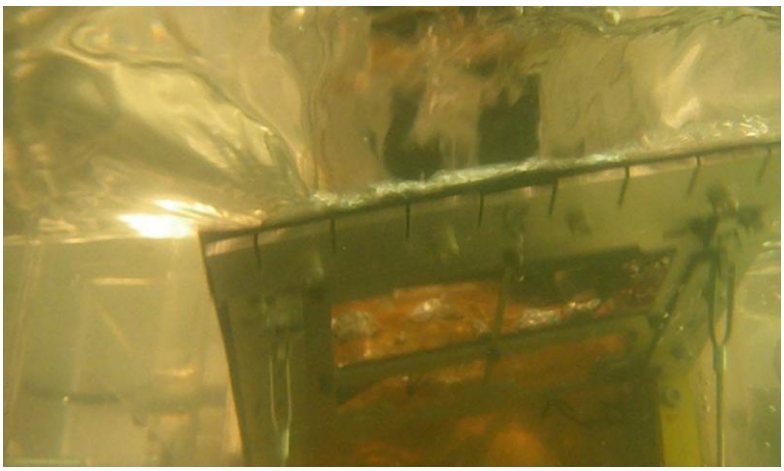

Figure 10.16: 6-Blade Flap Wheel Shortly after Making contact with the upstream surface.

The distorted area in the top third of the picture is created by the depressed free surface of the fluid and both inner and outer flaps are in the process of opening to allow fluid to pass, alleviating both drag and impact pressure. Also of interest is the line of bubbles just visible along the outer edge of the blade seals where a vortex is just beginning to form.

10.3.2 Cell Filling

Cell filling is a complex, turbulent process closely associated with the bluff body drag of the flat-plate blades. The sequence of events involved at two different rotor speeds are shown in Figure 10.17.

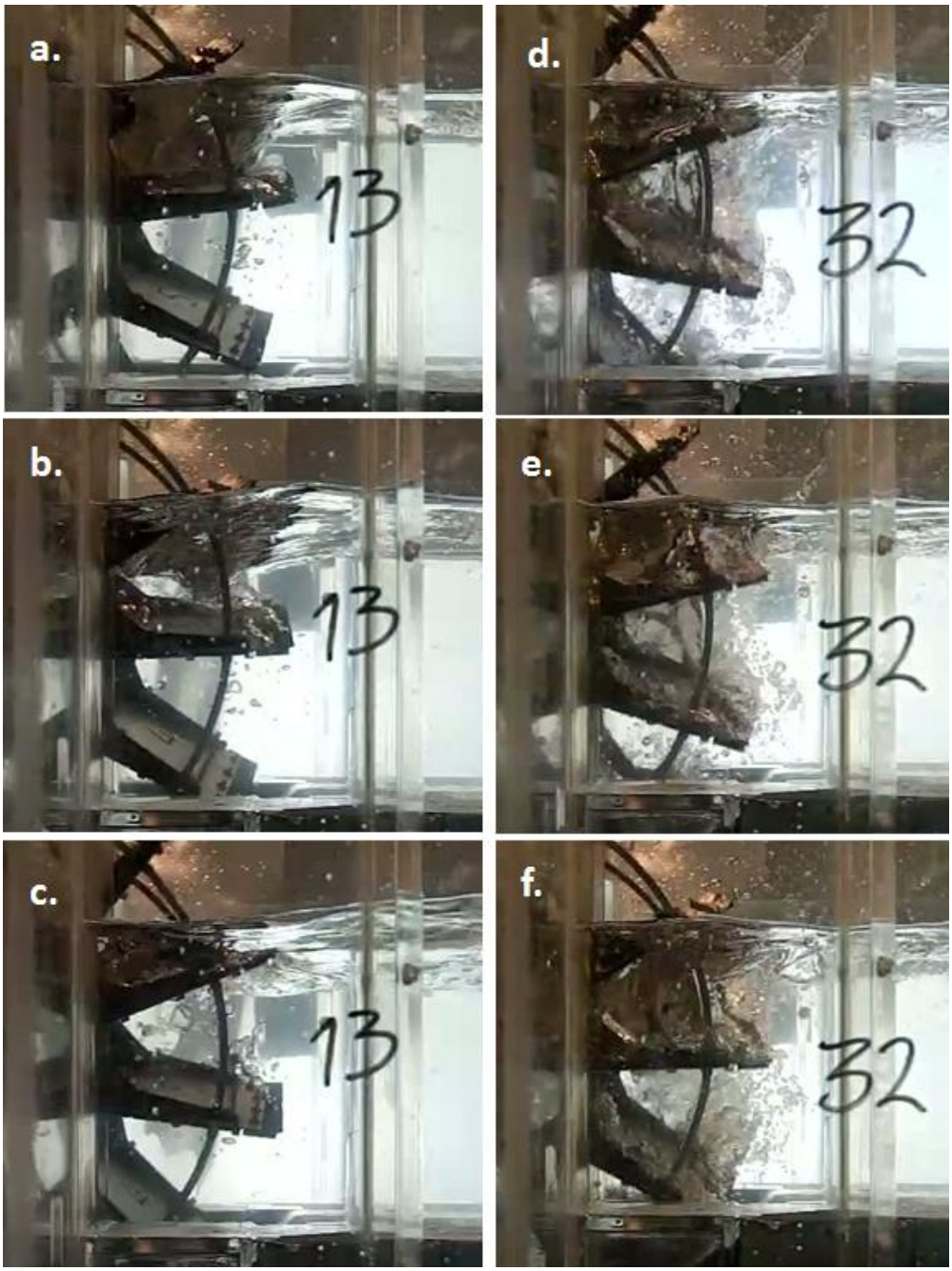

Figure 10.17: The Cell filling Sequence a-c 13 rpm, d-f 32 rpm

Rotation proceeds from top to bottom in the figure with a rotor turning at 13 rpm on the left and at 32 rpm on the right hand column of pictures. Cell filling develops as follows:

a. At low speed, blade entry initiates the start of cell filling with a bluff body separation bubble forming behind the blade, extending to the free surface of the fluid.

b. As the blade continues to advance, the separation bubble is reduced as water enters the cell and a vortex starts to form from the outside edge of the blade.

c. Filling is complete. The motion of the entrapped air bubbles by this point have lost any horizontal component of velocity, rising in response to buoyancy, giving a useful visual marker of completion of the cell filling process.

At the higher speed, the basic elements of cell filling are repeated, but complicated by the presence of the following blade.

d. The upper blade has just entered the flow producing a separation bubble extending to the free surface. However, the separation bubble behind the next lower blade is now bounded by the underside surface of the upper blade.

e. Fluid is starting to enter the cell behind the lower blade, indicated by the distinct region of bubbles. This entry is surprisingly evenly distributed across the arc of the cell.

f. Following the final sudden collapse of the separation bubble by the incoming water, entrapped air bubbles once again lose their horizontal velocity component.

The variation of rotation angle required for cell filling was quantified for both 12 and 6 blade rotors at 1/12A test condition water levels by direct measurement of blade angle from the video sequences. Slow motion video footage was advanced frame by frame until air bubble motion indicated that filling was completed. Measurement of the blade angle was then taken and the results plotted in Figure 10.18, for later comparison with theory. From these curves we note that a similar variation in cell fill-depth with rotor speed occurs in both 6 and 12 blade rotors, but that the 6 blade unit fills slightly more quickly, presumably due to the greater blade pitch reducing blocking of the separation bubble by the following blade.

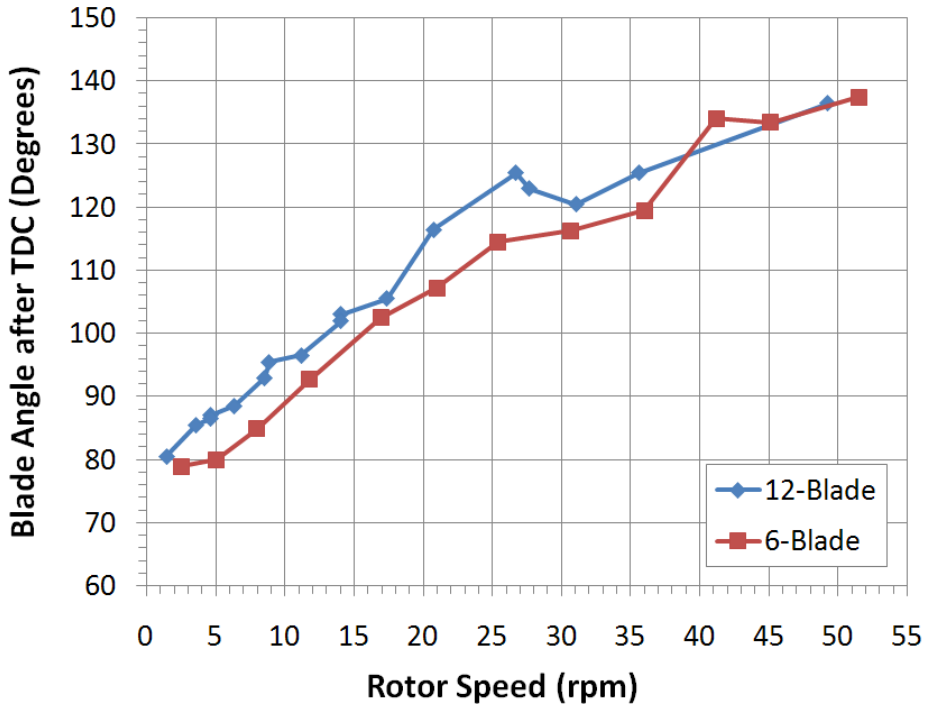

Figure 10.18: Variation of Cell Filling Angle with Rotor Speed for 6 & 12 Blade Rigid Rotors

10.3.3 Transit, Power and Cell Draining

Following completion of the filling process, cell contents move at the same speed as the blades, gaining pressure as rotation increases the depth beneath the water surface. During this period, little or no fluid enters or leaves the cell, and a sequence of pictures, detailing all of the rotor process following cell filling at 6 rpm are presented in Figure 10.19. These sequences show few observable changes in fluid behaviour between cell filling and the start of the emptying process, but do reveal the complexity of the interaction between cell-emptying and the power extraction process.

In each picture, the blade under study is marked with a centre line while water levels in the cell, wheel exit channel and main downstream channel are indicated with white, yellow and red markers respectively.

Even at this low speed, variations in water levels are significant and the bottom picture suggests that the cell emptying process directly impacts forces exerted on at least two blades passing through the working section of the 12 blade rotor – supporting the '2 stage' power extraction process identified by the time series data.

This offers an additional clue regarding the importance of the cell draining and ventilation process. So far, theory considers only the additional energy losses caused by delay in releasing fluid into the downstream flow if ventilation is inadequate. The time series data has shown that a more important power loss arises from delaying the point of rotation at which full pressure differential is developed across blades during the power stroke, which directly reduces the effectiveness of the primary energy extraction process. This is confirmed by comparing water levels during emptying and power strokes in 6 and 12 bladed rotors shown in Figure 10.20.

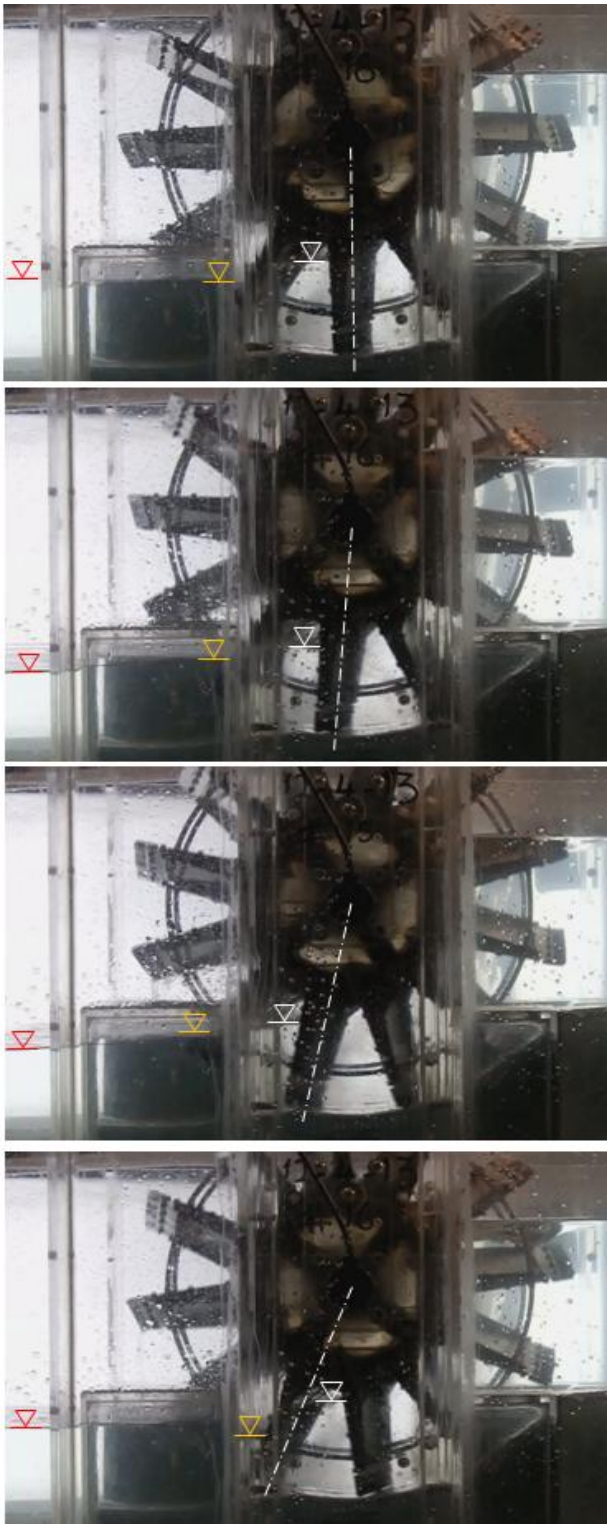

Figure 10.19: Dwell, Power and Cell Drain Processes: *Blade marked by centreline, water levels marked: cell (white), exit (yellow), downstream (red)*

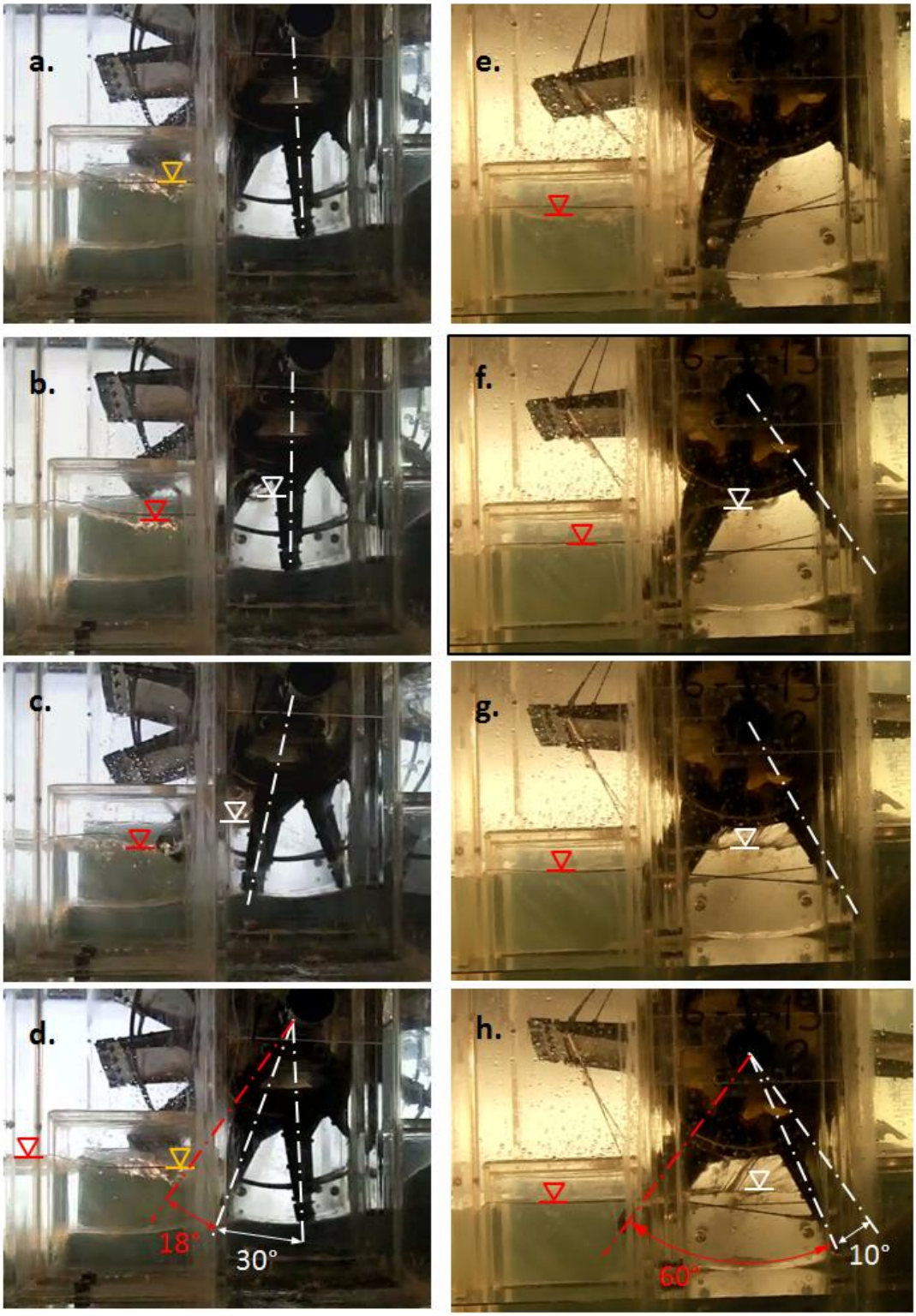

Figure 10.20: The interaction of Cell draining and the power stroke: 12-Blade rotor *(left)*, 6-Blade rotor *(right)*

In the figure, equivalent stages of cell emptying are arranged side by side, with the 12 blade unit displayed on the left. Both rotors are turning at around 10 rpm.

The sequence develops as follows:

a& e: Both cells are completely full of fluid, and emptying is about to start. The cell is bounded by the 'leading blade' which has just reached the limit of the shoe profile and the 'following blade' which, in these pictures has been marked with a centre-line. We will consider the forces generated at the 'following blade' by the differential pressure acting across it, in this sequence of images.

b& f: The leading blade has cleared the shoe profile and the cell is now 'open', releasing fluid to the downstream side through the gap developing between the outer edge of the blade and shoe profile. Water levels inside the cells are starting to fall as fluid drains. Note the localised drop in exit channel water level adjacent to the blade evident in image b. This is a result of fluctuations in exit water velocities caused by variation in the rate of release of fluid by the cells at these low rotor speeds.

c& g: There is a noticeable slowing in the fall of cell fluid levels in the 12 blade rotor, with the draining process apparently halting temporarily as the restricted in-flowing air acts as a gas spring. This slowing was only momentary and not so easily observed in the 6 blade unit.

d& h: Draining in both cells is now complete with cell water levels matching those downstream. Full pressure differential is achieved across the 'following blade' at this point, and Power extraction reaches its peak level. The advantage of the 6 blades compared with 12 for this shoe geometry becomes evident from the contrasting angles marked on the images. The angle of blade rotation between the start and finish of the cell draining sequence is marked in white: 25° for the 12-Blade compared with only 10° required in the larger cells of the 6-Blade unit. Of even greater importance are the differing lengths of the power stroke marked in red at only 18° for the 12 Blade rotor compared with the 60° of rotation for which blade force is available to do work in the 6 blade unit.

These observations support the earlier findings from the time series data. However, from the picture sequences, it is clear that the 6 blade rotor geometry allows a much

quicker evacuation of water from the cell, which in turn enables full pressure differential to be developed across the blade far earlier in the power stroke. It is very likely that this is partly the result of an excessive arc length being selected for the shoe intended for use with a 12 blade rotor although as already mentioned a separate test using a 30° shoe with a 12 blade machine would be required to confirm this.

What is less clear is the extent to which a longer power stroke aids efficient energy extraction. Should rotor and shoe combinations be designed to maximise the length of the power stroke, or is the short duration application of blade force achieved by a properly matched shoe length in rotors with a larger numbers of blades equally effective?

As already demonstrated, the use of fewer blades leads to a substantial increase in the 'torque ripple' effect produced at the output shaft and the optimum combination of blade number and shoe length remains far from clear.

10.3.4 Blade Exit

In the 'Deep Water' test series described in chapter 9, a significant increase in what was termed 'Blade Drag' was observed which offset efficiency gains achieved by reduced acceleration and ventilation losses as downstream water depths were increased.

However, detailed study of the sequence of pictures in Figure 10.21 reveals that this 'Blade Drag' in the exit-channel actually has two components, only one of which results in an energy loss.

Linton (2009) observed that a useful side effect of employing flexible blades in a rotor was that their deflection gives a clear visual indication of the direction of resultant blade forces active at each stage of rotation.

The images in the figure were taken from under water, looking back at the rotor from downstream as the blades advance from bottom dead centre (BDC), to blade exit. The position of the flexible membrane elements is of importance here.

Image 'a' shows the blade at BDC. Note the black membrane is held flat against the supporting structure as the pressure difference across the blade extracts power.

In image 'b' membranes are still held flat as the blade advances. By this stage, this

positive force on the blade is not due to hydrostatic pressure difference, but rather to a momentum exchange occurring between the blade and the exit fluid. Both fluid and blade have a matching horizontal velocity at BDC but, as the blade advances, the changing rotor angle causes a reduction in the horizontal velocity component of the blade. Since it is now moving more slowly than the fluid and offers a substantial blockage of the exit channel, momentum exchange takes place resulting in an additional power extraction by the rotor.

By the time blade rotation has reached the position shown by image 'c', the vertical velocity component of the blade has become significant, generating an energy loss as the blade seeks to accelerate the exit flow which, prior to this stage, possessed no vertical velocity component.

In the case of a Flap Wheel blade, the membrane deflects under the influence of fluid drag forces to reduce this negative force, as indicated by the white arrow in the figure. In the case of a rigid blade, this upward force exerted by the blade on the water results in 'water lifting' behaviour observed during higher speed operation.

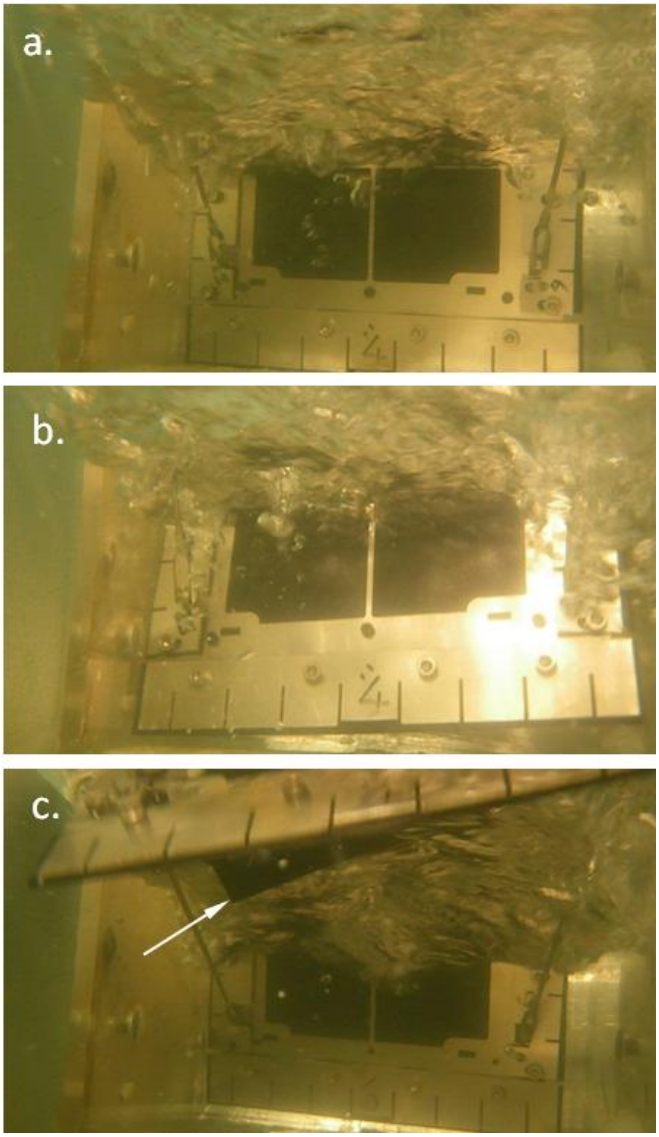

Figure 10.21: Drag Forces During Blade Exit:
Flexible Blade: a. at BDC, b. advancing , c. near exit

The deeper the downstream water depth, the more significant this effect becomes as illustrated by the deep water test case shown in Figure 10.22. The volume of fluid raised by the blade is outlined in red.

The degree of visible lifting appears to be dependent on the rate at which fluid can flow away from the rising blade, compared with the speed with which the blade is moving. The important point to note is that although water lifting is only visible at higher rotor speeds, this loss component must be present to a degree under all operating conditions.

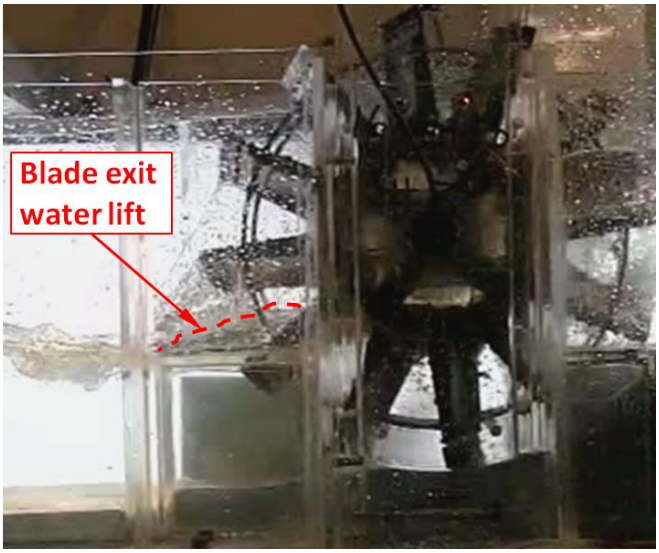

Figure 10.21: 'Water Lifting' due to the vertical velocity component of advancing blades

10.3.5 Summary of Key Findings from Video Observations

In this section we have been able to directly observe rotor–fluid interactions during the main processes occurring during rotation of the HPM.

The following important deductions can be made regarding energy exchanges:

1. The improvement in performance obtained from the 6-blade compared to the 12 blade rotor can be attributed to two factors. These are the more efficient emptying of the larger cells and, the significant increase in the length of the power stroke over which maximum cell pressure difference is applied obtained with this shoe geometry. It is likely that a correct match between blade pitch and the arc of the shoe profile are important design parameters for efficient operation of these machines.

2. Two 'drag' mechanisms are active during the blade exit phase of rotation, both related to momentum exchanges occurring due to relative velocity changes between the advancing blade and the exit flow. Horizontal velocity changes result in an additional power extraction, while vertical velocity components result in energy losses that produce the 'water lifting' behaviour observed at higher rotor speeds

Chapter 11: Overall Discussion

11.1 Introduction

The overall goal in undertaking this programme of research was to enable the design of future HPM devices and installations to be carried out more reliably. This was an ambitious undertaking and a great deal of new information has been gathered during the wide range of experiments already presented in this thesis.

In this chapter we will briefly collect and review these key findings, before considering how this new knowledge may impact the design of future HPM installations.

While development of a comprehensive design theory has proved to be beyond the time constraints of the current work, very basic models for selected cell processes will be briefly presented, the full derivation of which are contained in the Appendix.

Throughout this chapter, our stating point will be the operational experience gained from the Prototype HPM installation, which was designed using the knowledge then available at the start of this research. We shall then seek to understand how the observations and results from our experiments may be expected to impact the design of the Partenstein installation, if such a project were to be started now.

11.2 Prototype Machine – Highlighted Issues

Operational experience and performance testing of the prototype, identified the following key issues:

1. Excessive levels of splash and noise on blade entry to the upstream flow which limited the operating speed of the device to 6 rpm compared with the 10.5 rpm required to achieve maximum power output.
2. Generally lower than expected machine performance, with peak power output in particular being substantially lower than the anticipated design value.
3. The sensitivity of the machine performance to variations in downstream water levels.

4. Excessive noise generated by 'suction' during draining of the cells. This was entirely unexpected and further limited the practical operation speed range of the machine to less than 4 rpm.
5. Severe difficulties in control of the machine during sustained operation, particularly following changes in up and downstream water levels. This resulted in excessive noise as the control system exhibited 'hunting' around a sustainable operating point, and ultimately led to premature transmission failure due to the high cyclic speed / torque variations encountered.

A general explanation, supported by qualitative and quantitative data has been generated by the model test programme for all of these highlighted issues.

11.3 Cell Processes

The 'Four Stroke' analogy and cell process diagrams already presented in Chapter 10 are a simple but very effective aid to interpreting the behaviour of the HPM during operation.

The most important concept behind these diagrams is to understand the function of the HPM as a series of connected but separate fluid – rotor interactions. In this respect it is quite different from more conventional hydropower devices; the hydraulic processes occurring within a Kaplan turbine, for example, can be considered quasi-statically, with the majority of energy exchanges considered to be steady at a given operating point. This leads to relatively stable velocities as fluid passes through the machine, with only small variations in power output, torque or speed occurring during rotation.

The situation in an HPM is very different and much more akin to behaviour in an internal combustion piston engine, for example, where energy exchanges are anything but constant, power output is not at all even throughout rotation and considerable attention needs to be paid in the design in order to maintaining an even speed and torque output.

The Cell Process concept also helps the designer to consider the various trade–offs in machine geometry which need to be made. The 'ideal' geometry for the HPM rotor differs at each phase of rotation: for example, the large flat blades required during power extraction directly contribute to energy losses and excessive water splash

generated on blade entry. While this may be self evident to the careful designer, the value of the current research is that we are able to quantify these trade-offs to some extent, and at the very least estimate the relative importance of energy loss or extraction mechanisms during each cell process at each phase of rotation.

We will consider each of these processes in turn in the following sections.

11.4 Blade Entry

11.4.1 Model Observations

The splash generated at blade entry by the prototype machine was qualitatively reproduced at model scale for both 12 and 6 blade rotors. As already noted, splash generation was actually worse in the 6 blade rotor, since the upstream fluid had more time to return to nominal water levels between impacts.

The only rotor designs to show any reduction in impact splash were those using flexible blade elements able to deflect on impact to reduce the projected area of the blade contacting the water surface. The 'Flap Wheel' design could certainly be applied to future HPM designs or retrofitted to the existing prototype to positive effect, provided that steps are taken to ensure the longevity of the flexible membranes.

However, high impact forces on blade entry are fundamentally a function of the very low blade inclination angles employed on the current generation of HPM designs, and some means of estimating how a change in this angle will affect the size of forces produced would be very useful.

11.4.2 Simplified Blade Impact Analysis

A very basic mathematical model, based on Von Karman's work on sea plane floats (Von Karman, 1929) has been developed for the HPM. This is fully presented in the Appendix and will not be repeated here to avoid delaying our current discussion. Instead the approach will be briefly summarised before the results obtained are compared with model test data from 1/12A rotors turning at different speeds.

Von Karman considered seaplane floats impacting the level surface of water during landing as a momentum exchange with vertical velocity component only. One of his findings was that the angle of 'Chine' of the float hull has a significant effect on the peak

impact produced with more acute hull angles exhibiting much lower forces, while a flat bottom to the float resulted in infinite theoretical forces being developed. His was the first attempt to understand the phenomenon today referred to as 'Water Slamming' and of continued interest in ship design and the development of planing craft.

The geometry of an HPM blade encountering the upstream surface during blade entry is complex, and simplifying assumptions are necessary. In the analysis here, the blade is considered as a plate, set at the appropriate inclination angle, but falling with vertical velocity only. This velocity varies with rotor angle and is assumed to be the vertical component of angular velocity occurring at the centre of the blade area (Figure 11.1).

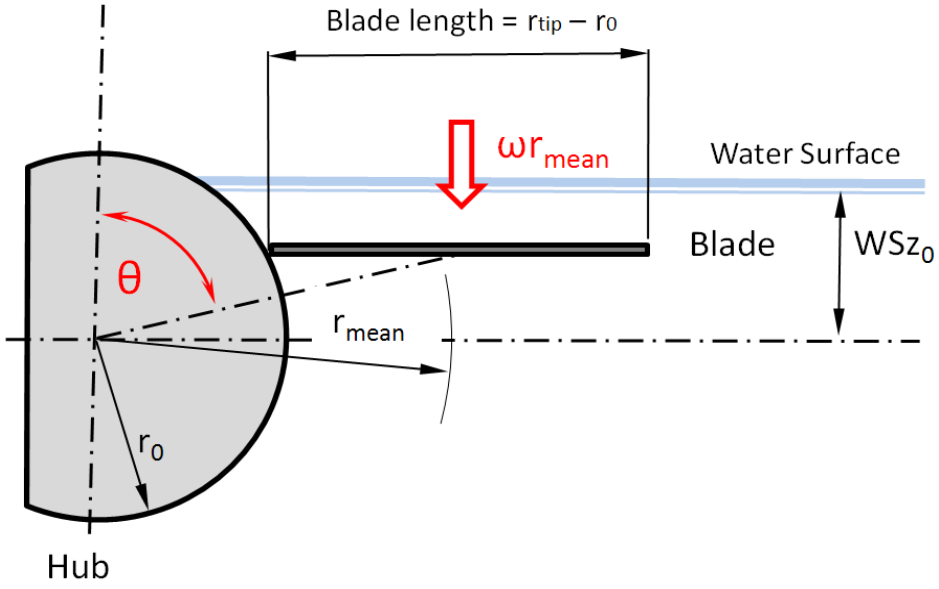

Figure 11.1: Blade Motion simplified to vertical component only

The water is assumed initially to be stationary, but following contact with the falling blade, is accelerated. The volume of fluid accelerated by blade contact is assumed to be contained in a semi-cylinder with a diameter equal to the width of the blade submerged, and extending from the outer blade edge to the hub surface (Figure 11.2).

Since the blade is non-porous, the water it contacts must accelerate to a matching speed and an impulse momentum exchange takes place, the reaction to which generates forces on the blade opposing its motion.

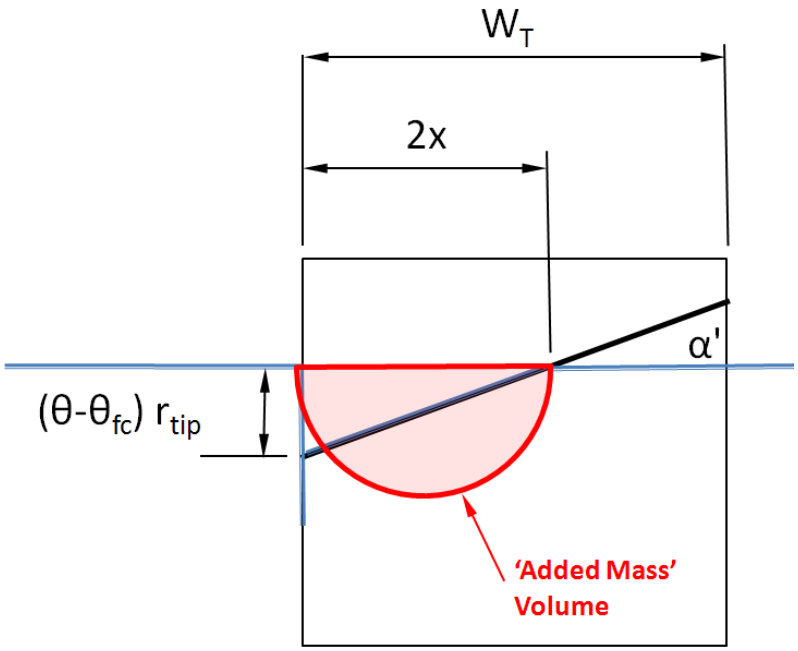

Figure 11.2: 'Added Mass' during blade impact.

The system of equations was solved using simple finite difference methods for the machine geometry at each operating speed considered. This analysis generated the following useful insights:

1. As found by Von Karman, blade forces are inversely proportional to the Tangent of the blade inclination angle. This point is important – if blade splash and impact forces are to be reduced then the surface of the blade must be introduced to the water at a more acute angle unless flexible blades are employed.
2. Blade forces and torques increase with the square of angular velocity – hence the speed restrictions necessary with the existing prototype.
3. Blade forces increase in proportion to the mean radius of the blade and torque with the square, implying that shorter chord blades of greater width may be more effective.

4. Impact force increases as the upstream water level falls, reaching a maximum when the water surface is level with the hub axle. Higher water levels tend to progressively reduce the impact forces experienced – a result which is slightly counter intuitive.

The results of this analysis are compared with rotor torque measurements in Figure 11.3. The theory over-predicted peak forces considerably, and so an arbitrary correction factor of 0.6 was applied. This is not ideal but, since the added-mass volume assumed in the analysis is also somewhat arbitrary, such a correction factor is to be expected.

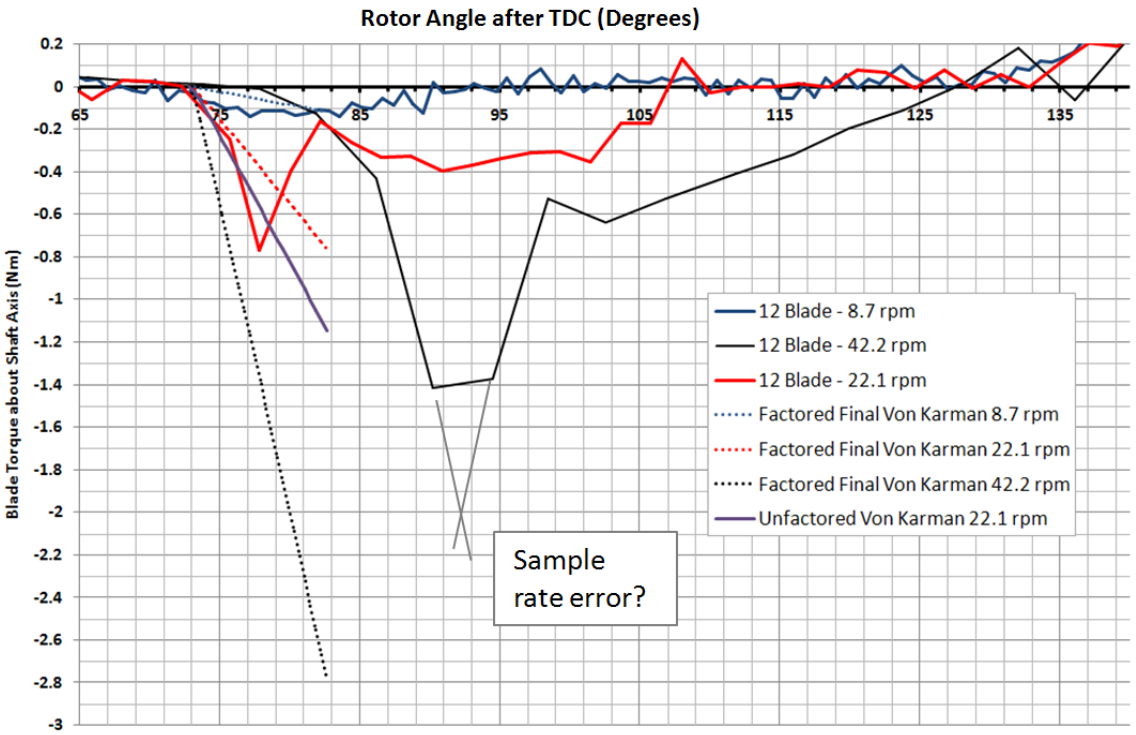

Figure 11.3: Comparison of Impact Theory with Model Test Results

The gradients of the theory lines are a poor match to measurements, due to the simplifications in blade geometry used in the analysis. However, with the 0.6 factor applied, the peak blade forces are predicted reasonably well at both 8.7 and 22.1 rpm, while overestimated at 42.2 rpm. The figure may also show a reading error due to the

low sample rate during data collection – the 'blunted' peak in the 42.2 rpm force plot suggesting that the maximum value was reached between readings.

There is also a phase shift between the angle at which blade impact begins in the analysis, compared with measured results from the scale model. This is explained by the differences in water level position assumed by analysis, compared with those encountered by the rotor at increasing speed. The analysis assumed the blade encountered an undisturbed water surface while observations already presented in chapters 9 and 10 reveal a 'depression' of the local surface of the water formed following the rapid succession of blade impacts occurring at higher rotor speeds.

However, despite the simplifications in the model, this theory aids the designer in enabling first approximations to be made both of the peak blade impact forces encountered and, by considering the area under the theoretical impact curve, the energy loss likely to result from a given combination of rotor speed, blade inclination and water level.

11.4.3 Summary of Blade Entry Findings

Our results have shown that water splash, impact forces and energy losses are all a result of the predominantly flat blade contacting the upstream water surface.

The simple analysis presented here suggests that the magnitude of impact is a function of the blade inclination angle, position of the upstream water surface relative to the axle of the rotor, and the rotational speed, with impact force increasing with the square of angular velocity.

Designers must take active steps to reduce blade entry forces in future designs, either by employing 'Flap Wheel' concepts, by substantially increasing the angle at which blades encounter the incoming flow or by using a different principle to introduce fluid into the machine as in the Zuppingerrad. In addition, since slamming forces increase with mean blade radius, designs using greater rotor widths to enable reduced radius blades to be employed while maintaining the same flow rate, may be beneficial.

11.5 Cell Filling

11.5.1 An Important Process

Cell filling is a fundamental process when considering the energy losses occurring during HPM operation.

Direct energy losses are caused by high drag forces produced by the predominantly flat blades as they are drawn through the upstream water. Indirect energy losses are caused primarily by the reduction in the static head of the upstream fluid resulting from the high local accelerations produced in the flow during the highly turbulent filling process and by the overall depression of the water surface in the area of the blades, already noted during our discussion of blade entry behaviour.

In addition, if cell filling cannot be completed before the cell passes into the working section of the installation, further fluid cannot enter the machine and the fill ratio is reduced, resulting in a proportionate loss of extracted power.

Cell filling therefore forms a significant part of the limiting process that sets the maximum effective rotor speed of a given installation.

11.5.2 Observed Behaviour

Observations indicate that at all but the lowest rotor speeds, cell filling appears to result from the drag of the passing rotor.

The bluff form of the blade creates a 'Separation Bubble' in the fluid as it advances (Figure 11.4), which initially extends up to the free surface of the water.

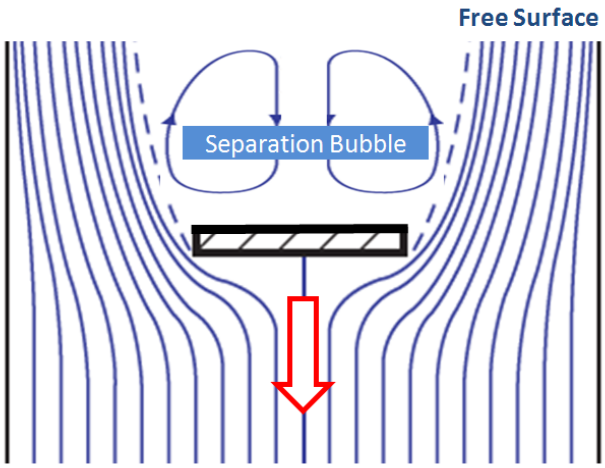

Figure 11.4: Schematic of flow around advancing Blade

This process is represented in simplified form in the schematic of Figure 11.5. The filling process develops as follows:

a. On initial blade entry, the rapid displacement of fluid by the advancing blade forms a steep edge front to the surrounding water along the leading side of the blade, while a splash jet is frequently observed on the trailing side of the blade.

b. As rotation continues, the hydrostatic pressure of the surrounding water begins to collapse the separation bubble and water starts to enter the cell. This is initially from the leading side of the blade while distinct water surface fronts begin to form along the remaining free edges.

c. As rotation continues, water enters the cell from all sides of the machine, until the cell pressure is equalized and cell filling is complete. Residual air bubbles are frequently trapped by this highly turbulent process and at laboratory scale provide a useful visual reference for judging when cell filling is complete.

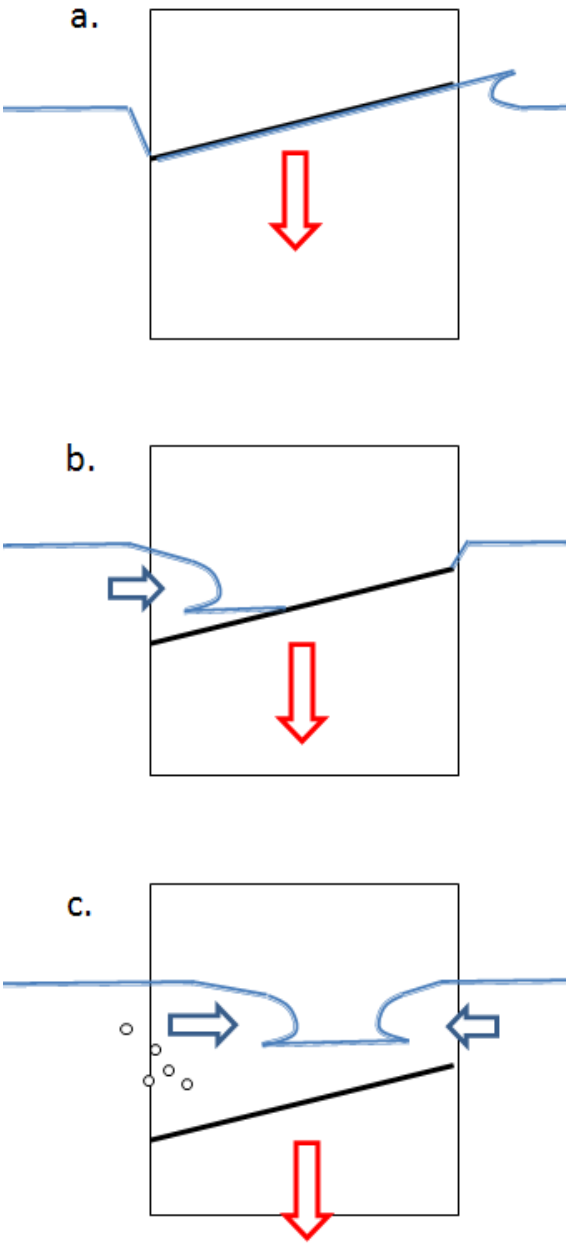

Figure 11.5: Schematic of Cell Filling Process

11.5.3 Simplified Cell Filling Analysis

It would be useful to be able to make at least a preliminary estimate of the drag forces and energy losses produced during cell filling as well as the likely rotor speed at which

the filling process starts to break down. For this purpose a very simple analysis has been carried out, which is summarised here and fully presented in the Appendix.

As a first approximation, we simplify the filling process to a series of quasi steady state conditions, with the water crossing the boundary of the cell approximating to discharge through a small submerged orifice. Inertia and acceleration effects are ignored.

As with the blade entry analysis, we further simplify the situation by considering the blade as a horizontal plate centered at the mean blade radius of the rotor axis. As the blade descends we assume that it has sufficient velocity to form the separation bubble leaving a void behind the blade at atmospheric pressure. This void increases with rotation until the cell is sealed by the following blade at which no further increase in volume is possible.

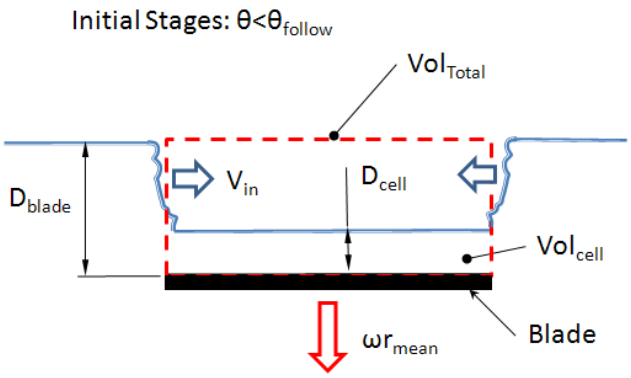

Figure 11.6: Initial stage of cell filling

Following initial contact with the surface of the water, it is assumed that the blade creates an abrupt change in depth in the fluid along the free perimeter. No fluid is assumed to enter the cell until the blade is in full contact with the water, following directly after the blade impact stage analysed above. The initial stage of cell filling is represented schematically in Figure 11.6. The depth of water behind the blade (D_{cell}) at a given instant is estimated by assuming the cell contents are uniformly distributed over the area of the blade. During later stages of cell filling, the situation is complicated by the presence of the following blade which, at some point, makes contact with the water surface (Figure 11.7)

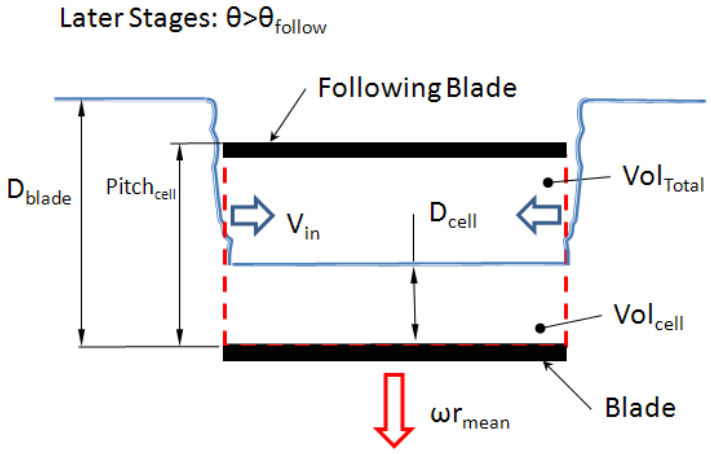

Figure 11.7: Cell filling after water contact by the following blade

Total cell volume has now reached its maximum value set by the geometry of the rotor and, in addition, pressure within the cell will increase with rotation since the following blade now prevents ventilation to atmosphere. The velocity and discharge equations are modified accordingly and this system of equations solved iteratively to estimate the angle of rotation at which cell filling is completed.

A by-product of calculating volume of water in the cell is that we effectively obtain an estimate for the pressure difference across the blade during rotation from which blade force can be calculated. The pressure within the cell is assumed to be hydrostatic and is obtained directly from the depth of the cell water. The pressure ahead of the blade is assumed to be equal to the hydrostatic pressure depth of the blade centre below the free surface of the inlet channel, less the dynamic head of the water moving ahead of the blade due to blade passage and turbulence. This is assumed to have a mean velocity equal to the velocity of the blade.

The calculated rotation of the machine to produce full cell filling is compared with the measured values obtained from the video record for a number of different operating speeds in Figure 11.8.

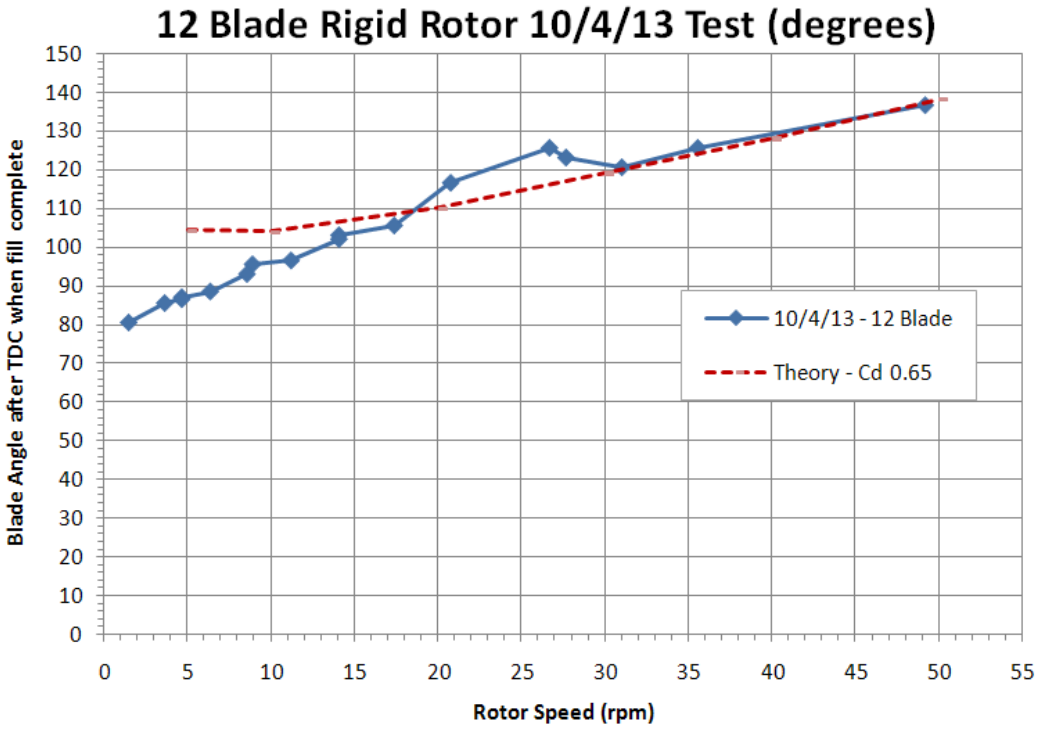

Figure 11.8: Comparison of Cell Filling Theory with Experimental Data

Despite the very large range of assumptions made, simple filling theory shows surprisingly good agreement with measurements across most of the speed range although the assumption that no fluid enters the cell until after full blade contact has occurred, may well explain the divergence from test results for rotor speeds below 10 rpm. The ‘ hump’ in the data between 20 and 30 rpm was initially thought to be a measurement error, but appears across all rotors tested indicating some other physical effect is present, possibly due to some interaction between wave generation and the cell filling process.

However, for such a basic theory, these cell filling prediction results are encouraging.

Both blade impact and cell filling theory are compared with blade torque measurements at 8.7, 22.1 and 42.2 rpm in Figure 11.9.

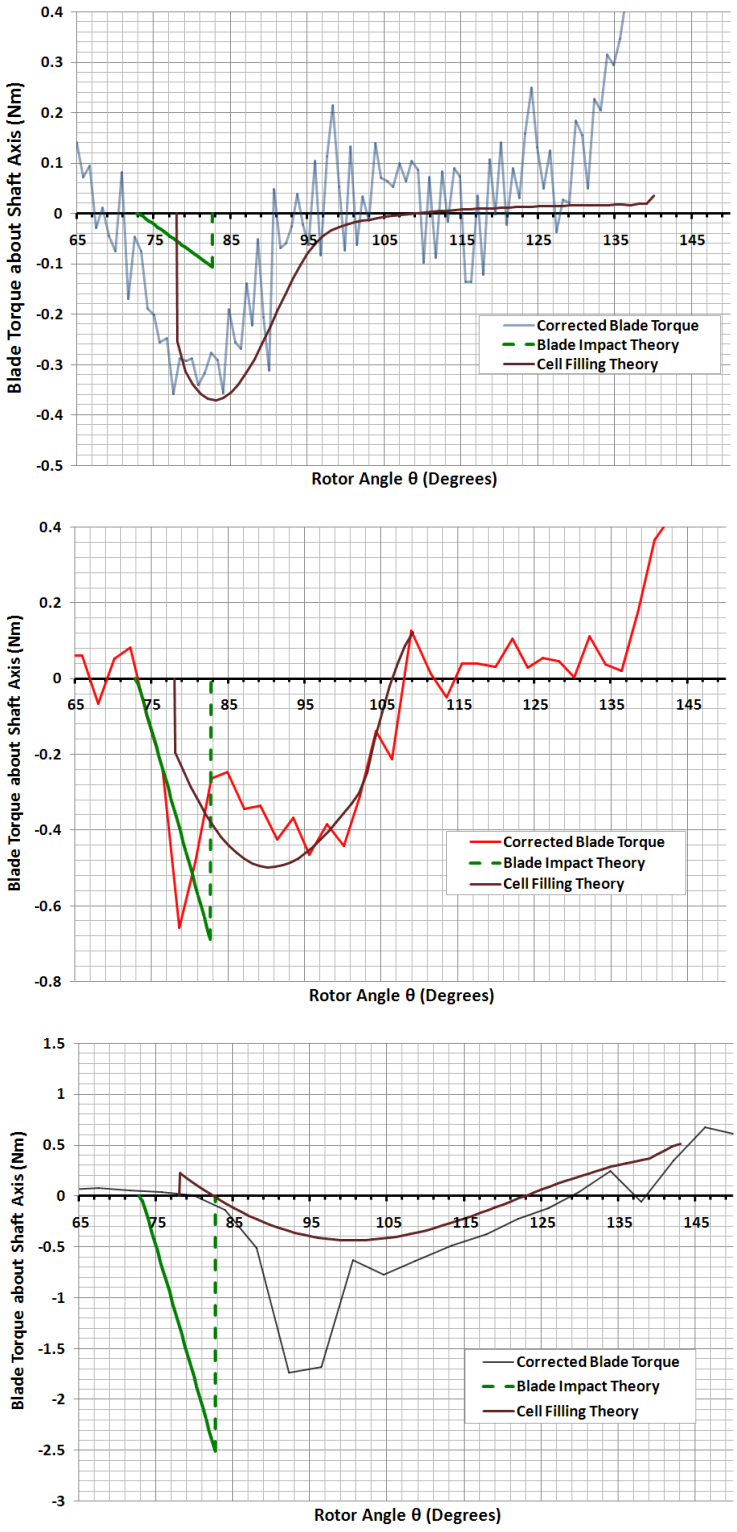

Figure 11.9: Blade Entry and Cell Filling Theory Compared with Measurements: 3.7 rpm (top), 22.1 rpm (middle), 42.2 rpm (bottom)

The fit between theory and measured rotor torques are crude, but reasonably good at both 8.7 and 22.2 rpm, with cell filling theory offering a better match to test results than the blade entry theory. Having said that, both the magnitude and form of the experimental blade torque plots are reproduced by theory, with the area under the curves giving reasonable approximations to measured energy losses. The errors in theory primarily seem to lie with difference in phase angle, due to the basic assumptions made in the analysis. However, at the high rotor speed of 42.2 rpm, cell filling theory significantly underestimates measured rotor behaviour although, once again, the general form blade torques produced during cell filling are represented by the theory.

We can conclude that this basic theory gives a reasonable estimate of both the angle of rotation required to achieve cell filling and the direct energy losses produced at the rotor due to the cell filling process, which is a useful first step to a more comprehensive treatment.

11.5.4 Summary of Cell Filling Findings

Cell filling losses have been shown by time series measurements to represent a significant source of energy loss in the HPM rotors tested. In many respects, cell filling may be considered as a continuation of the blade entry process, with closely related causes and remedies regarding machine geometry.

Flap Wheel model tests showed only modest gains in efficiency at peak power of around 3% and it seems probable that the same approach recommended previously to reduce impact forces will have a similarly beneficial effect on reducing cell filling losses. In this way, increasing the angle of blade entry to the fluid and introducing higher velocity flows into the cells are both likely to improve performance, particularly at higher speeds.

Thus far, our findings through model tests and simple analysis, has informed our approach to resolving the first of our issues highlighted by the prototype machine listed at the head of this chapter. Items 2, 3 and 4 on this issues list are all closely related and have significant implications for the detail geometry of future machine designs which will be considered in the next few sections.

11.6 Transit Phase

11.6.1 Observations

During the transit phase of rotation, very little change in fluid behaviour could be observed from the video evidence in Chapter 10, and the blade torque plots confirm that at low to medium speeds at least, energy exchanges appear to be small.

Since the angle of rotation required for cell filling increases with rotor speed, the length of the transit phase must steadily reduce – time series plots for the 12 blade unit suggesting that at 42 rpm, cell filling is just completed as blades pass into the working section with no distinct transit stage any longer visible.

11.6.2 Implications for Design

The end of the transit stage of rotation is set by the geometry of the side walls and shoe profile which define the start of the working section. As we shall see later in this chapter, getting the correct match between rotor blade pitch and shoe angle appears to be very important to maximize power extraction. However, if the working section is entered too soon, upstream static pressures over the blade will be lower than optimal and cell filling may not be completed at higher operating speeds.

The Transit phase can therefore be seen as a 'buffer' in the machine geometry – its end point corresponding to the maximum rotor speed at which 100% cell filling can be achieved.

11.7 Power Phase

11.7.1 Observations

It was impossible to carry out any direct observation of events occurring during the power stroke in the prototype installation since this process occurs within the working section of the machine, hidden from view. However, while the transparent side wall of the model test flume enabled water level changes to be observed in the working section, it is the direct blade torque time series measurements presented in chapter 10 that furnish the most useful information. That chapter noted that for the 12 blade rotor, the power stroke appeared to take place in two stages: the 'Dwell' stage and the 'Power' Stage, and the causes of this will be investigated in the simple summary of pressure-force analysis presented in the next section.

However, the performance results of Chapter 9 also show very clearly that a 6 blade rotor gave a much better performance with the existing shoe and side blade geometry than the original 12 blade units – apparently due to the better match between blade pitch and shoe segment angle producing a higher pressure difference across the blade.

The simple pressure-force analysis summarized below is a crude but useful aid to develop our understanding of the geometry required in the working section. Once again, only a summary is presented here for brevity with the full derivation contained in the Appendix.

11.7.2 Pressure Changes through the Working Section

Basic performance theory assumes that pressure differences are due entirely to the static heads prevailing on up and downstream sides of the rotor and that this pressure is constant throughout the working section.

However, as the torque and pressure plots presented in chapter 10 suggest, the reality is rather more complex and, for 12 blade rotors at least, appears to be closely related to the cell emptying process.

The cell emptying process is complex and a method of modeling pressure variation with rotation has not been possible within the scope of the current project. This will be discussed in more detail in a later section but, for this study, a simplified pressure variation is assumed.

Figure 11.10 compares the measured hub pressure for the 12 bladed rotor at 8 rpm with the simplified representation used in this analysis. From the upstream static head at the centre of the blade at entry to the working section, a linear decline in pressure is assumed. At blade opening, we further assume, that the cell pressure immediately falls to a negative value, corresponding to the suction produced by the height of the free surface above exit channel levels in a fully unventilated cell. This negative pressure is then assumed to be applied until rotation progresses to permit full ventilation, at which point pressure returns to atmospheric.

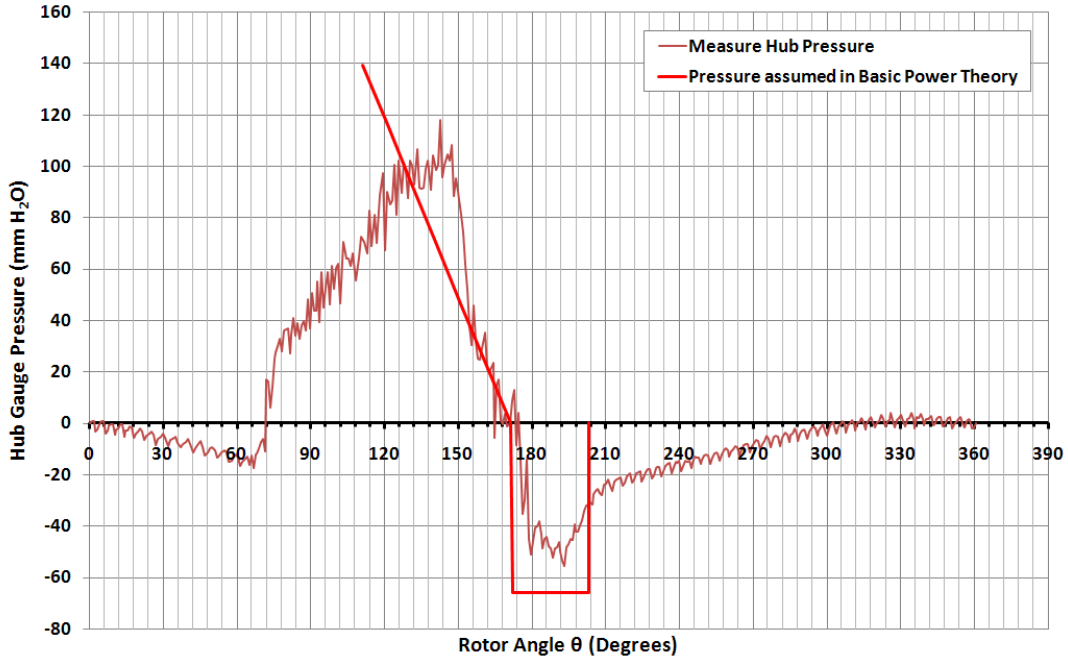

Figure 11.10: Pressure Variation Assumed in the Analysis

11.7.3 Pressure – Blade Interactions in the 12 blade rotor

The changes in cell pressures either side of a given blade of a 12 blade rotor as it passes through the working section are summarized in the sequence of graphics presented in Figure 11.11.

The sequence of events covering both 'dwell' and 'power' stages progress from top to bottom of the figure, with the blade position under consideration marked along with the corresponding angle of rotation.

Θ = 126°: The start of the 'dwell' portion of power extraction. Following the transit phase, the blade 'closes' the leading cell as it rotates between the side plates. Pressure behind the blade is at full upstream static pressure. The pressure in the leading cell starts at upstream pressure but, since it is now isolated by the closed blade, cell pressure must fall as energy is extracted. Therefore,

$$p_{closed} = f(\theta)$$

Θ= 156°: Rotation continues until the blade ahead of the leading cell reaches the crest of the shoe profile. We make the assumption that by this point, cell free surface pressure in the leading cell (which is of course 1 blade pitch ahead of the blade we are studying), has reduced to zero. We assume a linear decline in cell pressure with rotation angle.

Θ= 186°: From θ = 156° to 186° the blade enters the second 'power' stage of energy extraction. Closed cell pressure continues to fall as power is extracted. However this is compensated for by the negative pressure formed in the leading cell shortly after opening.

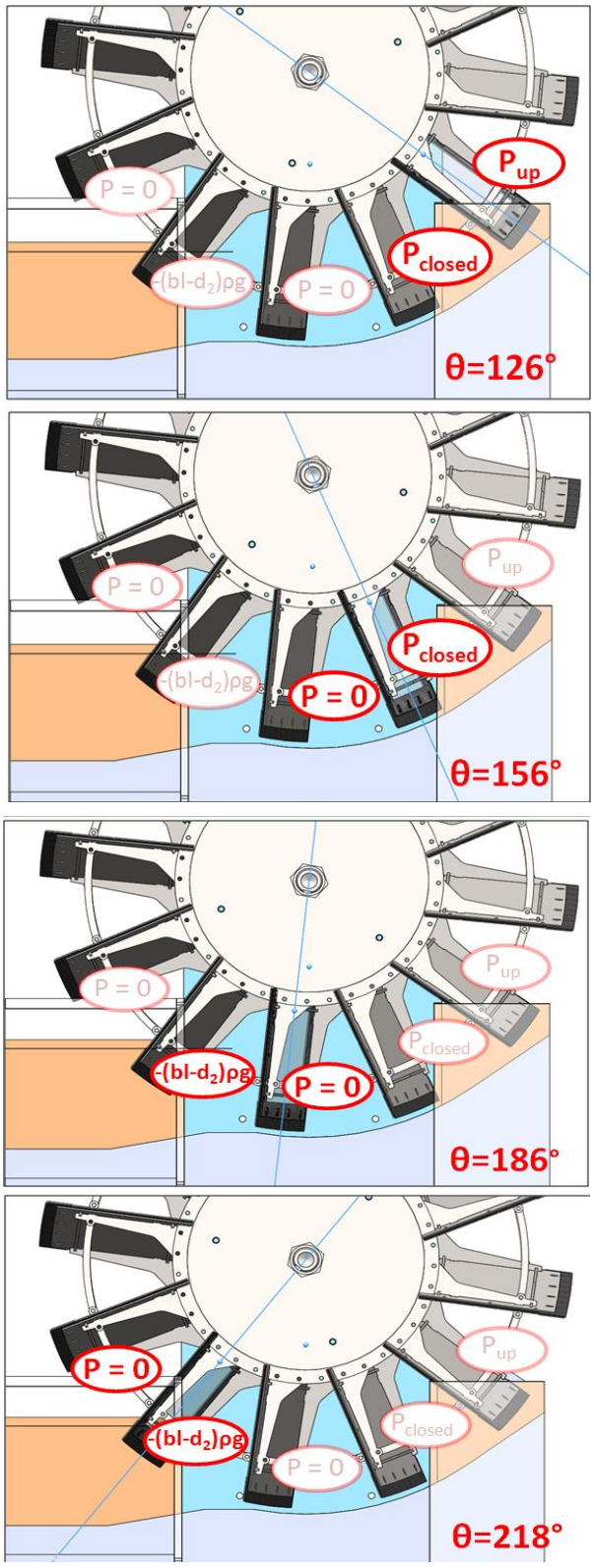

Figure 11.11: The Working Section

Θ= 218°: Thus far, the negative pressure in the exit cell has aided power extraction. However, as the blade clears the shoe, the negative pressure applies a negative torque to the rotor.

The results of the simple model based on this sequence of events are compared with measured rotor torques in Figure 11.12.

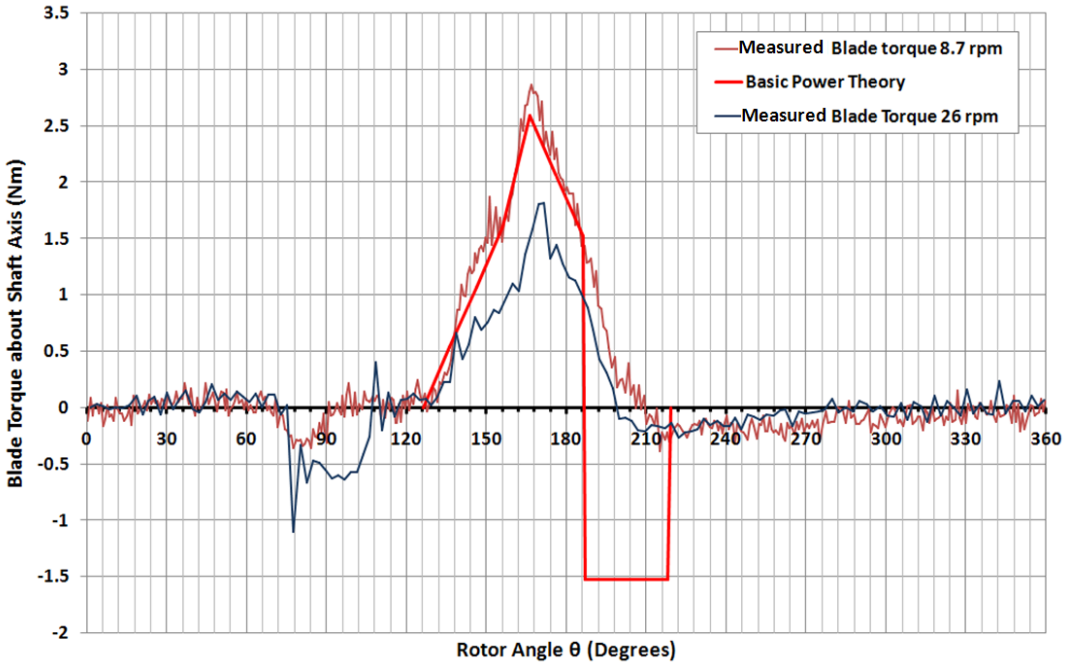

Figure 11.12: Simple Pressure-Blade Theory in the Working section compared to measurements

The fit of the calculation with data is surprisingly good during the initial 'Dwell' stage of power extraction, and assumptions made regarding reducing pressures in closed cells during power extraction appear to be justified. Peak torque corresponds to the application of full negative cell pressure on the exit side of the blade which at this stage aids power extraction. The 'digital' change in torque after 186° is a result of the pressure assumptions made in the model – a more realistic treatment of pressure is likely to have produced a better match in the later stages of power extraction. However, the negative torque produced by the negative cell pressures acting on the blade between 186° and 218° are almost entirely absent from measured data. Our assumptions during this stage of rotation could be entirely wrong, although it seems possible that additional

blade forces, ignored in this analysis, are exerted during cell emptying which extract energy from the flow, and largely compensate for any direct forces due to suction. This would also explain why negative hub pressures appear to have such a small effect on measured blade torque across the operating range, evident in the time series data of chapter 10.

This analysis helps to explain why employing a 6 bladed rotor produced such an improvement in performance compared with the 12 blade unit. In the 6 blade rotor the P_{closed} pressure phase is eliminated and the blade experiences full up and downstream pressure differential throughout the single stage power stroke. Since the upstream side of the cell remains vented to upstream water pressure, there is no fall in pressure to zero by the end of the stroke and a much more effective energy transfer takes place (Figure 11.13).

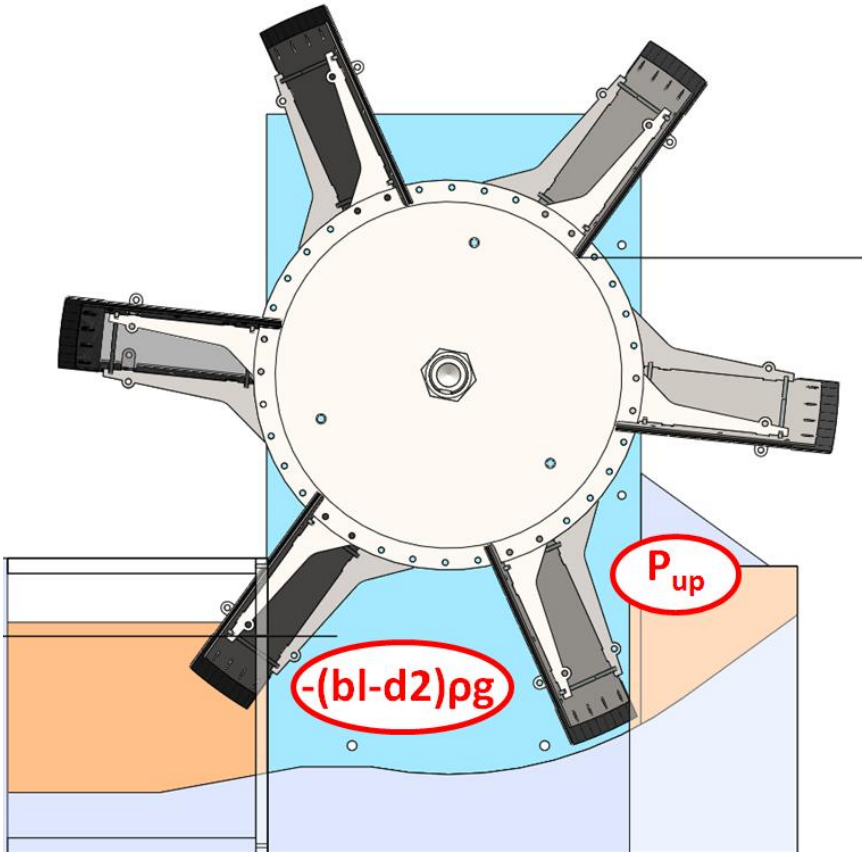

Figure 11.13: Higher Blade pressure differences in a 6 blade rotor.

11.7.4 Summary of Power Stroke Findings

Time series data presented in chapter 10 showed a clear increase in power extraction using a 6 blade unit compared to the original 12 blade device.

The analysis, summarized above, offers a reasonable explanation for this – having two cells progressing through the working section erodes the available pressure in both, compared with the full pressure difference available when a single cell is in contact with the shoe. Other factors may also be present and the exact interaction of stroke length, cell pitch and shoe angle are not fully understood.

However, it is clear that designers should arrange installation geometry so that the shoe length is a close match to the pitch of an individual cell and it is reasonable to assume that side plate profiles should be set accordingly.

11.8 The Exhaust Phase

11.8.1 Drain Process

The draining process is very complex and although suction pressure losses are accounted for empirically in the new performance theory developed in Chapter 7, no model of the process itself has so far been developed.

A schematic of a cell during draining is shown in Figure 11.14.

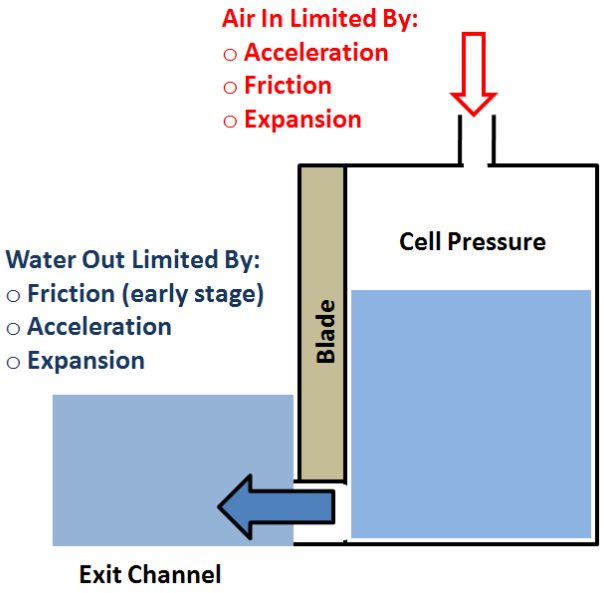

Figure 11.14: Schematic of the Cell Draining Process

As the blade advances past the end of the shoe, a gap develops beneath the blade through which fluid escapes. However, in the existing machine, the rate at which the cell discharges is limited by three factors: the losses in the escaping water, the falling air pressure above the free surface of the cell

and the terminal velocity of air being drawn into the cell via gaps in the blade and hub seals. These air velocities can be quite high which accounts for the noise generated by the prototype unit. Performance tests in chapter 9 indicated that losses due to poor ventilation accounted for 15 % of the power output in the machine, while the action of the membranes in the modified flap wheel unit provided an effective means of early cell ventilation.

Video observations in chapter 10 indicated that the ventilation process was more effective in the 6 blade rotor unit compared with the 12, presumably since ventilation affected twice the volume of fluid in any given cycle.

Increasing downstream water levels were found to decrease suction losses, although the new performance theory indicates that most of the performance gain obtained during these experiments was due to reductions in acceleration losses occurring as fluid leaves the cell. The short, deep water test series carried out with a 6 blade rotor using an increased exit channel width also appear to show that attention should be paid to ensuring fluid can leave the cell as easily as possible.

11.8.2 Blade Exit

Observation reported in chapter 10 showed that two energy exchange processes occur as the blades rotate out of the exit flow. The falling horizontal component of blade velocity results in a positive momentum exchange with the fluid, which contributes to the output power of the machine. On the other hand, the increasing vertical component of blade velocity accelerates the exit flow upwards, which at higher speeds results in the 'water lift' behaviour observed. This is an energy loss to the machine which the deepwater tests revealed as a limiting factor in matching the machine to downstream water levels.

11.8.3 Implications for Design

It is clear from observations that designers need to ensure that fluid is able to leave the HPM during the exhaust phase as quickly as possible. Side plate profiles should be matched with rotor geometry to ensure the free passage of air into the cell as soon as blades reach the end of the working section. It also appears advisable to increase the area of the exit channel allowing fluid to leave from at least one side of the blade as well as from underneath.

Matching downstream water levels to be nearer to the bottom of the hub will also reduce ventilation and exit acceleration losses, although this needs to be balanced against the potential energy losses due to water lifting. For the model geometry, setting the rotor to achieve 90% immersion of the blade appeared to offer the best compromise, although it is not clear how valid this would be for other blade aspect ratios.

The combination of shorter blades with a wider basic rotor design as suggested above as a means to reduce blade entry forces, may also be of benefit in reducing blade exit losses.

11.9 Output Torque Variations

11.9.1 Torque variations in the Complete Rotor

So far this chapter has applied the results of this research to address the first four operational issues highlighted by the prototype installation, listed in section 11.2. Next we will examine possible causes of the fifth issue listed: the control system resonance and hunting experienced with the prototype machine.

The Proney brake system used throughout these model tests is a constant torque device. Any variation in output torque produced by the machine, therefore, results in variation in rotor speed – as already presented in chapter 10. However, the individual blade torque measurements can be recombined, at the appropriate phase angle, to produce an approximate output torque plot for the complete machine and this exercise is presented for both 12 and 6 blade units at the 1/12A test condition in Figure 11.15. To reduce the impact of signal noise, 3 point moving averages are applied to each trace on the graphs.

The individual 'Maintain Peak' profiles as each cell passes through the working section of the machine can be quite clearly seen in all plots below rotor angles of 180°. However, above this value, the wave forms become distorted, particularly for the 6 blade unit. This is almost certainly due to the formation of 'beats'- the localized reinforcement of wave amplitudes caused by small differences in frequency and phase

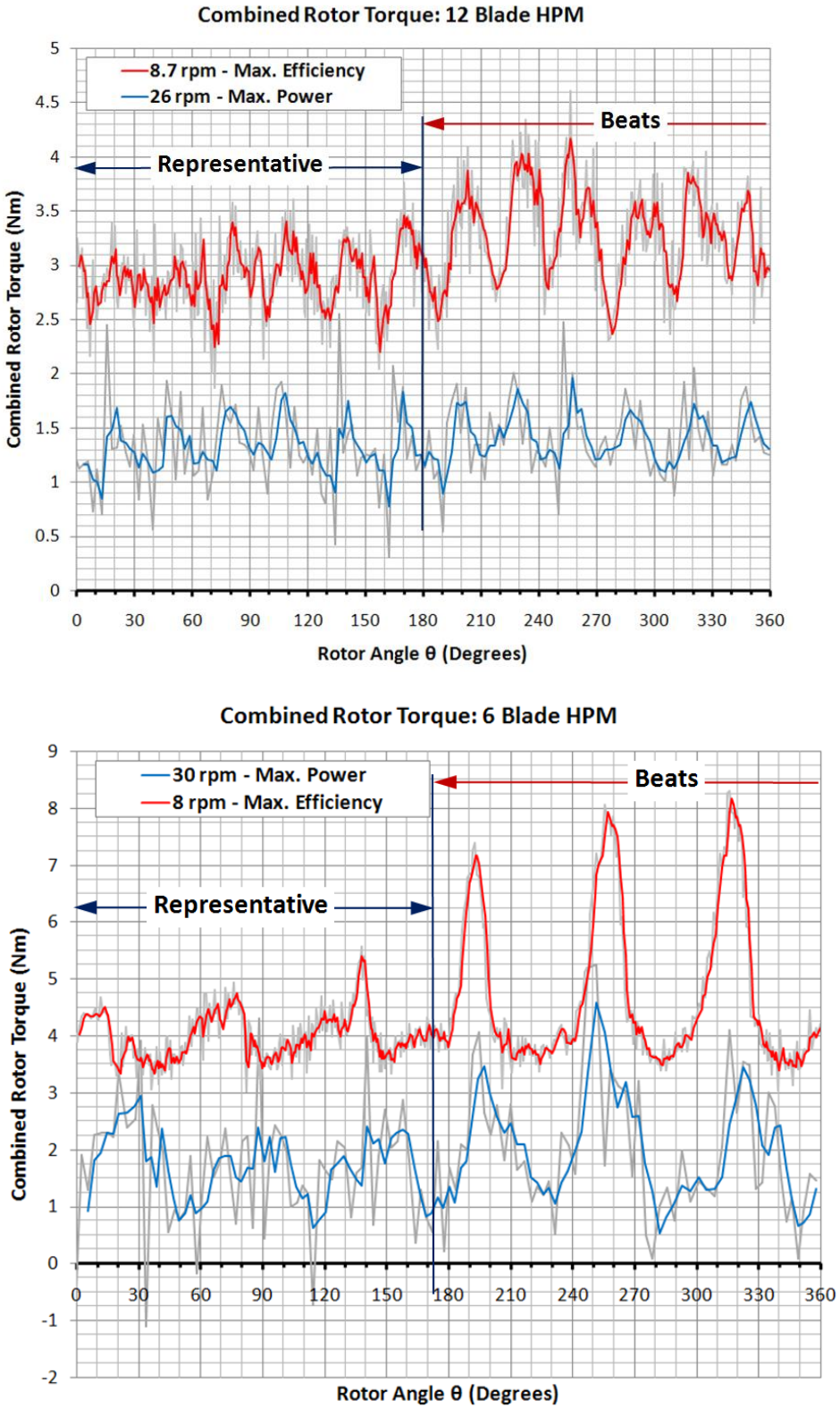

Figure 11.15: Combined Output Torque at 1/12A test condition

angle between individual blade torque plots, which is a by-product of the recombination process, rather than representing true rotor behaviour. For this reason, only wave forms to the left of the marked lines in figure 11.15 are used to estimate rotor torque variations.

Fluctuations in torque are very high in both machines: for the 12 blade unit amounting to +/- 24% of mean torque at 8.7 rpm rising to +/- 38% variation measured at 26 rpm. The results from the 6-blade unit show a similar pattern with +/- 18% torque variation at 8 rpm rising to +/- 50% at 30 rpm. While blade impact, ventilation and other energy losses make some contribution to these torque variations, they are primarily driven by the short duration of the power extraction occurring as blades pass through the working section and as such are an inevitable feature of the current HPM concept.

Bearing in mind that these torque values are theoretical approximations extrapolated from measured results and therefore have to be treated with some caution, it is interesting to note that variations in rotor speeds recorded during experiments were much less severe, reducing as rotor speeds increased. This suggests that the fly wheel effect of the inertia of the rotor had a significant effect on actual machine output and if further increased, may enable these torque variations to be significantly attenuated.

In the absence of such a flywheel, it is no surprise that the prototype control system struggled to control machine operation – attempting to regulate such large and rapid variations in loading is a significant engineering challenge and may represent a fundamental weakness in the existing HPM architecture.

11.9.2 Implications for Design

Torque variation may be reduced by increasing the number of blades in the rotor, although this is likely to introduce additional energy loss during cell filling. An alternative in split rotor designs referred to in Chapter 7, may be to offset the pitch of the blade in adjacent sections so that the two 12-blade sections of a single machine, will produce a power output corresponding to a 24 blade pitch. This is similar to the effect of adding additional pistons to an internal combustion engine. In addition, incorporating a flywheel will also ease the situation, particularly at higher rotor speeds.

However, such approaches are clearly going to be more complex to design and

manufacture and will therefore increase installation costs. A far simpler mechanical engineering solution will be to incorporate a flywheel into the PTO design, sized to maintain nominal system speeds within tolerable levels. This could be achieved by adding mass directly to the machine rotor itself – preferably at as large a radius as possible to maximize the polar mass-moment of inertia. The advantage of this approach is that it would reduce stress fluctuations throughout the PTO system, however, since the energy storage capacity of a flywheel is inversely proportional to the square of rotational speed (Shigley & Mischke, 1990), the masses involved for low rotor speeds may be excessive, and alternative flywheel placements within the transmission may prove to be more cost effective.

An alternative approach is the use of a more sophisticated control system, perhaps incorporating an element of predictive load control in the light of experimental measurements. In such a system, it also seems essential that, the speed of the rotor be measured directly, rather than relying on generator speed monitoring as used in the prototype. However, such a control system is likely to add significantly to over installation costs.

12 Future HPM Developments

12.1 Introduction

The results presented in this thesis significantly increase our knowledge both of the basic performance modeling of HPM installations and the detail of energy exchanges taking place at each phase of rotation *in the current machine concept*.

However, engineering design is an iterative process, and the value of this research will be measured by the extent to which it influences development of future machines and the degree by which their performance and operating characteristics are improved.

In this chapter we will briefly consider how the knowledge gained from both prototype and model test programmes may influence the next generation of HPM developments.

12.2 Divergent Futures

12.2.1 Power Take-Off Design – the Strategic Factor

In the engineering assessment of the prototype installation presented in chapter 7, the cost and complexity of the low, variable speed power take off system required for electrical generation was highlighted along with a number of hydraulic performance issues.

While the results of this research should enable significant improvements in machine performance to be made, low, variable speed operation is inherent to the existing HPM design concept. In the authors' opinion, this will cause the development of practical HPM devices in the future, to develop along two divergent paths, dependant on the PTO design philosophy adopted by future workers.

12.2.2 Accepting Low & Variable Speed – Developing the existing HPM Concept

Some teams may conclude that cost effective transmission and control systems can be matched to the very low speed characteristics of the HPM and that the additional costs of the necessary high torque gearboxes and low speed generators is more than compensated for by the low cost and simplicity of the existing HPM concept. Adopting this approach, full size machines will continue to operate in the 2 – 10 rpm speed range.

Following this philosophy, the results of this research will be directly applicable with future HPMs being derivatives of the existing concept.

Designers should pay attention to:

- Minimising splash and energy losses during the induction phase through appropriate selection of blade angles and inlet channel design.
- Matching the blade pitch exactly to the segment angle of the shoe profile to maximize both the pressure difference generated across the blade and the proportion of the power stroke over which this is applied.
- Shaping of the side plates to maximise ventilation of cells during the emptying process.
- Shaping of the exit channel to minimize turbulence losses as far as possible.

In addition the 'Flap Wheel' concept demonstrated during model testing showed significant performance advantages although these need to be balanced against the potential increase in maintenance overhead due to wear of the membranes. The split rotor concepts outlined in Chapter 7 may also be worth considering as a means of reducing the range of operating speeds to be accommodated by the transmission.

12.2.3 High Speed HPM Concepts

An alternative development path for HPM concepts revolves around a perceived need to increase the operating speed range of the HPM rotor considerably to the 20 – 40 rpm range already described in Chapter 7.

This approach is driven by the belief that low speed power take offs are inherently expensive and, given the proportion of the installation cost represented by the power take off, some additional machine complexity in order to simplify transmission design will result in the most cost effective overall solution. In addition, the following secondary benefits are offered:

- Speed variations and 'torque ripple' effects are reduced at higher speeds due both to the shorter duration of pressure variations within the rotor and the additional fly wheel effect produced by the mass of the spinning machine as a whole.
- A higher speed rotor will be proportionately smaller in physical size, reducing basic machine costs and the extent of civil works required.

Such an approach will result in an HPM very different to its current form and future

designs should focus on the following:

- Minimise energy losses during the induction phase. In chapter 3 we noted how the Zuppingerrad neatly avoided most of these energy losses by feeding pre-accelerated water directly into the cells, without drawing the blades through the upstream standing water; an approach that future designers are likely to follow.
- The lessons learned from this research regarding blade pitch, shoe and side wall geometries will be equally important to these new devices.
- At higher basic rotor speeds, the dynamic head energy content of both the inflow and exit water can no longer be neglected and steps must be taken to recover as much of this energy as possible. Some of the momentum exchange techniques used by established turbines, described in chapter 2 may be applicable here.
- Paudel et.al (2013) showed that significant improvements in performance could be obtained using a simple open diffuser in the exit channel of an HPM, and attention to design in this area will be particularly important as exit flow velocities increase.

12.3 A Future for HPMs?

Potential remains to develop the basic HPM concept into a practical, cost-effective machine suitable for ultra low head applications. In the author's opinion, the most likely route to success will be via the high speed HPM approach, since transmission and control costs proved to be so significant in the Prototype installation.

However, considerable scope remains for innovations in the basic conceptual design of these machines which is necessary if these devices are to achieve a level of performance comparable with more established hydropower energy converters.

Chapter 13: Conclusions

The overall goal of this research was to develop sufficient new knowledge regarding the basic characteristics of Hydrostatic Pressure Machines to enable future design to be carried out more effectively. A substantial contribution to that goal has been achieved in the current work, through the construction of a full scale prototype machine for field trials and the gathering of high quality performance data, extensive detailed testing of the performance of a scale model unit and direct measurement of blade forces and cell pressure variations occurring within the laboratory HPM unit during operation.

A significant improvement to account for the 3D geometry of real machines, and variations in downstream water level has been made to the existing HPM performance theory, while preliminary modeling of selected cell processes demonstrates that such an approach is potentially useful, showing surprisingly good agreement with measured data.

The following key findings should be noted:

1. Over the normal operating speed of these machines and, within the margin of error of experimental readings, no scale effects were found between the 1/6 scale laboratory model and the full size prototype unit. This implies that provided care is taken to represent the geometry of the machine accurately, and that the inflow channel of the test flume is sufficiently deep to prevent the formation of critical flows, the performance of full scale devices can be predicted accurately from model test data.
2. The new performance theory developed to account for both a 3 dimensional machine and variations in downstream water level is a good predictor of performance at both full and model scales: empirical coefficients found from model tests being equally applicable to the full size unit. In comparing theory with performance test data, the importance of considering absolute power output and efficiency values rather than simply relying on parametric measures has also been demonstrated.
3. The prototype unit delivered a lower than expected performance and exhibited a greater than expected sensitivity to variations in downstream water levels. In addition, operation of the machine was limited by excessive splash generation during blade entry, 'suction' noise generation during cell emptying and

difficulties in obtaining a steady operating speed under varying conditions with the basic control system employed.

4. A 'Four Stroke' analogy of machine operation was devised. At laboratory scale a further series of 'Cell Processes' were identified that occur successively during rotation of the machine. The effect of these processes on machine operation was assessed through a combination of performance testing, detailed observation and direct measurements of blade forces and cell pressure during rotation.
5. The performance of several modified rotor designs were compared with the model of the prototype and all were found to improve power output and efficiency. The 'Flap Wheel' design addressed many of the issues found in the prototype; reducing blade splash and suction and improving performance. However, reducing the number of blades in the rotor from 12 to 6 was found to offer a greater increase in performance although both blade splash and speed variations also increased.
6. The following geometry details were found to be important in the current HPM design concept:
    - Increasing Blade inclination angle reduces impact 'slamming' forces on blade entry. It is also suggested that a wider machine with shorter chord blades may be of benefit.
    - The segment angle of the shoe profile should be matched to the pitch angle of the blades to ensure the maximum pressure difference is developed across each blade during its transit through the working section of the machine.
    - Side plates must be shaped to permit the free entry of air into the cell as soon as the draining process begins. Failure to do this in the prototype machine contributed substantially to the 'suction' noise produced and reduced efficiency by up to 15%.
    - There is some evidence to suggest that widening the exit channel to enable flow to leave the cell from the side as well as from beneath the advancing blade will also improve efficiency, both reducing the magnitude of exit accelerations required, and increasing the area available for discharge of cell contents.

- The rotor height should be arranged so that downstream water levels are closer to the bottom of the hub tube; for the prototype geometry, best performance was obtained by immersing the blade to 90% of its length. However, drag forces due to the vertical velocity component of the blade as it rises through the exit flow, are a significant cause of energy loss at greater downstream depths which limits blade immersion for maximum efficiency.

7. The 'time series' measurements of blade force and cell pressure variations during rotation were found to be an invaluable aid to interpreting cell process behaviour. Although the limited data reading rate of available equipment meant that these measurements had to be regarded as indicative, preliminary analysis of selected cell processes were found to offer a good approximation to blade torque traces obtained. This approach offers considerable scope for further investigation.
8. The output torque from the existing HPM concept shows significant variation as each blade passes through the working section. This is a result of the high, short duration energy transfer that takes place at each blade during the power stroke, and is not a function of errors made in design of the machine geometry. These torque variations are high with estimates based on blade torque measurements ranging from +/-18% to 50% of mean, depending on rotor configuration and operating condition, with +/- 34% representing a typical value.
9. These torque variations largely account for the control system difficulties encountered with the prototype machine (along with power output variations with changing downstream water levels), and the design of cost effective transmission and control systems is identified as *the* strategic issue to be addressed in future HPM designs.
10. Possible avenues for future HPM developments were identified, strongly influenced by the approach adopted in the design of the transmission and control system. The development of a derivative device operating at higher rotor speeds than the existing HPM concept is recommended.

Chapter 14: Recommendations

14.1 Scope

The recommendations outlined in the following sections address three areas of future work; modifications to be applied to the existing full scale prototype in the light of the new experimental data, areas of fundamental research still required to further our understanding of the existing machine behaviour and finally, the development of future HPM architectures and designs.

14.2 Modifications to Existing Full Scale Prototype

The adverse operating characteristics of the existing prototype were compared to the findings of the current research in chapter 11 and a number of possible approaches to their solution described. While, remedial modifications to the existing field trial unit will be limited by constraints in time and budget, significant improvements to the basic machine are essential if reliable long term operation is to be achieved. The following actions are recommended:

1. Modify the existing blades to the 'modified flap wheel' standard developed during model testing. While the technical risk of introducing the novel, flexible membranes will need to be managed by careful material selection and sound detail design, this approach represents the only practical way, short of replacing the complete machine, of controlling blade entry splash, eliminating suction noise during cell emptying and increasing power output from the existing installation to realistic levels.

At the time of writing, blade splash limits machine speed to below 5 rpm and if downstream water levels are merely elevated to reduce suction noise, maximum shaft power output will be restricted to below 2.1 kW. With the recommended flap wheel modification, maximum acceptable wheel speeds will be increased, delivering peak shaft power outputs of 4.4 kW at around 13 rpm. In addition, provided that a suitably flexible material is selected for the inner flap (see section 9.3.2.1), suction noise should be eliminated at all operating water levels while the modular design of the prototype machine enables blades to be removed to simplify the modification process.

2. Add a flywheel to the rotor or power take off system to reduce speed and torque variations. This research has established that substantial torque variations are an inevitable result of the power extraction process of the HPM and not simply a by-product of energy loss mechanisms. The most practical way of managing these torque variations is through the use of a flywheel which if correctly sized, will limit variations in machine speed, reduce transmission stresses, simplify machine control and reduce noise levels induced by fluctuating loads applied to the inverter and generator. As already described in Chapter 11, the mechanically simplest solution will be to add mass to the existing blades. Provided this mass is balanced, additional bearing and shaft loads will be negligible, although the relationship between rotor speed and flow rate will be modified as cell volumes are reduced. If insufficient mass can be added to the system in this way, one or more additional flywheels will need to be fitted further along the transmission system, although this is likely to entail significant modification to the installation in order to achieve the necessary clearances.

However the benefits of this modification are significant, eliminating the torque variations driving control system resonance and belt failure mechanisms at source and, will greatly extend transmission operating life.

3. Modify control system to account for variations in water levels.

In order to successfully control the HPM installation, the control system needs to be able to modify power output in response to *both* the flow rate available from the river *and* changes in head across the machine due to fluctuations in up and downstream water levels. In the existing system, the Ingateam inverter is only able to relate power output and rotor speed through a single performance curve and therefore 'hunts' if water levels deviate significantly from those experience during system set up (described in section 6.2.6). An additional means of accounting for power variations due to head changes is therefore required if hunting is to be eliminated.

The ideal solution would be achieved through selection of an inverter capable of combining output power, rotor speed and head, into a single 3 dimensional characteristic surface, linked to wheel speed and external up and downstream water

level sensors. However this level of sophistication is likely to be beyond the capacity of inverters in this class and may prove prohibitively expensive.

A more practical approach may be to compensate for variations to river levels externally from the inverter and two possible solutions are suggested.

a. A series of separate control curves, corresponding to different water levels could be stored in a separate Programmable Logic Controller (PLC) or Micro computer, linked to up and downstream water level sensors. If river levels change beyond a prescribed limit, the PLC stops the rotor, uploads a control curve appropriate to the changed conditions to the inverter memory and restarts the system under the updated inverter control. This sequence would take around 10 minutes to perform and may be expected to occur 5 or 6 times over a typical 24 hour period. It presupposes that fully automatic system stop / start has been implemented (see recommendation 4 below) but has the advantage of requiring very little additional equipment and only a basic level of control system programming (with suitable support from the inverter manufacturer), while minimizing the loss of energy capture by the system.

b. A series of ballast resistors could be installed between the generator and the inverter selected by a PLC unit in response to changes in water level. The inverter control curve would be set up to correspond with a high nominal downstream water level, and any additional power generated due to increases in head caused by any subsequent fall in downstream river level absorbed by electrical heating of the ballast resistors. This approach is very similar to that of Electronic Load Controllers commonly employed to regulate pico-hydropower installations, which have proved to be both low cost and highly reliable in operation. Although this solution reduces the peak electrical generating capacity of the system, (by approximately 400W per 100 mm of water level fall), ballast resistors could be employed for hot water heating in the mill, to yield some secondary value to the energy rejected. While rather energy inefficient, this solution is very simple to implement and set up on a limited budget and therefore may prove to be the most practical of these two engineering solutions.

4. Motorise the sluice gate actuation and automate the startup / shutdown / restart process for the machine.

Although this recommendation does not strictly arise from the current research, in the authors' opinion, it is an essential system modification if the prototype installation is to be set up for long term hydropower generation. In the absence of automation, any shut down of the generator results in free-wheeling of the rotor, generating high levels of splash and noise and if allowed to continue unchecked, draining down the upstream water levels in the river. Such a system will require the addition of an electric motor drive at the sluice stem, in conjunction with an uninterruptable power supply to ensure shut down in the event of local grid failure, while the programming of the existing system PLC should be modified to control gate movement in addition to the generator start and shutdown process.

14.3 Fundamental Research Areas

The following areas of fundamental research extending the work of this study of the existing HPM configuration are recommended:

5. Direct experimental comparison of 6 and 12 blade rotor performance with shoe angles of 30° and 60°.

This work should test the presumption made in earlier chapters, that the performance benefit found with the 6 blade rotor was entirely due to the better pressure differential applied across the blade created by the shoe angle matching that of the blade pitch. If that assumption is correct, then a similar performance improvement would be expected if a 30° shoe angle were applied to a 12 blade rotor and, by extension to other blade pitch/shoe angle combinations. This series of tests would be well suited in scope to an MSc. research project, the results of which are of fundamental importance to the design of future machines.

6. Experimental investigation into side plate geometries and exit channel width required for best performance.

The present research has identified the importance of the exhaust cell processes to

overall machine efficiency and performance, but so far little experimental data exists to enable the most appropriate side plate profiles to be selected to promote cell ventilation and emptying with minimum energy losses. In addition, the preliminary tests described in section 9.3.1.3 suggest that there *may* be some benefit in widening the exit channel immediately downstream of the shoe profile to enable flow to exit around the sides of the advancing blade as well as under the leading edge. This could be readily clarified during this proposed test series with the scope of this work once again being suitable for an MSc research project.

7. Repeat 'time series' testing at much higher data rates.

The 'time series' data collected during the current research has proved to be invaluable, despite the inadequacy of the equipment used. Such experiments should be repeated with attention paid to the following:

a. A much higher data reading rate (500Hz to 1kHz), is required for all instruments to ensure adequate data resolution is obtained across the full machine operating range. This will also enable smoothing and filtering operations to be carried out without risk of losing essential data.
b. Great care needs to be exercised in the measurement of flow rates, particularly at very low machine speeds. These measurements are essential for peak efficiency calculations.
c. Similarly, setting up the model to minimise friction and leakage effects is important, particularly the avoidance of any intermitted contact friction during experiments.
d. Additional instrumentation could be usefully added to the tests, which should include additional pressure transducers to enable pressure variation in cells either side of a blade to be monitored, and the direct measurement of rotor shaft torque output.

8. Extend basic cell process theory to include the 'Exhaust' Phase

In the present work, very basic cell process theory is developed covering the 'Induction', 'Compression' and 'Power' phases of operation. However no theory was developed to cover the 'Exhaust' phase , despite the important impact that this process was found to

have on overall machine performance. Cell process theory needs to be extended to include the 'Exhaust' phase, taking account of the physics involved in cell ventilation, cell emptying and the kinetic energy exchanges occurring as the blade leaves the flow in the exit channel.

9. Refine cell process theory and validate through parametric testing

In the present work, complex physical processes have been modeled very simply, and considerable scope exists to refine the analysis, to relate energy exchanges more accurately to machine geometry. A more sophisticated approach could yield much useful information and should enable the empirical coefficients used in the modified performance theory to be estimated by calculation.

Any theoretical developments should be validated through parametric performance testing, and if successful, should enable machine geometry to be optimised for a given set of operating conditions in future machine designs – a potentially very significant development.

10. Extend performance theory to account for the width of the exit channel and investigate exit channel shaping to enable kinetic energy recovery.

At higher machine speeds, the behaviour of the flow in the exit channel becomes increasingly important, but is currently neglected by the present theory. It is suggested that:

a. The 3D theory of HPM performance needs to be extended to include variations in width and depth of the exit channel.
b. The exit channel needs to be designed to recover a portion of the dynamic head contained in the flow leaving the machine. Very little work has been carried out on the use of open channel diffusers for such a process and considerable scope exists for innovative design in this area. Such work would also be applicable to other higher speed water wheel concepts such as the Zuppingerrad.

14. 4 Future HPM Architectures

Chapters 11 and 12 explored how the results of the present research and cell process theory in particular should impact the geometry of future machines and the selection of power take off solutions. The implication is that the HPM is likely to evolve into a very different form from the current device in order to become commercially viable.

While the fundamental areas of research described above represent important pieces of work, it is equally important that alternative machine configurations employing the hydrostatic pressure energy exchange are developed and tested.

The following areas of study are recommended:

11. A 'Split Rotor' concept should be tested (as suggested in section 7.4.4), to enable the range of operational speeds required by the device to be reduced. This should also enable the machine to operate efficiently at lower river flow rates than is possible with the current arrangement. However, the best configuration to be adopted in order to ensure efficient cell filling and ventilation is not clear and should be investigated through a series of model tests as will be the impact of leakage flow, which may be expected to be slightly higher compared to the existing device.

12. 'High speed' rotor concepts should be developed and tested, following the principles suggested in Chapters 11 and 12. Such designs will need to avoid many of the energy loss mechanisms inherent in the original HPM configuration and are likely to incorporate:

- High angle of attack blades
- An alternate means of introducing fluid to the rotor
- Exit channel geometry designed to recover as much kinetic energy as possible from the flow.

Although much efficiency gain can be achieved with rigid, fixed blade concepts, the remaining potential of flexible and variable geometry designs should not be neglected.

13. Alternative Power Take Off and Control Configurations.

HPMs are almost unique in their low speed, and variable speed operating

characteristics, and as the experience of the prototype demonstrates, control system design is far from a trivial exercise. Although many potential solutions exist, identifying a robust, low cost solution presents a significant challenge which greatly impacts the direction of HPM machine development.

The following need to be considered:

a. Cost comparisons between variable speed generator and inverter systems using fixed ratio gearboxes, fixed speed generators using variable ratio transmission system, or some combination of the two. In evaluating the alternatives, details of the necessary control systems to meet electrical grid export requirements must be fully considered.
b. The potential to integrate the generator directly into the HPM rotor, eliminating the need for a mechanical transmission. While the cost of this approach is prohibitive for small volume manufacture, it may become a viable option in the context of the large numbers of standard units required to exploit the potential applications described in section 2.2, and should therefore be studied seriously.

References & Bibliography:

Alben, S., Shelley, M., 2004. How flexibility induces streamlining in a two-dimensional flow. *Physics of Fluids, Volume 16, Number 5*

Alexander, K.V., Giddens, E.P., Fuller, A.M. 2009. Axial-flow turbines for low head microhydro systems.*Renewable Energy 34 (2009) pp35-47*

Applegate Group, 2010. Exploring the Viability of Low Head Hydro in Colorado's Existing Irrigation Infrastructure: Interim Report – Summary of Available Low Head Turbine Technologies.*Colorado Department of Agriculture.*

Armstrong, G., Aprahamian, M., Fewings, G., Gough, P., Readre, N., Varallo, P., 2010.Environment Agency Fish Pass Manual.*Document – GEHO 0910 BTBP-E-E, Environment Agency*

Bacon, I., Davison, I., 2004. Low Head Hydro Power in the South-East of England – A review of the Resource and Associated Technical, Environmental and Socio-Economic Issues. *TV Energy 2004*.

Bassett, D.E., 1989. A Historical Survey of Low-Head Hydropower Generators and Recent Laboratory Based Work at the University of Saltford. *Ph.D. Thesis, University of Saltford, 1989.*

Baroudi, J.A., Ã, V.D. & Knight, A.M., 2007.A review of power converter topologies for wind generators. *Renewable Energy*, 32, 2369-2385.

Bodmir, G, R., 1895. *Hydraulic Motors*, Fredonia Books.

Boelli, M., 2008. Promotion of Small Hydropower in Switzerland - an overview, *Proc. Hidroenergia 2008*

Bozhinova, S., Petkova, S., Kisliakov, D., Muller, G., Schneider, S., 2012: Large Scale Model design and monitoring -HPM. *EC Services Deliverable Report No. 3.2*

Bozhinova, S., Hecht, V., Kisliakov, D., Muller, G., Schneider, S., 2012: Hydropower converters with head differences below 2.5 m. *Energy*, *Proc. Inst. Civil Engineers 2012*

Brada, K. 1999. Wasserkraftschnecke ermoglicht Stromerzeugung uber Kleinkraftwerke. *Maschinenmarkt Wuzburg, Mitteilung 14, 52-56*

Brinnich, A. 2001. Hydropower StemPressureMachine. *Company article originally availableat: www.oewatec.de*

Brinnich, A. 2011. Hydropower StemPressureMachine. *Company article available at: www.wicon.at, (accessed 7th February 2013)*

British Hydropower Association, 2005. A guide to UK Mini-Hydro Developments, *The British Hydropower Association, 2005*

British Hydropower Association, 2012. The feed-in Tariff Scheme, *The British Hydropower Association, 2012*

BS ISO 8363:1997: Measurement of liquid flow in open channels - General guidelines for the selection of method: *British Standards Institute, 1997*

BS ISO 1438:2008: Hydrometry- Open channel flow measurement using thin-plate weirs: *British Standards Institute, 2008*

Datos 300- 225 generator, 2011. Manufacturers Test Report, *Permagsa S.A. 18-1-12*

DoECC , 2010. England and Wales Hydropower Resource Assessment - Final Report, *Department of Energy & Climate Change, October 2010*

Durin, R., 2010. ECO-Turbines : A new sector for pico- and micro- hydropower without threats to watercourses. In *Proc. Hidroenergia 2010*.

Eichenberger,P., Scherrer, I., Chapallaz, J., Wiget, M. Evaluation von Ultra-Niederdruckkonzepten fur Schweizer Flusse, *Bundesamt fur Energie BFE, Juli 2011*

Entec UK, 2010. Mapping Hydropower Opportunities and Sensitivities in England and Wales, *Environment Agency.*

Environment Agency, 2009.*The environmental assessment of proposed low head hydropower developments*, Environment Agency.

ESDU 70015: Fluid Forces and Moments on Flat Plates: *Engineering and Sciences Data Unit, 1970*

ESDU 80024: Blockage Corrections for Bluff Bodies in Confined Flows: *Engineering and Sciences Data Unit, 1998*

Etnier, S., Vogel, S., 2000. Reorientation of daffodil *(Narcissus: Amaryllidaceae)* flowers in wind: drag reduction and torsional flexibility. *American Journal of Botany 87: 29-32*

ETSU, 1989. Small Scale Hydroelectric Generation Potential in the UK, *Energy Technology Support Unit, the Department of Energy, 1989*

Frank, N.W. & Toliyat, H.A., 2009. Gearing Ratios of a Magnetic Gear for Wind Turbines.*Proc. IEEE*, 1224-1230.

Gallagher, P. and McGregor, R. C., 1986, 'Slamming simulations: an application of computational fluid dynamics',*Proceedings XVI Symposium on Naval Hydrodynamics,* Berkeley, CA,

Goring, O., 2000. Wiring Up the Thames. *International Water Power & Dam Construction*, (November), 34-35.

Gosselin, F., Langre, E., Machado-Almeida, A., 2010. Drag reduction of flexible plates by reconfiguration. *Journal of Fluid Mechanics (2010), Volume 650, pp 319-341*

Gotoh, M., Kowata, H., Okuyama, T., Katayama, S., 2000. Damming-up Effect of a Current Water Wheel set in a Rectangular Channel. World Renewable Energy Congress VI, pp 1615-1618.

Gotoh, M., Kowata, H., Okuyama, T., Katayama, S., 2001. Characteristics of a current water wheel set in a rectangular channel. Proceedings of FEDSM'01, ASME Fluids Engineering Division Summer Meeting, 2001

Gulliver, J. & Arndt, R., 2006. Hydropower Engineering Handbook. *McGraw Hill, New York,*

Hamill, L. 2001. Understanding Hydraulics, 2nd Edition. *Palgrave McMillan.*

Hansson, H.G., 1977. Development of the Kaplan Turbine. *Water Power and Dam Construction*

Harder, D.L., Speck, O., Hurd, C.L., Speck, T. 2004.Reconfiguration as a Prerequisite for Survival in Highly Unstable Flow-Dominated Habitats. *Journal of Plant Growth Regulation, (2004) 23:98-107*

Harvey, A., 1993. *Micro-Hydro Design Manual*, Practical Action Publishing.

Heller, V. 2011. Scale effects in physical hydraulic engineering models, *Journal of Hydraulic Research Vol 49, No. 3 (2011), pp. 293-306*

Hoerner, S.F., 1965. Fluid-Dynamic Drag. *Hoerner Fluid Dynamics, Bakersfield, California.*

HydroWatt Company Web Site: *www.hydrowatt.de/sites/english/gallery/g-wr-06.htm*

Ingram, G., 2009. Basic Concepts in Turbomachinery. *Ventus Publishing*

Kane, M. & Sison-lebrilla, E., 2006. Statewide Small Hydropower Resource Assessment. *Contract*, (June).

Kibel, P., Coe, T., 2008. Archimedes Screw Turbine Fisheries Assessment. Phase 2: Eals and Kelts, *Fishtek Consulting Ltd.*

Klaka, K., Penrose, J.D., Horsley, R.R., Renilson, M.R., 2005. Hydrodynamic tests on a fixed plate in uniform flow. *Experimental Thermal and Fluid Science 30 (2005) pp 131-139*

Krogstad, P.,A., 2009. Introduction to Hydraulic Machinery. *Lecture notes for course TEP 4135 NTNU - Trondheim.*

Langre, E., 2008. Effects of Wind on Plants. *Annual Review of Fluid Mechanics 2008:40:141-168*

Lashofer, A., Kaltenberger, F., Pelikan,B. 2011. Wie gut bewahrt sich die Wasserkraftschnecke in der Praxis?. *WasserWirtschaft 7-8, 2011*

Linton, N., Muller, G. & Batten, W., 2010. Potential benefits of flexible blades applied to hydrostatic energy converters in very low head applications .In *Proc. Hydroenergia 2010*.

Linton, N., 2009. The Design and Development of Hydrostatic Pressure Machines for Small Hydropower Applications. *MSc Thesis, University of Southampton, School of Engineering, 2009*.

Majeed, Z., 2006. Developing Hydropower Schemes on Existing Irrigation Networks. *Water Management*, (September 2006), 25 - 27.

Malcherek, A., Kulisch, H., Maerker, C., 2010. The Steffturbine - a small hydropower generating device based on a continuous belt. I*nternal Report available at www.steffturbine.com accessed 7th February 2013*

Mayo, W.,L., 1945. Analysis and Modification of Theory for Impact of Seaplanes on Water. *Report No. 810*,*National Advisory Committee for Aeronautics*, *Langley Field*, (August 20, 1945)

McGarry, L. 1999: Quotation taken from The West Wing, Series 2, Episode 12, *Sorkin, ODonnel & Antonio, Warner Bros Entertainment.*

Mead & Hunt, 2009. Feasibility Study for Hydropower, Mississippi River Lock and Dam Nos. 20,21 and 22. *FERC Project Nos. 12723, 12724 & 12725 City of Quincey*

Mosonyi, E.1987: Water Power Development: Volume 1 - Low-Head Power Plants 3rd Edition, *AkademiaiKiado, Budapest, 1987*

Muller, G., Bozhinova, S., Hecht, V., Kisiakov, D., Schneider, S., 2013. Review of Hydropower converters for very low head differences below 2.5m. *Manuscript submitted to Journal of Hydraulic Research*

Muller, G. & Kauppert, K., 2002. Old watermills — Britain ' s new source of energy ? *Civil Engineering*, 150(November), 178-186.

Muller, G. & Senior, J., 2009. Simplified theory of archimedian screw.*Journal of Hydraulic Research, Vol.47, No.5 (2009) pp. 666-669*

Muller, G., Saenger, N., Schneider, S., Batten, W., 2012.Empirical Framework for HPM Converter. Internal Task Report: Task 2.1, Hylow Project.

Muller, G. & Wolter, C. 2004. The breast-shot waterwheel: design and model tests. *Proceedings of the Institution of Civil Engineers, Engineering Sustainability 157, 2004 pp. 1-9*

Narrain, P., Wright, N., 2012. Converter Optimisation. *Internal Task Report: Task 9.3, Project Hylow.*

Nguyen Minh Duy 2010. Micro Hydroelectric Power Plant with Chain Turbine. *Project Report: accessed via www.frenchriverland.com/chain_turbine_by_nguyen_minh_duy.htm*

(NHE) Nepal Hydro Electric pvt: picture accessed via: *www.nhe.com.np/crrent-marsyangdi.htm*

Paish, O., 2002. Small hydro power : technology and current status. *Renewable and Sustainable Energy Reviews*, 6, 537-556.

Paudel, S., Linton, N., Zanke, U., Saenger, N., 2013: Experimental investigation on the effect of channel width on flexible rubber blade water wheel performance, *Renewable Energy*, Vol. 52 p. 1-7

Payne, G.S. et al., 2007. Efficiency and dynamic performance of Digital Displacement hydraulic transmission in tidal current energy converters. *Proc. IMechE, Part A: J. Power and Energy, 2007, 221(A2*, 207-218.

Pickard, C., Day, R. & Purseglove, J., 2003.*River Weirs – Good Practice Guide*, Environment Agency.

Pinches, M.J. & Ashby, J.G., 1989. *Power Hydraulics*, Prentice Hall International Ltd.

Polinder, H. et al., 2006. Comparison of Direct-Drive and Geared Generator Concepts for Wind Turbines. *Energy*, 21(3), 725-733.

PowerPal picture accessed via: www.powerpal.co.uk/pp500tim.html, *(checked January 2014)*

Rangnekar, S. & Krishnamachar, P., 2005. Small Hydropower Plants at Drops on Multi-Use Water Courses. *Shp News*, Winter.

Reinertsen, D., Smith, P., 1998, Developing Products in Half the Time, *Van NostrandReinHold, New York*

Rose, R., 2011. Linton Falls and Low Wood Hydropower Schemes - utilising Scheduled Monuments to harbour modern power generation. *UK Water Projects 2011, pgs 197 - 202*

Salter, S.H., Taylor, J.R. & Caldwell, N.J., 2002.Power conversion mechanisms for wave energy. *Proc. Instn Mech. Engineers*, 216(January), 1-27.

Schneider, G, D., 2009. Marine and Hydrokinetic Energy Technology: Finding the Path to Commercialization.

Schneider, S., 2010. Design Flow for the Partenstein Mill, *Internal Project Report, TU Darmstadt, 2010*

Schneider, S., Linton, N., Muller, G., 2012. Converter Technology Development - HPM and HPC. *Internal Task Report: Task 2.6, Project Hylow.*

Schneider, S., Muller, G., Saenger, N., 2012. Converter Technology Development - HPM and HPC. *Internal Task Report: Task 2.4, Project Hylow.*

Senior, J., 2009. Hydrostatic Pressure Converters for the Exploitation of Very Low Head Hydropower Potential. *PhD Thesis, University of Southampton, School of Civil Engineering and the Environment, 2009.*

Senior, J., 2008. The Rotary Hydraulic Pressure Machine For Low Head Hydropower Sites. *Civil Engineering*, 1-8.

Senior, J., Saenger, N., Muller, G., 2010. New hydropower converters for very low-head differences.*Journal of Hydraulic Research Vol. 48, No. 6 (2010), pp 703-714*

Senior, J., Wiemann, P., Muller, G., 2008. The rotary hydraulic Pressure machine for very low head hydropower sites. *Proceedings of Hidroenergia 2008, Bled/Dolvenia, Session 5B.*

Shigley, J.,E., Miscke, C., R., 1990. Mechanisms: A Mechanical Designers' Workbook. *McGraw-Hill, Inc.*

Singh, P., Nestmann, F., 2009. Experimental optimization of a free vortex propeller runner for micro hydro application. *Experimental Thermal and Fluid Science 33 (2009) pp 991-1002*

Turnpenny, A.W.H., Clough, S., Hanson, K. P., Ramsey, R., McEwan, D., 2000. Risk Assessment for Fish Passage Through Small Low Head Turbines, *Report No. ETSU H/06/00054/REP, Department of Trade and Industry*

Turnpenny , A.W.H., 2005. Howsham Weir Hydroelectric Project: Assessment of Fisheries Issues, J*acobs Babtie Aquatic, for MannPower Consulting Ltd.*

Turnpenny, A.W.H., O'Keeffe, N. (2005). Screening for Intake and Outfalls: a best practice guide. *Science Report SC030231. Almondsbury, Bristol: Environment Agency.*

Voith Hydro: picture accessed via: *www.voith.com/en/products-services/hydro-power/turbines/kaplan-turbines-560.html.*

Von Karman, T., 1929. The Impact of Seaplane Floats During Landing, NACA TN321, *Washington, DC.*

Warnick, C.C., Mayo, H.A, Carson, J.L., Sheldon, 1985. Hydropower Engineering, P*rentice-Hall Inc., Englewood Cliffs.*

Weisbach J. (1883). Die Satik der Bauwerke und die Mechanik der Umstriebsmachinen. 5. Auflage, Vieweg&Sohn, Braunschweig/Germany.

Wheaton-Green, K., 2006. Community Hydropower in Somerset and Dorset.

Wiemann, P. & Senior, J., 2008. Review of Current Developments in Low Head Small Hydropower. *Civil Engineering*, (1), 1-10.

Appendix: Basic Cell Process Theory

A.1 Introduction

This appendix presents the derivations of the very basic models for selected cell processes that were briefly discussed in Chapter 11.

These simple models were developed to approximate the observations and measurements presented in chapters 9 and 10, and are offered as a starting point for future workers to develop more rigorous and comprehensive theory in due course.

A.2 Blade Entry

A.2.1 Characteristics

At all but the lowest rotor speeds, blade entry is characterised by a great deal of water splash, noise and wave generation as reported in Chapters 6 and 10. The primary cause of this entry splash appears to be the very rapid increase in blade area in contact with the upstream water surface as rotation progresses from initial water contact. This blade contact results in a sharp rise in the volume of fluid being acted upon by the rotor and since water cannot pass through the blade, an impulse momentum exchange takes place as the fluid is accelerated rapidly to match the velocity of that of the blade surface.

This momentum is dissipated in the fluid by the creation of splash and generation of waves, as already observed, which are experienced by the rotor as a negative torque of large magnitude but short duration. The process appears to be related to the 'Water Slamming' phenomenon first analyzed to identify the design forces experienced by sea plane floats during landing by Von Karman in 1929 and we will adapt this classical analysis to the blade entry problem under consideration here.

A.2.2 Von Karman Analysis applied to HPM Blade Entry

Von Karman considered a sea plane float falling at an initial vertical velocity into a fluid at rest. As the float contacts the water, fluid is pushed aside by the 'chine' of the hull and a momentum exchange takes place with the aircraft slowing while the fluid is accelerated. Von Karman assumed that the volume of displaced fluid would be relatively small and so neglected buoyancy effects. In addition, the effect of change in water surface elevation was also ignored.

A key concept in this analysis was to set an arbitrary boundary on the fluid with which the float interacts by employing the concept of 'Added Mass'. In hydrodynamics, a long established approximation for the inertia of a long submerged plate undergoing acceleration is to take a virtual 'Added Mass' equal to the mass of fluid contained in a circular cylinder with a diameter equal to the width of the plate.

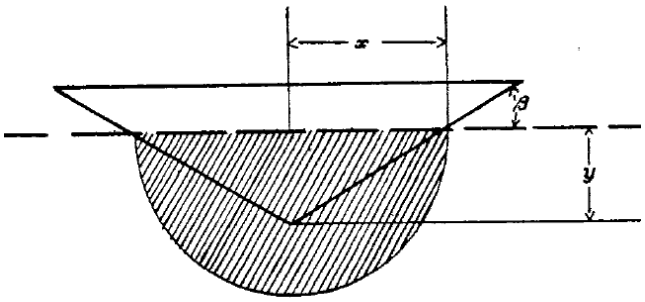

Figure A.1: The 'Added Mass' at an instant 't' used by Von Karman. (From Mayo 1945)

Since the float pierces the surface of the water and is not fully submerged, Von Karman assumed that, in his case of water slamming, only half of the 'Added Mass' would be included consisting of a semi cylinder with a diameter equal to the width of float in contact with the water surface at a given instant in time (Figure A.1).

There are key differences between Von Karman's seaplane floats and the HPM which make the analysis more complex:

1. The sea plane float analysis represents a momentum exchange where the float is brought to rest by the fluid: the blade of the HPM is effectively powered, hence will overcome initial impact forces and continue its rotation.
2. The float presents a constant hull angle to the flow and is moving in the vertical direction only. The true geometry of rotating, inclined blades in the HPM is considerably more complex (as shown in Figure A.2), and simplification is required for the analysis to proceed.
3. The blades of the HPM are effectively 'over-topped' by the fluid as the blade advances, unlike the water tight hull of the sea plane float, therefore the analysis is only valid for a limited range of rotation.

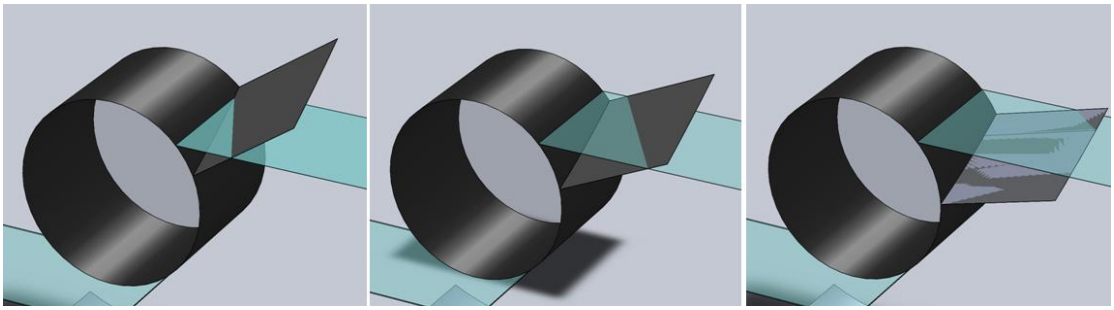

Figure A.2: Actual HPM Blade Geometry: Rotation proceeding left to right

A.2.3 Simplified Geometry

The following simplifications to machine geometry are made in this approximate analysis:

1. Blade rotation is simplified to a horizontal blade surface moving with the vertical component of velocity only: the horizontal velocity of both the blade and inflowing water is ignored (Figure A.3).
2. Observation suggests that rotation following initial blade entry into the water produces little splash and impact forces appear to be concentrated into the later stages of blade contact. In this analysis, impact is assumed to commence when the outer tip of the leading side of the blade contacts the water surface, while impact is assumed completed when the tip of the trailing side reaches the water (Figure A.4).

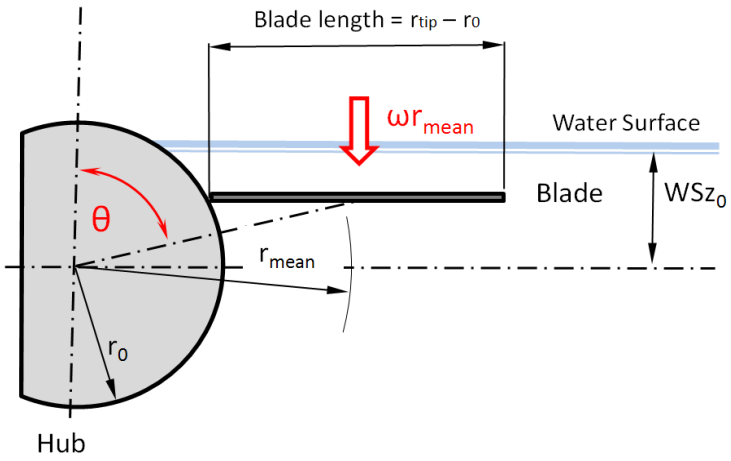

Figure A.3: Blade Motion simplified to vertical component

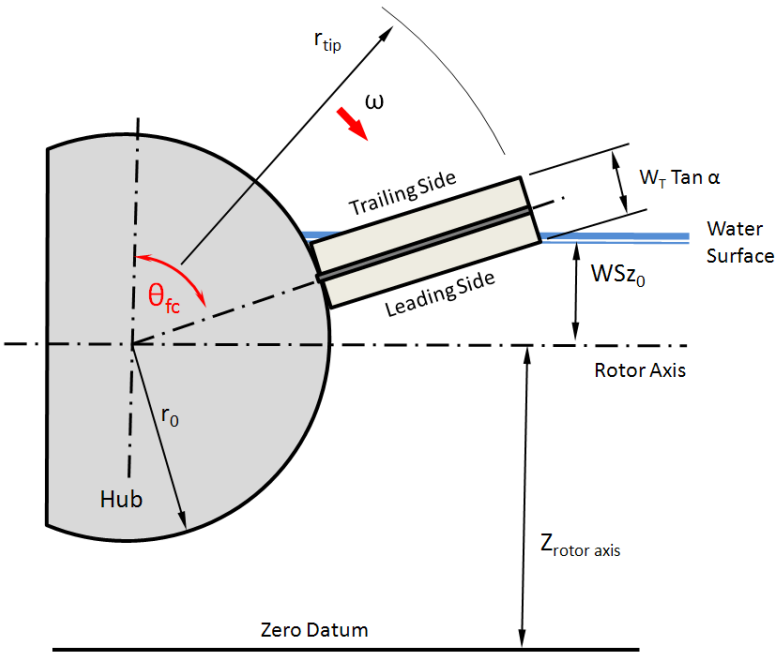

Figure A.4: Limits of rotation used in Impact analysis: the assumed start of impact is shown in the figure, and proceeds until the tip of the trailing side of the blade contacts the water surface

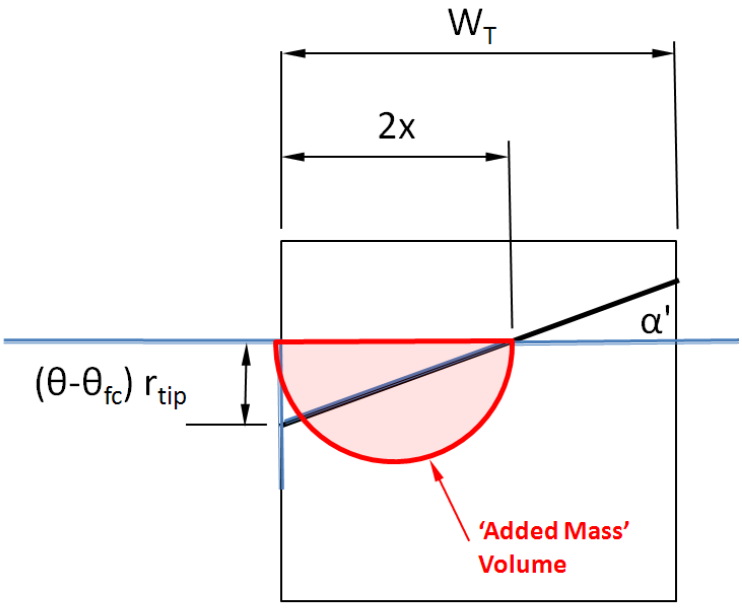

Figure A.5: 'Added Mass' at an instant

3. The HPM uses blades with an inclination angle 'α' to the horizontal. This angle is modified slightly to ensure full blade contact occurs between the limits of rotation already described – denoted as α'. As rotation progresses the leading edge of the blade penetrates beneath the water surface, and the length of blade in contact with the water '2x' increases. Figure A.5 shows the assumed semi cylinder of the 'added mass' volume as it propagates across the width of the rotor. This volume is assumed to be prismatic across the length of the blade.

A.2.4 Simplified Impact Analysis

Limits of Blade Contact

Impact is assumed to begin when the tip of the leading side of the blade contacts the undisturbed upstream water surface.

Allowing for the blade inclination angle this is approximated by:

$$WSZ_0 = \frac{W_T}{2}\tan\alpha + r_{tip}\cos\theta \qquad \text{- (A.1)}$$

Thus:

$$\theta_{fc} = \cos^{-1}\left(\frac{W_T - 0.5\ \tan\alpha}{r_{tip}}\right) \qquad \text{- (A.2)}$$

Similarly, impact is assumed to be complete when the full blade is in contact with the water surface at rotor angle 'θ_{fblade}':

$$\theta_{fblade} = \cos^{-1}\left(\frac{W_T + 0.5\ \tan\alpha}{r_{tip}}\right) \qquad \text{- (A.3)}$$

To ensure full blade contact occurs across the full width of the rotor when calculating added mass volumes in the following section, a small correction to the blade incidence angle is made:

$$\alpha' = \tan^{-1}\left(\frac{(\theta_{fblade} - \theta_{fc})r_{tip}}{W_T}\right) \qquad \text{- (A.4)}$$

Added Mass, Velocity and Momentum

At some rotation between these limits, the leading edge of the blade penetrates below the undisturbed water surface and from figure 7, the radius of the added mass volume will be:

$$x = \frac{(\theta - \theta_{fc}).r_{tip}}{2\tan\alpha'} \quad \text{- (A.5)}$$

The length of the blade of the rotor 'bl' is:

$$bl = r_{tip} - r_0 \quad \text{- (A.6)}$$

The volume of the added mass is therefore:

$$Vol_\theta = \frac{bl\pi x^2}{2} \quad \text{- (A.7)}$$

Recall that we are assuming the blade moves with the vertical component of velocity based on the mean radius of the blade:

$$V_\theta = \omega r_{mean} \sin\theta \quad \text{- (A.8)}$$

Where 'ρ' is the density of water, the momentum of the added mass is:

$$Mom_\theta = \frac{\omega r_{mean} \sin\theta \rho.bl.\pi.x^2}{2} \quad \text{- (A.9)}$$

From Newton's second law, force on the blade 'F' is:

$$F_{\theta\ 1,2} = \frac{Mom_{\theta\ 2} - Mom_{\theta\ 1}}{\Delta t} \quad \text{- (A.10)}$$

Recognising that:

$$\Delta t = \frac{\theta_2 - \theta_1}{\omega} \quad \text{- (A.11)}$$

Blade force and torque about the rotor axis are found as functions of angular velocity:

$$F_{\theta\ 2,1} = \omega^2 r_{mean} \frac{(\rho.bl.\pi)(x_2^2 \sin\theta_2 - x_1^2 \sin\theta_1)}{2(\theta_2 - \theta_1)} \quad \text{- (A.12)}$$

$$T_{\theta\ 2,1} = \omega^2 r_{mean}^2 \frac{(\rho.bl.\pi)(x_2^2 \sin\theta_2 - x_1^2 \sin\theta_1)}{2(\theta_2 - \theta_1)} \quad \text{- (A.13)}$$

This system of equations may be solved using a finite difference method for the given machine geometry and upstream water level condition.

A.3 Cell Filling

Cell filling is a fundamental process to developing rotor loss theory since it defines the distance over which the majority of fluid acceleration takes place.

In addition, if cell filling cannot be completed before the cell is closed to upstream flows by the side plate and shoe geometries, then the fill ratio of the rotor falls with a proportionate loss of extracted power.

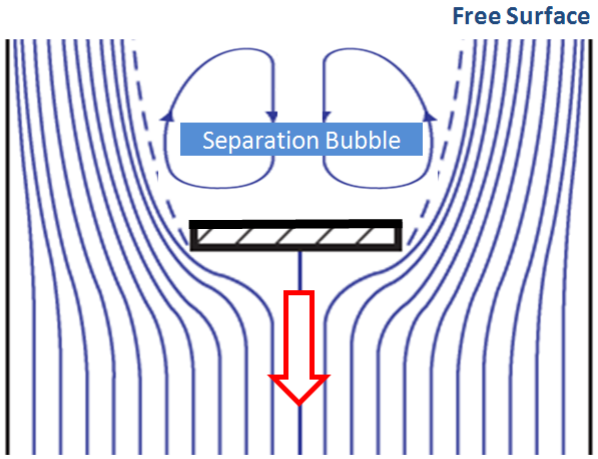

Figure A.6: Schematic of flow around advancing Blade

Cell filling therefore forms a significant part of the limiting process that sets effective maximum rotor speed.

A.3.1 Observed behavior

Prototype observations already presented in chapters 6 and 10, show that cell filling is linked to the depression in surface water elevation caused by both the impact of blade entry and the bluff body drag of passing blades. The bluff form of the blade creates a 'Separation Bubble' in the fluid behind it (Figure 9), initially extending up to the water surface.

Based on observation, we suggest the complex and highly turbulent cell filling process can be represented by the simplified form shown schematically in Figure 10a –c.

- a. On initial blade entry, the rapid displacement of fluid by the advancing blade forms a steep edge front to the surrounding water along the leading side of the blade, while a splash jet is frequently observed on the trailing side of the blade.

- b. As rotation continues, the hydrostatic pressure of the surrounding water begins to collapse the separation bubble and water starts to enter the cell. This is initially from the leading side of the blade while distinct water surface fronts begin to form along the remaining free edges.

- As rotation continues, water enters the cell from all sides of the machine, until the cell pressure is equalized and cell filling is complete.

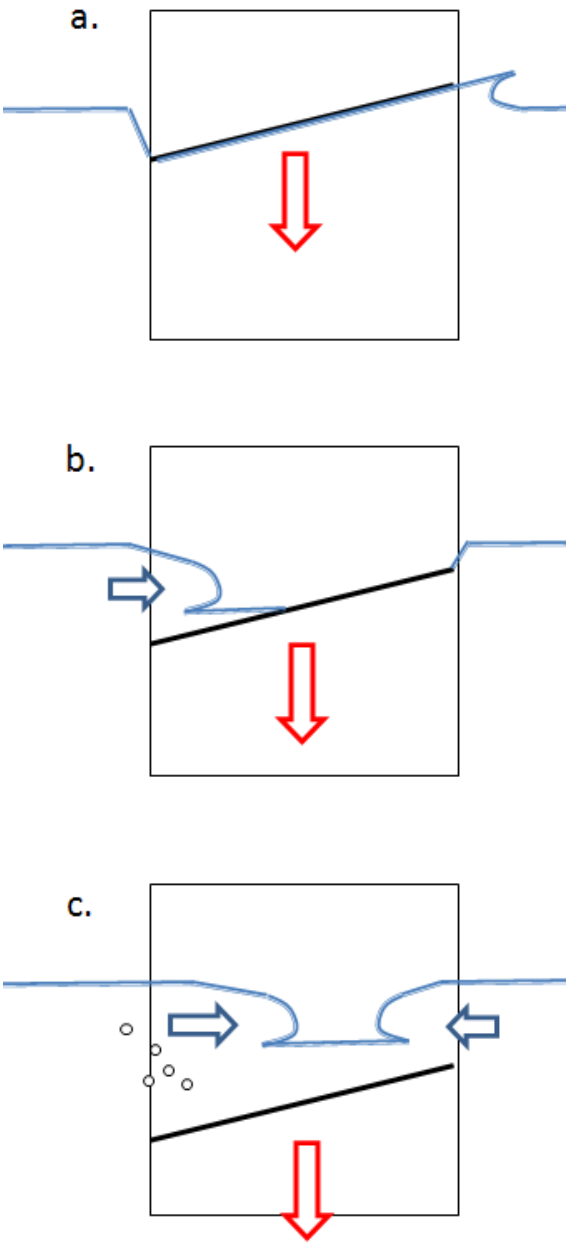

Figure A.7: Schematic of Cell Filling Process

Residual air bubbles are frequently trapped by this highly turbulent process and at laboratory scale provide a useful visual reference for judging when cell filling is complete.

A.3.2 Simplified Cell Filling Model

As a first approximation, we simplify the filling process to a series of quasi steady state conditions, with the water crossing the boundary of the cell approximating to discharge through a small submerged orifice. Inertia and acceleration effects are ignored.

We further simplify the situation by considering the blade as a horizontal plate centered at the mean blade radius of the rotor axis (Figure A.8).

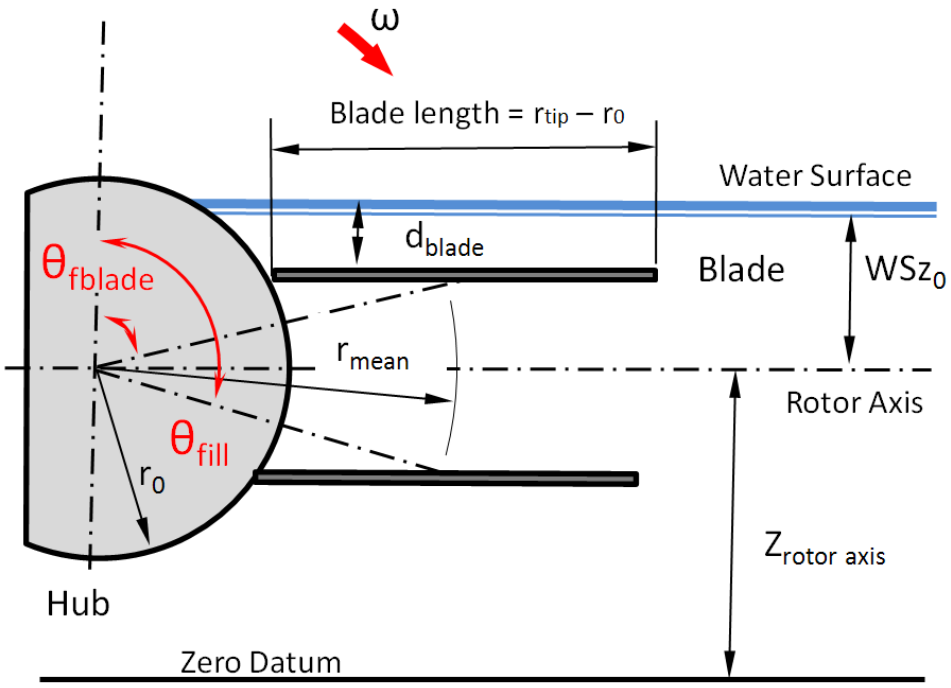

Figure A.8: Simplified Blade Geometry for Cell Filling

As the blade descends we assume that it has sufficient velocity to form the separation bubble leaving a void behind the blade at atmospheric pressure. This void increases with rotation until the cell is sealed by the following blade at which no further increase

in volume is possible.

Following initial contact with the surface of the water it is assumed that the blade creates an abrupt change in depth in the fluid along the free perimeter.

No fluid is assumed to enter the cell until the blade is in full contact with the water at angle 'θ_{fblade}'.

The initial conditions at the start of the assumed cell filling process are shown in Figure A.9.

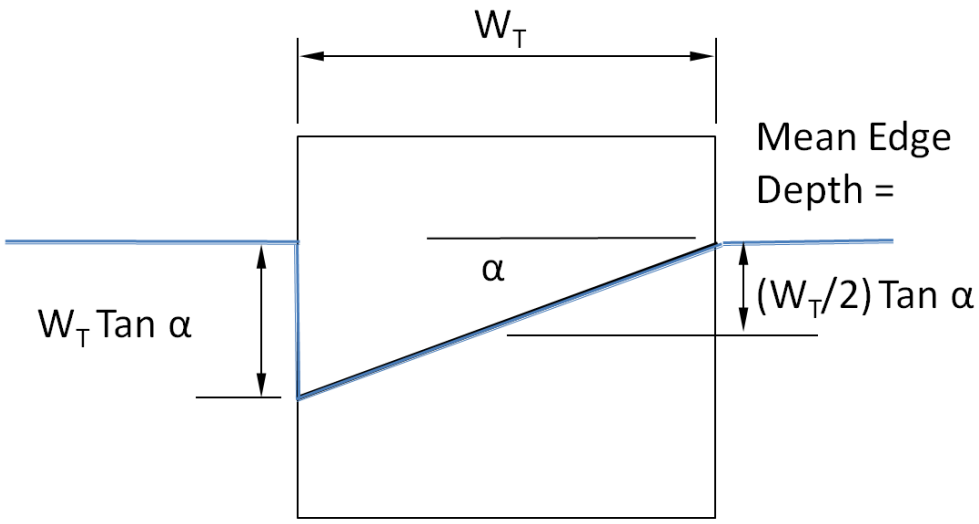

Figure A.9: Conditions at start of Cell Filling

The angle of rotation at which the blade is fully in contact with the water surface has already been given by equation A 3.

At this position, the average depth of the blade edges beneath the undisturbed water surface is shown in Figure A.9. The variation of blade edge depth with rotation angle is given by:

$$D_{blade\theta} = WSZ_0 - r_{mean}\cos\theta - 0.5W_T\tan\alpha \qquad \text{-A.14}$$

The area along the perimeter of the blade through which fluid may enter is:

$$A_{in\theta} = D_{blade\theta}(W_T + 2bl) \qquad \text{-A.15}$$

And the volume of the cell at a given angle is:

$$Vol_{Total\theta} = D^2_{blade\theta}(W_T + 2bl) \qquad \text{-A.16}$$

The notation used during the initial stages of cell filling is shown in Figure A.10.

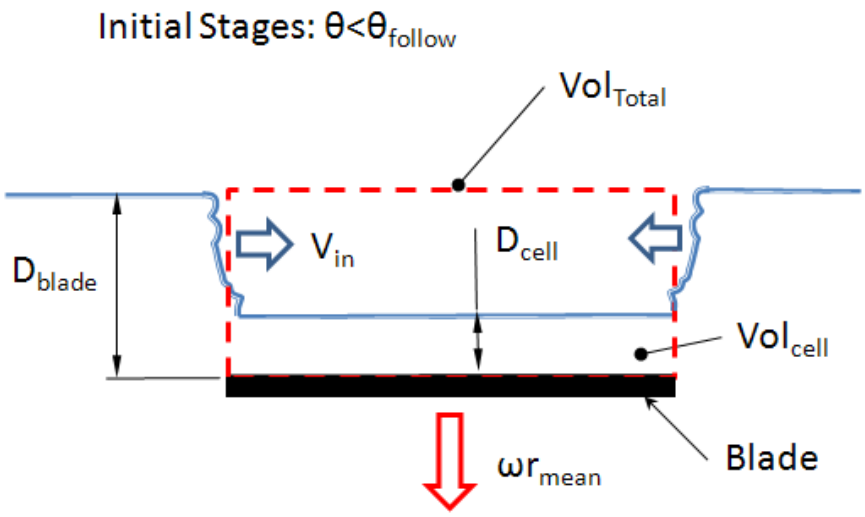

Figure A.10: Initial stage of cell filling

The velocity for ideal flow through a submerged small orifice under steady conditions can be readily shown to be:

$$V = \sqrt{g(D_{up} - D_{down})} \qquad \text{(Hamill 2006)} \qquad \text{-A.17}$$

Where:

D_{up} = upstream water depth

D_{down} = downstream water depth

g = acceleration due to gravity

Despite significant deviations from the assumptions used to derive equation 7-18, it will be used here to estimate the inflow velocity of fluid to the cell:

$$V_{in\theta} = \sqrt{g(D_{blade\theta} - D_{cell\theta})} \quad \text{- A.18}$$

'D_{cell}' is the depth of water that has already entered the cell. Initially, D_{cell} =0 but increases as cell filling progresses, the equation for which will be described a little later.

The volume flow rate at a given angle can be estimated as:

$$Q_\theta = C_{dis} V_{in\theta} A_{in\theta} \quad \text{- A.19}$$

'C_{dis}' is a discharge coefficient intended to provide some means of correcting for the deviation of conditions from the theoretical ideal. In practice the results were found to be quite insensitive to the value of C_{dis} chosen.

We assign an initial value:

$$C_{dis} = 0.65 \quad \text{-A.20}$$

The volume of fluid entering the cell over a small time period 'Δt' is:

$$\Delta Vol_{in} = Q_\theta \Delta t \quad \text{-A.21}$$

Since we will be solving the system of equations using finite difference methods and noting that:

$$\Delta t = \frac{\Delta\theta}{\omega}$$

Equation 7.35 is more conveniently re-written as:

$$\Delta Vol_{in\theta 1,2} = \frac{\Delta\theta_{1,2}}{\omega}\left(\frac{Q_{\theta 1}+Q_{\theta 2}}{2}\right) \qquad \text{-A.22}$$

The total volume of fluid in the cell then becomes:

$$Vol_{cell\ \theta} = \sum_{\theta}^{\theta_{fblade}} \Delta Vol_{in} \qquad \text{-A.23}$$

We next need to turn our attention to the depth of fluid in the cell.

Initially the cell is empty but, as fluid enters the cell it is assumed this volume is uniformly distributed over the area of the blade:

$$D_{cell\theta} = \frac{Vol_{cell\ \theta}}{bl.W_T} \qquad \text{- A.24}$$

We have now developed all the expressions required to model cell filling during the initial phases. However, the situation is complicated by the presence of the following blade which at some point comes into contact with the water surface (Figure A.11).

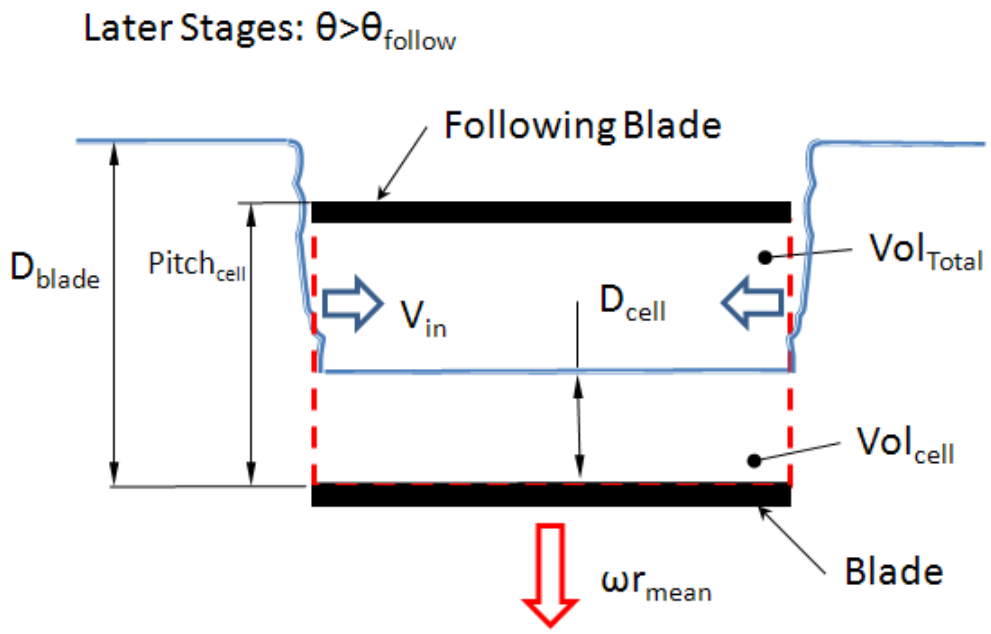

Figure A.11: Cell filling after water contact by the following blade

This requires our system of equations to be modified for all rotor angles after this point.

For a given machine geometry the 'Cell Pitch' length is a function of the number of blades fitted to the rotor:

$$Pitch_{cell} = r_{mean}\frac{2\pi}{N} \qquad \text{-A.25}$$

Where N = number of blades

When the following blade first contacts the water surface:

$$\theta = \theta_{follow}$$

And clearly,

$$D_{blade} = Pitch_{cell}$$

So

$$\theta_{follow} = \cos^{-1}\left(\frac{r_{mean}\frac{2\pi}{N} - WSZ_0 - 0.5W_T \tan\alpha}{r_{tip}}\right) \quad \text{-A.26}$$

Total volume has reached its maximum at:

$$Vol_{Total\theta} = Pitch_{cell}^2(W_T + 2bl) \quad \text{-A.27}$$

As has the perimeter area:

$$A_{in\theta} = Pitch_{cell}(W_T + 2bl) \quad \text{-A.28}$$

A further change is required to the equation 7-32 governing the inlet velocity of the flow since the following blade now closes the cell and prevents its venting to atmosphere.

Pressure within the cell will now increase with water depth as rotation proceeds:

$$V_{in\theta} = \sqrt{g\left(D_{blade\theta} - D_{cell\theta} - (D_{blade\theta} - Pitch_{cell})\right)}$$

Which simplifies to:

$$V_{in\theta} = \sqrt{g(Pitch_{cell} - D_{cell\theta})} \quad \text{-A.29}$$

Finally we introduce a term to help track how cell filling is progressing. This is the 'Fill Ratio' which we define here as:

$$Fill\ Ratio_\theta = \frac{Vol_{cell\,\theta}}{Vol_{Total\,\theta}} \quad \text{-A.30}$$

A.3.4 Estimation of Blade Drag Forces

As stated previously, cell filling is an important process defining blade drag with fluid on the upstream side, as flow is accelerated from approach to rotor velocities.

A by-product of calculating volume of water in the cell is that we effectively obtain an estimate for pressure difference across the blade during rotation from which blade

force can be estimated as follows:

The pressure inside the cell is obtained directly from the cell depth as:

$$p_{inner\theta} = D_{cell\theta}\rho g \qquad \text{-A.31}$$

Since this fluid is moving with the blade, it has no velocity relative to the blade, and therefore no correction for dynamic head loss needs to be applied.

The situation in front of the blade is a little different, with the fluid containing significant velocities due to cell filling, and turbulence.

We assume that the dynamic head in front of the blade can be averaged to the mean speed of the blade, therefore pressure in front of the blade is:

$$p_{outter\theta} = \left[D_{blade\theta} - \frac{\omega^2 r_{mean}^2}{2g}\right]\rho g \qquad \text{-A.32}$$

Therefore, Torque is given by:

$$T_{cell\ \theta} = bl.W_T r_{mean}(p_{inner\ \theta} - p_{outter\ \theta}) \qquad \text{-A.33}$$

A.4.1 Pressure Changes through the working Section

The changes in cell pressures either side of a given blade of a 12 blade rotor as it passes through the working section are summarized in the sequence of figures below.

Following the transit phase, the blade 'closes' the leading cell as it rotates between the side plates.

Pressure behind the blade is at full upstream static pressure.

The pressure in the leading cell starts at upstream pressure, but since it is now isolated by the closed blade, cell pressure must fall as energy is extracted.

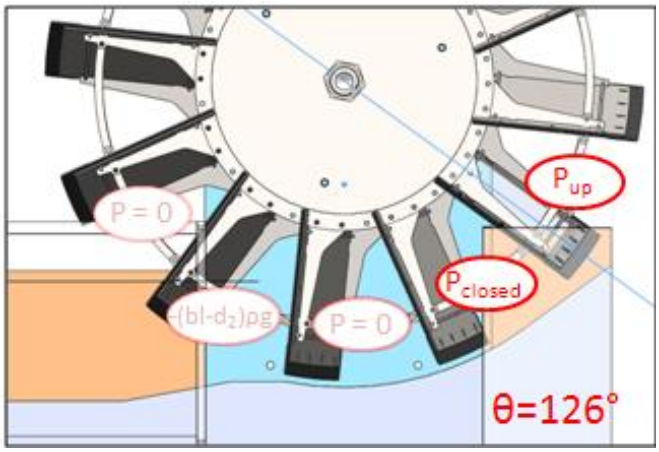

Figure A.12: The point of leading cell closure

$$p_{closed} = f(\theta) \qquad \text{-A.34}$$

And Blade force during this period of rotation is given by:

$$F_{blade\ \theta} = bl.W_T(p_{up} - p_{closed}) \qquad \text{-A.35}$$

Rotation continues until the blade ahead of the leading cell reaches the crest of the shoe profile. We make the assumption that, by this point, cell free surface pressure in the leading cell (which is of course 1 blade pitch ahead of the blade we are studying), has reduced to zero.

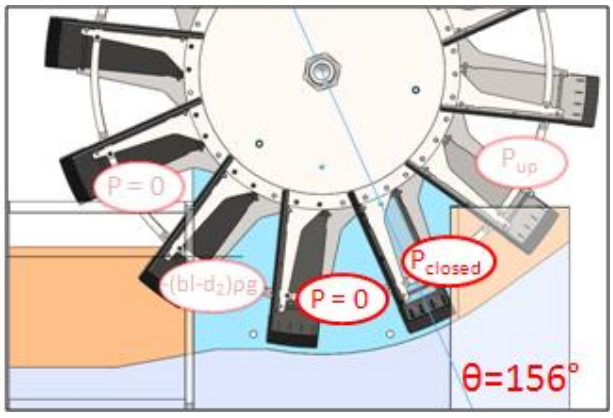

Figure A.13: During the power stroke, with the leading cell on the point of opening

If we assume a linear decline in cell pressure, and use angles in radians, pressure

during power extraction becomes:

$$p_{closed\ \theta} = p_{up}\left(1 - \frac{(\theta - 2.199)}{(3.2463 - 2.199)}\right) \qquad \text{-A.36}$$

Blade torque between θ= 126° and 156° can thus be written as:

$$T_{(126-156)} = blW_T r_{mean}(p_{up} - p_{closed}) \qquad \text{-A.37}$$

From θ = 156° to 186° the blade enters the second stage of the power stroke.

Closed cell pressure continues to fall as power is extracted. However, this is compensated for by the negative pressure formed in the leading cell shortly after opening.

It was noted in the prototype installation, that strong suction noises occurred as air was pulled past the hub and blade seals during emptying. We also observed that reducing the rate of emptying reduced this suction noise appreciably.

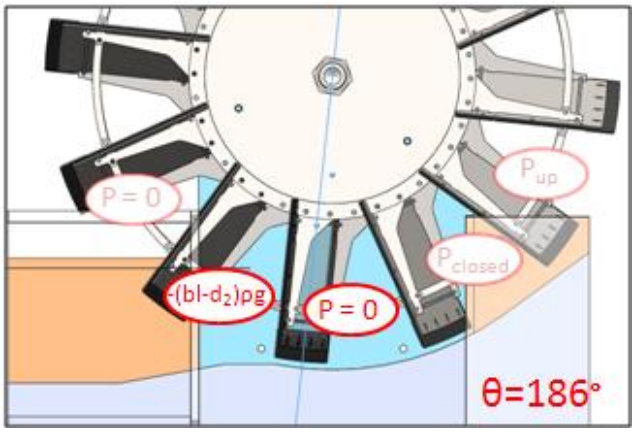

Figure A.14: At the end of the 2nd stage of the power stroke: as the blade opens a negative pressure results from lack of ventilation.

The explanation is that, as the blade clears the downstream end of the shoe profile, a gap develops between the edge of the blade and the downstream bed. This gaps acts as a submerged orifice, which increases in area as rotation continues. With the surface pressure of the cell initially at atmospheric, water exits the cell. However, this volume of fluid needs to be replaced at the top of the cell, but the only route for air to enter is via the very small gaps between the side walls and the hub seals. Losses along this inflow path are very high, resulting in a low terminal velocity for the incoming air. The volume flow rate of incoming air, being lower than the volume flow rate of outgoing

water, results in a drop in pressure above the free surface of the cell. This drop in pressure reduces the exit flow rate of water until equilibrium is restored.

In this present analysis we will consider the extreme case where no air is able to enter the cell via the hub seals.

In this event, out-flowing water almost immediately produces a balancing partial vacuum at the free surface, negative and equal to the net head between the fluid in the cell and the prevailing downstream water level. In this simple analysis we assume that this partial vacuum is maintained until the blade uncovers the side ventilation areas at θ = 218°.

Force on the blade during this stage is therefore:

$$F_{blade\ (156-186)} = bl.W_T(p_{closed} + (bl - d_2)\rho g) \qquad \text{-A.38}$$

$$T_{(156-186)} = blW_T r_{mean}(p_{closed} + (bl - d_2)\rho g) \qquad \text{-A.39}$$

Thus far, the negative pressure in the exit cell has aided power extraction. However, as the blade clears the shoe, the negative pressure applies a negative torque to the rotor.

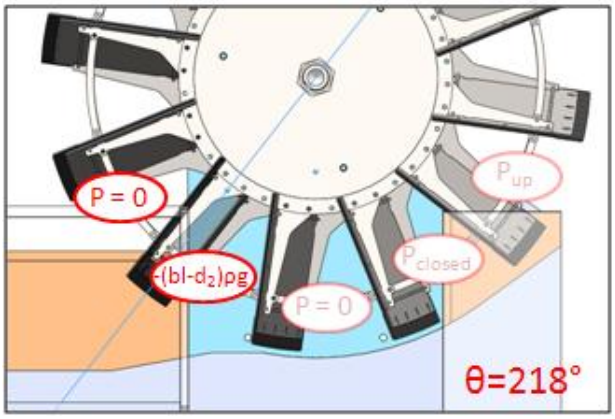

Figure A.15: With the leading cell vented to atmosphere, negative blade torque occurs.

Blade forces between θ= 186° and 218° can thus be written as:

$$F_{blade\ (186-218)} = -bl.W_T(bl - d_2)\rho g \qquad \text{-A.40}$$

And Torque:

$$T_{(186-218)} = -blW_T r_{mean}(bl - d_2)\rho g \qquad \text{-A.41}$$

Remarks:

- The above partially explains the benefit of switching from 12 to 6 blades – the P_{closed} pressure phase is eliminated and the blade experiences full up and downstream pressure differential throughout the single stage power stroke. Since the upstream side of the cell remains vented to upstream water pressure there is no fall in pressure to zero by the end of the stroke (Figure A.16).
- The weakness of the above analysis is that rotor speed is not taken into account which will inevitably impact both the magnitude and duration of the pressure reduction due to cell emptying. Since it neglects both the real leakage of air (which reduces the magnitude of negative pressure at low rotor speeds) and inertia effects (which seem to increase negative pressures at higher rotor speeds) these errors are likely to be significant.

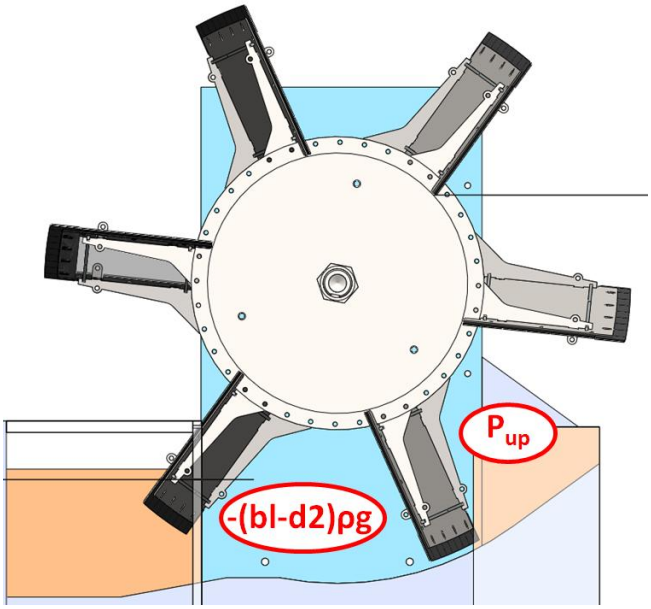

Figure A.16: Higher Blade pressure differences occurring in the working section of a 6 blade rotor.